Fakultät für Mathematik und Physik
Albert-Ludwigs-Universität Freiburg

QCD background estimation for Supersymmetry searches with jets and missing transverse momentum with the ATLAS experiment at the Large Hadron Collider

Kathrin Störig
aus Kassel

Dissertation zur Erlangung des Doktorgrades der Fakultät für Mathematik und Physik der Albert-Ludwigs-Universität Freiburg im Breisgau

Dekan:	Prof. Dr. Michael Růžička
Referent:	Prof. Dr. Gregor Herten
Korreferent:	Prof. Dr. Karl Jakobs
Tag der Verkündigung des mündlichen Prüfungsergebnisses:	27.11.2012

For Askan

Preface

Some of the most interesting questions mankind might ask are closely related to the field of astro- and particle physics: What are the fundamental building blocks of our universe and how do they interact? Will there eventually be a theory that can describe everything?

During the last decades, particle collision experiments unraveled various aspects of these mysteries - and a very successful theory emerged: the *Standard Model (SM)* of particle physics: As of today's knowledge, matter consists of *fermions*, the quarks and the leptons. Among these, four fundamental interactions are known: the strong, the weak, the electromagnetic and the gravitational force. These interactions are mediated by *bosons* (force carriers). The SM, being a relativistic quantum field theory, describes the interplay between fermions and bosons, but the inclusion of gravity is still pending and not a straight-forward task.
Furthermore, the Standard Model has in total 19 independent parameters, such as the masses of particles and the strengths of the coupling, which cannot be predicted but need to be determined by measurements. Nevertheless, it has been probed in lots of high precision measurements. Quantitative predictions of the existence of the top-quark and the tau-neutrino have been confirmed successfully and besides the small, yet finite neutrino masses, which could indicate for physics beyond the Standard Model, there has been no direct hint (yet).
But various fundamental questions remain unanswered and so the SM is considered as an effective low-energy approximation of a yet unknown, but more complex theory. Some examples of those unexplained aspects of the SM are described below:

- The SM seems to be structured showing a distinct pattern of repeating properties, the *generations*. Both an explanation for the underlying structure of the model and the number of these generations is missing.

- The *matter-/ antimatter asymmetry* of the universe: everything seems to be made of matter although we expect that matter and anti-matter were originally produced in equal proportions.
- Galactic rotation curves and the cosmic microwave background provide strong evidence for the existence of additional matter than we cannot see, the *dark matter*.
- The observed expansion of the universe at an accelerated rate is commonly attributed to a hypothetical form of energy, the *dark energy*, that permeates all of space.
- A *unification* of all forces would be aesthetically appealing, but the *hierarchy* between electroweak and Planck-scale is extremely large.
- From theory we expect all particles to be massless, however many particles have mass; in particular, the weak bosons are very heavy. The *Higgs-mechanism* was invented to explain how these particles get mass; it predicts the existence of an associated Higgs-boson in addition. Although recently a new bosonic particle was discovered, being compatible with the SM predictions from first observations, still all the details need to be studied in order to confirm or deny the (SM) Higgs-mechanism.

In the attempt to remedy the above problems, various extensions of the SM were developed. One aesthetically appealing solution is *Supersymmetry (SUSY)*, which imposes an additional internal symmetry between bosons and fermions and thus predicts the existence of a partner for each fundamental particle with the same quantum numbers but different spin. Chapter 1 discusses in detail the theoretical aspects necessary to understand the thesis: the SM, its unresolved problems and SUSY.

The *Large Hadron Collider (LHC)* at CERN is designed to collide protons at a nominal centre-of-mass energy of $\sqrt{s} = 14$ TeV and hosts both multipurpose experiments such as ATLAS or CMS and smaller specialized detectors for e.g. *b*- or heavy ion physics such as LHCb or ALICE. It offers excellent opportunities to search for physics *beyond the Standard Model (BSM)* because of the unprecedented energy ranges it can explore. If *squarks* and *gluinos* - the supersymmetric partners of quarks and gluons - are light enough (which is favoured by theory in order to remedy some shortcomings of the SM), they are expected to be copiously produced at the LHC. If furthermore the lightest SUSY particle is stable, it will be a perfect candidate for dark matter. While the experimental setup is introduced in Chapter 3, Chapter 2 is dedicated to more technical details such as event simulation and jet algorithms.

BSM physics has many different signatures, thus in order not to miss it, one needs to perform as much as possible *model-independent* analyses which cover large parameter spaces of those models. One of these analyses is the inclusive Supersymmetry search *with jets and missing transverse energy* in a channel without leptons, the *0-lepton* channel, where the major phase-space cuts are driven only by the available triggers. This 0-lepton channel is the most powerful due to the strong interaction yielding much higher QCD cross-sections, but on the downside it suffers from larger QCD background than e.g. channels with leptons. This thesis discusses the estimation of the QCD multijet background, one of the most challenging ones to determine, for the inclusive Supersymmetry search in the 0-lepton channel at the ATLAS experiment. Since QCD, however, is just a sub-dominant background, the precision requirement on its determination can be modest, but nevertheless it needs to be studied carefully for various reasons: the QCD cross-section is several orders of magnitude higher than a SUSY signal cross-section would be and both the experimental efficiency and theoretical predictions have a large uncertainty. Thus, data-driven (or at least semi-data-driven) estimates are of great importance.

While Chapter 4 introduces the basic physics objects, Chapter 5 concentrates on the selection of a reliable dataset and the simulations used. Both form an important building block for the actual SUSY analyses being presented in Chapter 6, holding as well basic introduction on how to determine the QCD background in SUSY searches.
Chapter 7, however, elaborates on a new approach to estimate the QCD background using an extrapolation technique, based on the $E_{\mathrm{T}}^{\mathrm{miss}}$ -dependent ratio between QCD control and signal region, including a full discussion on relevant systematic uncertainties.

Chapter 8 presents the application of the newly developed method on the *complete 2011* analysis dataset of $4.7\,\mathrm{fb}^{-1}$. How the QCD background estimation finally fits together with the other parts of the SUSY analysis to allow possible SUSY discoveries/exclusion limits, is shown in Chapter 9 together with the current exclusion limits for supersymmetric particles.
The conclusions are presented in Chapter 10.

Contents

Part I

Introduction

Chapter 1

Theory

This Section reviews the basic principles of the Standard Model (SM) of Particle physics, focusing only on those theoretical aspects necessary to understand the content of the following chapters. Special emphasis is laid on the unanswered questions in the SM, which will motivate SUSY as an extension to resolve some of these issues.
These Sections are based upon the following References [15–17].

1.1 The Standard Model of particle physics

The Standard Model [18–22] is a relativistic quantum field theory, developed over the last century. It is a gauge theory based on the non-Abelian symmetry group

$$\mathrm{SU(3)_C} \times \mathrm{SU(2)_L} \times \mathrm{U(1)_Y} \tag{1.1}$$

and describes the fundamental interactions between particles. Y refers to the hypercharge of the particles, C to the quark colour and L to left-handed fields. The SM might be one of the most successful achievements in modern physics, as it does not only provide a very elegant theoretical framework, but also describes experimental facts in particle physics with high precision [23].

The matter constituents are given as fermions (spin-$^1/_2$-particles). While gravity is not (yet) included, the strong, electromagnetic and weak interactions are carried by spin-1 gauge fields introduced to preserve local gauge symmetry: the massless photon (γ) for the electromagnetic, the eight massless gluons (g) for the strong force and three massive bosons, the $W^\pm$ and the Z, for the weak force (see Table 1.1).

	spin	mass [GeV]	coupling strength	range [fm]
gluon g	1	0	$\alpha_{\mathrm{S}} = \frac{g^2}{4\pi\hbar c} \approx 1$	< 1
photon γ	1	0	$\alpha_{\mathrm{em}} = \frac{e^2}{4\pi\hbar c} \approx \frac{1}{137}$	∞
$W^{\pm}$	1	80.399 ± 0.023	$Gm^2 = 1.01 \cdot 10^{-5}$	$< 2 \cdot 10^{-3}$
Z	1	91.1876 ± 0.0021		
graviton G	2	0	$\frac{\gamma m_{\mathrm{n}}^2}{\hbar c} \approx 5.76 \cdot 10^{-39}$	∞

Table 1.1: Basic properties of the four fundamental forces. G denotes the Fermi coupling constant, m the proton (nucleon) mass and γ the gravitational coupling constant. Note that the graviton has not yet been discovered.

matter	generation I	generation II	generation III	electrical charge	colour	weak isospin left-handed	weak isospin right-handed	spin
leptons	ν_e	ν_μ	ν_τ	0	–	$1/2$	–	$1/2$
	e	μ	τ	-1			0	
quarks	u	c	t	$+2/3$	r,g,b	$1/2$	0	$1/2$
	d	s	b	$-1/3$			0	

Table 1.2: Quarks and leptons inside the Standard Model.

The fermions can be grouped into leptons and quarks and exhibit a threefold family structure. Particles from the different families have identical properties besides their masses and flavour quantum numbers. The quarks are named *up*, *down*, *charm*, *strange*, *top*, and *beauty*; the leptons are *electron*, *muon* and *tau*.

$$\begin{bmatrix} \nu_e & u \\ e^- & d' \end{bmatrix}, \begin{bmatrix} \nu_\mu & c \\ \mu^- & s' \end{bmatrix}, \begin{bmatrix} \nu_\tau & t \\ \tau^- & b' \end{bmatrix} \tag{1.2}$$

Each quark appears in three different colours, whereas leptons are colour neutral. Therefore, quarks participate in the strong interactions, while leptons are affected only by the electroweak interactions. As neutrinos are electrically neutral, they are only affected by the weak force (see Table 1.2). For each particle there is a corresponding anti-particle with reversed inner quantum numbers such as opposite electrical charge.

$$\begin{bmatrix} \nu_l & q_{\mathrm{u}} \\ l^- & q_{\mathrm{d}} \end{bmatrix} \equiv \begin{pmatrix} \nu_l \\ l^- \end{pmatrix}_{\mathrm{L}}, \begin{pmatrix} q_{\mathrm{u}} \\ q_{\mathrm{d}} \end{pmatrix}_{\mathrm{L}}, \; l^-_{\mathrm{R}}, \; q_{\mathrm{uR}}, \; q_{\mathrm{dR}}. \tag{1.3}$$

Under $\mathrm{SU(2)_L}$ the left-handed fields are weak-isospin doublets, the right-handed fields are singlets. Within the Standard Model neutrinos are considered massless, thus only left-handed neutrinos exist.

1.1.1 The electroweak interaction

Every quantum field theory is described by its Lagrangian $\mathcal{L}$, which in general is a function of generalized coordinates (in the Standard Model the fields) and their time-derivatives. Ideally, the Lagrangian is determined by a set of symmetry requirements, leaving the action $S = \int \mathcal{L}\, d^4x$ invariant. Minimizing S one can derive the equations of motion (*Euler-Lagrange equations*). Operations, however, that leave $\mathcal{L}$ unchanged, correspond to conserved currents J_μ and conserved charges $Q = \int d^3x\, J_0$, e.g. time-invariance is connected to the conservation of energy (*Noether's theorem* [24, 25]). Another observation is the invariance of $\mathcal{L}$ under gauge transformations.

The electroweak theory is a gauge theory with the gauge group $\mathrm{SU(2)_L} \times \mathrm{U(1)_Y}$, the generators of which are called the isospin ($\mathrm{SU(2)_L}$) and the hypercharge ($\mathrm{U(1)_Y}$) operators. As this group is non-Abelian (i.e. the commutators do not commute), self-interactions between gauge bosons arise.
The requirement of local gauge symmetry results in the necessity to introduce four massless gauge fields: the local phase transformation of $\mathrm{U(1)_Y}$ is compensated by B_μ and three fields ($W^i_\mu, i = 1, 2, 3$) are related to the transformations of $\mathrm{SU(2)_L}$. Each two of the massless fields mix to form the charged ($W^i_\mu, i = 1, 2$) and neutral (W^3_μ and B_μ) bosons respectively (see below). The Lagrangian density reads as

$$\mathcal{L}_{\mathrm{EW}} = \overline{\psi}\gamma_\mu D^\mu \psi - \left(\tfrac{1}{2} tr W^{\mu\nu} W_{\mu\nu} + \tfrac{1}{4} B^{\mu\nu} B_{\mu\nu}\right) \tag{1.4}$$

with the contravariant derivative

$$D^\mu = i\partial^\mu - g\,\mathbf{T}\cdot\mathbf{W}^\mu - g' Y B^\mu \tag{1.5}$$

where $\mathbf{T}$ is the weak isospin, g and g' denote the couplings. The field strength tensors $W_{\mu\nu}$ and $B_{\mu\nu}$ are defined as

$$\mathbf{W}_{\mu\nu} = \partial_\mu \mathbf{W}_\nu - \partial_\nu \mathbf{W}_\mu - ig\,[\mathbf{W}^\mu, \mathbf{W}_\mu] \tag{1.6}$$

$$B_{\mu\nu} = \partial_\mu B_\nu - \partial_\nu B_\mu. \tag{1.7}$$

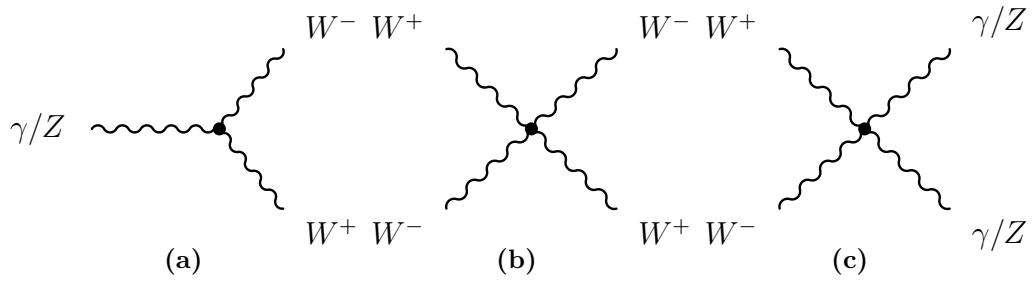

Figure 1.1: Gauge boson self interaction vertices of electroweak theory. $\mathrm{SU}(2)_L$ does not contain purely neutral gauge boson vertices, thus a pair of charged W bosons is always present.

Cubic and quartic self-interactions between the gauge fields are given rise due to the quadratic term in the field strength $\mathbf{W}_{\mu\nu}$ (see Figure 1.1). The coupling strength g is the same as in the fermionic part.

The interactions of fermionic fields and gauge bosons, contained in the derivative in the Lagrangian (see Equation (1.4)), result in *charged-current interactions* with the boson field $W_\mu^\pm \equiv {}^1/\sqrt{2}\left(W_\mu^1 \mp W_\mu^2\right)$. As a result, only left-handed fermions and right-handed anti-fermions couple to the $W^\pm$, thus parity $\mathcal{P}$ (the *symmetry between left and right*) is broken as well as the charge conjugation $\mathcal{C}$ (the *symmetry between particles and antiparticles*). However, $\mathcal{CP}$ is conserved.

The decay channels of the W^- are given by

$$W^- \to e^-\overline{\nu}_e,\ \mu^-\overline{\nu}_\mu,\ \tau^-\overline{\nu}_\tau,\ d'\overline{u},\ s'\overline{c}, \tag{1.8}$$

where q' denote the weak eigenstates, which are a mixture of the three down-type quarks and thus different from the mass eigenstates d, s, b. The unitary matrix $\mathbf{V}$ characterises the flavour mixing.

$$\begin{pmatrix} d' \\ s' \\ b' \end{pmatrix} = \mathbf{V} \begin{pmatrix} d \\ s \\ b \end{pmatrix}. \tag{1.9}$$

Furthermore, the experimental evidence of neutrino oscillations requires that neutrinos are also mixtures of mass eigenstates.

Equation (1.4) also contains interactions with the *neutral* gauge fields W_μ^3 and B_μ, which are flavour-conserving. The singlet gauge boson B_μ, however, cannot be identified with the electromagnetic field as the photon couples equally to both fermion chiralities while the Z-couplings differ for left- and right-handed particles. A mixture of the neutral

fields gives the physical fields A_μ and Z_μ

$$\begin{pmatrix} W_\mu^3 \\ B_\mu \end{pmatrix} \equiv \begin{pmatrix} \cos\theta_\mathrm{W} & \sin\theta_\mathrm{W} \\ -\sin\theta_\mathrm{W} & \cos\theta_\mathrm{W} \end{pmatrix} \begin{pmatrix} Z_\mu \\ A_\mu \end{pmatrix}, \tag{1.10}$$

which are identified as photon and Z boson field respectively. The two coupling constants g and g' determine the weak mixing angle (or *Weinberg* angle) θ_W

$$\cos\theta_\mathrm{W} = \frac{g}{\sqrt{g^2 + g'^2}}. \tag{1.11}$$

They are also related to the electric charge e,

$$g \sin\theta_\mathrm{W} = g' \cos\theta_\mathrm{W} = e. \tag{1.12}$$

Using the Dirac matrices γ^μ, γ^5, the vector and axial-vector couplings, c_V^f and c_A^f, and the fermion electric charge q_f,

$$c_\mathrm{V}^f = T_3^f - 2\sin^2\theta_\mathrm{W} q_\mathrm{f} \tag{1.13}$$

$$c_\mathrm{A}^f = T_3^f \tag{1.14}$$

the coupling of the Z boson can be written as

$$-i\frac{g}{\cos\theta_\mathrm{W}}\gamma^\mu \frac{1}{2}\left(c_\mathrm{V}^f - c_\mathrm{A}^f \gamma^5\right) \tag{1.15}$$

and the charged boson coupling is

$$-i\frac{g}{\sqrt{2}}\gamma^\mu \frac{1}{2}\left(1 - \gamma^5\right) \tag{1.16}$$

While the charged gauge bosons ($W^\pm$) couple to left-handed particles only, both the photon and the Z boson couple to particles of both chiralities.

Gauge symmetry forbids mass-terms both for gauge bosons and fermionic fields, as these would explicitly break the gauge symmetry by mixing the left- and right-handed fields and destroy the renormalisability. The generation of the gauge boson masses through the Higgs-mechanism via spontaneous symmetry breaking will be discussed in Section 1.1.3.

1.1.2 The strong interaction

The large number of observed hadronic states is a clear indication for the existence of a deeper level of elementary constituents of matter, the *quarks*. The theory describing the interactions between these particles is called *Quantum Chromodynamics (QCD)*. QCD is based on the gauge group $\mathrm{SU(3)_C}$, where C stands for the colour and represents another quantum number, introduced to explain bound states composed of obviously identical quarks (e.g. the hadrons made of sss), which are otherwise forbidden by the Fermi-Dirac statistics.

The Lagrangian of QCD reads

$$\mathcal{L}_{\mathrm{QCD}} = \bar{q}\gamma_\mu D^\mu q - \frac{1}{4}\mathbf{G}_a^{\mu\nu}\mathbf{G}^a_{\mu\nu} \tag{1.17}$$

with the contravariant derivative

$$D^\mu = i\partial^\mu - g_\mathrm{s}\,\frac{\lambda^a}{2}\cdot\mathbf{G}^\mu_a \tag{1.18}$$

and the gluon field strength tensor

$$\mathbf{G}^a_{\mu\nu} = \partial_\mu\mathbf{G}^a_\nu - \partial_\nu\mathbf{G}^a_\mu - g_\mathrm{s}f^{abc}\mathbf{G}^b_\mu\mathbf{G}^c_\nu \tag{1.19}$$

where g_s denotes the coupling constant of the strong interaction, $\mathbf{G}^a_\mu\,(a = 1, 2, \ldots, 8)$ the 8 gluon fields, $f^{abc}\,(a, b, c = 1, 2, .., 8)$ the real and totally anti-symmetric structure constants and $\frac{1}{2}\lambda^a$ the generators of the SU(3) group. The third term in Equation (1.19) is the result of the SU(3)-matrices not commuting.

This Lagrangian can be decomposed into three main parts:

$$\mathcal{L}_{\mathrm{QCD}} = \mathcal{L}_{\mathrm{quark}} + \mathcal{L}_{\mathrm{int}} + \mathcal{L}_{\mathrm{gluon}}. \tag{1.20}$$

$\mathcal{L}_{\mathrm{quark}}$ describes free quarks of a given colour and flavour and generates the free Dirac equation for spin-1/2-particles. Just as the photon in QED, the spin-1 gluon field interacting with these quarks restores the local gauge invariance, resulting in the quark-gluon interaction term:

$$\mathcal{L}_{\mathrm{int}} = g_\mathrm{s}\,\overline{q}_\mathrm{i}\frac{(\lambda^a)^i_\mathrm{k}}{2}\gamma^\mu q^k\mathbf{G}^a_\mu. \tag{1.21}$$

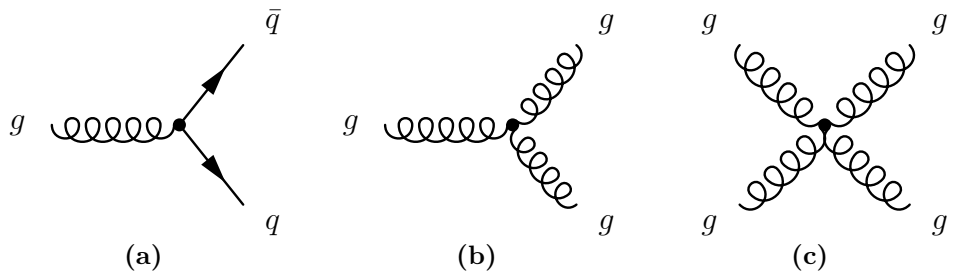

Figure 1.2: Interaction vertices of QCD.

The indices i, k represent the colour. In contrast to QED, with the photon being uncharged, the gluons carry two colour charges, leading to gluon-gluon interactions. Due to the self interactions among gluons the coupling strength of the strong interaction increases with distance. As a result, both free quarks and free gluons cannot be observed experimentally (they are *confined* within colour singlets). The colour-neutral bound states are divided into two categories: pairs of quarks, the *mesons (M)*, and groups of three quarks, the *baryons (B)*. Other combinations such as groups of four or five quarks are currently being searched for, however, conclusive evidence of their existence has yet to be found.

$\mathcal{L}_{\text{gluon}}$ finally describes the propagation of the gluon fields. Local gauge invariance once again implies that the gauge bosons are massless. In contrast to its QED analogon $B_{\mu\nu}$, the gluon Lagrangian is more complicated and generates for triple and four gluon vertices (see Figure 1.2). Despite the gluons being massless, however, the range of the strong interaction is limited.

While for long distances the strong coupling strength is too large to use perturbation theory (and effective theories or phenomenological models are required), with the vanishing coupling strength on short scales perturbation theory does describe the asymptotically free quarks and gluons.

1.1.3 The Higgs mechanism

Reviewing the previous sections, one finds an impressive theoretical framework that already incorporates QED, QCD, gauge boson self-interactions, renormalisability through gauge symmetry and electroweak unification etc. Still, experimental evidence points out a weak point of this theory: all particles, especially the gauge bosons, are considered massless but measurements show that $W^{\pm}$ and Z are massive particles and only the photon and gluons, γ and g, are indeed massless (see Table 1.1).

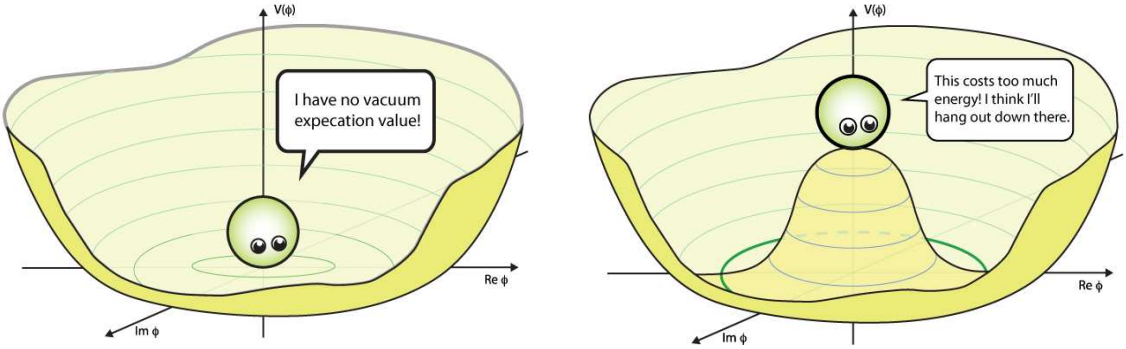

(a) (b)

Figure 1.3: This is the ground state of the Higgs-Potential for $\lambda > 0$, $\mu^2 > 0$ (see Figure 1.3a) and $\mu^2 < 0$ (see Figure 1.3b). Pictures taken from Reference [26].

As any mass-like terms of the form $\frac{M^2}{2} W_\mu W^\mu$ would destroy local gauge invariance, in order to generate the masses of the heavy gauge bosons a different approach has to be chosen: the gauge symmetry must be broken, but for the sake of renormalisability, the Lagrangian must still be fully symmetric. If a subgroup of the gauge group does not leave $\mathcal{L}$ invariant, this can be achieved with a degenerate set of states of minimal energy transforming non-trivially under those transformations instead. By selecting one of these degenerate states as ground state, the symmetry is said to be *spontaneously broken (SSB)*. A physical example of such a systemis provided by a ferromagnet where in the ground state all electron spins are aligned into one arbitrary direction. In the case of the Standard Model, this means there is a symmetric Lagrangian with a non-symmetric vacuum.

Starting with a complex scalar field Φ and a certain potential V,

$$\Phi(x) = \begin{pmatrix} \Phi^+ \\ \Phi^0 \end{pmatrix} = \frac{1}{\sqrt{2}} \begin{pmatrix} \Phi_1 + i\Phi_2 \\ \Phi_3 + i\Phi_4 \end{pmatrix}, \tag{1.22}$$

$$V(\Phi) = \mu^2 \Phi^\dagger \Phi + \lambda \left(\Phi^\dagger \Phi\right)^2, \quad \lambda > 0, \tag{1.23}$$

the Lagrangian $\mathcal{L}$ is invariant under SU(2), where $\Phi(x) \to \Phi'(x) \equiv e^{i\theta}\Phi(x)$.

$$\mathcal{L} = (D_\mu \Phi)^\dagger (D^\mu \Phi) - V(\Phi) \tag{1.24}$$

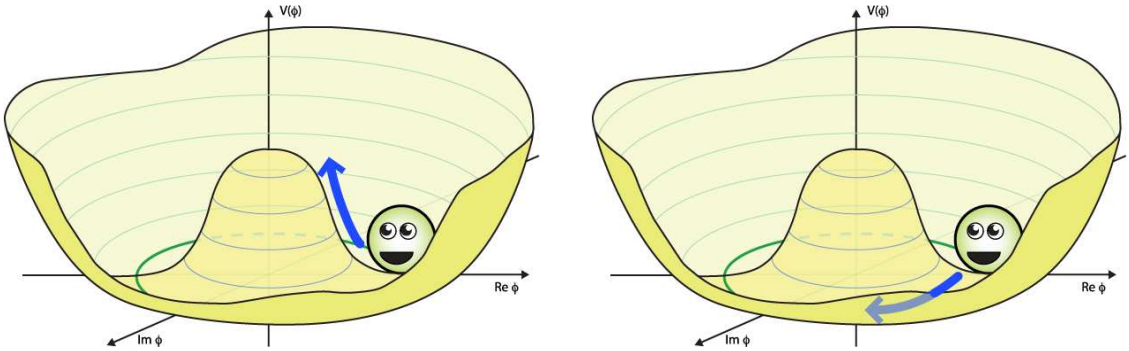

(a) **(b)**

Figure 1.4: Figure 1.4a illustrates a massive state φ_1, Figure 1.4b however a degenerate state with minimal energy φ_2: a so-called Goldstone boson. Pictures taken from Reference [26].

With $\mu^2 > 0$, the only minimum at $|\Phi| = 0$ is trivial, describing a massive scalar particle with mass μ. Selecting $\mu^2 < 0$, the ground state of V is now degenerate (see Figure 1.3) and determined by

$$\Phi^\dagger\Phi = \frac{1}{2}\left(\Phi_1^2 + \Phi_2^2 + \Phi_3^2 + \Phi_4^2\right) = -\frac{\mu^2}{2\lambda} \equiv \frac{v^2}{2}, \quad V\left(\Phi_0\right) = -\lambda v^4. \tag{1.25}$$

Due to the phase invariance of $\mathcal{L}$, the number of states with minimal energy is infinite and the symmetry gets spontaneously broken by choosing a particular solution, such as $\Phi_1 = \Phi_2 = \Phi_4 = 0$ and $\Phi_3 = v$, resulting in the vacuum expectation value

$$\langle\Phi\rangle = \frac{1}{\sqrt{2}}\begin{pmatrix}0\\ v\end{pmatrix}. \tag{1.26}$$

By parametrising the excitations of the ground state as $v + \varphi_1(x) + i\varphi_2(x)$ (φ_1, φ_2 real scalar fields) and reinserting the rewritten field into the Lagrangian, it follows that φ_1 describes a massive state while φ_2 describes massless excitations along the direction which leaves the potential unchanged (see Figure 1.4).

This general property of such a SSB of a continuous symmetry, the existence of massless excitations, is known as the Goldstone theorem.

Now applying the same potential V on the Standard Model Lagrangian, the results obtained are very similar. In particular, the vacuum expectation value of the scalar field

reads

$$|\langle 0|\Phi_0|0\rangle| = \sqrt{\frac{-\mu^2}{2\lambda}}. \tag{1.27}$$

More details about the Higgs-mechanism can be found in [27–30].
Due to the spontaneously breaking of the symmetry by choosing an explicit value for Φ, the $\mathrm{SU(2)_L} \times \mathrm{U(1)_Y}$-symmetry gets broken with only the electromagnetic subgroup $\mathrm{U(1)_{QED}}$ surviving as an unbroken symmetry. According to the Goldstone-theorem, in total three massless states appear.

Parametrising $\Phi(x)$ in a different form with four real fields $\theta_\mathrm{i}(x), i = 1, 2, 3$ and $H(x)$

$$\Phi(x) = exp\left\{i\frac{\sigma_\mathrm{i}}{2}\theta_\mathrm{i}(x)\right\}\frac{1}{\sqrt{2}}\begin{pmatrix}0\\ v + H(x)\end{pmatrix}, \tag{1.28}$$

the fields $\theta_\mathrm{i}(x)$ are identified with the expected massless Goldstone-bosons. Only $H(x)$ remains.

Using the unitary gauge, the structure of the Lagrangian is further explored by inserting the vacuum expectation value (see Equation (1.26)) in it, thus reducing the covariant derivative to

$$D_\mu \langle\Phi\rangle = -\left[\frac{ig}{2}\begin{pmatrix}W_\mu^3 & W_\mu^1 - iW_\mu^2\\ W_\mu^1 + iW_\mu^2 & -W_\mu^3\end{pmatrix} + \frac{ig'}{2}B_\mu\right]\frac{1}{\sqrt{2}}\begin{pmatrix}0\\ v\end{pmatrix}. \tag{1.29}$$

$(D_\mu \langle\Phi\rangle)^\dagger (D_\mu \langle\Phi\rangle)$ produces several terms quadratic in the fields, which can be simplified using the Equations (1.11) - (1.14)

$$\begin{aligned}(D_\mu \langle\Phi\rangle)^\dagger (D_\mu \langle\Phi\rangle) &= \frac{1}{8}v^2g^2\left(\left(W_\mu^1\right)^2 + \left(W_\mu^2\right)^2\right) + \frac{1}{8}v^2\left(g'B_\mu - gW_\mu^3\right)^2 &(1.30)\\ &= \left(\frac{1}{2}vg\right)^2 W_\mu^+ W^{-,\mu} + \frac{1}{4}v^2\left(g^2 + g'^2\right)Z_\mu Z^\mu. &(1.31)\end{aligned}$$

This shows that, by means of the Higgs mechanism, the gauge bosons have acquired mass (see Equation (1.31)), i.e.

$$M_{\mathrm{W}}^2 = \left(\frac{1}{2}vg\right)^2 \tag{1.32}$$

$$M_{\mathrm{Z}}^2 = \frac{1}{4}v^2\left(g^2+g'^2\right) \tag{1.33}$$

$$M_{\gamma}^2 = 0 \tag{1.34}$$

The W and Z masses are related by

$$\frac{M_{\mathrm{W}}}{M_{\mathrm{Z}}} = \cos\left(\theta_{\mathrm{W}}\right) \tag{1.35}$$

which is in good agreement with experimental data.

The vacuum expectation value v of the Higgs-field is related to the Fermi-constant G_{F}

$$v^2 = 4\frac{M_{\mathrm{W}}^2}{g^2} \approx \frac{1}{\sqrt{2}G_{\mathrm{F}}} \approx (246\ \ \mathrm{GeV})^2\,. \tag{1.36}$$

Introducing a complex scalar Higgs doublet into the electroweak theory results in four additional degrees of freedom. Three of those are absorbed by the heavy gauge bosons Z and $W^{\pm}$. Since $\mathrm{U}(1)_{\mathrm{QED}}$ is not broken and the photon is thus massless, the remaining degree of freedom is associated with another physical particle, the *Higgs boson*. Besides its mass, all other parameters of the Higgs boson predicted by the SM. Fermion masses can be generated by introducing *Yukawa* couplings to the Higgs doublet,

$$\mathcal{L}_{\mathrm{Yu}} = \frac{M_{\mathrm{d}}}{v}\left(\overline{u},\overline{d}\right)_{\mathrm{L}}\begin{pmatrix}H^+\\H^0\end{pmatrix}d_{\mathrm{R}} + \frac{M_{\mathrm{u}}}{v}\left(\overline{u},\overline{d}\right)_{\mathrm{L}}\begin{pmatrix}(H^0)^*\\-H^-\end{pmatrix}u_{\mathrm{R}} + \frac{M_{\mathrm{e}}}{v}\left(\overline{\nu_e},\overline{e}\right)_{\mathrm{L}}\begin{pmatrix}H^+\\H^0\end{pmatrix}e_{\mathrm{R}} + h.c. \tag{1.37}$$

Table 1.3 gives an overview of the expected Higgs-couplings.

Having a high significance as of 5.9 standard deviations, clear evidence of a new neutral boson with a mass of 126.0 $\pm$ 0.4(stat) $\pm$ 0.4(syst) GeV has recently emerged [31], being compatible so far with the production and decay of a Standard Model Higgs boson. Figure 1.5 shows some key distributions of this observation. While the combined 95% CL exclusion limits on the production of the SM Higgs boson cover the m_H

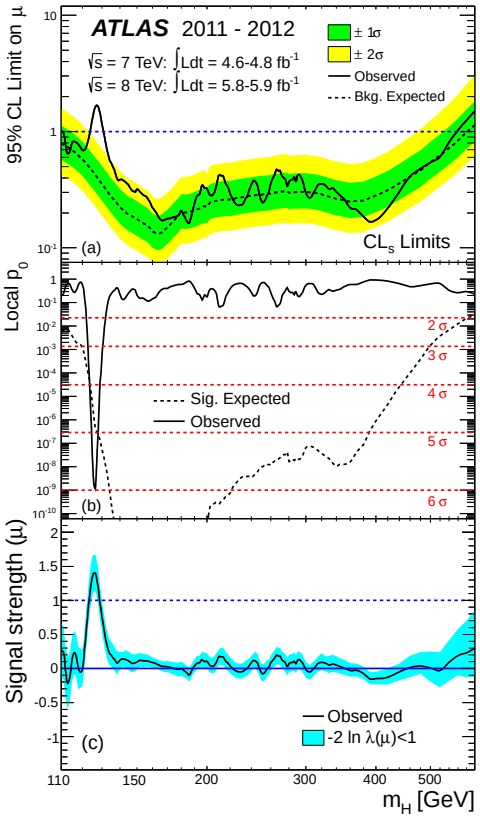

(a) Combined search results: (a) The observed (solid) 95% CL upper limit on the signal strength as a function of m_H and the expectation (dashed) under the background-only hypothesis. The dark and light shaded bands show the plus/minus one sigma and plus/minus two sigma uncertainties on the background-only expectation. (b) The observed (solid) local p_0 as a function of m_H and the expectation (dashed) for a Standard Model Higgs boson signal hypothesis ($\mu = 1$) at the given mass. (c) The best-fit signal strength $\hat{\mu}$ as a function of m_H. The band indicates the approximate 68% CL interval around the fitted value.

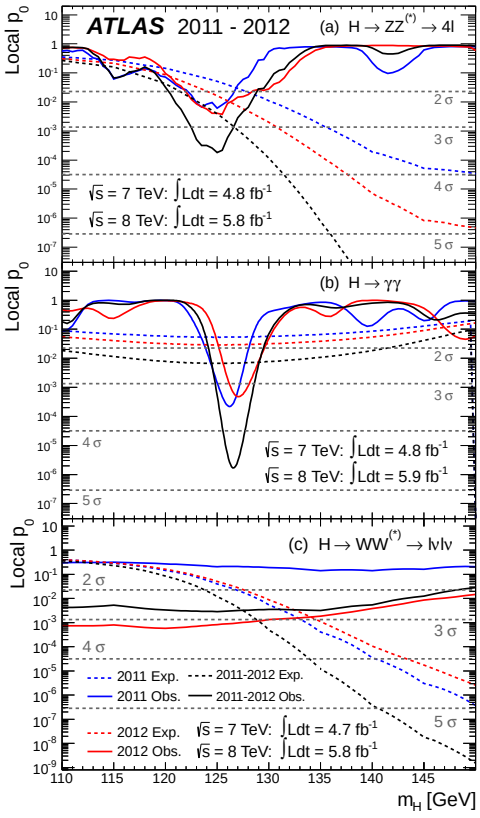

(b) The observed local p_0 as a function of the hypothesized Higgs boson mass for the (a) $H \to ZZ(^*) \to 4\ell$, (b) $H \to \gamma\gamma$ and (c) $H \to WW(^*) \to \ell\nu\ell\nu$ channels. The dashed curves show the expected local p_0 under the hypothesis of a SM Higgs boson signal at that mass. Results are shown separately for the $\sqrt{s} = 7$ TeV data (dark, blue), the $\sqrt{s} = 8$ TeV data (light, red), and their combination (black).

Figure 1.5: Key distributions of the observation of a new bosonic particle [31].

particle	coupling	strength
fermions	g_{Hff}	$-\frac{ig}{2M_{\mathrm{W}}}m_{\mathrm{f}}$
Z	g_{HZZ}	$-\frac{ig}{2\cos(\theta_{\mathrm{W}})}m_{\mathrm{Z}}g^{\mu\nu}$
W	g_{HWW}	$igm_{\mathrm{W}}g^{\mu\nu}$
Higgs self-coupling	g_{HHH}	$-\frac{3ig}{2M_{\mathrm{W}}}m_{\mathrm{H}}^2$

Table 1.3: Expected Standard Model couplings of the Higgs boson.

range from 110 GeV to 582 GeV, only the regions with 111-122 GeV and 131-559 GeV can be excluded experimentally so far. An excess of events, however, is observed near $m_H \sim 126$ GeV from a $H \to ZZ(^*) \to 4\ell$ and a $H \to \gamma\gamma$ channel, providing both fully reconstructed candidates with high resolution in invariant mass, and supported by the other channels with a wider mass resolution. The largest local significance, p_0, is found for a SM Higgs boson mass hypothesis of m_H =126.5 GeV, reaching up to 6.0 standard deviations (whereas a SM Higgs boson at that mass is expected to yield a 4.9 σ deviation).

1.1.4 Unanswered questions

Although the Standard Model provides a beautiful framework to accommodate today's knowledge about electroweak and strong interactions and passes some precision tests at the level of a few per mill (see Figure 1.6), it is considered to be *just an effective theory*. Too many important questions stay unanswered in order to consider the Standard Model as a complete description of the fundamental forces:

- Why are there exactly three nearly identical copies of fermions, with the only obvious difference being their (increasing) masses, exist? Why exactly this pattern of masses and mixings? What is the origin of the flavour structure? Why do the quarks show a similar three-fold generation structure to the leptons, although these particles do not seem to be linked otherwise. Why does the elementary charge of an electron exactly cancel with the proton charge, when the latter is a bound state and the former fundamental?

- In total more than twenty-four *free parameters* are needed to make the Standard Model work:
  While the scalar and gauge sector is described by only four free parameters which

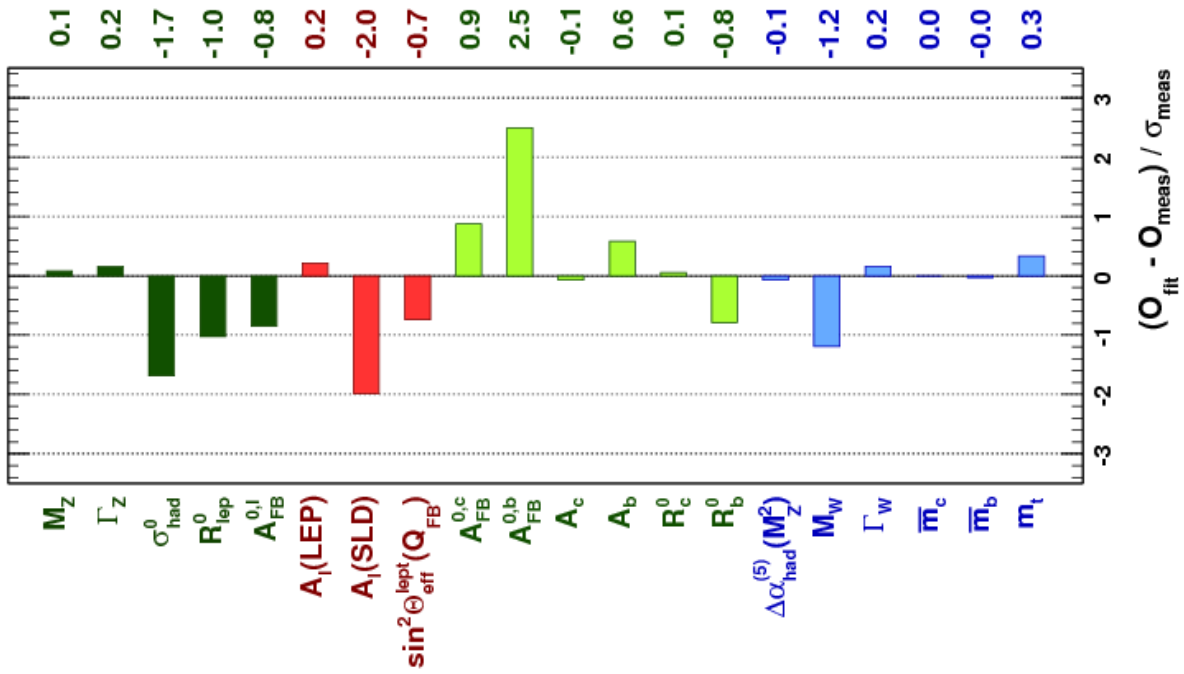

Figure 1.6: Comparing fit results of a global electroweak fit of the Standard Model with direct measurements: pull values for the complete fit (see [32]).

can be chosen as α, M_{Z}, G_{F} and M_{H}, the fermionic flavour sector has an additional thirteen parameters: nine fermion masses, three quark mixing angles and one phase. In order to accommodate non-zero neutrino masses, three more mass parameters need to be added as well as their mixings (three angles and one/three phases for Dirac-/Majorana neutrinos).
This proliferation of parameters is mainly due to the unknown Yukawa-couplings in Equation (1.37), thus the origin of masses, mixings and the family structure seem to be the main open problems of electroweak physics. The scalar sector of the Standard Model induces the problem of fermion mass generation, which is also closely related to the electroweak spontaneous symmetry breaking.

- A fundamental explanation for the observed $\mathcal{CP}$-violation is still missing. Although the Standard Model in principle offers a mechanism for $\mathcal{CP}$-violation via a single phase, occurring in the CKM-matrix which is in perfect agreement with present laboratory experiments, the source of the $\mathcal{CP}$-violation is not enough to explain the existing matter-antimatter asymmetry in the universe.

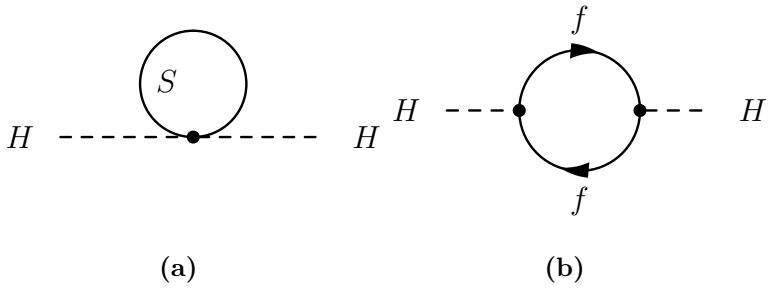

(a) **(b)**

Figure 1.7: Examples of one-loop Feynman diagrams with scalars (Figure 1.7a) or fermions (Figure 1.7b) that lead to quadratically divergent contributions to the Higgs mass.

- At low energy scales gravity is negligible because of its weakness, but around energies of the Planck scale ($M_{\mathrm{Pl}} \approx 1.2 \cdot 10^{19}$ GeV), gravitational quantum effects become strong. But until now, all attempts to include *gravity* into a quantum field theory and incorporate it into the Standard Model have failed due to general relativity not being renormalisable.

- The mass hierarchy directly induces another problem, the *fine-tuning* problem. With electroweak precision measurements indicating the Higgs mass to be around 100 GeV and assuming the Standard Model being valid up to a large energy scale, Λ (*the cut-off*), the Higgs mass suffers from corrections of $\mathcal{O}(\Lambda^2)$ (see Figure 1.7), resulting in a Higgs mass of the same size as Λ at the cut-off scale. In order to realize a Higgs mass close to the electroweak scale, the bare Higgs mass must be fine-tuned at the cut-off scale to m_H/Λ, requiring a precision up to a level of 10^{-34} when assuming $\Lambda^2 \approx M_{\mathrm{Pl}}^2$.

- There is an impressive hierarchy between the various Standard Model masses, e.g. the masses of the neutrinos and the Z boson differ by more than ten orders of magnitude.

- The three couplings in the three Standard Model gauge groups are arbitrary. Extrapolating the measurements of these couplings strengths towards higher energies (see Figure 1.8) shows a close approximation of the running couplings but no convergence in one single point. This indicates that the SM might be embedded in a more fundamental, more predictive symmetry group, broken at low energies. Such a *Grand Unified Theory (GUT)* implies a unification of the electroweak and strong interaction at a higher energy scale, the *GUT scale*.

- From astrophysics we know that only $\approx 4\%$ of the matter in the universe is baryonic, i.e. made of SM particles, while $\approx 21\%$ is considered to be so-called *cold dark*

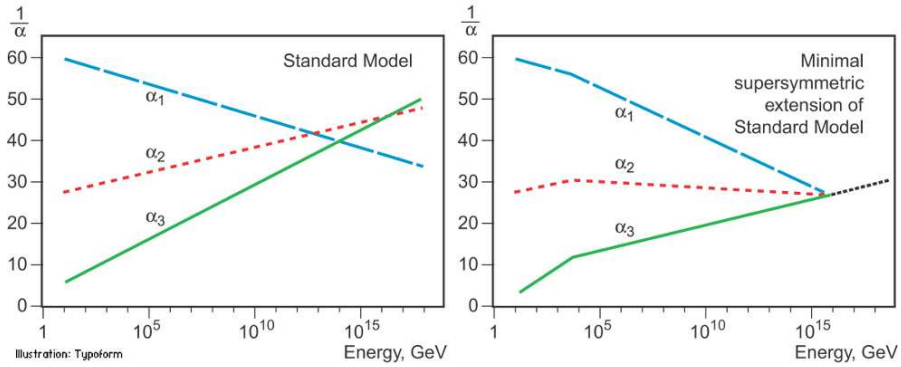

Figure 1.8: The evolution of the inverse coupling constants with energy, in the Standard Model*(left)*, these do only come close, but do not actually converge into one single point, which is realized in some of its possible extensions like SUSY- with an apparent unification at a scale around 10^{16} GeV *(right)*. Picture taken from [33].

matter (CDM) and the remaining fraction is assigned to dark energy, but neither is explained by the SM.

- Last but not least, the Higgs boson still is the last main missing piece of the Standard Model. In spite of precision electroweak measurements confirming the assumed pattern of SSB via testing quantum corrections, the assumed Higgs mechanism is not yet validated: Any deviation would be a clear indication for completely new phenomena. Although recently a Higgs-like particle was discovered at the LHC, additional precision measurement are needed to help answer some of these unanswered questions.

1.2 Supersymmetry

Several scenarios seem conceivable for extending the Standard Model. One commonly favoured model is *Supersymmetry (SUSY)* [34–42], providing possible solutions to some of the unanswered questions; the fine-tuning problem, the unification of forces (see Figure 1.8) and the origin of cold dark matter. Furthermore, SUSY is a key ingredient for string theory.

SUSY establishes a symmetry between bosons and fermions [41]. The operator Q changes the particle spin by $1/2$ like

$$Q|S\rangle \sim |S \pm 1/2\rangle \tag{1.38}$$

$$\Rightarrow \quad Q|boson\rangle \sim |fermion\rangle \tag{1.39}$$

$$Q|fermion\rangle \sim |boson\rangle. \tag{1.40}$$

With Q changing only the spin of the particles, it is expected that the mass of the superpartners (*sparticles*) is identical to those of their SM partners. But since no sparticles have been found yet, this symmetry cannot be exact and the supersymmetric Lagrangian must contain symmetry-breaking terms. Furthermore, it is not possible to identify any of the known particles as super-partners of each other, thus SUSY predicts new partners for every known SM particle. While in the SM only one Higgs-doublet is required, SUSY needs at least two of them in order to accommodate for the masses both of up and down-quarks and cancel gauge anomalies (i.e. symmetries of the Lagrangian density broken because of quantum effects, destroying renormalisability) related to the hypercharge Y.
If SUSY is realized in nature, the masses of the sparticles must be of the scale 100 GeV to 10 TeV in order to provide solutions to the SM problems:

- fine-tuning problem: Bosonic and fermionic divergences cancel each other. A SUSY breaking can be constructed such that this cancellation holds while the masses of fermions and bosons differ, the so-called *soft-breaking*.
- gauge coupling unification: a unification of the running couplings around an energy of 10^{16} GeV is possible as long as the masses of are of $\mathcal{O}(1$ TeV).
- The *lightest supersymmetric particle (LSP)*, if stable, provides a perfect dark matter candidate.
- The EWSB has to be introduced inside the Standard Model through a specific choice of parameters in the Higgs potential. In some SUSY models this occurs naturally.

But despite of all these promising features, SUSY can also not be the final theory of particle phenomena. It still leaves too many important questions of the Standard Model unanswered: SUSY does not resolve (but only shift) the hierarchy problem, explain why there are three generations of fermions or predict particle masses and mixing angles.

Instead, it introduces a large number of new parameters (as long as the breaking of the symmetry is still an unknown): even the minimal scenario contains 124 parameters. Finally, there is currently no evidence for the presence of SUSY in nature.

1.2.1 R-parity

A general supersymmetric Lagrangian has lepton- and baryon-number violating terms. In order to avoid these, a new multiplicative quantum number R is introduced with

$$R = (-1)^{(3B-L)+2S}, \tag{1.41}$$

where B and L are the baryon- and the lepton-number respectively, and S denotes the particle spin. As a consequence, all Standard Model particles have $R = 1$ and all sparticles have $R = -1$. The conservation of this quantum number results in sparticles being produced in pairs and the lightest sparticle (the so-called *LSP*) being stable. Because of cosmological bounds, the LSP cannot carry electromagnetic or strong charge. Only weakly interacting, it is difficult to detect and thus an appealing candidate for the cold dark matter. As R-parity violation is experimentally not ruled out, SUSY searches must consider both scenarios with *R-parity conservation (RPC)* and with *R-parity violation (RPV)*. Within this thesis, only RPC is assumed.

1.2.2 The Minimal Supersymmetric Standard Model

The Minimal Supersymmetric Standard Model (*MSSM*) [41, 43] describes the simplest model with the smallest number of new particles and interactions. An overview is given in Table 1.4. The naming convention is the following: The names of the supersymmetric partners of fermions begin with "s-", the boson-partners end with "-ino". In general, the super-partners of the gauge bosons are called gauginos. However, except for the gluino, which is the only color-octet fermion, gauginos and higgsinos have the same quantum numbers, and will therefore mix to form the physical particles.

While the neutral higgsinos and gauginos (photino and zino) mix to *neutralino* mass eigenstates ($\tilde{\chi}^0_{\mathrm{i}}$, $\mathrm{i} = 1, 2$), the charged higgsinos and the wino mix to *chargino* mass eigenstates ($\tilde{\chi}^{\pm}_{\mathrm{i}}$, $\mathrm{i} = 1, 2, 3, 4$), each one separately ordered by increasing mass. With the original fermions having two (spin-related) degrees of freedom, each one has two spinless super-partner sfermions, which are sometimes loosely referred to as left-handed

R-parity: +1			R-parity:−1			
spin	name	symbol	spin	name	symbol	
1/2	*quark*	q	0	*squark*	$\tilde{q}_{\mathrm{R}}$, $\tilde{q}_{\mathrm{L}}$	
1/2	*lepton*	ℓ	0	*slepton*	$\tilde{\ell}_{\mathrm{R}}$, $\tilde{\ell}_{\mathrm{L}}$	
1/2	*neutrino*	ν	0	*sneutrino*	$\tilde{\nu}$	
1	*gluon*	g	1/2	*gluino*	$\tilde{g}$	
1	*photon*	γ	1/2	*photino*	$\tilde{\gamma}$	$4 \times \tilde{\chi}^0$
1	W-, Z-*boson*	$W^{\pm}, Z$	1/2	*wino, zino*	$\tilde{W}^{\pm}, \tilde{Z}$	*and* $2 \times \tilde{\chi}^{\pm}$
0	*Higgs*	$H^{\pm}, H^0,$ $\tilde{h}, \tilde{A}$	1/2	*higgsino*	$\tilde{H}_1^0, \tilde{H}_2^+,$ $\tilde{H}_1^-, \tilde{H}_2^0$	(*neutralino* /*chargino*)

Table 1.4: Particle content of the MSSM.

and right-handed sfermions, although they have no standard handedness or chirality. Since sfermions also have identical quantum numbers, they will mix to form the physical particles. This mixing depends on the mass of the Standard Model fermions, thus the third-generation fermions are expected to mix most.

1.2.3 The MSSM Lagrangian

In SUSY, the supersymmetric multiplets are generated by superfields being a function of superspace (extension of space-time with additional fermionic coordinates). There are two different types of superfields: the chiral ones representing matter and the vector fields representing the vector gauge fields and their supersymmetric partners.

One can divide the Lagrangian of the MSSM into three main components

$$\mathcal{L}_{\mathrm{MSSM}} = \mathcal{L}_{\mathrm{kin-gauge}} + \mathcal{L}_{\mathrm{W}} + \mathcal{L}_{\mathrm{soft}} \tag{1.42}$$

The first term, $\mathcal{L}_{\mathrm{kin-gauge}}$, is constructed in complete analogy to the Standard Model with kinetic terms for scalar and fermionic fields, gauge interactions and gauge self-couplings. $\mathcal{L}_{\mathrm{W}}$ contains all additional terms that do not change the Lagrangian when applying gauge or supersymmetric transformations. It also contains the superpotential W, a gauge-invariant function of the chiral superfields. In general, W consists of two parts:

one is R-parity conserving, the other one R-parity violating. This later term is neglected as only RPC-scenarios are considered here.

The SUSY breaking occurs at a high energy scale and is parametrised by *soft-breaking* SUSY mass terms. Because these mass terms are sufficiently small and do not alter the soft ultraviolet behaviour of the theory, they are called *soft*. They are parametrised in the Lagrangian in $\mathcal{L}_{\text{soft}}$.

In general, $\mathcal{L}_{\text{soft}}$ introduces more than 100 additional free parameters, whose number can be reduced by making certain assumptions, mostly motivated by theoretical prejudices and few experimental evidence: the measured amount of CP-violation should be predicted by SUSY as well as the Kaon mixing, the limits on flavour changing neutral currents (FCNCs) and the electric dipole moments of the electron and neutron.

By requiring that the scalar mass matrices are proportional to the unity matrix,

$$\mathbf{m} = m \cdot \mathbf{1}, \tag{1.43}$$

the trilinear couplings are proportional to the Yukawa couplings

$$\mathbf{a}_{\text{x}} = A_{\text{x}} \frac{\mathbf{m}_{\text{x}}}{v_{\text{x}}} \tag{1.44}$$

and all parameters are real - reduces the number of free parameters drastically. These assumptions are justified as large deviations would lead to contradictions with experimental data.
In order to reduce the arbitrariness, an underlying simplicity or symmetry of the Lagrangian at very high energies might be imposed furthermore.

1.2.4 SUSY breaking: mSUGRA

The MSSM itself does not provide any explanation for the origin of the SUSY breaking [44]. Among the SUSY breaking scenarios, the theories with gravity-mediated and gauge-mediated breaking are the most popular ones currently. But all these theories share one common assumption: SUSY is broken in a hidden sector and the breaking is then transmitted to the visible sector via messenger fields, which interact with both sectors.

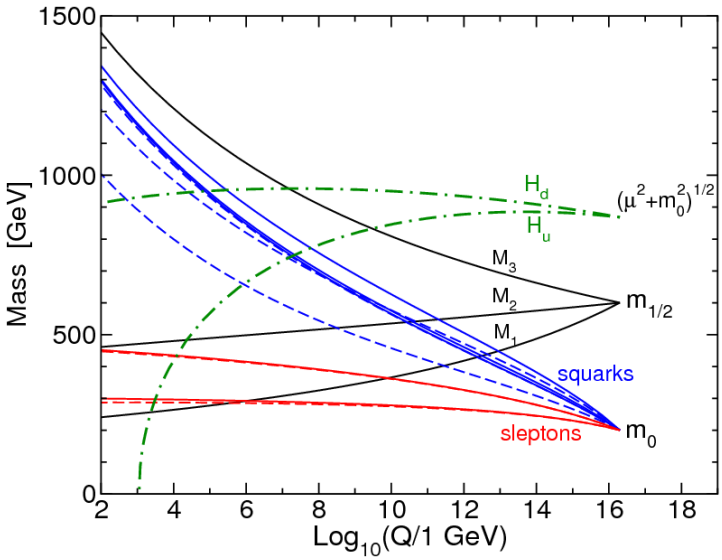

Figure 1.9: An exemplary running of masses of SUSY particles from the GUT-scale down to observable energy scales [42].

Gravity-mediated SUSY breaking models, the so called *SUGRA models*, assume that the spontaneous local SUSY breaking *(Super Higgs mechanism)* takes place at an energy scale $\sqrt{F}$ in a hidden sector, thus giving rise to a gravitino of mass

$$m_{3/2} = \frac{F}{\sqrt{3}M_{\mathrm{P}}} \tag{1.45}$$

It is the gravitational interactions that transmit the breaking to the visible sector because gravity couples to all massive fields both in the hidden and in the visible sector. The resulting (low energy) theory consists of the unbroken MSSM together with all possible soft SUSY breaking terms. If the couplings of all gauginos and scalars to the hidden sector superfield are assumed to be equal at M_{GUT}, the model becomes the *mSUGRA* model [45, 46].

In this model, the SUSY parameters are reduced to five, commonly chosen as

- the universal scalar particle mass at the GUT-scale m_0,
- the universal gaugino mass at the GUT-scale $m_{1/2}$,
- the universal trilinear coupling A_0,
- the ratio of the vacuum expectation values of the two neutral Higgs fields $\tan\beta$ and
- the sign of the Higgsino mass parameter $sign\,(\mu)$.

The masses of the SUSY particles at the weak scale as well as the couplings can be calculated using RGEs (renormalisation group equations, see Figure 1.9).

The gauge-mediated breaking *(GMSB)* is another framework for SUSY breaking as well as Anomalous U(1)-Mediated SUSY Breaking and Conformal Anomaly-Mediated SUSY breaking - details might be found in [42].

1.2.5 SUSY discovery prospects for the LHC at $\sqrt{s}$ =7 TeV

When the LHC decided after the 2008 incident (see Section 3.1) to begin its initial data-taking at reduced centre-of-mass energy of 7 TeV instead of 14 TeV, the author contributed to a (purely simulation-based) study [3, 4] to investigate the discovery prospects for SUSY searches under this new circumstances.

Assuming R-parity conservation (resulting in the pair-production of any SUSY particles and the LSP being stable), the SUSY search strategy makes use of the generic signature of missing transverse energy, $E_{\mathrm{T}}^{\mathrm{miss}}$ (from the escaping LSP), and several high-p_{T} objects - at the LHC preferably jets due to the strength of the strong force. Various different SUSY points, distributed radially in the m_0-$m_{1/2}$ of a *mSUGRA* model with $\tan(\beta) = 10$, $A_0 = 0$ and $\mu > 0$, are considered. The effective mass (M_{eff})-distribution[1] of different channels, consisting of 2-4 jets, 0-2 leptons, where $\ell = e, \mu$, and $E_{\mathrm{T}}^{\mathrm{miss}}$, are scanned for deviations from the Standard Model and the significance of the excess is calculated. The uncertainty in the determination of the sum of the various Standard Model backgrounds is conservatively estimated to be of the order of 50% (assuming data-driven techniques for the main backgrounds of W, Z, *top*) to 60% for the sub-dominant QCD background.

For the discovery reach plots, only the jet-multiplicity channel with the biggest significance at a certain point in the mSUGRA-grid is used. The influence on the SUSY discovery reach of both, different data statistics ($\mathcal{L}$=0.5 fb^{-1} - 2 fb^{-1} with 70% - 35% uncertainty respectively) and different combined statistical and systematic uncertainties (50%, 70% and 90%), is studied. In the baseline scenario (see Figure 1.10) with $\mathcal{L} = 1\,\mathrm{fb}^{-1}$ and 50% combined uncertainty the signals with a squark (first and second generation, others decoupled) and gluino masses up to 700 GeV could be discovered in

[1] M_{eff} is the scalar sum of the transverse momenta of the jets, the leptons and the missing transverse energy. It has previously proven to be a powerful observable for SUSY searches [47].

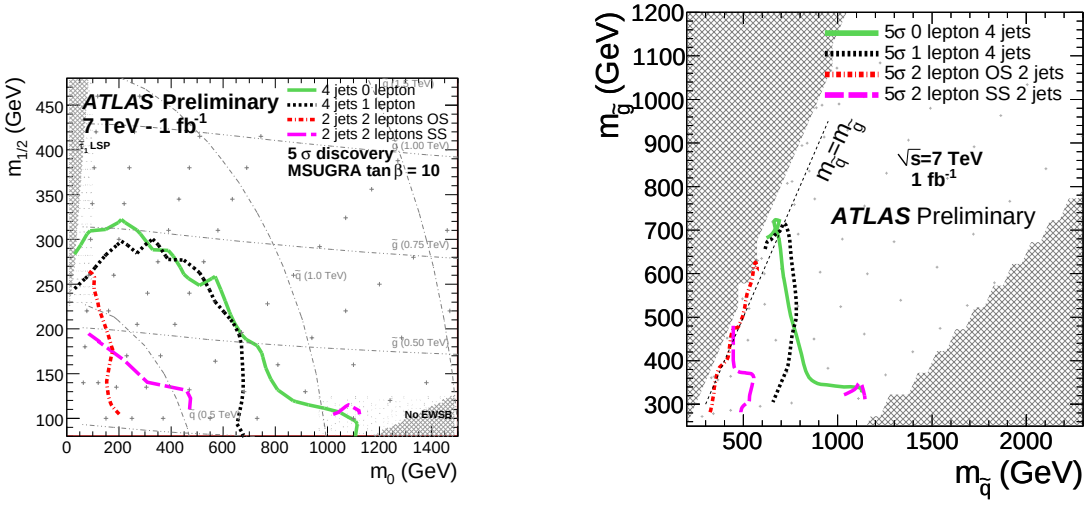

(a) 5σ discovery reach as a function of m_0 and $m_{1/2}$

(b) 5σ discovery reach as a function of squark and gluino masses, $m_{\tilde{q}}$ and $m_{\tilde{g}}$

Figure 1.10: Discovery prospects for SUSY searches in a *mSUGRA* scan with $\tan(\beta) = 10$ at the LHC operating at 7 TeV: Channels with 2-4 jets, 0-2 leptons and missing transverse momentum were studied, assuming an overall error of 50%(stat.+syst.) and an integrated luminosity of $\mathcal{L} = 1\,\mathrm{fb}^{-1}$. Only the jet-multiplicity channel with the highest significance is displayed.

a scenario where the gluino mass is similar to the mass of the light squarks. Hereby, the fully hadronic channel yields the best sensitivity.

1.2.6 Experimental constraints

This Section presents experimental constraints on the masses of SUSY particles. It summarizes [48] and reflects the existing limits as of 2010. See [49] for recent updates.

SUSY limits are obtained from various different sources, where hadron collider experiments such as the LHC[2] and the Tevatron[3] [50, 51] represent only one key ingredient. Other contributions result e.g. from direct astrophysical searches like WMAP [52], limiting the possible dark matter contribution of SUSY, or WIMP measurements, where an LSP-candidate is almost certainly to be electrically and colour neutral. Finally, the overall picture is completed by indirect constraints from high-precision electroweak observables and low-energy data from flavour physics experiments. Examples for these measurements are the anomalous magnetic moment of the muon, the cosmological dark

[2] pp-collider with a centre-of-mass energy of up to 14 TeV
[3] $p\bar{p}$-collider, centre-of-mass energy 1.8 TeV - 1.96 TeV

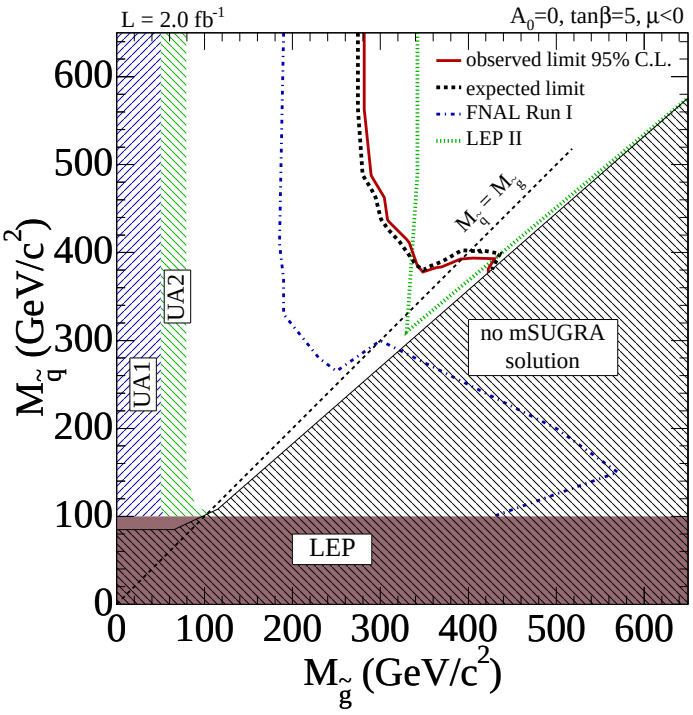

Figure 1.11: Region in the ($m_{\tilde{g}}$, $m_{\tilde{q}}$) plane excluded by CDF Run II and by earlier experiments [48].

matter relic density, limits on rare B-meson and K-meson decays such as $B_s \to \mu^+\mu^-$, the electric dipole moments, the proton-decay and the WIMP-nucleon cross-section.

With all SUSY particles besides the gluinos being democratically produced at the *Large Electron Positron Collider*[4] *(LEP) [53–55]* via the electroweak interaction, results can be interpreted in a fairly model-independent way as the searches are naturally directed towards the lightest SUSY particles, typically the NLSP. Assuming furthermore a specific model, different searches can be combined to obtain constraints on model parameters. LEP limits the masses of the SUSY particles (besides the gluinos) to be larger than $\sim$100 GeV, and an indirect lower limit of 47 GeV for the mass of a neutralino LSP is provided.

In proton-collisions, however, the most frequently produced particles are coloured, i.e. squarks and gluinos, and their decay chains are heavily influenced by the pattern of the lighter SUSY particles. The constrain of SUSY particles masses hence does not work without the assumption of a certain, underlying model: the squark and gluino mass lower limits are 379 and 308 GeV, respectively, within the *mSUGRA* framework

[4] e^+e^- collider at CERN, centre-of-mass energy 91.2 GeV - 209 GeV

Particle	Mass limit [GeV]	Constraints
$\tilde{N}_1^0$	46	all $tan\beta$, m_0, $m_{\tilde{N}_2^0} - m_{\tilde{N}_1^0}$
$\tilde{N}_2^0$	62.4	$1 < tan\beta < 40$, all m_0 and $m_{\tilde{N}_2^0} - m_{\tilde{N}_1^0}$
$\tilde{N}_3^0$	99.9	$1 < tan\beta < 40$, all m_0 and $m_{\tilde{N}_2^0} - m_{\tilde{N}_1^0}$
$\tilde{N}_4^0$	116	$1 < tan\beta < 40$, all m_0 and $m_{\tilde{N}_2^0} - m_{\tilde{N}_1^0}$
$\tilde{C}_1^{\pm}$	94	$1 < tan\beta < 40$, $m_{\tilde{C}_1^{\pm}} - m_{\tilde{N}_1^0} > 3$ GeV , all m_0
$\tilde{e}$	107	all $m_{\tilde{e}_R} - m_{\tilde{N}_1^0}$
$\tilde{\mu}$	94	$1 \leq tan\beta \leq 40$, $m_{\tilde{\mu}_R} - m_{\tilde{N}_1^0} > 10$ GeV
$\tilde{\tau}$	81.9	$m_{\tilde{\tau}_R} - m_{\tilde{N}_1^0} > 15$ GeV, all θ_τ
$\tilde{q}$	379	$tan\beta = 3$, $\mu > 0$, $A_0 = 0$, any $m_{\tilde{g}}$
$\tilde{b}$	89	$m_{\tilde{b}_1} - m_{\tilde{N}_1^0} > 8$ GeV, all θ_b
$\tilde{t}$	95.7	$\tilde{t} \to c\tilde{N}_1^0$, $m_{\tilde{t}} - m_{\tilde{N}_1^0} > 10$ GeV, all θ_t
$\tilde{g}$	308	any $m_{\tilde{q}}$
	392	$m_{\tilde{q}} = m_{\tilde{g}}$

Table 1.5: 95% confidence level mass limits for the MSSM sparticle content [48].

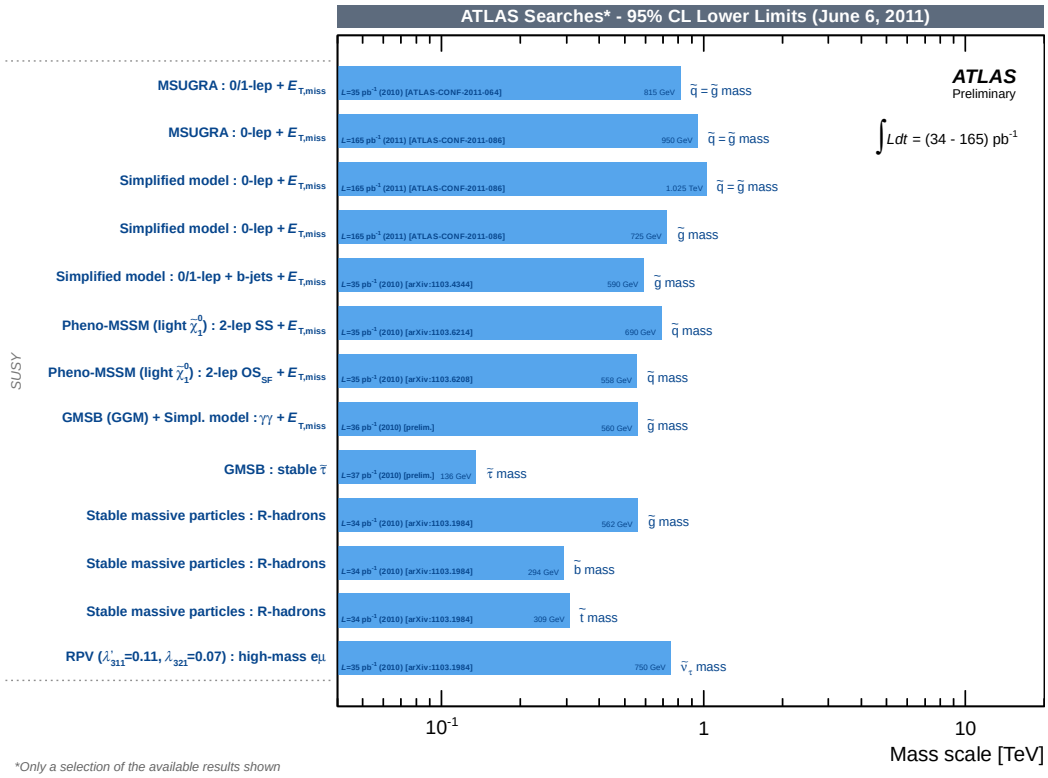

Figure 1.12: ATLAS limits on SUSY particles as of June 2011. This table shows only a selection of results, for more details see [56].

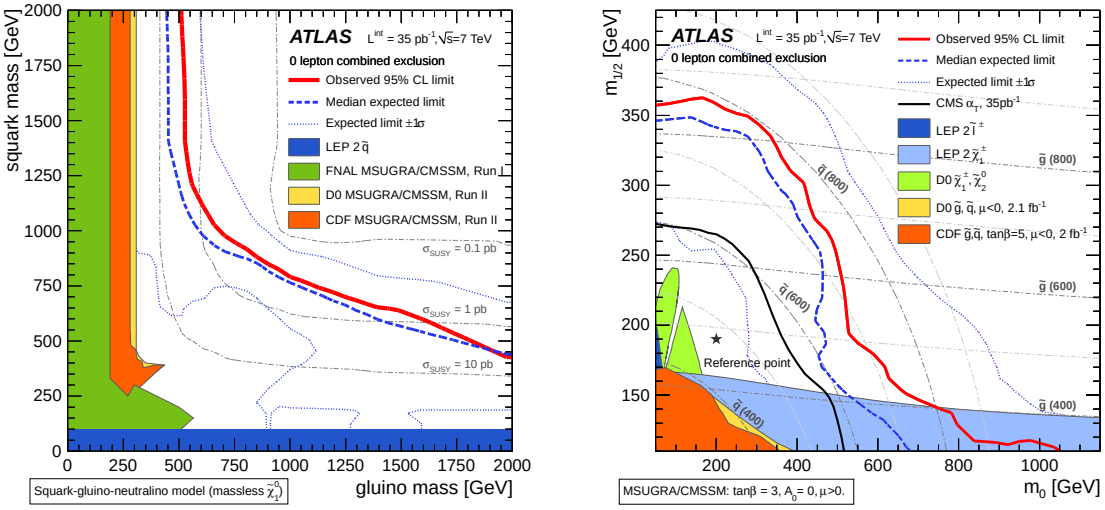

(a) 95% C.L. exclusion limits in the (gluino, squark) mass plane together with existing limits [57, 58]. Comparison with existing limits is illustrative only as some are derived in the context of MSUGRA/CMSSM or may not assume a massless neutralino.

(b) 95% C.L. exclusion limits in the $\tan(\beta) = 3$, $A_0 = 0$ and $\mu > 0$ slice of mSUGRA/CMSSM, together with existing limits with the different model assumptions given in the legend [57, 58].

Figure 1.13: 95% C.L. exclusion limits [57, 58] for different SUSY models with 35 pb^{-1} of ATLAS data.

at low $\tan(\beta)$ (see Figure 1.11), and chargino masses up to 170 GeV are excluded for favorable choices of slepton masses. An overview about the SUSY exclusion limits prior to LHC is given in Table 1.5.

Figure 1.12 shows an overview of a selection of SUSY limits obtained with the first ATLAS data. Even with the early data samples of only $\mathcal{L}$ =35 pb^{-1} [57, 58] - 165 pb^{-1} [7, 8], previous limits were significantly extended (see Figure 1.13).

Chapter 2

Phenomenology of hadron colliders

The first part of this Chapter briefly introduces the terminology common to hadron colliders as well as event- and detector simulations. The second half of this Chapter introduces the general idea of SUSY searches at the LHC.

2.1 General aspects

Protons are composite particles consisting of gluons and quarks, the *partons*, held together by the strong force. Thus they belong to a group of particles called hadrons. While the so-called *valence quarks* of a hadron determine its quantum numbers, the indefinite number of virtual *sea quarks* and *gluons* do not affect them.

Hadrons in general are in a non-perturbative QCD bonding state, though at high energies they can be described as collection of their constituents (*factorization theorem*). Thus, a high energetic collision between protons looks like an interaction of their partons. The majority of these pp interactions at a hadron-collider are large-distance, or soft collisions where the momentum transfer is small. Collisions with large momentum transfer, which are the only ones to be calculable perturbatively, are called hard scattering and these result in particles with large transverse momentum (see below).

Only a small fraction of partons take part in the hard scattering, thus the remaining partons carry away a significant amount of the original energy. While the initial transverse momentum of any parton inside an accelerated proton should be close to zero, the initial longitudinal proton momentum is split between all partons and thus each of them carries an unknown fraction. Due to this unknown longitudinal momentum distribution,

it is convenient to describe objects resulting from collisions of partons in terms of the their transverse energy E_{T} or transverse momentum p_{T}.

The total number N of recorded events of a given process can be calculated with

$$N = \sigma \cdot L \cdot \varepsilon, \tag{2.1}$$

where σ is the cross-section of the given process, $L = \int \mathcal{L} dt$ is the integrated luminosity and ε is the recording efficiency of the detector. Using the number of hadrons inside the colliding bunches, n_{a} and n_{b}, and the frequency f of the collisions, the instantaneous luminosity is finally given by

$$\mathcal{L} = f \frac{n_{\mathrm{a}} n_{\mathrm{b}}}{A_{\mathrm{eff}}}, \tag{2.2}$$

where the denominator represents the effective interaction area $A_{\mathrm{eff}} = 4\pi\sigma_x\sigma_y$ with σ_x and σ_y being the standard deviations of the Gaussian beam profiles in the horizontal and vertical direction. While luminosity is expressed in units of $\mathrm{cm}^{-2}\,\mathrm{sec}^{-1}$, cross-sections are given in units of *barn* with

$$1\,\mathrm{b} = 10^{-28}\,\mathrm{m}^2. \tag{2.3}$$

With the colliding particles being composite objects, also the effective centre-of-mass energy of the system, $\sqrt{\hat{s}}$, is reduced. Let x_1 be the momentum fraction of the first colliding parton with respect to the total proton and let x_2 be the momentum fraction of the second parton respectively (see Figure 2.1). The effective centre-of-mass energy is then given by

$$\sqrt{\hat{s}} = \sqrt{x_1 x_2 s}. \tag{2.4}$$

2.2 Factorisation, parton distribution functions and cross-sections

Figure 2.1 shows a schematic view of an important process at hadron colliders: $pp \to q\bar{q}$. Using the hard scattering cross-section, $\hat{\sigma}$, for $q\bar{q} \to q\bar{q}$, the leading-order (LO) cross-

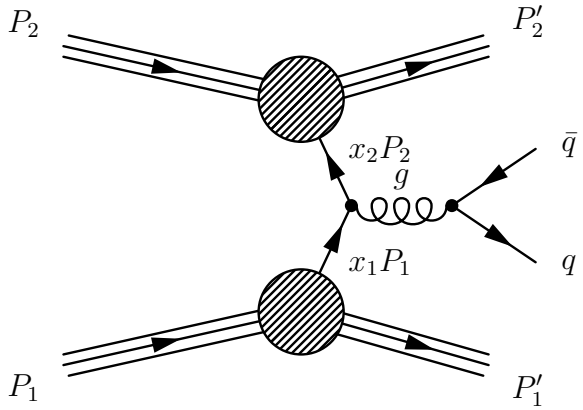

Figure 2.1: Schematic view of a pp-interaction, where $pp \to q\bar{q}X$. x_1 and x_2 denote the momentum fractions carried by the specific partons. The hard scattering process consists of the $q\bar{q}$ annihilation. The remaining hadron fragments will fragment into further hadrons.

section for this process is given by

$$\frac{d\sigma}{dQ^2} = \sum_{q,\bar{q}} \int dx_1 \int dx_2 \left[f_q\left(x_1, Q^2\right) f_{\bar{q}}\left(x_2, Q^2\right) + f_{\bar{q}}\left(x_1, Q^2\right) f_q\left(x_2, Q^2\right) \right] \frac{d\hat{\sigma}}{dQ^2}, \quad (2.5)$$

where Q^2 is the 4-momentum exchanged in the interaction and f_q and $f_{\bar{q}}$ are the *Parton Distribution Functions* (*PDFs*, see below) of the quark and anti-quark respectively. As LO calculations might suffer from large uncertainties, the calculation of the full cross-section requires higher-order contributions from virtual corrections such as the emission or absorption of real and virtual gluons. For most processes at hadron colliders, at least next-to-leading-order calculations are available to date.

Some typical cross-sections are shown in Figure 2.2. At the LHC, the dijet cross-section is more than two orders of magnitude smaller than the total inelastic cross-section. Physics processes of interest such as SUSY typically possess cross-sections being even smaller than the dijet cross-section by several orders of magnitude.

Processes involving strong interactions can be factorised into a short-distance (hard) part and a long-distance (soft) one as in Equation (2.5), see e.g. [62]. While the hard part depends on the specific process and is calculable with perturbative QCD, the soft part is not calculable, but universal and is to be determined experimentally with global fits to data from various different experiments.

The *PDFs* $f_i(x, Q^2)$ (see Figure 2.3) are a key ingredient to describe the initial state of hadronic interactions: they represent the energy-dependent probability of finding a parton of type i, carrying a momentum fraction between x and $x+dx$ of the total hadron

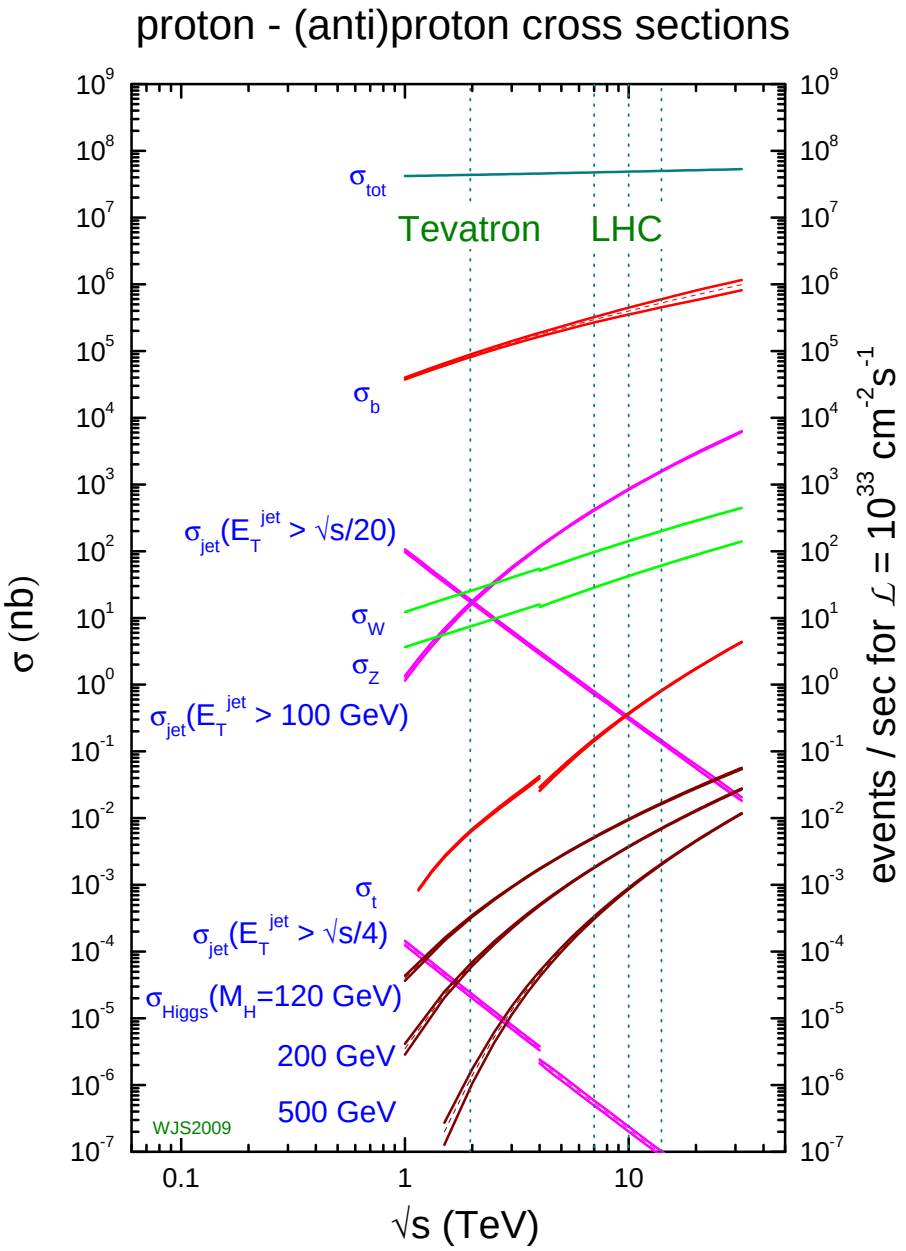

Figure 2.2: Cross-sections [61] for LHC (pp) and Tevatron ($p\bar{p}$) for different processes.

momentum. Just as the PDFs cannot be calculated, also the formation of hadrons in the final state is not calculable: thus *universal fragmentation functions*, measured e.g. at LEP, are defined - in full analogy to the description of the partonic substructure of the proton in PDFs. These fragmentation functions give the probability that a quark produces a hadron with a fraction of the quark energy. The *factorisation scale* μ_f finally characterises the boundary between the soft and hard energy regimes, typically chosen to be around the scale Q of the hard interaction, while the renormalisation scale μ_R is used in regulating divergent terms in the perturbation expansion. The dependence of the cross-section on those scales decreases as more terms are included in the perturbation series. If calculations could be performed to all orders in perturbation theory, the dependence on those scales would drop out completely. In order to avoid large corrections, one usually chooses scale values close to the typical momentum scale of the considered process.

Different theoretical approaches exist for describing this fragmentation. two popular ones are briefly introduced in the following: the *Lund string fragmentation model* [63] (*SF*, applied amongst others in `PYTHIA`) and the cluster fragmentation model [64, 65] (applied e.g. in `HERWIG`).

While the colour charges in a $q\bar{q}$ colour dipole separate, the confinement potential grows linearly. The resulting colour flux tube between the original $q\bar{q}$ dipole stretches up to the point, where enough energy is available to create an additional $q'\bar{q}'$ pair in-between and two colour-neutral objects, $q\bar{q}'$ and $q'\bar{q}$, form. The above procedure is repeated until the invariant masses of all remaining objects are of the order of hadron masses, typically a few GeV. The simplest model, accommodating both the causality of the picture and Lorentz-invariance, uses a relativistic string without transverse degrees of freedom. In addition, the Lund model assigns a transverse mass $m_T^2 \equiv m^2 + p_T^2$ to the $q'\bar{q}'$ pair and a tension κ to this string, where its break-up is attributed to quantum tunneling with a Gaussian probability $e^{-\pi m_T^2/\kappa}$ which depresses the heavy-quark formation as experimentally observed.
Inside the *cluster fragmentation* model, however, the outgoing gluons are forced to split up in pairs of $q\bar{q}$ or diquark/anti-diquark at the final state of the parton showering. Nearby quarks in the colour field then recombine to colour singlet clusters, finally decaying into hadrons or directly forming the lightest hadron of the associated flavour if too light.

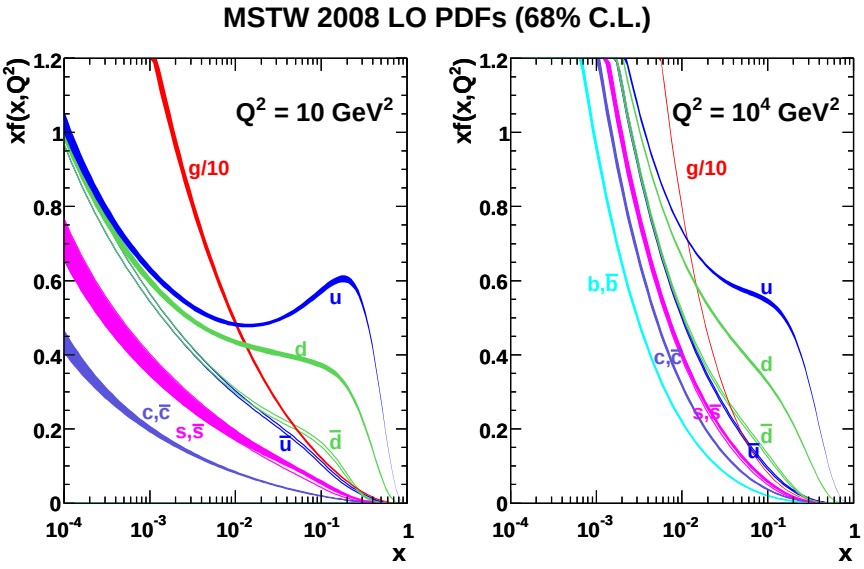

Figure 2.3: Leading-order parton distribution function from MSTW [61, 66–68] at different values of Q^2. For low values of Q^2, the proton properties are dominated by the valence quarks, while at higher values (right) more and more of its fine structure becomes visible.

2.3 Initial and final state radiation, underlying event and pile-up

Apart from the hard scattering, the following aspects must be taken into account additionally since they influence both final event kinematics and particle multiplicities:

- *Initial State Radiation (ISR)*: Radiation of e.g. a gluon or a photon from one or more incoming particles is summarized as ISR. It affects both the cross-section and the event topology.
- *Final State Radiation (FSR)*: Same as ISR, but the outgoing particles are affected. Both ISR and FSR represent higher-order corrections.
- *Beam Remnants*: Only a small fraction of partons takes part in the hard scattering; the remnants of the proton carry the remaining energy and are not colour-neutral. This can also effect the event topology.
- *Underlying event (UE)*: The term UE refers to the remaining parton interactions, which take place in the same pp-interaction as the hard scattering.

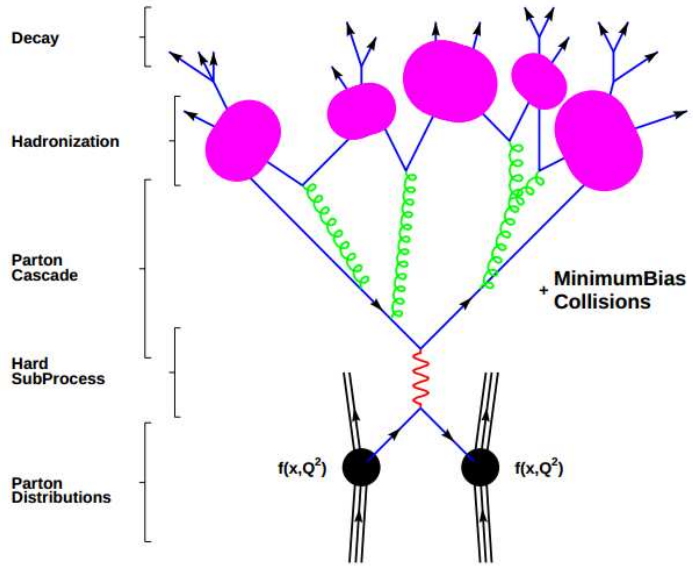

Figure 2.4: The process of MC event generation from Feynman diagrams to final hadronisation into stable particles [71].

- *Pile-Up*: In a high-luminosity environment, each bunch crossing can contain several interactions originating from different pp collisions. During the current LHC conditions ($\sqrt{(s)} = 7$ TeV, year 2011) each bunch-crossing contains on average an overlay of 11 interactions.

2.4 Event simulation

The complexity of the processes involved in a particle collision and the identification of the collision products makes a direct comparison of theoretical predictions and experimental results very complicated. Thus simulations by Monte Carlo generators are a key ingredient for all modern high-energy physics experiments, allowing particle physicists to model different descriptions of the physical world and determine - if this model is realized in nature - what is likely to happen in particle collisions and how it will look in the detector. Simulations are not only used as a reference to compare real experimental data with the theory but also to make predictions for future experiments.
Further introductions to MC generators might be found in [69, 70].

In order to examine the complex processes at hadron colliders such as the LHC the 4-vectors of the final products from the interesting interactions are generated in a first step, where the relevant variables are selected randomly from the predicted probability

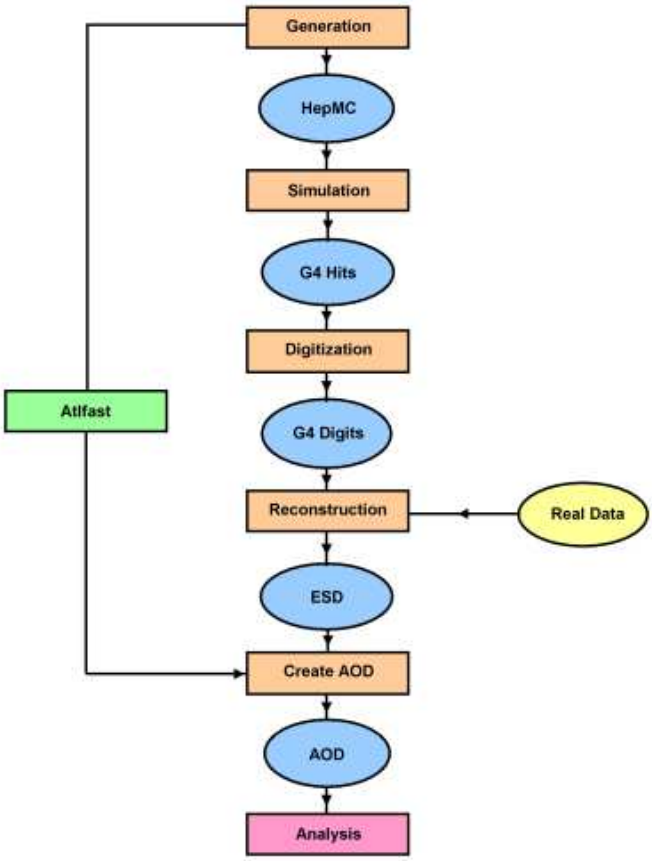

Figure 2.5: Preparations to be taken for both simulated and real raw data for use in physics analysis at ATLAS. Taken from Reference [72].

distributions. Then the event is processed through a detector simulation, the output of which has the same format as real measurements and can be further processed in exactly the same way as the real data. The simulated events will be referred to as "MC events".

Figure 2.4 shows the evolution of an event, starting with the hard process of the partons, whose initial momenta are determined by the PDFs. Additional radiation is here provided by parton showers, followed by the hadronisation into color-neutral states, which may decay further. In general, there is also radiation from the incoming partons (ISR) present, which is for simplicity not shown here. Once the event has been generated, the detector simulation propagates the generated particles through the different detector levels. The full simulation chain is demonstrated in Figure 2.5, which also demonstrates the handling of raw physics data recorded by ATLAS. For details about the experimental setup, see Chapter 3.

A comprehensive description of the detector geometry, magnetic fields and material distributions is provided to GEANT4 [73], a software tool that simulates the interaction of particles with the detector material and generates "hits". It also models the decay of long-lived particles in the detector. These hits are then digitized, which mimics the response that a real particle of this type would create in the read-out electronics. The bytestream both of the simulation or real data is converted into *Raw Data Objects* (*RDOs*, e.g. pixel clusters), and reconstruction algorithms are to be run afterwards, producing *Event Summary Data (ESD)*. The *Analysis Object Data (AODs)* are produced in a further step, being smaller in size by focusing on those parts needed for physics analyses only (e.g. only one jet collection is chosen and single cluster-information is no longer available). While the ESDs possess an event size of roughly 500 $KB/event$, the AODs are reduced by a factor of five to 100 $KB/event$. In a last step, the AODs undergo another step of slimming and skimming - producing increasingly smaller and more manageable reductions of the data, which are easier to handle both for processing and distribution to local analysis centres for interactive analyses - ending up in *Derived Physics Data (DPD)*. Hereby, the content is adjusted to the needs of the different analyses by the various physics groups like Standard Model, Egamma or SUSY or even single physicists.
In addition to this full simulation (*FULLSIM*) procedure, there exists also a fast detector simulation called *ATLFAST II* [74], which replaces the very CPU and time intensive calorimetry simulation with an parametrised smearing of the momenta and energies of the particles based on the expected performance of the ATLAS detector as predicted by the full simulation.

2.5 Monte Carlo generators

Many different choices of Monte Carlo event generators are available on the market. While some of those simulate complete events including hadronisation, parton showering and the underlying event (e.g. PYTHIA [75, 76], HERWIG [77] and SHERPA [78]), others produce only the hard scatter event (e.g. ALPGEN [79], WHIZARD [80, 81] and PowHeg [82, 83]). Some of the matrix-element (ME) generators are available only in leading-order, some already in next-to-leading order. For getting a realistic MC event, the ME-generators in any case need to be interfaced to PYTHIA or HERWIG.
All of them contain different configuration parameters, which influence the details of the event production and thus need to be tuned to gain good agreement with experimental data (compare e.g. ATLAS Tune MC09 [84]). The parameter's influence is to be considered inside systematic studies either with variation of the parameters itself or by comparing the outcome of different generators for a specific process.

PYTHIA One of the various multi-purpose high-energy MC generators, that can simulate e^+e^-, $p\bar{p}$, ep and pp collisions, is PYTHIA [75, 76]. Its simulation includes all $2 \to 2$ Standard Model processes resulting from the collisions and also various new physics processes. The hard subprocess uses mostly leading-order matrix elements and is supplemented by parton showering. Additionally, coloured partons are hadronised into colorless hadrons. ISR and FSR are approximated in PYTHIA using a parton shower method: it evolves the splitting of a mother particle into two daughter partons with a probabilistic approach, with momentum z and $1-z$ respectively, in a series of branchings using Altarelli-Parisi splitting functions $P(z)$ [85, 86]. With Q^2_{max} describing the energy scale of the hard interaction, the evolution of branchings is performed backward for ISR or forward for FSR until a lower scale $Q^2_{min} \approx 1$ GeV is reached. This ($k_\perp$-ordered) parton shower method describes well the radiation of collinear and soft partons, but has limited predictive power for the emission of hard and wide-angle partons which are usually originate from the hard subprocess itself. This intersection is a critical point of any MC generators.

ALPGEN Another event generator, which is mainly used for processes containing W or Z bosons, is ALPGEN [79]. While ALPGEN calculates the multiparton hard processes up to five-partons with a tree-level matrix element (for higher-orders, only real parton emissions at Born-level are used), parton showering, fragmentation and the simulation of the UE is still done by PYTHIA or HERWIG respectively. This ansatz might create a double counting when determining the $X + n$ *jets* cross-section

(where X denotes any final state and n the inclusive jet multiplicity), as extra jets in an event can be created either via parton showers or explicitly via calculating the Feynman diagrams. ALPGEN uses the so-called MLM-matching to address this problem: the samples for each exclusive parton multiplicity are generated separately. Then, matching jets to initial partons, the parton shower is simulated. If the parton multiplicity does not match the jet multiplicity, the event is rejected.

MC@NLO [87–90] is a parton shower MC generator, which calculates the partonic hard subprocesses by including the full NLO QCD corrections, i.e. the real and the virtual ones, in contrast to e.g. ALPGEN.
It is mainly used for the simulation both of single top and $t\bar{t}$ production.

HERWIG, HERWIG++ HERWIG++ [91, 92] is a re-implementation of the former fortran-based HERWIG [77, 93] generator in C++. It uses the JIMMY [94] multiple parton interaction model for the simulation of the underlying event and kept defining features of the old version: the HERWIG cluster hadronisation (see Section 2.2) and an improved version of the angular-ordered HERWIG parton shower (in contrast to e.g. PYTHIA using a $k_\perp$-ordered showering). Furthermore, it contains a large process library with spin-correlation in the decays.

SHERPA [78] uses its own matrix-element calculator/generator, an extensive machinery for CKKW matching to showers, but PYTHIA for multiparton interactions and hadronisation.

WHIZARD is designed for the efficient calculation of multi-particle scattering cross sections and simulated event samples for LHC, ILC, CLIC, and other High Energy Physics Experiments. Besides the Standard Model, it also supports various models for new physics such as e.g. the MSSM, Little Higgs models, UED and gravitinos.

PROSPINO [95, 96] provides the NLO cross-sections for normalizing the SUSY signal samples, generated by HERWIG++.

ISAJET [97, 98] is based on perturbative QCD plus phenomenological models for parton and beam jet fragmentation to simulate $p\bar{p}$, pp and e^+e collisions at high energies. It not only contains perturbative QCD cross-sections, but also initial and final state QCD radiative corrections in the leading-log approximation, independent fragmentation of quarks and gluons into hadrons, and for the beam jets a model tuned to hard-scattering and minimum-bias data. One part of ISAJET is ISASUSY, evaluating branching fractions for the minimal SUSY extension of the Standard Model

(MSSM). Within the current studies, `ISASUSY` is used to calculate the SUSY decay tables, and to guarantee consistent electroweak symmetry breaking.

2.6 Jet algorithms

Created in the initial pp collision, the outgoing particles - both charged and uncharged - leave energy deposits along their way out of the detector. The tracks of charged particles such as electrons or charged hadrons are seen by the inner tracking detector, whereas neutral particles such as photons or neutral hadrons deposit their energy only in the calorimeter.
Due to confinement, quarks and gluons cannot be observed individually, but happen to manifest in a bunch of colour-neutral hadrons flying into a similar direction in phase-space, the *jets*. The kinematic properties of these jets (p_{T}, η[1], φ) are to be associated to the kinematic properties of the original partons produced from the hard scattering process. Thus, it is a *jet algorithm* which defines how signals in the detector (experimental) or partons (theory) are grouped into jets, see e.g. [99–101] for further details.
There are several criteria that qualify a "good" jet algorithm:

- It describes several levels of the jet (parton, particle and detector level) and is detector-independent.
- It is infrared and collinear safe, thus neither the emission of a soft or collinear gluon nor the splitting of an outgoing particle into two collinear ones changes the results, i.e. the number of jets, and their properties stay the same. It is the vulnerability to infrared and collinear divergences which limits how well one can compare experimental results with theoretical calculations.
- It uses a minimum of computer resources and can be calibrated easily.

Many different jet-algorithms exist and it depends on the use-case which to choose. Some popular ones will be introduced in the following paragraphs, an overview can be found in Figure 2.6.

[1]The pseudorapidity is given by $\eta = -\ln\tan\vartheta/2$, see Section 3.2.2 for details.

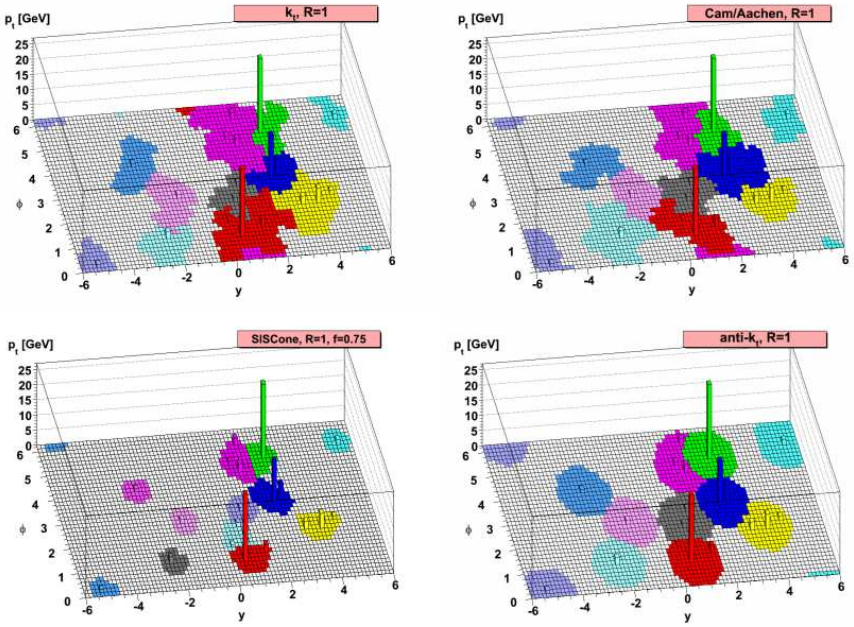

Figure 2.6: A sample parton-level event, together with many random soft "ghosts", clustered with four dierent jets algorithms, illustrating the "active" catchment areas of the resulting hard jets. For k_t and *Cam/Aachen* the detailed shapes are in part determined by the specic set of ghosts used, and change when the ghosts are modied. Taken from [99].

2.6.1 The cone algorithm

The cone algorithm has a simple geometric motivation: to search for stable cones in the η-φ plane where the jet four-momentum is defined along the cone axis.
It starts with a list of proto-jets, usually above a certain seed energy for time issues. Beginning from any (or the highest energetic) available object in the list, the energy-weighted centre of all objects within a radius R of the initial proto-jet is calculated, which then becomes the reference point for the next cone to draw. The procedure is repeated until the final cone is stable and all proto-jets are grouped inside jets. Overlaps must be resolved by splitting or merging.

While this algorithm in its basic form is neither infrared nor collinear safe and depends on the choice of the seeds, there exists some modifications such as the *Seedless Infrared-Safe Cone* (SIS-CONE) algorithms which are. A CONE algorithm with a radius of $R = 0.4$ was used e.g. in the studies for the 7 TeV *SUSY discovery prospects* (see Section 1.2.5).

2.6.2 Clustering algorithms: k_t and anti-k_t

These algorithms use to group together near-by objects pair-wise following a certain definition of distance D between to objects i and j, see e.g. [99, 100]:

$$D_i = p_{T,i}^{2x} \tag{2.6}$$

$$D_{i,j} = min(D_i, D_j)\frac{\Delta R_{i,j}^2}{R^2}, \tag{2.7}$$

where the radius R is a config-parameter to be chosen and $\Delta R_{i,j}^2 = (\varphi_i - \varphi_j)^2 + (\eta_i - \eta_j)^2$ reflects the geometrical distance between the according objects (for details about coordinate frames, see Section 3.2.2). After computing all possible pairs of $\{D_{i,j}, D_i\}$ and $d = min(\{D_{i,j}, D_i\})$, jet i and j are merged when $d = D_{i,j}$ and declared as final object otherwise. x denotes the different type of algorithm: while the default k_t-algorithms with $x = 1$ chooses the geometrically closest objects first, the anti-k_t-algorithms with $x = -1$ start with the objects with highest p_{T} . $x = 0$ characterises algorithms called *Cambridge/Aachen* (see Figure 2.6).

As every object is unambiguously assigned to one of the jets, there is no need for any split- and merge procedure. The algorithms are both infrared and collinear-safe.

While performance studies showed a similar performance for the different jet algorithms in physics studies, clustering algorithms, especially the anti-k_t-algorithms, are less sensitive to pile-up effects and UE than SIS-CONE.

The ATLAS anti-k_t algorithm

ATLAS is currently using an anti-k_t algorithm with a radius of $R = 0.4$, where the three-dimensional clusters of calorimeter cells, seeded by those with an energy significantly above the measured noise, serve as input seed. With treating each of these cluster as an $(E, \vec{p})$ four-vector with zero mass, the jet momenta are calculated by summing up the four-vectors. Due to the calorimeter non-compensation and inhomogeneities, these jets afterwards undergo several corrections: p_{T} and η-dependent calibration factors, based on Monte Carlo (MC) and validated with extensive test-beam and collision-data studies [102], are applied and its direction is shifted so that it points to the primary vertex instead of the geometrical detector centre with the primary vertex being that vertex with the highest summed track p_{T}^2.

2.7 SUSY searches at the LHC

There are many good reasons to believe in physics beyond the Standard Model. In the past 30 years, this theory has been successfully tested and nicely confirmed with dozens of high-precision measurements without any larger deviations. Nevertheless, there are a few short-comings and it is common knowledge that this model cannot be the finite answer of the universe to all our open questions as already outlined in the previous chapter. One of the possible candidates to extend the Standard Model via heavy coloured (i.e. strongly interacting) particles is SUSY.
Whatever might be your favourite theory for new physics, there is one thing all searches for physics beyond the Standard Model have in common: One has to precisely understand the background of Standard Model processes.

2.7.1 General idea

Provided SUSY is located within the energy regime of the LHC, squarks and gluinos ($\tilde{q}$ and $\tilde{g}$ respectively) are expected to show up copiously. Possible decay scenarios do con-

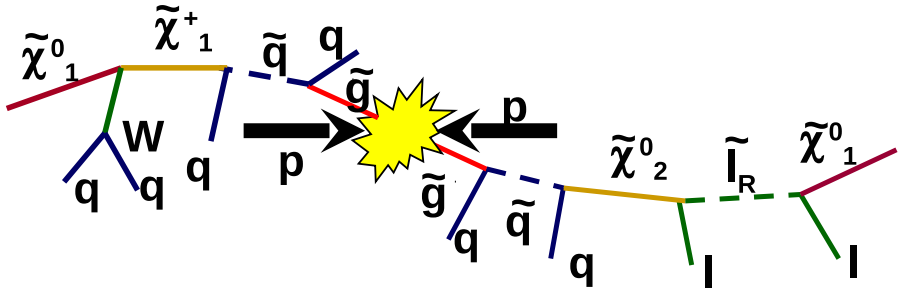

Figure 2.7: A pair SUSY of SUSY particles decaying exemplarily in a long decay chain.

tain long decay chains (see Figure 2.7), thus one can end up with final states containing various jets, leptons and missing transverse energy.
If furthermore R-parity is conserved, the lightest SUSY particle, the *LSP*, which is expected to interact only weakly or through the gravitational force, escapes unseen, producing the signature of large missing transverse energy. Therefore, the "easiest" SUSY signature to search for at the LHC is that of jets + $E_{\mathrm{T}}^{\mathrm{miss}}$ (missing transverse energy, for details see Section 4.5).
The SUSY decay chains involving leptons, photons or b-jets are treated in dedicated analyses which are not to be discussed here.

2.7.2 Production and decay of SUSY particles

At hadron colliders, SUSY particles can be produced either via the weak or the strong interactions. While the sub-dominant electroweak interactions result in the production of charginos, neutralinos and sleptons, coloured particles such as squarks and gluinos are produced mainly via the strong interaction. Figure 2.8 sketches the squark and gluino production at leading-order via gluon-gluon-, gluon-quark fusion, as well as quark - anti-quark annihilation and quark-quark scattering. Whichever production is dominant depends on the masses of the squarks and gluinos, which differ strongly in the various SUSY models.

Above the respective mass thresholds, the cross-sections for the production of supersymmetric particles are comparable to the cross-sections for the production of the respective Standard Model partners at same Q^2, since the couplings of SUSY particles are assumed to be equal to the couplings of their Standard Model partners.

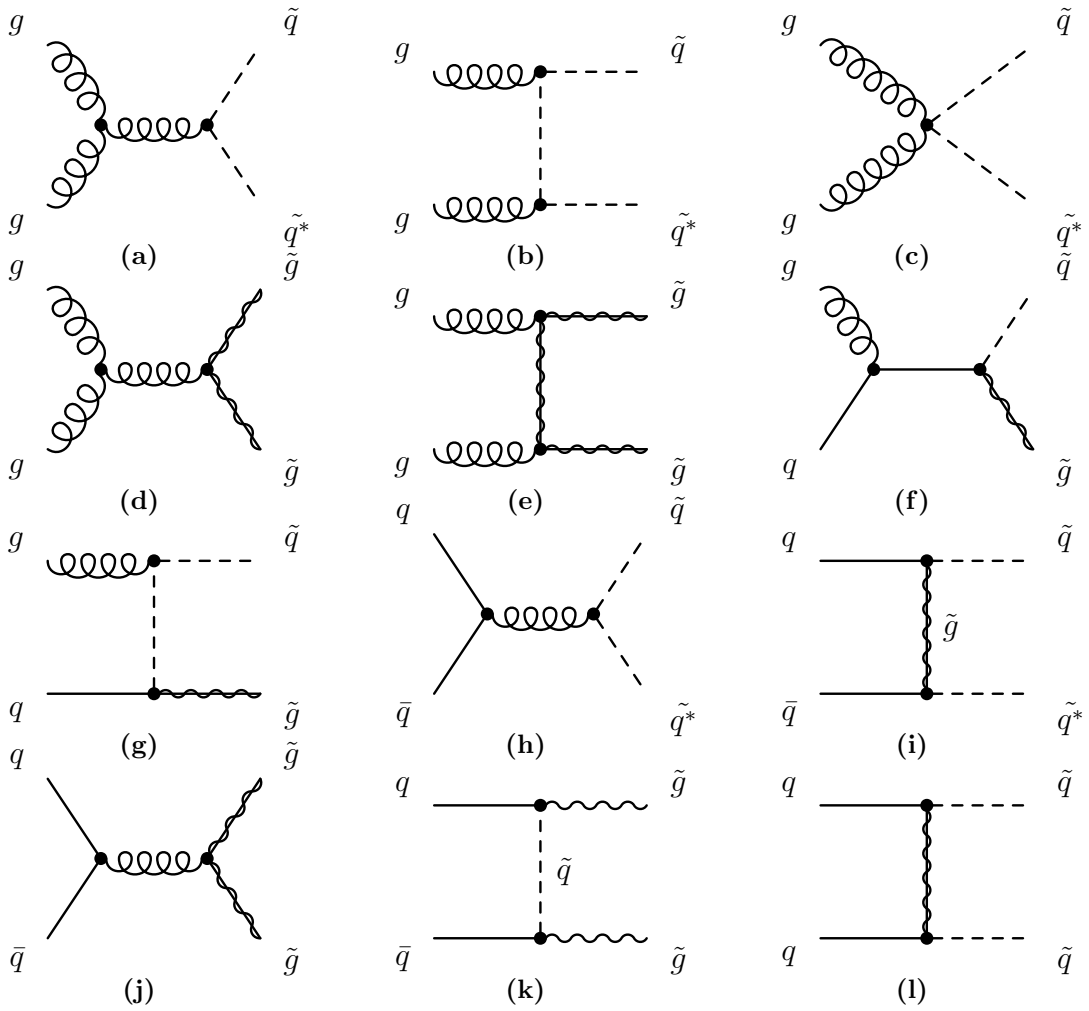

Figure 2.8: Examples of squark and gluino pair production at leading-order via gluon fusion (Figure 2.8a - Figure 2.8e), quark-gluon fusion (Figure 2.8f - Figure 2.8g), quark anti-quark annihilation (Figure 2.8h - Figure 2.8k) and quark-quark scattering (Figure 2.8l).

In R-parity conserving SUSY models, charginos and neutralinos decay directly or via cascades into the LSP and Standard Model particles. The decays are mediated by gauge bosons or sfermions.

If the squarks are heavier than the gluinos, the strong decay $\tilde{q} \to q\tilde{g}$ will dominate. Otherwise, they will decay weakly to charginos ($\tilde{q} \to q\tilde{\chi}_{\mathrm{i}}^{\pm}$) or neutralinos ($\tilde{q} \to q\tilde{\chi}_{\mathrm{i}}^{0}$), which decay further to the lightest neutralino (LSP). Gluinos can only decay via the strong interaction, where the process $\tilde{g} \to q\tilde{q}$ is the most dominant, provided the involved squark has a lower mass than the gluino. If all the squarks are heavier than the gluino, it will decay via an off-shell squark producing a chargino, $\tilde{g} \to qq'\tilde{\chi}_{\mathrm{i}}^{\pm}$, or a neutralino, $\tilde{g} \to qq'\tilde{\chi}_{\mathrm{i}}^{0}$. Thus, gluino-decay-chains are expected to contain at least two jets and decaying squarks produce only a minimum number of one jet, which leads to different event topologies for the different possible decays $\tilde{q}\tilde{q}$ ($\geq 2jets$), $\tilde{q}\tilde{g}$ ($\geq 3jets$) and $\tilde{g}\tilde{g}$ ($\geq 4jets$). Cascade decays of heavy particles tend to increase the final state multiplicity. In all cases, the LSP escapes unseen producing a large amount of $E_{\mathrm{T}}^{\mathrm{miss}}$ in addition to the jets.

2.7.3 General analysis strategy

With increasing integrated luminosity, the LHC experiments will achieve sensitivity to the production of supersymmetric particles [3] exceeding that of the Tevatron experiments [50, 103]. Being the highest-energetic collider to date, background estimations at the LHC cannot rely on simulations only, but data-driven methods are a key ingredient for any physics analyses in the first years of LHC running.

A general search strategy to cover a wide range of different SUSY models is the selection of events with large $E_{\mathrm{T}}^{\mathrm{miss}}$ and reconstructed jets with large transverse momentum. The phase space regions where ATLAS has a maximum sensitivity to possible SUSY signals, coming from the production and decay of squarks and gluinos, define the *signal regions*, in which the agreement between background expectations and data is tested. The total coverage of the search in the squark and gluino mass plane, however, defines the number of signal regions and the final cuts. Since no particular high-scale model is assumed when defining these signal regions, those regions are expected to be sensitive to a large region in the new physics parameter space including various non-supersymmetric models. Hereby, special emphasis is laid on providing also model-independent limits on the event yields and cross-sections of new physics, being still compatible with the experimental observations.

In addition, the final expectations are also based on *control region* measurements (e.g. for the QCD prediction) and Monte Carlo estimates (amongst others for W + jets, Z + jets and top pair production), which are also verified with various measurements in those control regions.

2.7.4 Transfer factors

Starting from the observed numbers of events in the control regions, normalized Standard Model background estimates for the SR are obtained with a likelihood fit, which is used to determine the statistical significance of observations in the signal regions as well. This procedure accounts for the contamination of the individual CRs - both from other Standard Model backgrounds and/or possible SUSY signals.

In order to convert the observations inside the CRs into estimates for the signal regions, one needs various *transfer factors (TFs)*: another key ingredient for the likelihood fit, determined separately for each background process, between the SR and each CR, as well as between the individual CRs.
With the number of observed background events of a certain process in the according control region, $N(\mathrm{CR}, \mathrm{obs}, \mathrm{proc})$, the final estimated number in the signal region, $N(\mathrm{SR}, \mathrm{est}, \mathrm{proc})$, is given by:

$$\mathrm{N}(\mathrm{SR}, \mathrm{est}, \mathrm{proc}) = \mathrm{N}(\mathrm{CR}, \mathrm{obs}, \mathrm{proc}) \cdot \left[\frac{\mathrm{N}(\mathrm{SR}, \mathrm{raw}, \mathrm{proc})}{\mathrm{N}(\mathrm{CR}, \mathrm{raw}, \mathrm{proc})}\right], \tag{2.8}$$

where the ratio of the raw, un-normalised estimates of the contributions from the process to the SR and CR, $N(\mathrm{SR}, \mathrm{raw}, \mathrm{proc})$ and $N(\mathrm{CR}, \mathrm{raw}, \mathrm{proc})$ respectively, represents the actual TFs. Similarly, the TFs connecting the different CRs are defined, enabling a coherent normalization across all CRs.

In order to provide a full comprehensive background estimation, one does not only require the TFs themselves to be measured precisely (with data-driven techniques where possible, otherwise completely determined on MC simulations, but extensively validated on data), but also their associated uncertainties, both correlated and uncorrelated ones. The above construction of the TFs is very advantageous because many systematic uncertainties such as the Jet Energy Scale (JES) uncertainties on MC estimates cancel in the ratio.

For the SUSY TFs, two different scenarios are to be considered:

- *search for an excess* The SUSY signal contamination in the control regions is assumed to be negligible, thus all SUSY TFs are set to zero.
- *exclusion of models* If no excess is found, model-specific TFs for each point of the MC simulation, including theoretical uncertainties on the SUSY production cross-sections, are calculated.

The according SUSY TFs together with the other fit inputs result in channel-wise sets of normalized background estimates and uncertainties for the SR as well as a p-value for the SR-observation.

2.7.5 Standard Model backgrounds

Although most Standard Model processes can be effectively suppressed by a cautious event selection and thus the expected Standard Model background is low, various Standard Model processes can give rise to similar event topologies directly or indirectly via misidentification of particles or only- apparently missing transverse energy.

This Section gives a brief overview about the most important backgrounds and the approaches to estimate them. Details about the Monte Carlo samples, however, can be found in Section 5.2.

W / Z + jets

The production of $W^{\pm}$ and Z bosons in association with jets is not only for the SUSY searches with leptons, but also for those without leptons expected to be one of the most important backgrounds. With the SUSY event selection requiring multiple jets in the final state, the modelling of multi-parton final states becomes extremely important.

The decay $Z \to \nu\nu + jets$, generating a large amount of true missing transverse energy, represents an irreducible background for SUSY analyses. Monte Carlo programs such as `ALPGEN`, `HERWIG` and `JIMMY`, which match parton showers with multi-parton matrix elements, describe the Z+jets production reasonably well, nevertheless it usually is estimated in a data-driven way from $\gamma + jets$, which is kinematically similar when treating the photon as Z, or from $Z \to \ell^+\ell^-$ where ℓ represents an electron or muon.

The dominant processes for the W are $W \to \tau\nu$ - where the hadronically decaying τ is reconstructed as jet - and the leptonic decays ($W^{\pm} \to \ell^{\pm}\nu$, $\ell = e, \mu$) where the neutrino generates true $E_{\mathrm{T}}^{\mathrm{miss}}$ and the electron or muon was lost due to either a limited detector acceptance or failing the identification criteria.

Top pair production

Hadronic tau decays in $t\bar{t} \to b\bar{b}\tau\nu qq$ and single top events can generate large $E_{\mathrm{T}}^{\mathrm{miss}}$ and thus contribute significantly. Especially in the high-jet multiplicities, a remarkable fraction of the background comes from $t\bar{t}$-events, where in a semi-leptonic decay the lepton was misidentified as jet.

QCD

For SUSY searches with and without leptons, the estimation of the QCD multijet background is important although the full set of selection criteria suppresses it already by several orders of magnitude: the cross-sections of QCD and expected strongly-interaction beyond-Standard Model signals are similar in magnitude at high $\sqrt{s}$.
QCD processes are most dominant for low p_{T}-jets and at low $\sqrt{s}$ because of their huge cross-sections. Typically, these events possess only few real missing transverse energy. Thus, it is mainly the rare/badly-understood processes that possibly enter the signal regions of SUSY searches.
Nevertheless, those QCD multijet events can still gain a large amount of additional $E_{\mathrm{T}}^{\mathrm{miss}}$ coming either from neutrinos in heavy-flavour decays (b- or c-jets with real missing energy, so-called heavy-flavour QCD) or the mismeasurement of at least one of the jets leading to only *apparently* missing transverse energy, which is the dominant reason for $E_{\mathrm{T}}^{\mathrm{miss}}$ in light-flavour QCD. Although the additional $E_{\mathrm{T}}^{\mathrm{miss}}$ due to the heavy flavour part is most probably well modeled by Monte-Carlo simulation, the heavy flavour cross-section depends heavily on the particle density function. The mismeasurements, however, are especially urgent at the beginning of a new experiment, when the detector is not yet fully understood. In case of a this type of mismeasurements as well as in case of HF jets fragmenting into neutrinos, one significant feature, which can be used for separation, is the fact that the $E_{\mathrm{T}}^{\mathrm{miss}}$ vector points alongside the direction of the mismeasured jet.

But also the use of MC simulations is limited: never before LHC, QCD-processes involving such high jet multiplicities have been probed at such high energies. The processes

of interest are rare, requiring an incredibly high statistics in the simulation when unfiltered or introducing a possible bias when applying generator-level filters. Finally, the simulation of only apparently missing energy (i.e. the simulation of mis-identifications and the exact detector resolution, especially jets from the uncertain tails of the jet resolution) is a highly complex and critical issue which needs lots of work in order to be understood and optimized before of any practical use for physics analyses.
The different methods to estimate the QCD multijet background will be discussed in detail in Section 6.5.

Chapter 3

Experimental Setup

The data analyzed in this thesis was collected in 2010-2011 by ATLAS, one of the two multi-purpose detectors running at the Large Hadron Collider (LHC) in Geneva, Switzerland. The LHC is located at CERN, the European centre for particle physics, and represents the highest energetic particle collider build by mankind to date.
A detailed description of the accelerator and the detector as well as the data taking procedure is given in the following Chapter, which is, being revised and updated, following closely Reference [104] and [1].

3.1 The Large Hadron Collider

The Large Hadron Collider [106–109] at CERN [110] is designed for proton-proton collisions at a centre-of-mass energy of 14 TeV. Its planning, started in 1984, anticipated many of the unanswered questions of the Standard Model, arising in the past decades.

Before starting the serial production of the various items needed to build a new accelerator, such as the magnets and cavities, but also the detectors, different technical proposals had to be developed, closely studied for feasibility and performance, and the most promising candidates were approved. Finally, the old twenty-seven kilometre circular tunnel of the LEP experiment [53, 54], the previous e^+e^-accelerator shutting down in November 2000, was freed and the installation process for the LHC began.

Between the Lake Geneva, the Jura Mountains and the Alps, geographically the LHC is situated close to Geneva, Switzerland - in a depth of 75 to 120 m (see Figure 3.1).
Two counter rotating proton beams (see Figure 3.2) are injected from the *super proton*

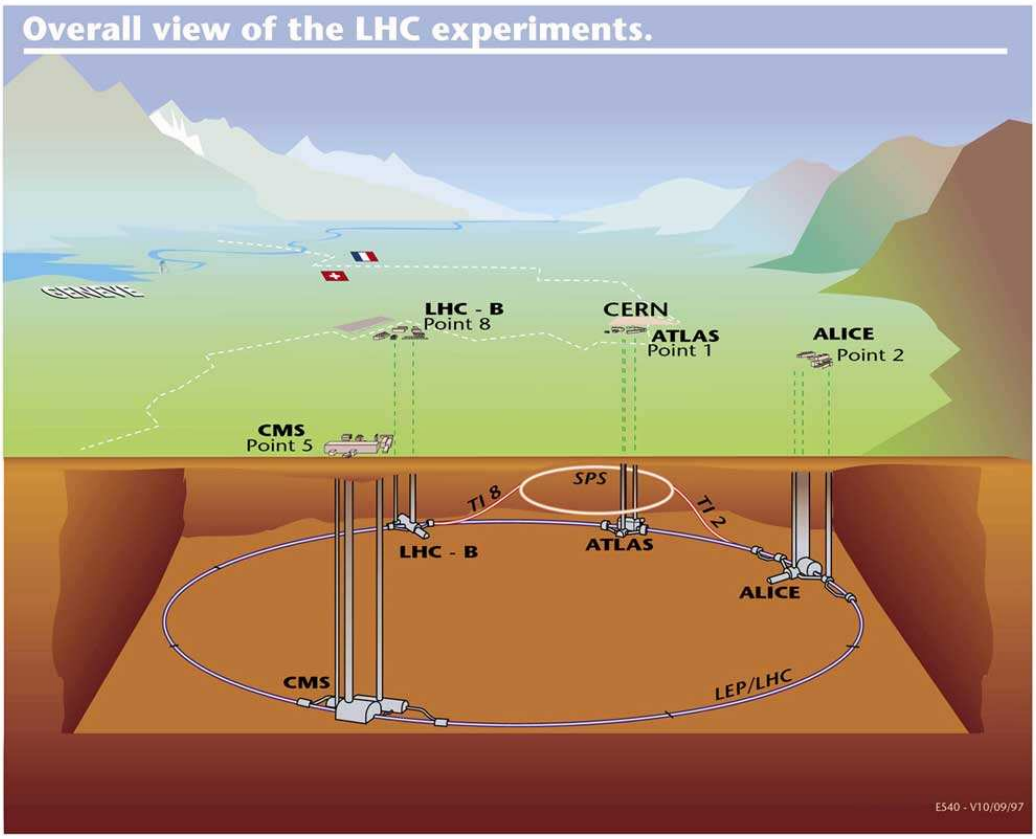

Figure 3.1: Scheme of the Large Hadron Collider [105]: The accelerator tunnel with its four main experiments ALICE, ATLAS, CMS and LHC-b, situated beneath the outskirts of Geneva, between the Alps, the Jura and the Lake Geneva.

synchroton (SPS) [1] into two separated beam pipes, located within the same supporting structure, with a nominal energy of 450 MeV. Eight radio frequency cavities per beam with a maximum field strength of about 5.5 MV/m accelerate the protons by alternating magnetic fields to a nominal energy of 7 TeV. A total number of 9,300 magnets with magnetic fields up to 8.33 T are needed to keep the protons inside the evacuated beam pipe: 1,232 dipole magnets, designed to combine the opposite magnetic fields into one magnet, bend the trajectories, 858 quadrupole magnets take care of a precise focusing and 6,208 additional magnets correct small deviations of the beam profile.
A large cryogenic system keeps the operating temperature of the whole accelerator beneath 1.9 K - LHC is one of the first accelerators completely cooled - as only superconducting [111] magnets can fulfill the enormous requirements concerning the magnetic field strength (HERA e.g. possessed only a super-conducting proton accelerator, while

[1] The SPS was build in 1976 and is the second largest machine in the CERN accelerator complex to date.

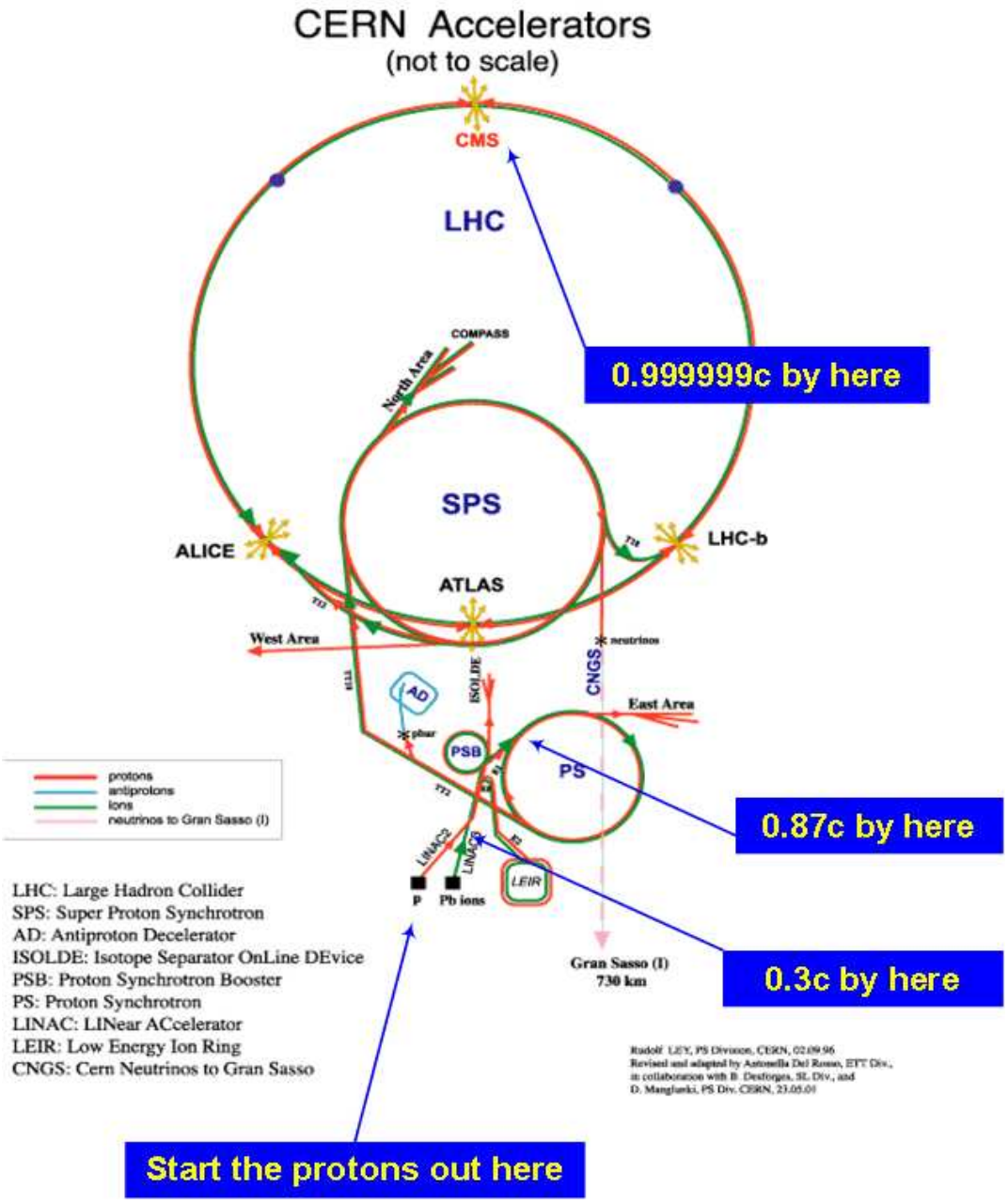

Figure 3.2: The CERN accelerators [105]. After proton generation, the beam is accelerated in several steps, until it is injected into the LHC ring for collisions.

the electron accelerator was traditional). Furthermore, the LHC is also designed to collide beams of heavy ions, such as lead, with a maximum total collision energy of 1,250 TeV - this is about twenty-eight times higher than at the Relativistic Heavy Ion Collider (RHIC) at Brookhaven Laboratory, USA.

The proton beams collide in the four locations of the four main experiments:

- ATLAS [104, 112–114] (*A Toroidal LHC ApparatuS*) and CMS [115–117] (*a Compact Muon Solenoid*) are multi-purpose detectors.
- ALICE [118] (*A Large Ion Collider Experiment*) is designed to search for a quark-gluon-plasma in heavy ion collisions - a state where the confinement of quarks and gluons shall be overcome.
- LHC-b [119, 120] (*the Large Hadron Collider Beauty experiment*) concentrates on high-precision measurements concerning b-physics.
- The measurements are rounded off by two smaller experiments called LHC-f [121, 122], a forward detector for ATLAS, and TOTEM [123, 124] (*Total Cross Section, Elastic Scattering and Diffraction Dissociation at the LHC*), associated with CMS in a joint diffractive/forward physics range.

About 10^{11}protons per bunch collide at a nominal bunch crossing rate of 40 MHz, leading to roughly 1 billion proton-proton collisions, one every 25 ns, being reduced in the start-up phase of the LHC to a bunch spacing of 50 ns, and yielding in total a design luminosity of

$$\mathcal{L} = 10^{34}\ \mathrm{cm}^{-2}\mathrm{s}^{-1}.$$

After an incident with the fragile connections between the superconducting magnets on September 19^{th} 2008 (see e.g. [125]), which caused some damage to the machinery and delayed the start-up by roughly one year, the management decided to reduce the beam energy in the first phase of data taking to only half of its design intensity, thus the centre-of-mass energy decreased from $\sqrt{s} = 14$ TeV to $\sqrt{s} = 7$ TeV, which resulted also in a lower total luminosity.

Nevertheless, the produced amount of data is to be carefully preselected by a *Trigger*, before it reaches manageable dimensions, even compared to today's standards. About $\mathcal{O}(100)$ events per second, each event representing a few MB, result in a final rate of 1 $^{\mathrm{GB}}/_{\mathrm{s}}$ in total. Considering the normal operation time of the LHC one can extrapolate the amount of data produced in one year to 15 PB (15 *million* GB), including the raw, preprocessed and simulated data.

Not only needs this enourmous quantity of data to be stored safely, but also want hundreds of researchers around the globus the data for analysis. Hence, the *GRID* was pushed, a new development for distributed computing. The LHC Computing Model [126]

divides the GRID into a hierarchical structure, split in four different levels.
CERN, the source of the data, houses the first level, called *Tier-0*. Copies of these data are distributed to a dozen major national computing centres (*Tier-1*), which are supplemented by regional *Tier-2*-centres, in total over 130 in research labs and universities, distributed in 31 countries around the world. The various analyses of the physicists are processed mainly by the *Tier-3*-centres, the lowest and most local level in this structure, while tasks of main interest, such as the alignment and a first reconstruction of the data, is reserved to the upper levels. In addition, a huge number of simulated events is needed for the analyses, exceeding the data requirements concerning computing power and disk space by a multiple. To conclude, this LHC Computing Grid project (*LCG*) currently operates the world's largest scientific Grid, including more than 10,000 CPUs and several PB of storage.

3.2 The ATLAS Detector

ATLAS (*A Toroidal LHC ApparatuS*)[112–114, 127] is the largest of the LHC experiments: it has a height of 25 meters and a length of 46 meters with a weight of 7,000 tons.

Like most multipurpose detectors, ATLAS possesses a typical onion-like structure (see Figure 3.3). The innermost part is a precise tracking system consisting of three subdetectors: *Pixel, Semiconductor* and *Transition Radiation Tracker*. It is surrounded by a *solenoid magnet* bending tracks of charged particles in the transverse plane and therefore allowing a measurement of their transverse momentum. With neutral particles not being seen by the trackers, *calorimeters*, situated in the detector middle, are needed for the detection of any neutral particles interacting either via the electromagnetic or the strong force, such as photons and neutrons. Hereby, one distinguishes between the *electromagnetic* and the *hadronic* calorimeter. Electrons and photons are to be measured precisely and stopped in the electromagnetic calorimeter, while the hadronic one is dedicated to the detection of hadrons. With muons being minimal-ionizing, they deposit only a small amount of their energy in both calorimeters during the transit. With the need of another layer of tracking detectors on the detector outside, the outermost part of ATLAS is represented by different types of *muon chambers* . These are located in the spaces between a large *toroidal magnet* providing a second independent measurement of the muon momentum in addition to the inner detector measurement.

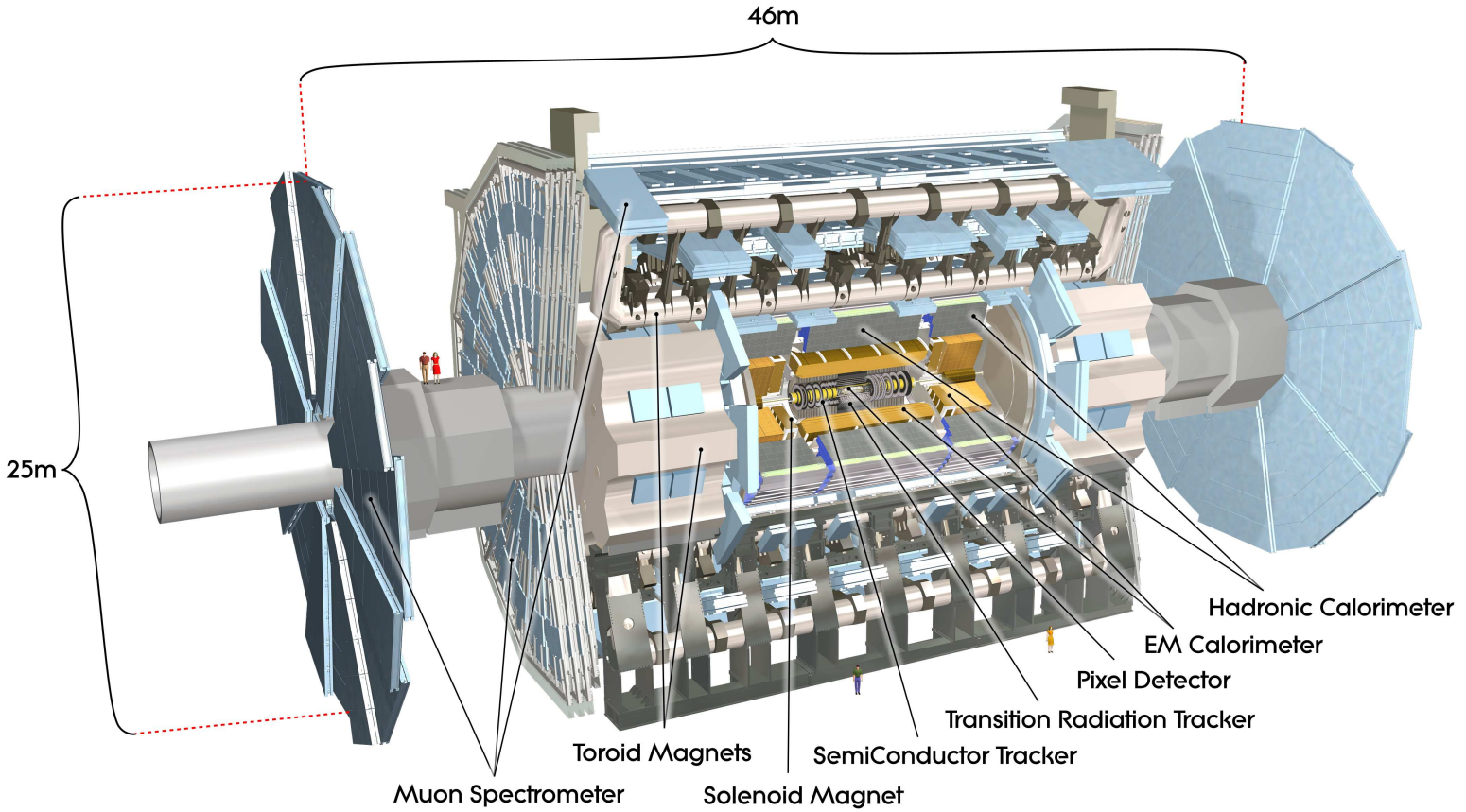

Figure 3.3: The different sub-detectors of ATLAS [105]: innermost a precise tracking system, in the middle the electromagnetic and hadronic calorimeters and outermost the muon chambers. The tracking system is surrounded by a solenoidal magnetic field while the muon chambers are placed between the components of a toroidal magnet.

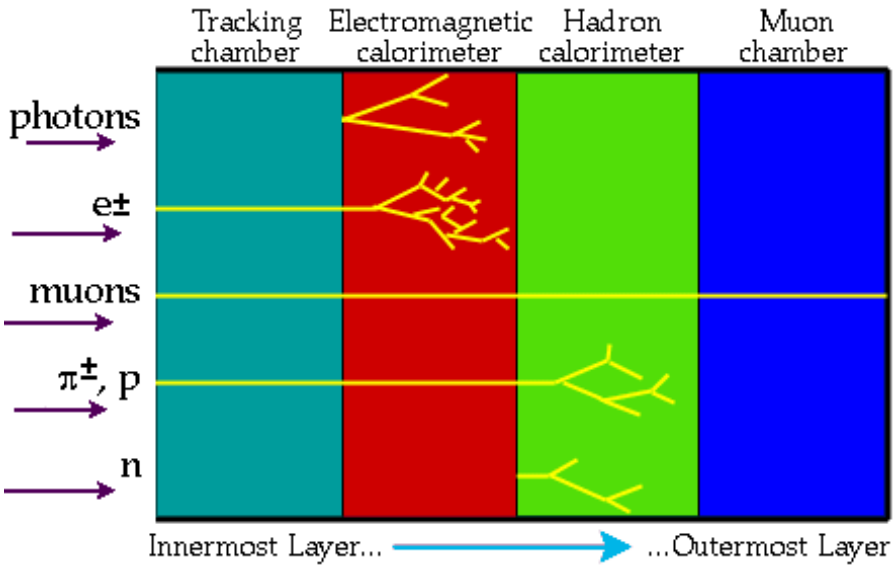

Figure 3.4: Particle detection in the different detector layers: each slice is specialized on the detection of particles of a certain type. As the matter-interactions of purely weakly-interacting particles, such as neutrinos, are rarely, these are not directly detectable and escape unseen creating a signature of missing energy and momentum. However, they can be reconstructed from the visible particles in the event via conservation laws. Picture taken from [128].

A graphical summary of which detector is capable of detecting which particle is given in Figure 3.4.

3.2.1 Required Performance

A set of global requirements for the detector performance can be derived (see Table 3.1) from the ambitious physics goals as well as technical needs (high interaction rates, particle multiplicities, -energies and radiation doses). The search for the SM Higgs defines only one of the various levelling bars.

- Coverage in pseudorapidity η (see Equation (3.1)) needs to be as high as possible for a minimum loss of particles in the forward region.
- A very good momentum resolution of charged particles is essential in the inner trackers such as a high reconstruction efficiency.
- Due to a very high particle density especially near the beam pipe, a very high granularity must be combined with a fast read-out and radiation hardness, both for sensors and for on-detector electronics.

Detector component	Required resolution				η coverage	
					Measurement	Trigger
Tracking	σ_{p_T}/p_T	$=$	$0.05\%\ p_T$	$\oplus$ 1%	$\lvert\eta\rvert \leq 2.5$	
EM calorimetry	σ_E/E	$=$	$10\%/\sqrt{E}$	$\oplus$ 0.7%	$\lvert\eta\rvert \leq 3.2$	$\lvert\eta\rvert \leq 2.5$
Hadronic calorimetry						
barrel and end-cap	σ_E/E	$=$	$50\%/\sqrt{E}$	$\oplus$ 3%	$\lvert\eta\rvert \leq 3.2$	$\lvert\eta\rvert \leq 3.2$
forward	σ_E/E	$=$	$100\%/\sqrt{E}$	$\oplus$ 10%	$3.1 < \lvert\eta\rvert < 4.9$	$3.1 < \lvert\eta\rvert < 4.9$
Muon spectrometer	$\sigma_{p_T}/p_T = 10\%$ (at p_T	$=$	1 TeV)		$\lvert\eta\rvert \leq 2.7$	$\lvert\eta\rvert \leq 2.4$

Table 3.1: Performance goals of the ATLAS detector [127]. Both, momenta and energies are measured in GeV.

- Also the calorimeters have to be excellent. Electron and photon identification are most important for the electromagnetic part while for the hadronic part accurate measurements of jets and missing transverse energy are indispensable together with a full η coverage.
- The muon spectrometer has to determine the charge and transverse momentum of muons over a wide range of momenta independently from the inner trackers.
- The trigger needs to reliably reduce the enormous data rates to a manageable level.

The performance of ATLAS has been widely studied in first data taking period, and the fulfillment of the ambitious requirements has been confirmed.

3.2.2 Coordinate Frames

The ATLAS global coordinate frame forms a right-handed coordinate system (see Figure 3.5) [129]. The x-axis points from the detector vertex towards the centre of the LHC ring and is denoted *GlobalX*. *GlobalY* is directed skywards with an inclination about 1.23°. *GlobalZ* is aligned parallel to the beam axis. *End Cap A* is situated in positive z direction, while *End Cap C* entitles the opposite side.

GlobalX and GlobalY span the transverse plane in which e.g. the transverse momentum, p_T, and the missing transverse energy, E_T^{miss} , are defined. *Global*φ corresponds to a rotation around GlobalZ in the transverse plane. Globalϑ is measured with respect to the beam pipe inside the longitudinal *R-Z* detector plane.

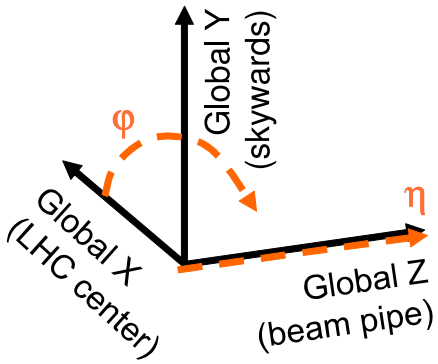

Figure 3.5: The ATLAS Global Coordinate Frame: The x-axis ($GlobalX$) points from the detector vertex towards the centre of the LHC ring. The y-axis ($GlobalY$) is directed skywards and the z-axis ($GlobalZ$) is aligned parallel to beam axis.

Finally, the pseudorapidity η is given by

$$\eta = -\ln \tan \vartheta/2. \tag{3.1}$$

Distances are measured in $\Delta R = \sqrt{(\Delta\varphi)^2 + (\Delta\eta)^2}$.

3.2.3 The ATLAS Inner Detector

The ATLAS Inner Detector (ID, [127, 130, 131]) consists of a solenoid and three different tracking detectors: a *pixel* detector, a *semiconductor* tracker and a *transition radiation* detector (see Figure 3.6).
Its main purpose is a precise measurement of the transverse momentum and a reliable identification of secondary vertices. Thus, not only the distance between measured hits and the primary vertex is essential but also the number and quality of each single hit.

The Solenoidal Magnet

The tracking system is placed inside a solenoidal magnetic field parallel to the beam axis. The magnet [127, 132, 133] is made out of a superconducting coil. It has an axial field strength of 1.998 T at a nominal current of 7.730 A, an operation temperature of 4.5 K and consists of 9.2 km high-strength Al-stabilised NbTi conductors. The length of the magnet is 5.8 m. Its radius is about 2.5 m and the coil mass is 5.4 t. The adjacent calorimeters serve as support, i.e. the steel of the hadronic calorimeter serves as flux return and the coils vacuum vessel is shared with the electromagnetic calorimeter.

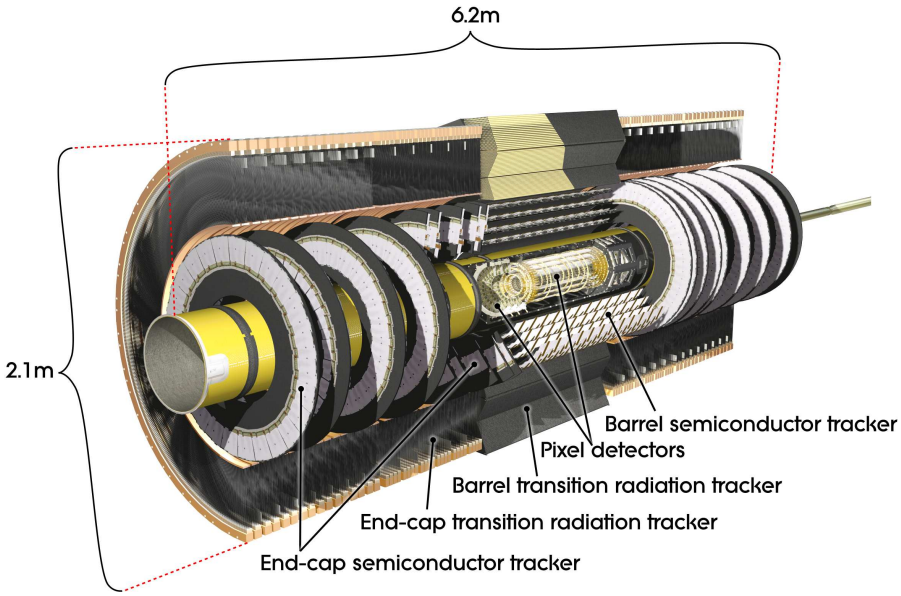

Figure 3.6: The ATLAS Inner Detector (ID) is divided into three sub-detectors. The beam pipe is surrounded by the Pixel Detector, followed by the Semiconductor Tracker, then the Transition Radiation Tracker which allows e.g. to distinguish between pions and electrons.

The Pixel detector

About 1000 tracks per event are expected within an $|\eta|$-range of 2.5. Thus, a fine granularity is essential in particular for the vertex detector. Both, Pixel and silicon micro-strip tracker (SCT) are arranged in concentric cylinders (see Figure 3.7) parallel to the beam axis. The end cap discs are perpendicular to the beam pipe on both sides.

The Pixel detector [135] consists of 1,744 identical modules. The minimum pixel size is $50 \times 400\ \mu\text{m}^2$. In total, there are about 80.4 million readout channels.
The modules are arranged into three barrel layers and 2×3 end cap discs, grouped in staves (modules with identical module-φ) in the barrel region and segments in the disks. The pixel staves (see Figure 3.7) are mounted on the barrel support structures with a tilt angle α of $+20°$ between the module and a barrel tangential vector. Two neighbouring staves overlap about 1 mm in R-φ direction in order to ensure full coverage.

The pixel sensors consist of oxygenated n-type wafers with an n+ doping on the read-out side and a p-type back contact. They have a thickness of 250 μm and their intrinsic resolution is $17 \times 115\ \mu\text{m}^2$ in $(R - \phi) \times z$.

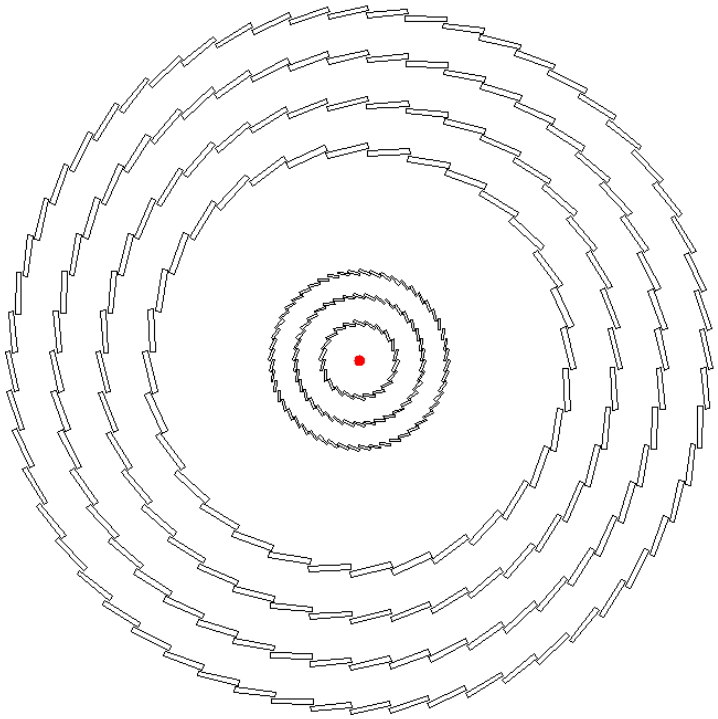

Figure 3.7: View of the silicon barrel detector geometry [134] in the R-φ-plane. The inner three layers belong to the Pixel detector. Its innermost layer has a radius of 5 cm. The outer four layers belong to the SCT, the outermost layer has a radius of about 55 cm. Modules are arranged with a small overlap in the R-φ-plane. The inclination α of Pixel and SCT modules is directed oppositely.

The modules are mounted onto the support structure such that the sensor side faces the beam line. In order to enhance the performance the best modules were placed in barrel layer 0.

The Semiconductor Tracker

The silicon micro-strip detector (SCT) is built up of 4,088 modules, where each is a combination of two single-sided parts. The modules are arranged in four barrel layers and 2×9 disks on each side, providing about four three-dimensional space points per track.

The average strip pitch of the rectangular modules in the barrel region is 80 μm leading to a intrinsic resolution of 17 μm in R-φ direction and 570 μm in z-direction. The strips of the trapezoidal modules in the end cap region have a slightly different pitch of 47-96 μm leading to an intrinsic resolution of again 17 μm in R-φ-direction and 570 μm in radial direction. The SCT covers an area of 63 m^2 active silicon and has approximately

6.3 million read-out channels.
Analogue to the Pixel tracker the modules are grouped in segments building disks and in staves for barrel (see Figure 3.7), with a tilt angle α of $-10°$ between the module surface and a barrel tangential vector. A significant overlap between neighbouring staves provides a maximum detector coverage and a minimum of geometrical holes.

Considerations of costs and reliability lead to the chosen classic single-sided design of p-in-n silicon with binary AC-coupled readout-strips which are mounted on the back of each other with a small tilt angle of 40 mrad. In the barrel region, alternating the inner or outer wafer of the modules is aligned parallel to the beam pipe. On the discs always one wafer of the module is aligned radially.

The Transition Radiation Tracker

In addition to the high-precision hits delivered by the silicon trackers, the transition radiation tracker (TRT) provides slightly different information for an overall robust pattern recognition: it offers a large number of one-dimensional R-φ hits (typically 36) per track with an intrinsic resolution of 130 μm. The TRT hit information improves the momentum resolution in the transverse plane. Additionally, the transition radiation signal allows to distinguish between electrons and pions as the amount of transition radiation depends on the mass of the particle.
In the barrel region the TRT consists of 4 mm diameter straw tubes filled with a xenon-based gas mixture, orientated parallel to the beam pipe. The barrel is split up nearly in the middle of the 144 cm long straws. It covers a region of $|\eta| \leq 2$. The end cap design differs slightly from the barrel, as the shorter straws are aligned radially. The TRT consists of approximately 351,000 read-out channels.

3.2.4 The ATLAS Calorimeters

For the ATLAS calorimeters (see Figure 3.8) different technologies were chosen according to the requirements concerning physics interests and radiation hardness [136, 137]. The goal is an energy measurement with the highest possible precision.
The electromagnetic (EM) calorimeter is a liquid-argon sampling calorimeter, placed outside the solenoidal magnet. It has a very high granularity and a good performance, both for energy and position resolution - this is very important since it allows to distinguish i.a. between e,γ and $\pi^0(\eta)$, which decay in $\gamma\gamma(\gamma\gamma\gamma)$. It supplements perfectly the

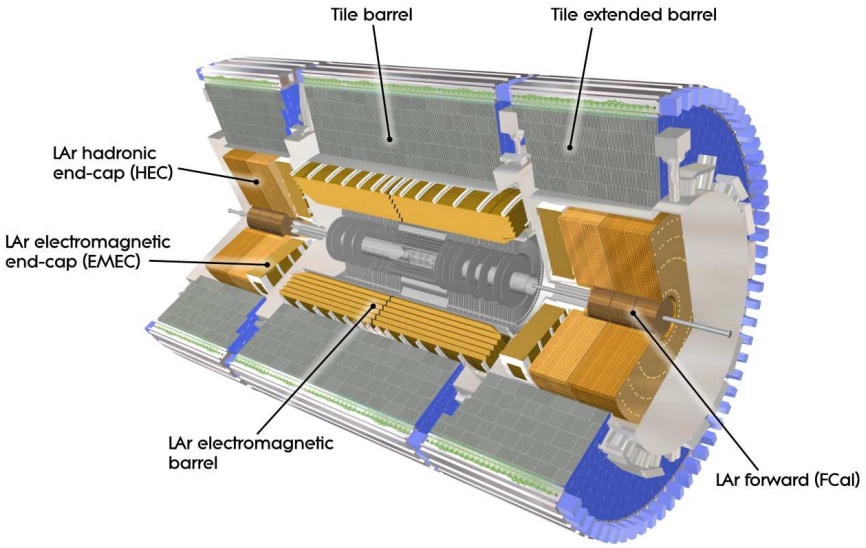

Figure 3.8: The ATLAS calorimeters. Innermost the liquid-argon electromagnetic calorimeter (LAr), then the scintillator-tile hadronic calorimeter. There is an additional combined forward calorimeter also built with liquid-argon technology ($FCal$) adding up to $|\eta| \leq 4.9$.

precision measurements of the Inner Detector. For the rest of the calorimeter a coarser granularity is sufficient, especially due to a higher particle density in the forward region and relatively lower requirements for the measurement of jets and $E_{\mathrm{T}}^{\mathrm{miss}}$. In the barrel region the hadronic calorimeter consists of three scintillator-tile cylinders - a big one in the middle extended by a smaller part on each side. However, the end caps are also designed with liquid argon technology. A combined forward calorimeter extends up to $|\eta| \leq 4.9$.

One of the main challenges for the calorimeters is given by a good energy resolution and jet containment. The ATLAS calorimeter, however, is *non-compensating* (i.e. its response to EM particles and to hadrons is not equal), therefore a calibration is needed to restore the full energy of hadronic particles.
The radiation length is a good indicator for the effective thickness of a calorimeter, as it shows the distance in which the particle's energy is reduced by factor e. The larger the radiation length, the less punch-throughs into the muon systems. The EM calorimeter has a total thickness of more than 22 radiation lengths while for the hadronic calorimeters nearly 10 radiation length suffice. In combination with the high η-coverage of the whole system a good $E_{\mathrm{T}}^{\mathrm{miss}}$ -measurement is achieved.

The Electromagnetic Liquid Argon Calorimeter

The electromagnetic calorimeter is dedicated to the measurement of electrons and photons. Two identical halves form its central part with a small gap of 4 mm at $\eta = 0$. Similarly, the end caps are split into an inner wheel for $|\eta| < 2.5$ and an outer wheel for $2.5 < |\eta| < 3.2$. The transition between barrel and end caps is situated at $|\eta| \approx 1.425$ with a small overlap in-between.
The EM calorimeter combines liquid-argon with lead-absorbers and accordion-shaped Kapton electrodes. It is split into two to three longitudinal sections and providing a totally symmetric φ-behaviour. For a good performance the material in front of the calorimeter has to be minimised. Thus, the solenoidal magnet and the central part share a common vacuum vessel. Additionally, a presampler of liquid-argon is installed in the central region to correct the energy loss in the Inner Detector and the solenoid.

The Hadronic Calorimeter

The central barrel of this sampling calorimeter is placed outside the EM calorimeter. It covers a range of $|\eta| \leq 1$. The two extended barrels reach $|\eta| \leq 1.7$.
The barrel is made of 3 mm thick scintillating tiles as active material and 14 mm thick steel plates which act as an absorber. The calorimeter is segmented azimuthally into 64 modules and longitudinally into three layers.

The liquid-argon hadronic end cap calorimeter (*HEC*) is connected to the outside of the EM end caps and shares the same cryostat. It is split up into two wheels per disk, each consisting of 32 wedge-shaped modules and separated longitudinally in two segments. It covers a range of $2.5 < |\eta| < 3.2$ providing an overlap both with the forward and the extended barrel calorimeters. The wheels are made of 25-50 mm-thick copper plates as absorber with gaps of 8.5 mm active material, liquid argon.

The Forward Calorimeter

The forward calorimeter (*FCal*) is a combined EM-hadronic calorimeter and covers a range of $3.2 < |\eta| < 4.9$. The FCal is divided into three longitudinal segments with a total thickness of nearly 10 radiation lengths. Because of the limited space available, the calorimeter makes use of a high-density design. The first segment is made of copper as an absorber and is mainly dedicated to electromagnetic measurements. The outer layers

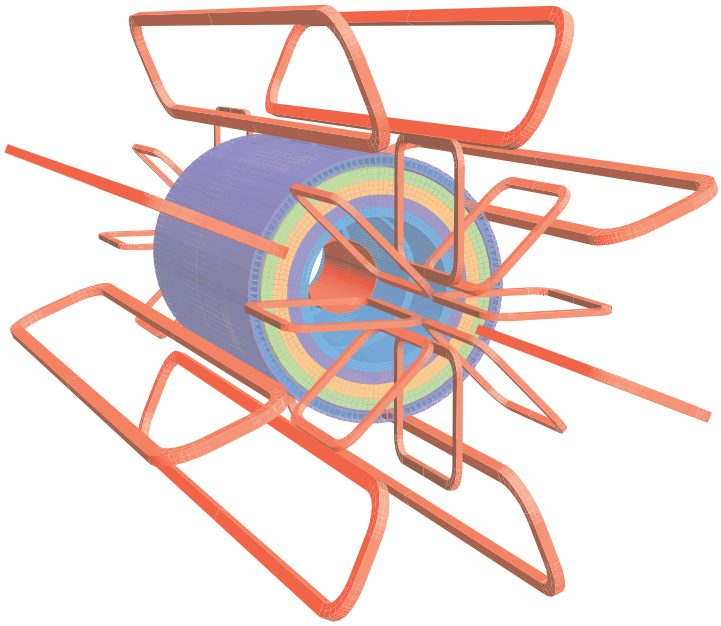

Figure 3.9: The ATLAS magnetic system with its solenoid surrounding the ID and the three toroids placed in-between the outer layers of the muon system.

consisting of Tungsten as absorber serve as hadronic calorimeters. For both segments liquid-argon is the active material. It is filled inside the concentric rods and tubes parallel to the beam pipe.

3.2.5 The ATLAS Muon System

The Toroidal Magnets

The whole ATLAS design is dominated by the choice of its toroidal magnets[132, 138, 139]. The air-core-system (see Figure 3.9) consists of a long barrel formed by 8 super-conduction interconnected coils inside individual cryostats and two smaller end cap toroids, each consisting of 8 coils. Roughly 100 km of superconducting cables, operating at a nominal temperature of 4.7 K, carry a current of 20.5 kA, leading to a stored energy of about 1 GJ in total.
Each end cap toroid is put inside one single cryostat. These three magnets generate an up to 4 T magnetic field orthogonal to the muon tracks, whereas the average magnetic field inside the muon spectrometer volume is only about 0.5 T. The magnets facilitate an additional measurement of the muon momentum, independent from the ID. Multiple scattering is minimised because of the light and open design.

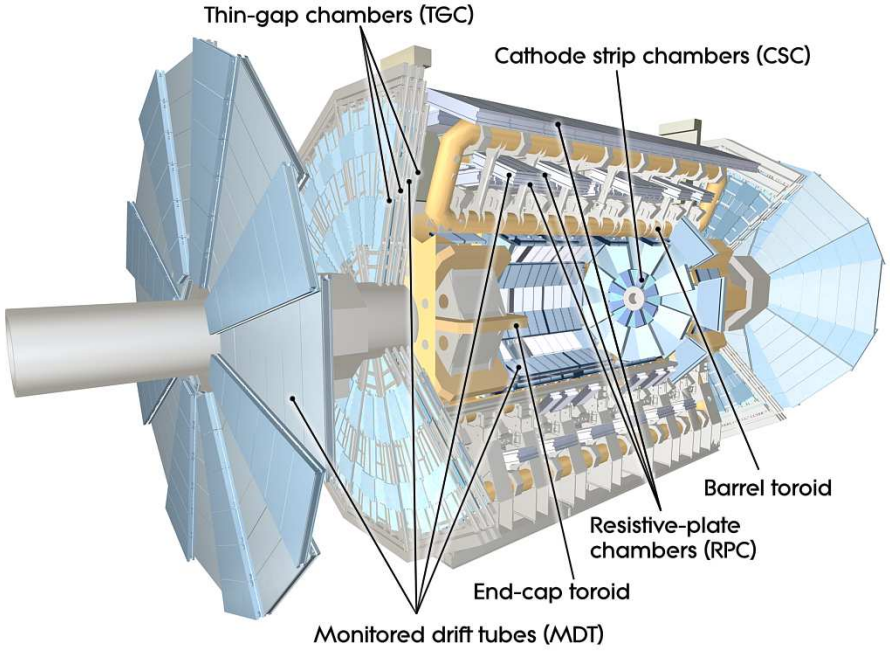

Figure 3.10: The ATLAS Muon System with its four different types of muon chambers.

The Muon Chambers

The muon spectrometer [140] is situated outside the hadronic calorimeter, between the coils of the toroidal magnets (see Figure 3.10). It covers a total area of $12,000$ m^2. Four different types of muon chambers are in use: the barrel mainly consists of Monitored Drift Tubes (*MDTs*) and Resistive Plate Chambers (*RPC*) while in the end caps there are Cathode Stripe Chambers (*CSC*) and Thin Gap Chambers (*TGC*). Its excellent muon resolution is achieved by three layers of high precision tracking chambers (MDTs and CSCs) and additional trigger chambers (RPCs and TGCs) with a timing resolution of 1.5−4 ns. The chambers of the barrel region are arranged in cylindrical layers around the beam pipe. In the transition and end cap region, the chambers are arranged perpendicular to the beam axis.

The MDTs provide a one-dimensional intrinsic single-hit resolution of 80 μm, the CSCs 40 μm. The RPCs have a two-dimensional spatial resolution of about 1 cm and the TGCs an azimuthal resolution of $2-3$ mrad.

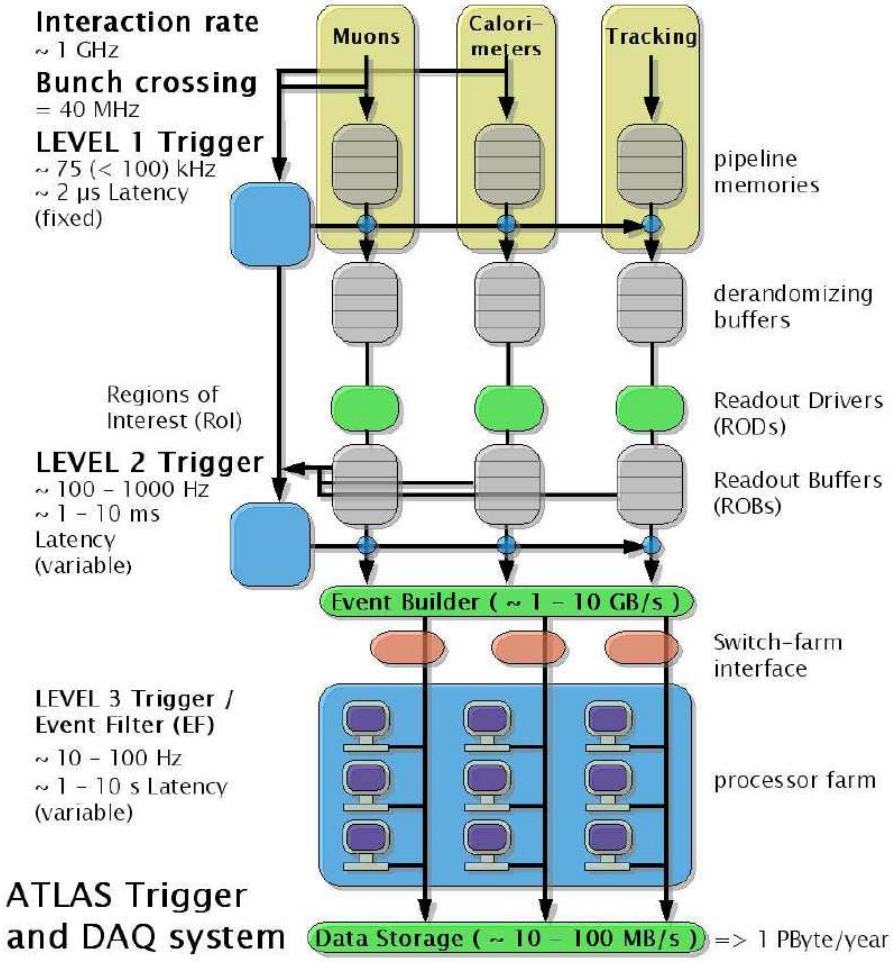

Figure 3.11: The ATLAS Trigger System [141, 142] is split into three levels. It provides a final data reduction from 1 GHz to approximately 300 Hz.

3.2.6 Trigger and Data Acquisition

With respect to technological and resource limitations the event data recording needs a severe preselection. A reduction of the 1 GHz proton-proton interaction-rate at the design luminosity of $\mathcal{L} = 10^{34}\ \mathrm{cm}^{-2}\mathrm{s}^{-1}$ by a factor of 5×10^6 is indispensable. Although the total number of recorded events must be reduced drastically possible new physics needs to be enriched at the same time, which makes the decision very hard.

ATLAS has a 3-levelled trigger system (see Figure 3.11). Level-1 (*L1*) [141] uses only information from the calorimeters and the muon trigger chambers to derive its decision and to define *Regions-of-Interest (ROIs)*. L1 reduces the data rate to about 75 kHz with a latency of fewer than 2.5 μs. Meanwhile the event information is buffered by the data acquisition system. Level-2 (*L2*) is only partially hardware-based. Together with the

pure software-based event builder and event filter (*EF*) it forms the High-Level-Trigger (*HLT*) [142]. They are run on dedicated computing farms and provide a final reduction to approximately 300 Hz. L2 refines the L1-ROIs and applies additional cuts. Finally, the EF combines the full detector information to reconstruct the whole event resulting in a total event size of 1.3 MB.

The trigger menu, i.e. the collection of all running trigger chains, consists not only of complex objects like e.g. high-p_{T} jet + $E_{\mathrm{T}}^{\mathrm{miss}}$, high-p_{T} same-sign dimuon or asymmetric multiple-jet triggers, but also of basic objects like single jet triggers with moderate p_{T}, which are needed both to study the performance of other, more-complex combined triggers, and as a preferably unbiased starting point for further studies. In order not to spoil the total allowed trigger rate with these basic triggers, chains yielding high rates need to be *prescaled*, i.e. only a certain amount of the physics-trigger accepted events is kept, like 1 out of 1000. These prescales can be applied on all three trigger levels independently, only the luminosity calculation need to be corrected during offline analyses accordingly.

The overall trigger menu is adjusted regularly during data taking according to the instantaneous luminosity and the detector status to keep the overall output-rate at a constantly high level.

Part II

Analysis

Chapter 4

Physics Objects

The ATLAS detector possesses roughly 100 million readout channels in total. For physics analyses, the stream of readout signals from the detector, the so called raw data, must be translated into basic physics objects such as leptons (ℓ), jets or missing transverse energy ($E_{\mathrm{T}}^{\mathrm{miss}}$) in order to gain an accurate estimate of the original interaction and its kinematics by measuring the different physics properties of a particle such as p_{T}, η and φ.
In a first step, the algorithms identify a set of candidates for the different physics objects. Then, the raw energy measurements associated with these candidates are - according to their dedicated calibrations - calibrated in order to later reconstruct the event kinematics as precisely as possible. A candidate object, however, can be faked or the type of the physics object itself be misidentified by certain detector effects such as noise. Thus, the algorithms must be optimized to gain both a high efficiency and a high purity at the same time. In the end, a possible double-counting of energy deposits between different candidate objects is resolved by the so-called overlap removal. The remaining final objects are unique and the term candidate is dropped.
This Section introduces in detail the physics objects of interest, which are needed for the later analyses, summarising [9, 10].

4.1 Jets

Based on an anti-k_t algorithm (see Section 2.6.2), jet candidates are reconstructed with four-momentum recombination The distance parameter is chosen to be $R = 0.4$ (in y[1] – φ space, see below) because SUSY events are expected to possess a large jet multiplicity. The jet algorithm is based on topological clusters [143] as input with the aim of reconstructing the three-dimensional shower topology of each particle entering the calorimeter.

The jet candidates obtain several corrections:

- The average energy gain by *pile-up* events is subtracted.
- The reconstructed jet-direction is no longer pointing to the geometrical detector centre but the *primary vertex*.
- As ATLAS has a non-compensating calorimeter (i.e. hadrons produce a lower response than electrons or photons), the measured jet transverse momentum at the *electromagnetic scale*, $p_{\mathrm{T}}^{jet,em}$, underestimates the hadron-level jet. This effect is further increased by the presence of dead material. Therefore, a calibration procedure called *Jet Numerical Inversion Correction* [144, 145] is applied, which corrects the transverse jet momentum as a function of $p_{\mathrm{T}}^{jet,em}$ and $|y^{jet}|$ with a factor C, extracted from MC:

$$p_{\mathrm{T}}^{jet} = C\left(p_{\mathrm{T}}^{jet,em}, \left|y^{jet}\right|\right) \cdot p_{\mathrm{T}}^{jet,em} \tag{4.1}$$

The above criteria together with two acceptance cuts ($p_{\mathrm{T}} > 20$ GeV and $|\eta| < 2.8$) are referred to as *loose jet selection* and subsequently retained.

Due to a temporary electronics failure in the LAr barrel calorimeter on 30$^{\mathrm{th}}$ April 2011 (period E onwards, affecting approximately 84% of the data), which created a dead region in its second and third longitudinal layers, approximately 1.4×0.2 in $\Delta\eta \times \Delta\phi$, the energy of jets pointing into this hole is reduced on average by 30%. While the impact on the reconstruction efficiency for jets with $p_{\mathrm{T}} > 20$ GeV is negligible, for safety reasons events will nevertheless be vetoed if any of the four leading jets is affected

[1] The rapidity y is defined to be $y = \frac{1}{2}\ln\left(\frac{E+p_{\mathrm{L}}}{E-p_{\mathrm{L}}}\right)$, being (numerically) close to the pseudorapidity η, which uses $|\mathbf{p}|$ instead of E.

Cut	Value/description
Algorithm	AuthorElectron
Acceptance	$p_{\mathrm{T}} > 20$ GeV, $\lvert\eta^{\mathrm{clust}}\rvert < 2.47$
Quality	Medium
Further cuts	Cut on quality flag and require not to be in the 'LAr hole'

Table 4.1: Selection criteria for medium purity electrons [9, 10].

- the main reason for this exclusion, however, being the fact that the MC simulation does not include this deficiency yet.

4.2 Electrons

A summary of the medium purity cuts, used for the reconstruction and identifications of electron candidates in ATLAS, is given in Table 4.1. The requirements also comprise cuts on the object quality flag, a LAr hole veto and a smearing procedure of the electron energy for MC. The acceptance cuts are $|\eta^{\mathrm{clust}}| < 2.47$ and $E_{\mathrm{T}ele} = E^{\mathrm{clust}}/\cosh\eta \geq 20$ GeV, where η is taken to be η^{track} if the track contains at least 4 silicon hits and η^{clust} otherwise.

4.3 Muons

Muons are passing two independent tracking detectors: the inner detector and the muon spectrometer. Thus, different reconstruction approaches exist [104]: while *combined* muons are made from tracks, being independently reconstructed in both the Muon Spectrometer (MS) and Inner Detector (ID) with the *STACO* algorithm, *segment-tagged* muons do not require a fully reconstructed MS track, but use it for tagging ID tracks as muons. Additionally, these muon candidates must be isolated (i.e. in a cone of $\Delta R < 0.2$, $\sum p_{\mathrm{T}}(\mathrm{tracks}) < 1.8$ GeV - excluding the muon track itself) and fulfill a list of quality requirements.
The overall acceptance cuts for muon candidates are $p_{\mathrm{T}} > 10$ GeV and $|\eta| < 2.4$. Similarly to electron candidates, also the p_{T} of muon candidates must be smeared within

Cut	Value/description
Algorithm	STACO, combined or segment-tagged muon
Acceptance	$p_{\mathrm{T}} > 10$ GeV, $\lvert\eta\rvert < 2.4$
Quality	Loose
Inner detector	≥ 1 pixel hit, ≥ 6 SCT hits, pixel holes + SCT holes < 3
	≥ 1 b-layer hit when it can be expected
track quality	If $\lvert\eta\rvert < 1.9$: $n_{TRT} \geq 6$ and $n_{\mathrm{TRT}}^{outliers} < 0.9\, n_{TRT}$
	If $\lvert\eta\rvert \geq 1.9$ and $n_{TRT} \geq 6$: $n_{\mathrm{TRT}}^{outliers} < 0.9\, n_{TRT}$

Table 4.2: Muon definition [9, 10]: n_{TRT} denotes the total number of TRT hits, including outliers.

MC to get better data/MC agreement. An overview of the selection criteria is given in Table 4.2.

4.4 Overlap removal

Applying the above object identification, different candidates can overlap with each other. Thus, strict rules are required to remove all but one of the overlapping objects and to avoid double counting. Based on previous studies [47], the overlap removal uses a simple geometric variable $\Delta R = \sqrt{(\Delta\varphi)^2 + (\Delta\eta)^2}$ for its selection.

Overlaps between candidate jets with $|\eta| < 2.8$ and leptons are resolved as follows: First, any such jet candidate lying within a distance $\Delta R \leq 0.2$ of an electron is discarded. Then, any electron (or muon equally) candidate remaining within a distance $\Delta R \leq 0.4$ of any surviving jet candidate is discarded. Finally, the electron, muon and jet candidates surviving this procedure are considered as "reconstructed", and the term "candidate" is dropped.

Following the object reconstruction described above, events are discarded if they contain any electrons or muons with $p_{\mathrm{T}} > 20$ GeV, or $p_{\mathrm{T}} > 10$ GeV respectively, to fulfill the requirements of a SUSY search without leptons.

4.5 Missing transverse momentum $E_{\mathrm{T}}^{\mathrm{miss}}$

The missing transverse momentum two-dimensional vector $\vec{P}_{\mathrm{T}}^{\mathrm{miss}}$ (and its magnitude $E_{\mathrm{T}}^{\mathrm{miss}}$) is based on complex calculations involving the transverse momenta of the electron and muon candidates, all jets which at the same time are not electron candidates as well, and all calorimeter clusters with $|\eta| < 4.5$, not associated to any of the other objects. It is re-calculated on AOD level with an object-based $E_{\mathrm{T}}^{\mathrm{miss}}$ algorithm (`MET_Simplified20_RefFinal`). Instead of cells, which typically serve as input for the calculations, topoclusters and egamma clusters are used because the former are not available any longer at this late stage of analysis. The individual clusters are associated with the high-p_{T} objects in order to identify the dedicated calibration to be applied, starting with electrons, then jets and muons in the end. The remaining clusters, not belonging to any of the previous high-p_{T} objects, are combined in the *CellOut*-term, and finally $E_{\mathrm{T}}^{\mathrm{miss}}$ is given by the formula:

$$(E_{\mathrm{T}}^{\mathrm{miss}})_{\mathrm{x(y)}}^{\mathrm{RefFinal}} = (E_{\mathrm{T}}^{\mathrm{miss}})_{\mathrm{x(y)}}^{\mathrm{RefEle}} + (E_{\mathrm{T}}^{\mathrm{miss}})_{\mathrm{x(y)}}^{\mathrm{RefJet}} + (E_{\mathrm{T}}^{\mathrm{miss}})_{\mathrm{x(y)}}^{\mathrm{RefMuo}} + (E_{\mathrm{T}}^{\mathrm{miss}})_{\mathrm{x(y)}}^{\mathrm{CellOut}} \qquad (4.2)$$

where each term is computed from the negative sum of calibrated cluster energies inside the corresponding objects.
All electrons with $p_{\mathrm{T}} > 20$ GeV passing medium purity criteria (before overlap removal) contribute to $(E_{\mathrm{T}}^{\mathrm{miss}})_{\mathrm{x(y)}}^{\mathrm{RefEle}}$, while jets above 20 GeV at the jet energy scale contribute to $(E_{\mathrm{T}}^{\mathrm{miss}})_{\mathrm{x(y)}}^{\mathrm{RefJet}}$. All candidate muons before overlap removal, passing a cut on $p_{\mathrm{T}} > 10$ GeV, end up in $(E_{\mathrm{T}}^{\mathrm{miss}})_{\mathrm{x(y)}}^{\mathrm{RefMuo}}$ independently of their isolation. The last term, $(E_{\mathrm{T}}^{\mathrm{miss}})_{\mathrm{x(y)}}^{\mathrm{CellOut}}$, contains the remaining topoclusters at the electromagnetic scale within $|\eta| < 4.5$, which were not included in any other reconstructed objects, i.e. especially jets with $p_{\mathrm{T}} < 20$ GeV.

Chapter 5

Data and Monte Carlo Samples

This chapter gives a brief overview about the different data and Monte Carlo samples used within the different analyses, recapitulating [9, 10]. More details about Monte Carlo simulations can be found in Chapter 2.

5.1 DATA

ATLAS collected the raw data samples used for the first part of the analysis (see Section 6.3) over the period 22$^{\text{nd}}$ March 2011 to 28$^{\text{th}}$ June 2011 (so-called data-taking periods B2 – H4, run numbers 178044 to 184169 respectively). Due to the reduced $\sqrt{s}$ during period C, this period is excluded.
The mean peak number of interactions per bunch crossing increased during this time from 2.6 in the beginning to 7.97 in the end while the peak instantaneous luminosity increased from 1.3×10^{30} to 1.26×10^{33} cm^{-2}s^{-1} in the same time. Figure 5.1 gives an overview about the chronological development of the ATLAS data-taking, its overall efficiency is during all different periods well above 90%. This leads to an integrated luminosity of 1.232 fb^{-1}of recorded raw data, which is reduced to 1.035 fb^{-1} after application of a *GoodRunList (GRL)*, a selection of data after basic *data quality* requirements and suitable for physics analyses (see Section 5.1.2). The systematic uncertainty on the luminosity is estimated to 4.5% [146].

Both, for the main analysis and the QCD background estimation, data from the *JetTauEtmiss* stream is used, whereas other control region estimates require data from the *Egamma* or *Muon* stream respectively. According to the ATLAS computing model (see Figure 2.5), the AODs from official productions are converted into SUSYD3PDs using

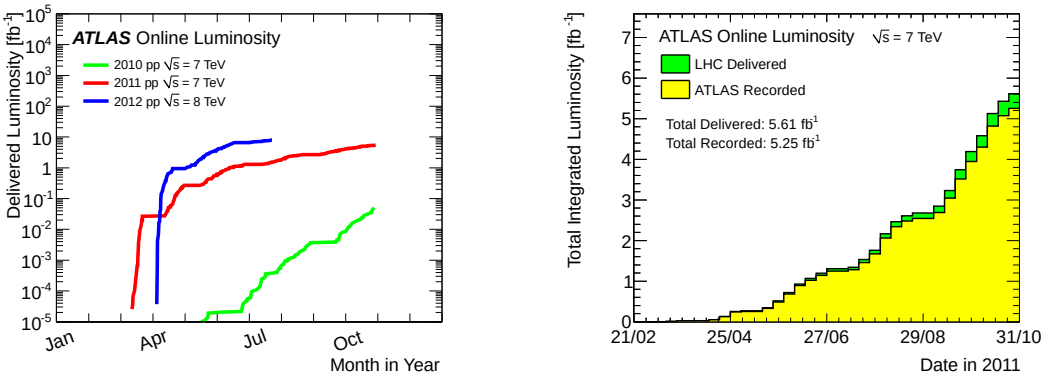

(a) Delivered luminosity versus time

(b) Recorded luminosity versus time

Figure 5.1: ATLAS data-taking versus time, taken from Reference [147]. The different colours in Figure 5.1a correspond to the different years of data-taking. Figure 5.1b compares the LHC-delivered and the ATLAS-recorded luminosity versus the weeks in 2011. The overall data-taking efficiency is well about 90%.

the SUSYD3PDMaker package [148] from the ATLAS production system corresponding to *tag p601/2*.

5.1.1 Trigger

The baseline triggers for this analysis are combined jet + $E_{\mathrm{T}}^{\mathrm{miss}}$ triggers [149, 150], unprescaled as important to any BSM analyses. The triggers per data period are listed in Table 5.1

2011 Period	A – B	D – H
Trigger Chain	EF_j75_a4_EFFS_xe45_loose_noMu	EF_j75_a4tc_EFFS_xe45_loose_noMu
L1 Seed	L1_J50_XE20	
L2 Chain	L2_j70_xe20_noMu	

Table 5.1: 2011 Signal Region trigger chains per period: The $E_{\mathrm{T}}^{\mathrm{miss}}$ calculation at Event Filter level does not contain the muon correction.

where *EFFS* denotes the *calorimeter fullscan* jet finding, which provides jet reconstruction in the complete detector rather than the L2 Regions-of-Interest (RoIs). While *a4* denotes the earlier trigger, using an anti-k_t algorithm based on trigger towers as input, the *a4tc*-trigger processes calorimeter cells into topoclusters which is more robust against pile-up and therefore used in the later data periods.

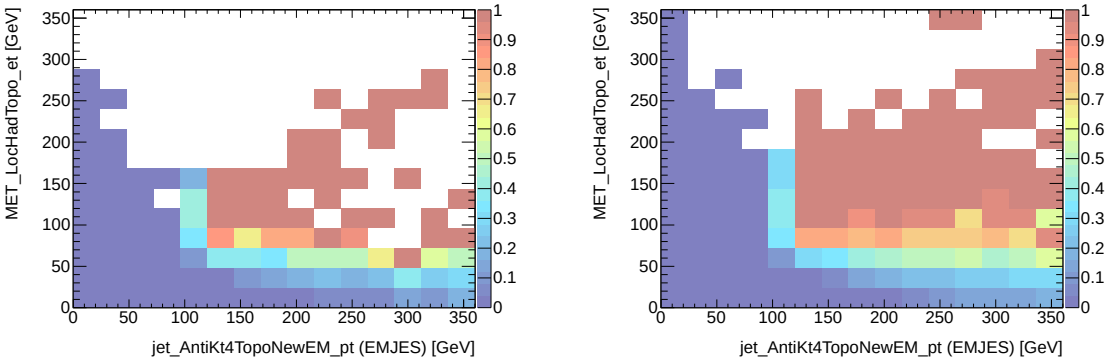

(a) EF_j75_a4_EFFS_xe45_loose_noMu trigger efficiency, period B

(b) EF_j75_a4tc_EFFS_xe45_loose_noMu trigger efficiency, period D

Figure 5.2: Efficiency of combined jet + $E_{\mathrm{T}}^{\mathrm{miss}}$ triggers (see Reference [10]).

2011 Data Period	run numbers		lumi-weighted prescale
	from	to	
B	178044	178109	1.0
D	179710	180481	158.1
E	180614	180776	430.1
F	182013	182519	494.3
G	182726	183462	590.2
H	183544	184169	570.6
total	178044	184169	402.9

Table 5.2: Lumi-weighted prescale factors per data taking period for QCD triggers (EF_j75_a4_EFFS in period B and EF_j75_a4tc_EFFS else).

Additionally, the QCD background estimate uses the prescaled single jet triggers, EF_j75_a4_EFFS and EF_j75_a4tc_EFFS respectively, in order to explore regions with lower $E_{\mathrm{T}}^{\mathrm{miss}}$ (see Table 5.2, average lumi-weighted prescale for this triggers is about 400).

The efficiency of a trigger is measured using a sample, triggered by another trigger with looser requirements. Results for the combined jet + $E_{\mathrm{T}}^{\mathrm{miss}}$ triggers are shown in Figure 5.2. Statistics in period B, however, are rather limited.
The turn-on curves are drawn as function of the offline variables p_{T} and $E_{\mathrm{T}}^{\mathrm{miss}}$: while the jet-p_{T} is computed at the EMJES scale of anti-k_t jets with a radius of 0.4, $E_{\mathrm{T}}^{\mathrm{miss}}$ is taken from the cells in topological clusters with applying a local hadronic calibration (LocHadTopo). Projections of the efficiencies in the plateau region are shown in Figure 5.3: the triggers reach their plateau with an efficiency close to 100% for jet-$p_{\mathrm{T}} > 130$ GeV and

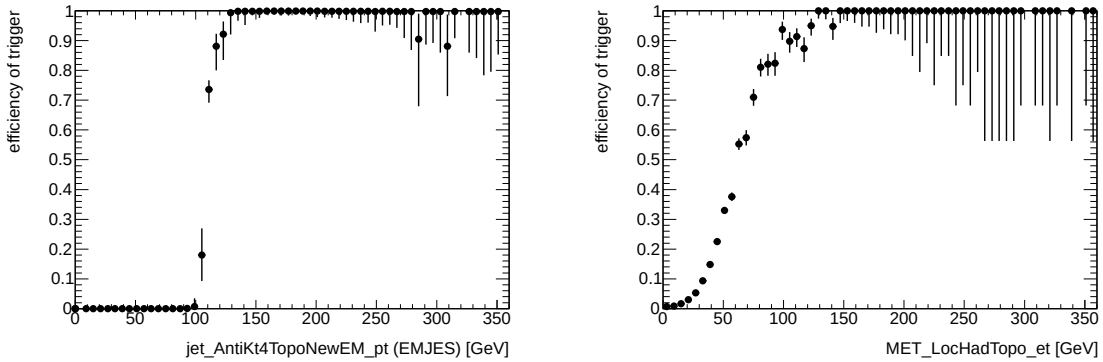

(a) Projections onto the jet p_{T} axis after a cut on offline $E_{\mathrm{T}}^{\mathrm{miss}}$ at 130 GeV.

(b) Projections onto the $E_{\mathrm{T}}^{\mathrm{miss}}$ axis after a cut on offline jet p_{T} at 130 GeV

Figure 5.3: Projections of the EF_j75_a4tc_EFFS_xe45_loose_noMu trigger efficiencies using data from period D (see Reference [10]).

MET_LocHadTopo> 130 GeV. Although this analysis does not use MET_LocHadTopo, but a simplified version of MET_RefFinal (see Section 4.5), similar conclusions hold nevertheless and the offline selection criteria are chosen accordingly in order to protect against a possible bias from the trigger turn-ons.

5.1.2 Data quality and event cleaning

An overview of the data quality criteria and event cleaning is given in Table 5.3. The motivation for the choice of individual cuts will be discussed further in the subsequent paragraphs.

Good Run Lists

The definition of a *good* dataset is one key ingredient for every physics analysis. ATLAS collects the Data Quality (DQ) information from the DQ group in dedicated lists of all valid runs and luminosity blocks of good data-taking conditions and possible other criteria, the *Good Run Lists (GRL)* [151]. Hereby, a luminosity block is defined as a short time interval, usually $(60 - 120)$ s, in which the conditions can be considered stable.
The building bricks of each GRL are the DQ status flags, which are traffic light-like indicators of the data quality, defined by ever subdetector and the combined performance groups, given for each luminosity block individually: The lowest level of flags is set by the *detector control system (DCS)* automatically, considering temperature conditions,

Cut	Description	Details
1	Data Quality (data only)	Run / lumi block appears in SUSY GRL `data11_7TeV.periodAllYear_DetStatus-v18-prod08-04_CoolRunQuery-00-03-98_Susy.xml`
2	Trigger	EF_j75_a4_EFFS_xe45_loose_noMu (data period B) / EF_j75_a4tc_EFFS_xe45_loose_noMu (data period $\geq$ D) / None (MC)
3a	Ev. cleaning - jets (data only)	No 'loose' bad jets after jet-lepton overlap removal with $p_{\mathrm{T}} > 20$ GeV and any η
3b	Ev. cleaning – jets (data and MC)	None of leading N selected jets with $p_{\mathrm{T}} > 100$ GeV after overlap removal in N jet analysis possess charged frac. chf < 0.05 and $\lvert\eta\rvert < 2.0$
3c	Ev. cleaning – jet timing	Energy-weighted mean time of leading N selected jets after overlap removal in N jet analysis $\lvert\langle t\rangle\rvert < 5$ ns.
3d	Ev. cleaning – LAr hole veto	None of leading up to 4 selected jets after overlap removal with $p_{\mathrm{T}} > A \times 40$ GeV possess $-0.1 < \eta < 1.5$ and $-0.9 < \phi < -0.5$, where $A = (1 - BCH\_CORR\_JET)/(1 - BCH\_CORR\_CELL)$ (data periods $\geq$E) or A=1 (MC, periods <E).
4	Ev. cleaning - LAr (data only)	LArError == 0
5	Ev. cleaning - Primary vertex	Leading primary vertex with > 4 tracks

Table 5.3: Event cleaning applied, see text for detailed discussions about individual cuts and motivation [9, 10].

humidity and whether the systems operated at nominal values e.g. modules at nominal voltages or the magnets at nominal fields. Another level of flags, the *online* flags, is given online during data-taking and/or by the detector shifters. Afterwards, the sub-detector experts review the DQ flags and provide the *offline* flags, which takes precedence over the online ones. In the end, the Combined Performance (CP) groups use both automatic tools and consistency checks - and dedicated DQ shifters.
While the status *yellow* is used only as temporary solution for online flags, indicating that at that moment of time, the decision could not be taken, *red* flags indicate data that have been declared bad. Thus, usually only *green* ones allow the recorded data to be used for physics analyses. A summary of these flags, the *LBSUMM*, is stored in the databases and used for the creation of GRLs.

But also GRLs for individual physics objects, trigger slices or complete analyses, based only on the relevant physics objects and sub-detectors, can be defined. The SUSY working group defined their official GRL for summer 2011 data analysis (see Section 6.3 for analysis details) called *data11_7TeV.periodAllYear_DetStatus-v18-prod08-04_CoolRunQuery-00-03-98_Susy.xml*.

Non-collision background

Non-collision backgrounds typically have a monojet-like signature of only one high-p_{T} jet and thus a large amount of apparent missing transverse energy when overlaid on a casual proton-proton interaction. Non-collision backgrounds originate from various different sources, whereas the most dominant ones are coherent noise in the Liquid Argon (LAr) electromagnetic calorimeters, spike noise in the hadronic LAr endcap-calorimeter, muons from cosmic-rays or beam halo, producing high-p_{T} photons during bremsstrahlung, and beam gas events, where a proton collides with a remnant gas molecule, left in the beam pipe.

Jet cleaning

The quality factor of the signal pulse shape as well as the timing and other calorimeter shower shape information can help to distinguish *fake* jets, created e.g. by calorimeter noise, from real jets, created at the primary vertex of the hard interactions. To allow a proper matching of these jets to the primary interaction point, the leading primary

Cut	Value
I	($f_{\text{hec}} > 0.5$ and $\lvert f_{\text{quality}}\rvert > 0.5$) or ($\lvert E_{\text{negative}}\rvert > 60$ GeV)
II	($f_{\text{em}} > 0.95$ and $\lvert f_{\text{quality}}\rvert > 0.8$ and $\lvert\eta\rvert < 2.8$)
III	($\lvert t\rvert > 25$ ns)
IV	($f_{\text{em}} < 0.05$ and $f_{\text{ch}} < 0.05$ and $\lvert\eta\rvert < 2.0$)
V	($f_{\text{em}} < 0.05$ and $\lvert\eta\rvert \geq 2.0$)
VI	($f_{\text{max}} > 0.99$ and $\lvert\eta\rvert < 2.0$,)

Table 5.4: Jet-cleaning cuts of the *summer 2011* analysis . For the description of the variables, see text [9, 10].

vertex, being the one with the highest scalar sum of associated tracks, is required to have at least five tracks associated with it (cut 5).

It is the *JetTauEtmiss-group* which defines the official cleaning recommendations. This analysis is following the *loose* cleaning (see cut 3*a*, Table 5.3) and according events are rejected, where any jet with $p_{\text{T}} > 20$ GeV (at EMJES scale) in any pseudo-rapidity (unless otherwise specified) is classified as *fake jet* according to the criteria in Table 5.4. The variables are defined as

- f_{em}: Fractional energy measured in EM calorimeter
- f_{hec}: Fractional Energy measured in HEC calorimeter
- f_{quality}: Fractional energy in cells flagged with a 'bad' quality.
- $\lvert E_{\text{negative}}\rvert$: Total negative energy of the cells contained in a jet
- f_{max}: Maximum fractional energy measured in one calorimeter layer
- f_{ch}: Charge fraction is the ratio of the sum of the transverse momenta of tracks associated to a jet and originating at the primary vertex, to the jet calorimetric transverse momentum. It is defined to be $\Sigma\lvert p_{\text{T}}^{\text{trk}}\rvert / p_{\text{T}}^{\text{jet}}$ where $p_{\text{T}}^{\text{jet}}$ is measured at the fully calibrated (EMJES) scale
- t: Jet time (energy-squared-weighted time of cells within a jet) with respect to the event time

While the first two cuts eliminate calorimeter noise, the series *III* - *VI* is targeted at fake jets from beam-halo and cosmic-rays.

Additionally, further cleaning is applied: leading jets (with $p_{\mathrm{T}} > 100$ GeV and $|\eta| < 2$) which have a low fraction (< 0.05) of their p_{T} carried by charged tracks, are vetoed (cut $3b$), which effectively suppresses any track-less background from cosmics, calorimeter noise or beam-halo. Moreover, the leading jets all are required to have consistent timing information from the calorimeters (cut $3c$).
Although the LAr hole was shown to have only little effect on the signal regions ($\leq 15\%$ signal loss, see Table 6.1 for SR definitions), especially the QCD control regions suffer from a potential bias as mismeasured jets cause (apparent) missing energy collaterally aligned with the jet direction, and thus all events would end up in the QCD control region. Therefore, cut $3d$ contains a veto on events, where one of the leading four jets is directly affected by the LAr hole, equaling SR and CR behaviour.

Cut 4 follows a recommendation from the LAr Data Quality group discarding events where the LArError-flag indicates bad events (WARNING indicating a significant amount of noise in the LAr electromagnetic calorimeter and ERROR denoting serious data integrity problems, coming from incomplete read-outs or hardware failures).

The estimated number of non-collision background events in the five signal regions have been studied with different methods and consistently shown to be ≤ 0.7 events or below.

5.2 Monte Carlo samples

Simulated Monte Carlo events are an important building block of many modern particle physics analysis: Not only was the basic analysis developed on MC, but also are most of the transfer functions, which help to extrapolate from the control region observations to signal region background estimations, derived from MC - for details about transfer functions, see Section 2.7.4.

The MC samples make use of the ATLAS MC10b parameter tune [152, 153] and the GEANT4 [73] based detector simulation.

5.2.1 Pile-up reweighting

The Monte Carlo samples are produced with the official ATLAS offline software framework, called Athena [154], in release 16, at a centre of mass energy of $\sqrt{s} = 7$ TeV. On

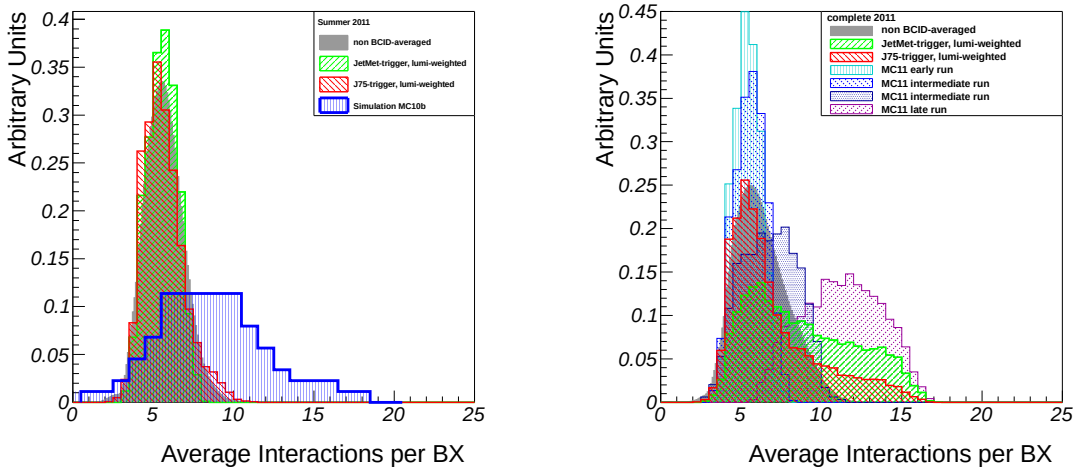

(a) *summer 2011* analysis **(b)** *complete 2011* analysis

Figure 5.4: *Average lumi-weighted number of interactions per bunch-crossing* for the different triggers compared to the μ*-values* simulated in MC and the *interactions per bunch crossing* needed for the non BCID[1]-averaged pile-up reweighting. Due to the clear differences between the data and MC for the *summer 2011* analysis (left), somewhat extreme values are needed when reweighting with the default procedure while the non-BCID averaged pile-up reweighting seems to fit better. The simulation for the *complete 2011* analysis (see Chapter 8) fits the data much better (right).

average $\langle\mu\rangle = 8$ interactions per bunch crossing are simulated, which is to be adjusted later to the specific pile-up conditions measured from data via *pile-up reweighting*. Since high μ values practically do not exist in the data, many MC events obtain a weight of 0 through the pile-up reweighting procedure, resulting in an inefficiency of $\sim$ 50% on MC events (see e.g. [155] and Figure 5.4a), while events with hard kinematics are rarely affected. This analysis uses two different techniques of pile-up reweighting: the central value is given by the BCID-averaged reweighting and the difference compared to the non-BCID averaged reweighting is assigned as systematic uncertainty.

5.2.2 Background samples

`PYTHIA` [75], in combination with the `MRST2007LO*` modified leading-order PDFs [156], is used to simulate QCD jet events, while `MC@NLO` [88, 157] and the Next-to-Leading Order (NLO) PDF set `CTEQ6.6` [158] are used for the simulation of top quark pair production (with a top quark mass of 172.5 GeV). This NLO PDF set (`CTEQ6.6`) is used within all NLO MC, whereas PDF set `CTEQ6L1` and `ALPGEN` [79] are used to produce samples of

W and Z/γ^* with accompanying jets. Single top production finally is simulated with MC@NLO [89, 90].
Fragmentation and hadronisation for the ALPGEN and MC@NLO samples is performed with HERWIG [77, 93], using JIMMY [94] for the underlying event.

An overview of the used Standard Model MC background samples can be found in Tables A.2, A.3 and A.4.

5.2.3 Signal samples

The SUSY benchmark models are generated with HERWIG++ [91], normalised using NLO cross-sections determined by PROSPINO [96], shown in Table A.1.

Chapter 6

Event selection and background estimation techniques

As the author has significantly contributed to the QCD background estimation, the other parts of the SUSY analysis such as the event cleaning or event selection have been introduced in previous chapters only as far as necessary to understand the QCD estimate. The "overall" picture - how the QCD background estimate fits together with the rest of the analysis - will be presented in Chapter 9 as well as the current exclusion limits of the 0-lepton SUSY analyses as of summer 2012.

While heavy SUSY particles, in a large number of R-parity conserving models generated in pairs, decay, they are expected to produce certain typical event topologies involving at least 2-4 high-p_{T} jets (from $\tilde{q}\tilde{q}$, $\tilde{q}\tilde{g}$ or $\tilde{g}\tilde{g}$ respectively[1]) and $E_{\mathrm{T}}^{\mathrm{miss}}$ from the escaping LSPs, weakly interacting neutralinos $\tilde{\chi}_1^0$ (see Section 2.7.2). These basic assumptions form the foundation of the following SUSY analyses, requiring leading jet p_{T} and $E_{\mathrm{T}}^{\mathrm{miss}}$ just beyond the trigger thresholds and additional mostly medium-p_{T} jets, thus defining several analysis channels of different jet multiplicities. Completed is this ansatz by the definition of a high-mass channel with tightened requirements, targeting at a maximum discovery reach in the SUSY mass spectrum (see Section 6.3.1).

Certain discriminating variables (see Section 6.1), such as the *effective mass*, M_{eff}, have been probed to be effective in the identification of these SUSY events. Cuts both on M_{eff} and especially $E_{\mathrm{T}}^{\mathrm{miss}}$, which suppress the QCD background significantly, have been successfully used as foundation in previous SUSY searches [57] and are still useful. Their inversion helps to define control regions, especially enriched e.g. in QCD processes.

[1] A decaying squark produces typically only one jet as in $\tilde{q} \to q\tilde{\chi}_1^0$ while the decay of a gluino usually produces at least two jets, as e.g. in $\tilde{g} \to q\bar{q}\tilde{\chi}_1^0$, see Section 2.7.2.

6.1 Variables

In order to perform searches for new physics, one needs to select regions in phase-space where a possible signal such as SUSY is not overwhelmed by the Standard Model backgrounds. Hence, the use of appropriate kinematic variables is essential. These are briefly introduced in this Section: i.e. the *effective mass* and the *ratio of missing transverse energy and the effective mass*.

6.1.1 The effective mass

In many SUSY models, so was found, the correlation between the effective mass and the sum of the initially created SUSY particles' masses in the event is very good.
Thus, combining the missing transverse energy, $E_{\mathrm{T}}^{\mathrm{miss}}$ (see Equation (4.2), Section 4.5), with the scalar sum of the transverse jet momenta in the event, one has a powerful variable sensitive to various different SUSY models. With n being the number of jets used in a specific channel (exclusively), the effective mass, M_{eff}, is given by

$$M_{\mathrm{eff}} \equiv \sum_{i=1}^{n} |\mathbf{p}_{\mathrm{T}}^{(i)}| + E_{\mathrm{T}}^{\mathrm{miss}} \,, \tag{6.1}$$

with $\mathbf{p}_{\mathrm{T}}^{(i)}$ being the transverse momentum of the i^{th} jet, ordered descending in $|\mathbf{p}_{\mathrm{T}}|$. There is also an *inclusive* version of M_{eff}, where the sum in Equation (6.1) runs over all selected jets above a certain threshold, e.g. with $p_{\mathrm{T}} > 40$ GeV.

Figure 6.1 displays some exemplary effective mass distributions for the four different analysis channels after the $E_{\mathrm{T}}^{\mathrm{miss}}$ -cut (see Section 6.3 for more details about the selection and channel definitions). All MC samples are normalized according to their cross-section, and the QCD MC has an additional k-factor of 1.06 applied, based on the $E_{\mathrm{T}}^{\mathrm{miss}}$ -distribution from a two-jet selection applying a reversed $\Delta\varphi$ cut. With the `PYTHIA` MC being only a LO Monte Carlo, the normalization of the QCD samples is a priori not expected to match the data.
Before any additional cuts, the higher regions are populated mainly by multijet events.

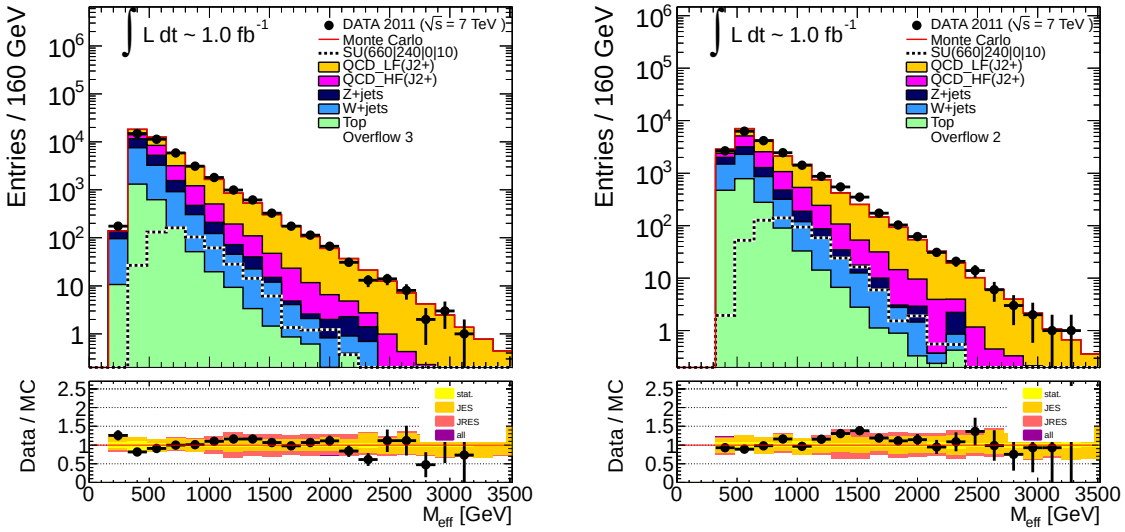

(a) two-jet channel

(b) three-jet channel

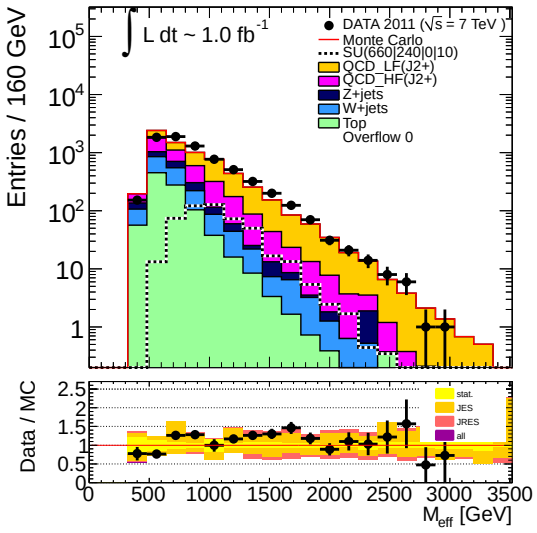

(c) four-jet channel

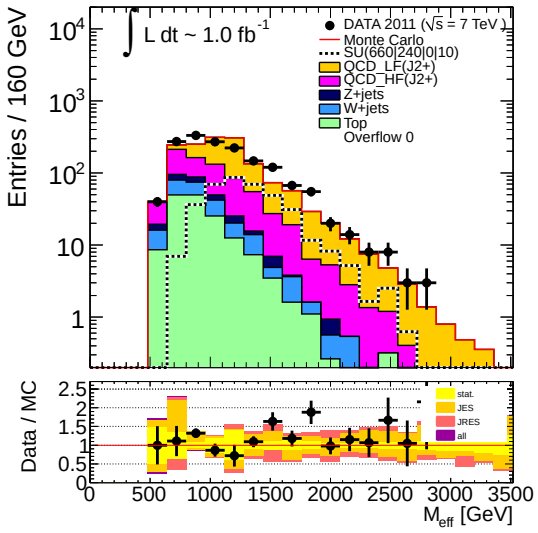

(d) high-mass channel

Figure 6.1: Distributions of the effective mass in different channels applying a cut on $E_{\mathrm{T}}^{\mathrm{miss}}$. The diagrams show the contributions of the different processes such as $W + jets$, $Z + jets$, top, QCD (being split into light- and heavy flavour, normalized on a separate control region for plotting) as well as one benchmark SUSY point right beyond the hitherto existing exclusion limits. Below the main diagrams, the data/MC ratio is plotted with statistical and systematic uncertainties (see Section 6.4).

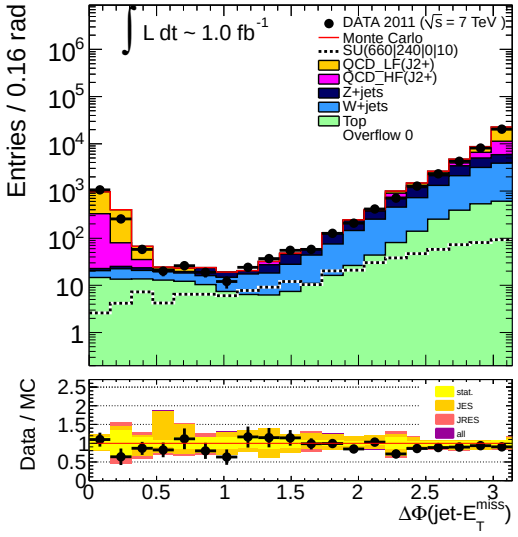

(a) leading jet

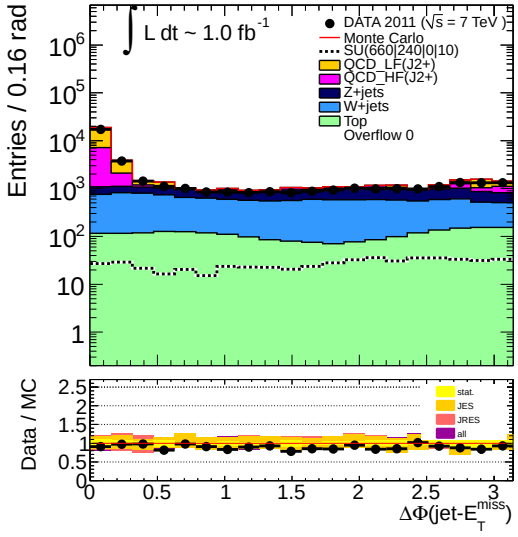

(b) sub-leading jet

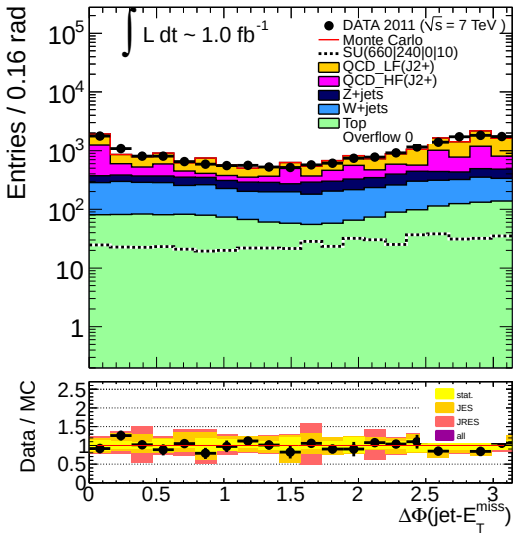

(c) 3^{rd}-leading jet

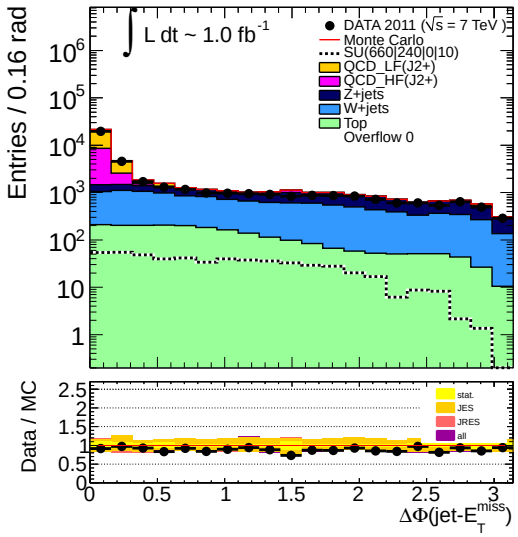

(d) minimum of leading three jets

Figure 6.2: Distributions of the angular separation between $\vec{P}_{\mathrm{T}}^{\mathrm{miss}}$ and each of the leading three jets and the minimal distances $\Delta\varphi^{min}\left(jet, \vec{P}_{\mathrm{T}}^{\mathrm{miss}}\right)$ (example: two-jet channel after a cut on $E_{\mathrm{T}}^{\mathrm{miss}}$): The shape of QCD events is different from the other Standard Model processes and also a possible SUSY signal - it shows a clear peak at low values.

6.1.2 The angular separation between jets and $\vec{P}_{\mathrm{T}}^{\mathrm{miss}}$

Typical QCD events may possess enough jets with high transverse momentum (even if the spectrum of those is steeply falling) but a QCD-event itself usually has low $E_{\mathrm{T}}^{\mathrm{miss}}$. In order for them to pass typical SUSY signal region selection cuts (e.g. $E_{\mathrm{T}}^{\mathrm{miss}} \geq 130$ GeV), an additional "source" of $E_{\mathrm{T}}^{\mathrm{miss}}$ is needed, either coming from a significant mismeasurement of at least one of the jets or from neutrinos inside the heavy-flavour decay of a *b*- or *c*-jet. In both scenarios, the missing transverse momentum points alongside the jet direction.
Therefore, a good measure to identify the background events especially from QCD multijet processes is the angular separation in the transverse plane between the jets and the missing transverse momentum vector $\vec{P}_{\mathrm{T}}^{\mathrm{miss}}$. Figure 6.2 gives an overview about the angular separation between $\vec{P}_{\mathrm{T}}^{\mathrm{miss}}$ and each of the leading three jets in an exemplary two-jet channel selection.

Previous studies [47] have shown that the minimum of the distances of the leading three jets to $\vec{P}_{\mathrm{T}}^{\mathrm{miss}}$ (the $E_{\mathrm{T}}^{\mathrm{miss}}$ 2-vector),

$$\Delta\varphi^{min} \equiv \min\left(\Delta\varphi\left(jet_1, \vec{P}_{\mathrm{T}}^{\mathrm{miss}}\right), \Delta\varphi\left(jet_2, \vec{P}_{\mathrm{T}}^{\mathrm{miss}}\right), \Delta\varphi\left(jet_3, \vec{P}_{\mathrm{T}}^{\mathrm{miss}}\right)\right), \tag{6.2}$$

where the jets are ordered in decreasing p_{T} , is a powerful tool to distinguish QCD from other processes, as both typical Standard Model processes such as *top* or *W/Z* and SUSY signals are expected to have a distribution with a (close to) flat shape (see Figure 6.3). While the QCD background drops only marginally when including the 4th jet in the calculation of $\Delta\varphi^{min}$, the SUSY signal efficiency would be drastically reduced.

With a cut value of $\Delta\varphi^{\ min} > 0.4$, a QCD-suppressed regions is defined (see Figure 6.4a), while applying a tightened $\Delta\varphi$ -cut (≤ 0.2), a region especially enriched in QCD multijet processes is created, which will serve as QCD control region later (see Figure 6.4b).

6.1.3 The ratio of effective mass and missing transverse energy

Similarly to the minimal angular separation between jets and $\vec{P}_{\mathrm{T}}^{\mathrm{miss}}$, $\Delta\varphi^{min}\left(jet, \vec{P}_{\mathrm{T}}^{\mathrm{miss}}\right)$, the ratio of the missing transverse energy and the effective mass has proven to be a good handle for the suppression of QCD multijet background. Figure 6.5 shows the distributions of the $E_{\mathrm{T}}^{\mathrm{miss}}/M_{\mathrm{eff}}$ ratio for the four different analysis channels (see Section 6.3

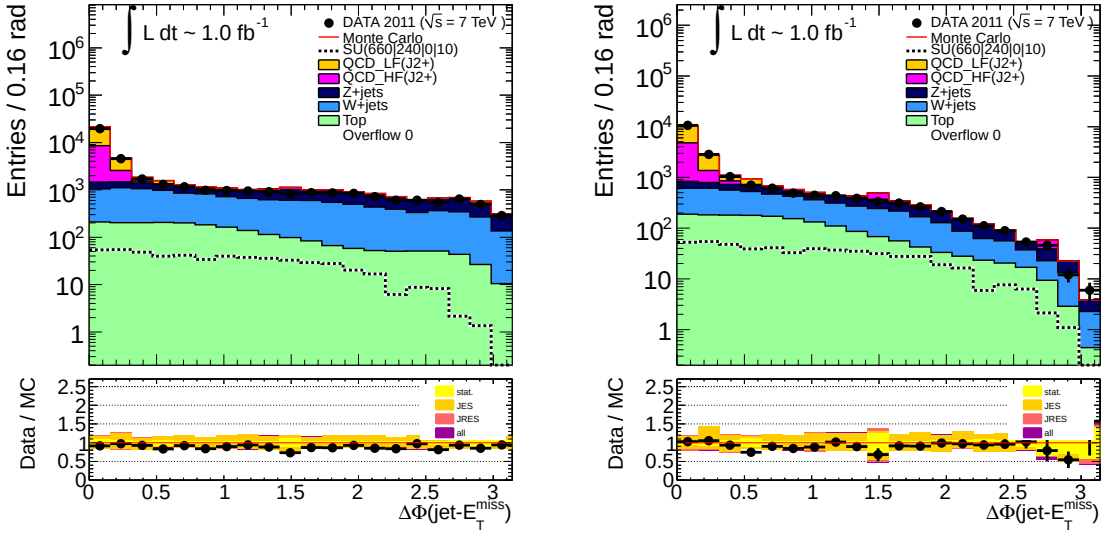

(a) two-jet channel

(b) three-jet channel

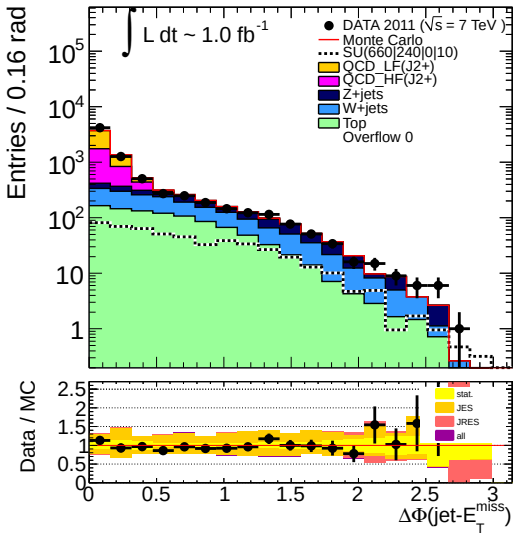

(c) four-jet channel

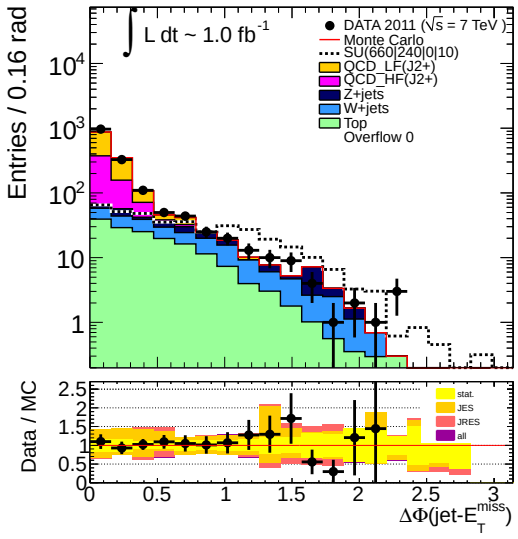

(d) high-mass channel

Figure 6.3: Distributions of the minimal distances $\Delta\varphi^{min}\left(jet, \vec{P}_{\mathrm{T}}^{\mathrm{miss}}\right)$ for all channels. The shape of QCD events is different from the other Standard Model processes and also a possible SUSY signal: it shows a clear peak at low values.

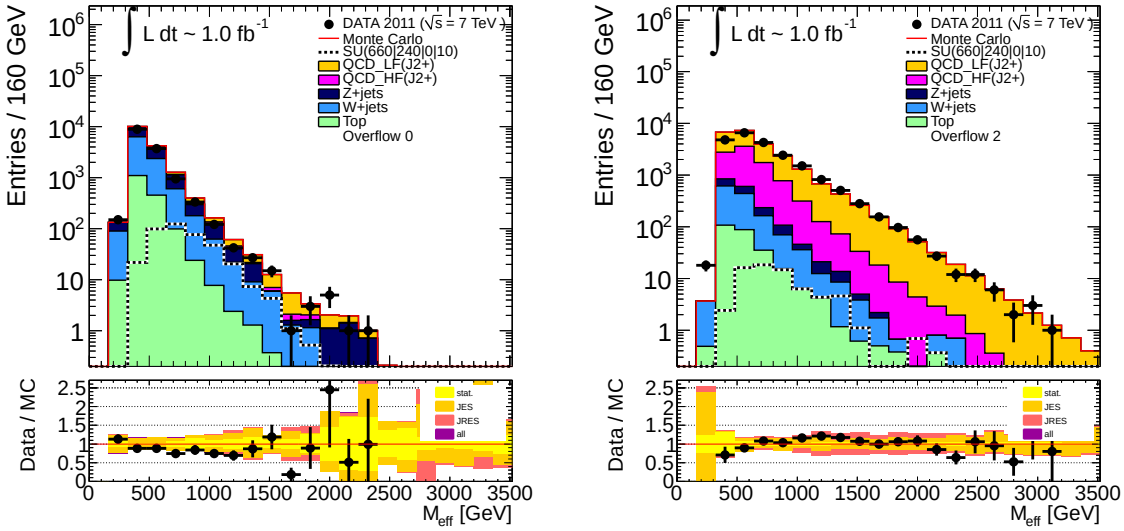

(a) regular $\Delta\varphi$ -cut **(b)** reversed $\Delta\varphi$ -cut

Figure 6.4: Distributions of the effective mass in a two-jet channel after applying a cut on $E_{\mathrm{T}}^{\mathrm{miss}}$: A $\Delta\varphi$ cut of 0.4 is chosen for the signal regions (see Figure 6.4a), which suppresses the multijet background drastically, while a reversed and tightened cut on $\Delta\varphi \leq 0.2$ creates a region particularly enriched in QCD (see Figure 6.4b).

for details) and Figure 6.6 illustrates the effect of the $E_{\mathrm{T}}^{\mathrm{miss}}/M_{\mathrm{eff}} > 0.3$ cut on the M_{eff} distribution of the two-jet channel. The reversing of the $E_{\mathrm{T}}^{\mathrm{miss}}/M_{\mathrm{eff}}$ cut creates another region enriched with QCD events: a good independent cross-check, being nearly orthogonal to the reversed $\Delta\varphi$ -region by selecting mainly light-flavour QCD at higher M_{eff}-regions instead of mixed light- and heavy flavour events at lower M_{eff}-values.

6.2 The first 2011 analysis with 135 pb^{-1}

Although the author also contributed to the first analyses of 2011 data with an integrated luminosity of 165 pb^{-1}, the focus in this thesis will be laid on a later analysis with an larger integrated luminosity of roughly 1 fb^{-1}.

The methodology for the estimation of the QCD background is identical, but the second analysis is far more advanced, and the systematic error calculation more mature.

The details about the earlier jets + $E_{\mathrm{T}}^{\mathrm{miss}}$ + 0-lepton analysis targeted at PLHC 2011 can be found in [7, 8].

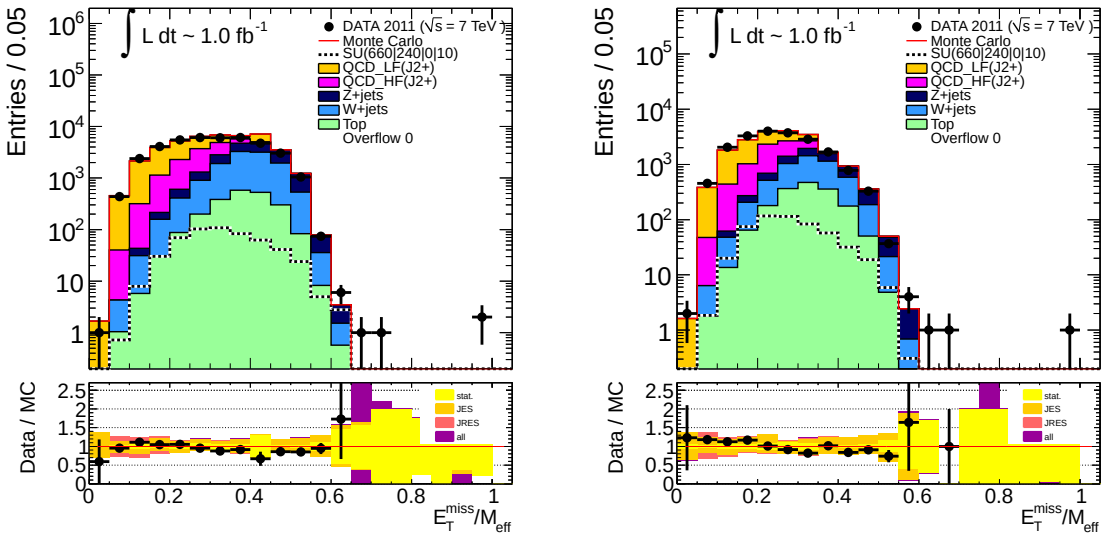

(a) two-jet channel

(b) three-jet channel

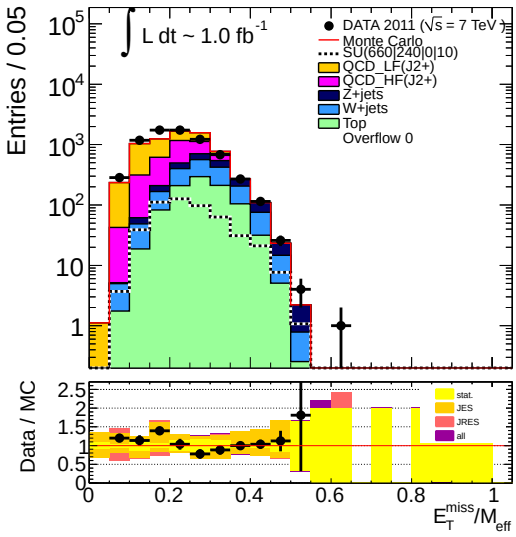

(c) four-jet channel

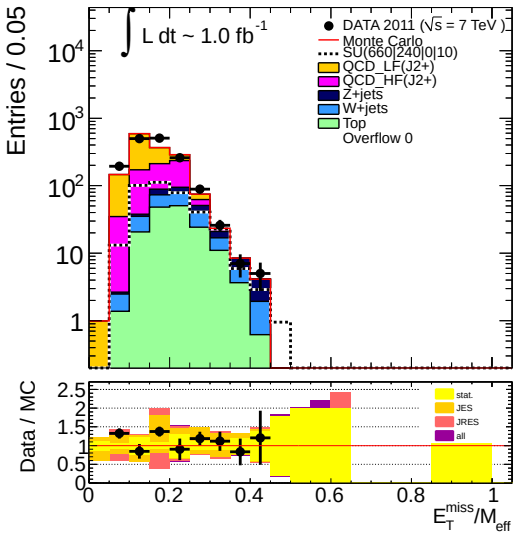

(d) high-mass channel

Figure 6.5: Distributions of the $E_{\mathrm{T}}^{\mathrm{miss}}$ $/M_{\mathrm{eff}}$-ratio of the four different channels applying a cut on $E_{\mathrm{T}}^{\mathrm{miss}}$.

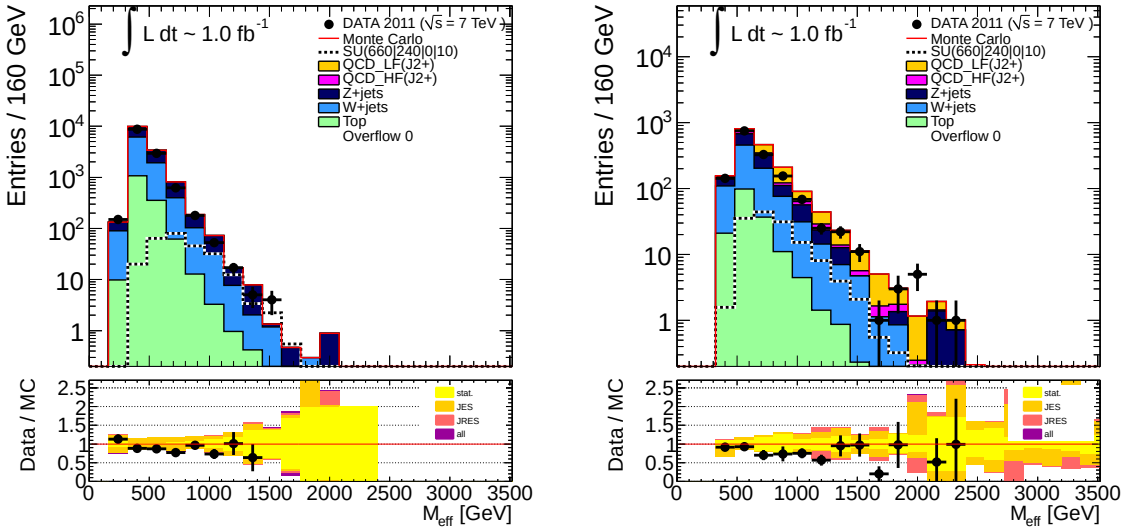

(a) regular $E_{\mathrm{T}}^{\mathrm{miss}}/M_{\mathrm{eff}}$ cut

(b) reversed $E_{\mathrm{T}}^{\mathrm{miss}}/M_{\mathrm{eff}}$ cut

Figure 6.6: Distributions of the effective mass in a two-jet channel after applying a $E_{\mathrm{T}}^{\mathrm{miss}}$ and $\Delta\varphi$ cut: A $E_{\mathrm{T}}^{\mathrm{miss}}/M_{\mathrm{eff}}$-cut of 0.3 is chosen for this signal regions (see Figure 6.6a), which suppresses the multijet background additionally, while a reversed cut on $E_{\mathrm{T}}^{\mathrm{miss}}/M_{\mathrm{eff}}$ creates another region particularly enriched in QCD (see Figure 6.6b).

The main differences, concerning the QCD background estimation, are:

- On 30$^{\mathrm{th}}$ April (period E onwards), half of a front end crate controller (6 FEBs) in the LAr electromagnetic calorimeter failed. This data was not included in the earlier note and requires a harsher event cleaning with a dedicated treatment of this new LAr hole.
- The estimation of the QCD background via the jet-smearing technique (see Section 6.5.1) gets significantly improved: i.a. the initial response is estimated from MC.

In addition, there are further improvements due to e.g. increased statistics in CRs, which allow to re-raise previously lowered cuts (concerning $W(\to \ell\nu)$ + jets (CR3) and $t\bar{t}$ (CR4)). Also the likelihood fitting technique is improved in the later analysis, taking e.g. into account the independent γ + jets (CR1a) and $Z(\to \ell\ell)$ + jets (CR1b) estimates of the $Z(\to \nu\nu)$ + jets background. Further *validation regions* are added for cross-checking the results of the likelihood fit for $W(\to \ell\nu)$ + jets and $t\bar{t}$ backgrounds.

6.3 The summer 2011 analysis search strategy with 1 fb^{-1}

This analysis with 1035 pb^{-1} was presented at EPS 2011 (see [9, 10]).
First, the definition of the signal and control regions are introduced, then different sources of systematic uncertainties are discussed. Afterwards, the QCD background estimation is presented.

6.3.1 Signal and control region definitions

Due to the variety of SUSY signatures, five signal regions (SR) with different jet multiplicities are defined within this analysis, aimed at achieving a maximal reach over the $(m_{\tilde{g}}, m_{\tilde{q}})$-plane. The two-jet selection is specialized on squark pair production, the three-jet selection is targeted at the associated squark-gluino and the four-jet channels at gluino pair production.
The first four channels differ from each other in the increasing jet multiplicity (see Table 6.1). The leading jet is required to have a transverse momentum of $p_{\mathrm{T}} > 130$ GeV, the other jets at least $p_{\mathrm{T}} > 40$ GeV (in order to reduce the impact of pile-up) and the missing transverse momentum must exceed 130 GeV.
The fifth *high mass* channel has more stringent requirements on the physics objects, so is the p_{T}-cut on the sub-leading jets increased to 80 GeV and the (inclusive) M_{eff}-cut (see below) is raised to 1100 GeV. This channel should maximize the reach especially for high-mass SUSY models by strongly suppressing the Standard Model backgrounds.

The lepton veto is targeted at $W(\rightarrow \ell\nu)$+jets and leptonic $t\bar{t}$ events where the missing transverse energy comes from the neutrinos, while cuts 7+8 in Table 6.1 ensure that the used triggers are inside their plateau region and the efficiency close to 100% (see Section 5.1.1).
The later cuts are optimized for background suppression, especially of the multijet background. While for events with true $E_{\mathrm{T}}^{\mathrm{miss}}$ from invisibly decaying particles, the distribution of $\Delta\varphi^{min}\left(jet, \vec{P}_{\mathrm{T}}^{\mathrm{miss}}\right)$ is expected to be flat, a mismeasured jet (from the multijet background) creates a peak close to 0, as the apparent $E_{\mathrm{T}}^{\mathrm{miss}}$ points along the direction of the mismeasured jet (see Section 6.1.2).
The subsequent cuts suppress the multijet background even further: Cut 13 requires the magnitude of $E_{\mathrm{T}}^{\mathrm{miss}}$ to exceed a specific fraction of the effective mass of the event (see

Cut	Description	Signal Region				
		A	B	C	D	E
	Label	$\geq$ 2-jet	$\geq$ 3-jet	$\geq$ 4-jet		High mass
6	Lepton veto	No selected e or μ after overlap removal with $p_{\mathrm{T}} > 20$.				
7	$E_{\mathrm{T}}^{\mathrm{miss}}$	> 130				
8	Leading jet p_{T}	> 130				
9	Second jet p_{T}	>40	> 40	> 40	> 40	> 80
10	Third jet p_{T}	–	> 40	> 40	> 40	> 80
11	Fourth jet p_{T}	–	–	> 40	> 40	> 80
12	$\Delta\varphi$ $(i = 1, 2(, 3))$	>0.4				
13	$E_{\mathrm{T}}^{\mathrm{miss}}$ $/M_{\mathrm{eff}}$	> 0.3	> 0.25	> 0.25	> 0.25	> 0.2
14	M_{eff}	> 1000	> 1000	> 500	> 1000	> 1100

Table 6.1: Definition of Signal Regions, M_{eff}, $E_{\mathrm{T}}^{\mathrm{miss}}$ and p_{T} in GeV. The exclusive M_{eff}, being constructed from the leading n jets where n corresponds to the number of jets in the appropriate signal region, is used in the $E_{\mathrm{T}}^{\mathrm{miss}}$ $/M_{\mathrm{eff}}$ cut, while an inclusive M_{eff}, constructed from all jets with a transverse momentum above 40 GeV, is used for the final selection in the high mass channel. The $\Delta\varphi$ cut is only applied on the first three leading jets.

Section 6.1.1). In combination with an explicit cut on M_{eff} (cut 14), this equates to a dynamic cut on $E_{\mathrm{T}}^{\mathrm{miss}}$:

$$\frac{E_{\mathrm{T}}^{\mathrm{miss}}}{M_{\mathrm{eff}}} > x \Leftrightarrow E_{\mathrm{T}}^{\mathrm{miss}} > x \cdot M_{\mathrm{eff}} \tag{6.3}$$

The $E_{\mathrm{T}}^{\mathrm{miss}}$ $/M_{\mathrm{eff}}$ fraction used in Cut 13 decreases with increasing jet multiplicity requirement because the typical $E_{\mathrm{T}}^{\mathrm{miss}}$ of SUSY signal events is inversely correlated with jet multiplicity on phase-space grounds[2].

Providing strong suppression of Standard Model backgrounds, Cut 14 finally selects events with hard kinematics. The effective mass, M_{eff}, is extremely useful to detect small differences between the SUSY mass states in the region $M_{\mathrm{eff}} > 500$ GeV and higher mass differences with a harsher cut on $M_{\mathrm{eff}} > 1000$ GeV. SRs A - D use an exclusive definition of the effective mass, according to the jet multiplicity n and thus

[2]Additional jets in a SUSY decay chain increase the probability that the LSP will be produced with low momentum through effective multi-body decays. Small mass splittings can also lead to low $E_{\mathrm{T}}^{\mathrm{miss}}$. The QCD cross-section is also suppressed at higher multiplicities, so the $E_{\mathrm{T}}^{\mathrm{miss}}$ requirement can be loosened.

CR	SR Background	CR process	CR selection
CR1a	$Z(\to\nu\nu)$+jets	γ+jets	Isolated photon
CR1b	$Z(\to\nu\nu)$+jets	$Z(\to\ell\ell)$+jets	$\lvert m(\ell,\ell) - m(Z)\rvert < 25$ GeV
CR2	QCD jets	QCD jets	Reversed $\Delta\varphi$ cut
CR3	$W(\to\ell\nu)$+jets	$W(\to\ell\nu)$+jets	30 GeV $< m_T(\ell, E_{\mathrm{T}}^{\mathrm{miss}}) <$ 100 GeV, b-veto
CR4	$t\bar{t}$ and single-t	$t\bar{t}\to bbqq'\ell\nu$	30 GeV $< m_T(\ell, E_{\mathrm{T}}^{\mathrm{miss}}) <$ 100 GeV, b-tag

Table 6.2: Definition of control regions: For each CR, the SR background, at which it is targeted, is shown together with the control region process used for background estimation and its dedicated selection criteria.

calculated from the leading n jets in the event, sorted by decreasing transverse momentum. SR E, however, uses an inclusive definition of the effective mass, constructed from all selected jets with a minimum transverse momentum ($p_{\mathrm{T}}>$ 40 GeV).

In addition to the above signal regions, each channel consists of five control regions (CR), defined by a similar event selection but enriched in one of the four main background processes in the associated SR (see Table 6.2). In order to minimise theoretical uncertainties arising from the extrapolation to harder scales, CRs are chosen to be kinematically as close as possible to the corresponding SRs.
The $Z(\to\nu\nu)$+jets background in the SR is estimated with two different ansatzes: from γ+jets (CR1a) and $Z(\to\ell\ell)$+jets (CR1b) events where the lepton (ℓ) is either an electron e or a muon μ. The kinematics of γ+jets events are expected to closely resemble those of $Z\to\nu\nu$ events in a region with $p_{\mathrm{T}}^{\mathrm{Z}} \geq m_{\mathrm{Z}}$. The method generates pseudo-events, where the photon is added to $E_{\mathrm{T}}^{\mathrm{miss}}$ in order to mimic the invisible two-neutrino decay, and applies the SR selection on these. CR1b works similarly to CR1a, however, the selection must be loosened due to a lack of statistics (the branching ratio of $Z\to\ell\ell$ is factor three smaller than $Z\to\nu\nu$). The loosening of the selection creates an additional uncertainty.

A harshened cut on the minimum angular separation in the transverse plane between the up to three leading jets and $E_{\mathrm{T}}^{\mathrm{miss}}$ is used to define the QCD CR (CR2). This will be further discussed in Section 6.5.

CR3 and CR4 require a lepton, missing transverse energy and a transverse mass of the lepton+$E_{\mathrm{T}}^{\mathrm{miss}}$ -system consistent with leptonic W boson decays (30 GeV $< m_T(\ell, E_{\mathrm{T}}^{\mathrm{miss}}) <$ 100 GeV) - this selecting $W(\to\ell\nu)$+jets and semi-leptonic $t\bar{t}$ back-

ground events with a b-jet veto (CR3) or a b-jet requirement (CR4).
Before applying the loosened SR cuts, any jet-dependent quantities such as the effective mass or the angular separation of jets and $E_{\mathrm{T}}^{\mathrm{miss}}$ are re-computed in this case, treating the preselected lepton as additional jet. As observations have confirmed that roughly $\sim$ 90 % of $W(\rightarrow \ell\nu)$+jets and semi-leptonic $t\bar{t}$ events do enter the signal regions because of misidentified jets from electrons or hadronically decaying tau-leptons, which are not treated separately within this analysis. The procedure in its simplicity does not take into account the mechanism, by which the lepton was lost. Nevertheless, a normalisation of these backgrounds can be obtained when applying the same assumptions on the MC-derived transfer factors (TFs, see Section 2.7.4) as well. Even without a dedicated CR, also the minor background of fully hadronic $t\bar{t}$ events is taken into account by using MC derived TFs. Furthermore, the fully-leptonic contribution is affected as well because of the semi-leptonic component in CR3, providing a proper normalization.
While other minor backgrounds involving heavy-flavour quarks such as single top and $Wb\bar{b}$ contribute to the CR4 TFs, the uncertainties resulting from the uncertain number of these events in the CRs and SRs, arising from cross-section uncertainties, are included in the systematic uncertainties of those TFs.

6.4 Systematic Uncertainties

Before any details about the according analyses are given, the main systematic uncertainties on the transfer factors (TFs, see Section 2.7.4), deriving background expectations in the SRs from the observations in the CRs, are to be introduced [10].
The occurring systematic uncertainties can be divided into different categories: *theory* uncertainties arising from SUSY, or in general any physics modelling or the limited precision of e.g. cross-section estimates and *experimental* uncertainties like the jet energy scale, jet energy resolution or in more general terms, the reconstruction performance in the presence of high pile-up.

In general, the treatment of systematic uncertainties can be summarized in the following way: The quantity under investigation is modified in the MC simulation according to its individual systematic uncertainties, then the TF is being determined and the difference between the TF, determined from the nominal simulation, and that TF, obtained from the modified simulation, is quoted as systematic uncertainty on the TF for this quantity.

The systematic uncertainties on the TFs are treated as uncorrelated and thus summed in quadrature:

$$\sigma_{tot}^{sys} = \sqrt{\sum_{i=1}^{n} (\sigma_i^{sys})^2}. \tag{6.4}$$

The ratio plots below the main diagrams are showing separately the influence of the statistical uncertainties, and the most dominant systematics, such as the jet energy scale and the jet energy resolution - the remaining systematics are combined.

6.4.1 Jet energy scale and resolution uncertainties

Jets originating from the fragmentation of quarks or gluons are the most common, but also the most complicated final state objects to be produced at a hadron collider, thus needing a dedicated and precise energy calibration, taking them from the EM-scale to the hadronic scale, as the ATLAS-calorimeter is non-compensating (see Section 4.1). There are various methods to derive a jet calibration: Either from MC simulations, using a combination of single hadron and dijet response measurements, using the balancing of a well-measured object such as a photon against a recoiling jet in $\gamma + jets$ events, comparing track and calorimeter jets or using momentum balance in multi-jet final state events.

Systematic uncertainties in the MC TF values arising from the Jet Energy Scale (JES) and the Jet Energy Resolution (JER) uncertainties are assessed using the standard ATLAS JES and JER tools provided by the Jet/ETmiss working group.

- The jet energy scale uncertainty has been measured from the complete 2010 data set using the procedure described in Reference [102]. It depends upon p_{T}, η and proximity to adjacent jets, and on average amounts to around 4%.
- The jet energy resolution measured with 2010 data [159] is applied to the MC jets (in the absence of updated figures for 2011), with the difference between the re-calibrated and nominal MC resolution taken as the systematic uncertainty.

Due to the high luminosity in the 2011 LHC run, pile-up - both in-time pile-up, i.e. multiple collisions within the same bunch crossing, and out-of-time pile-up, which arises from the detector response to neighbouring bunch crossings - affects the jet energy

	$0 < \|\eta\| < 2.1$	$2.1 < \|\eta\| < 4.5$
$20 < p_T < 50$ GeV	5%	7%
$50 < p_T < 100$ GeV	2%	3%
$p_T > 100$ GeV	0%	0%

Table 6.3: The additional uncertainty on the JES to be applied in quadrature to account for pile-up and beam conditions [10].

measurements, making an additional contribution to the JES and JER uncertainties[3], both in the central and the forward region.

Although forward jets are not explicitly used in the analyses, they enter the $E_{\mathrm{T}}^{\mathrm{miss}}$ calculations and hence the forward jet JES and JER uncertainties are important to consider: Table 6.3 shows the additional recommended uncertainties on the JES to cover the changing beam conditions and pile-up, while, in addition, the JER is observed to be increased such that an additional systematic uncertainty of $0.07 \cdot p_{\mathrm{T}}$ added in quadrature is applied to forward jets ($|\eta| > 2.8$).

For the in-time pile-up, the variation of the analyses cutflows as function of the primary vertices is studied showing little to no dependence as expected (as events in the SRs are dominated by very hard jets). The out-of-time pile-up is investigated by comparing data recorded with 75 or 50 ns bunch spacing and as function of the average number of collisions per bunch crossing.

6.4.2 Theory uncertainties

Although a dedicated choice of event selection reducing widely Standard Model backgrounds in the signal regions, the remaining events are all of a similar type, i.a. located at high M_{eff}-values, implying also a high jet-multiplicity, and thus prone to a possible mis-modelling of that certain feature inside the simulations.
Affecting the calculation of M_{eff}, the treatment of jet radiation is the dominant modelling uncertainty in the MC predictions. Different techniques have been developed to estimate this uncertainty, either using multileg LO generators such as `ALPGEN` or `SHERPA` or by matching NLO predictions to parton shower MC generators (e.g. `MC@NLO`). The number of outgoing partons in the ME calculations, however, is very limited and the

[3] JES and JER uncertainties were determined on the 2010 data with larger bunch-spacing.

uncertainties are estimated by comparing samples with a reduced number of outgoing partons to the reference samples ($W/Z+jets$ production with 0-4 instead of 0-5 partons) or by comparing different generators (ALPGEN versus MC@NLO for $t\bar{t}$-production).

Only a summary of the conclusions is to be repeated here:

- Even with the relative uncertainties on the raw numbers being relatively large, both signal and control regions suffer from a similar bias, cancelling to a small fraction of its original size when calculating the ratios in the TFs.
- Uncertainties from extra radiation for $W + jets$ are ranging from 15% in a two-jet channel up to 40% in a four-jet selection with large remaining statistical fluctuations.
- Uncertainties from extra radiation for $Z + jets$ are lower than 35% (or compatible with 0 within that uncertainty) in all signal regions.
- For the $t\bar{t}+jets$ estimate, the lack of statistics creates the need to lower some of the SR cuts (e.g. the M_{eff} threshold). The uncertainties arising from extra jet radiation in this case are lower than 25% (or compatible with 0 within the uncertainty on the bias) in all signal regions.

In order to estimate the consequences of the above results, a dedicated systematic uncertainty on the W, Z and *top* share is introduced by conservatively scaling the combined W, Z, *top* simulation up and down by $\pm 40\%$.

6.4.3 Scale uncertainties

The choice of renormalisation and factorisation scales as well as their variation and PDF uncertainties can have an influence on the event counts both in SRs and CRs. While the impact is observed to be as high as 100% on the absolute numbers for specific processes, the impact on the ratios used in the TFs is, however, much smaller (differences $<$40%, channel dependent).

Systematic uncertainties on the expected SUSY signal are estimated by varying the factorisation and renormalisation scales in PROSPINObetween half and twice their default values and by considering the PDF uncertainties provided by CTEQ6. Uncertainties are calculated for individual production processes ($\tilde{q}\tilde{q}$, $\tilde{q}\tilde{g}$ and $\tilde{g}\tilde{g}$) and are typically $\sim 35\%$ in the vicinity of the limits expected to be set by the analyses.

Jet energy scale and resolution, and pile-up uncertainties on SUSY signal expectations are typically smaller than $30 - 40\%$.

6.4.4 Other uncertainties

Also the heavy-flavour[4] part of QCD is conservatively scaled up and down by a factor of 2 in order to account for the large uncertainties on heavy-flavour QCD, resulting in an additional systematic uncertainty called accordingly *HF up/down*.

The *pile-up* systematics is based on half the difference between the outcome of the BCID-averaged and the BCID non-averaged reweighting (see Section 5.2.1).

6.5 The QCD background estimation

The QCD background, especially at higher jet multiplicities, is not only one of the more difficult backgrounds to estimate, but also it is affected by large uncertainties. Even though increasing the huge fractional uncertainties, the SUSY search strategy foresees harsh cuts to reduce the QCD background to a very small level, resulting in events passing the selection being rare both in MC and data-driven estimates. Nevertheless, the overall exclusion (or discovery) limits are not to be influenced by a QCD estimate in a significant way.

The QCD background estimates use different control regions with the overall goal to estimate scaling factors for correcting the MC: the main QCD CR is based upon the reversed and tightened $\Delta\varphi^{min}\left(jet, \vec{P}_{\mathrm{T}}^{\mathrm{miss}}\right)$ cut (see Section 6.1.2 and Table 6.1, SR Cut 12). Events are selected where the $E_{\mathrm{T}}^{\mathrm{miss}}$ vector is aligned with one of the leading three jets, resulting in events either with neutrinos from a heavy-flavour quark decays or with at least one of the leading jets being significantly mismeasured.
A second CR is given by reversing the $E_{\mathrm{T}}^{\mathrm{miss}}/M_{\mathrm{eff}}$-cut (see Section 6.1.3 and Table 6.1, SR Cut 13). In addition to the MC-based estimates, there exists a fully-data-driven approach, determining a *jet response function* to generate pseudo-events from data (see Section 6.5.1).

[4]Those events with at least one jet with $p_T > 30$ GeV and $|\eta| < 2.5$ associated with a parton-level b-quark are considered as *heavy* flavour.

6.5.1 The jet-smearing method

The next section briefly recapitulates the data-driven ansatz to estimate the QCD background, developed by the Sheffield-group and currently used as baseline method. It is used for comparisons when developing a new ansatz, discussing its advantages and disadvantages.

The jet response function includes both the effects of jet mismeasurement and contributions from neutrinos and muons in jets from heavy flavour decays (published in [10]). After measuring the response function from the fluctuations in jet p_{T}, it is convolved with the jet four-vectors in low-$E_{\mathrm{T}}^{\mathrm{miss}}$ multi-jet data events, generating higher $E_{\mathrm{T}}^{\mathrm{miss}}$ pseudo events. These are used to provide a minimally MC dependent estimate of QCD multi-jet distributions, including the distribution of $\Delta\varphi$ for high M_{eff} events.
The jet-smearing method proceeds in four steps:

(1) Selection of low-$E_{\mathrm{T}}^{\mathrm{miss}}$ *seed events* in the data which are used in steps (3) and (4).

(2) As a starting point for defining the response function one measures the function in Monte Carlo simulated data by comparing generator level jet energy to reconstructed jet energy.

(3) The response function from (2) is then modified by smearing the seed events from (1) until the smeared data (pseudo-data) agree with data in control regions.

(4) jet-smearing of the seed events from (1) with the data-constrained smearing function is used to obtain estimated distributions of key variables in the control and signal regions used in the main analysis.

The seed events are triggered using single jet triggers with additional cuts on $E_{\mathrm{T}}^{\mathrm{miss}}$ significance and jet-based $E_{\mathrm{T}}^{\mathrm{miss}}$ significance to ensure that only well measured events are selected. Matching truth jets from QCD MC to reconstructed jets with a $\Delta R < 0.1$, a first response function, binned in 20 GeV truth p_{T} bins, is derived as fraction

$$R = \frac{E_{\mathrm{reco}}}{E_{\mathrm{true}}}. \tag{6.5}$$

Drawing a random factor from the appropriate p_{T} response function, each jet four-momentum, $\vec{p}_{\mathrm{T}}$, is multiplied to generate smeared events and $\vec{P}_{\mathrm{T}}^{\mathrm{miss}}$ is recalculated with

$$\vec{P}_{\mathrm{T}}^{\mathrm{miss}\,\prime} = \vec{P}_{\mathrm{T}}^{\mathrm{miss}} - \sum_i \vec{p}_{\mathrm{T}}{}'(j_i) + \sum_i \vec{p}_{\mathrm{T}}(j_i), \tag{6.6}$$

where the primes are used to denote the smeared quantities.
This MC based response function is afterwards modified using:

(1) Additional Gaussian smearing to widen the jet response. p_{T}- and η-dependent widening in line with Ref [159] is applied by default to the reconstructed jets. To obtain agreement in the control regions, these Gaussian widths are increased by a constant value, $\sigma_{correction}$.

(2) 'DC' Offset (i.e. a uniform probability level) added to the low-side ($R < 1.0$) response tail to increase or decrease this tail. The offset is defined as DC_{LS}.

The uncertainties are obtained by varying each parameter until the estimate is no longer consistent with the statistical uncertainty of the data.

The shape of the jet response function is constrained using two different control regions: the *dijet analysis* for the Gaussian peak and the *Mercedes analysis* for the asymmetric tails. The first one selects events with two jets with $|\eta| < 2.8$ and $p_{\mathrm{T}} > 130, 40$ GeV (where there are no additional jets with $p_{\mathrm{T}} > 20$ GeV in the full η range). The dijet analysis uses the p_{T} asymmetry of the events:

$$A(p_{\mathrm{T},1}, p_{\mathrm{T},2}) = \frac{p_{\mathrm{T},1} - p_{\mathrm{T},2}}{p_{\mathrm{T},1} + p_{\mathrm{T},2}}, \tag{6.7}$$

where the indices correspond to the jet p_{T} ordering. This distribution is sensitive to the Gaussian response of the jets and the response tails, it is shown in Figure 6.7a.

The Mercedes analysis, aiming at the (especially low) tails of the jet response function, selects events with at least three jets to study the R_2 distribution of multi-jet events where topological cuts ensure one jet to be unambiguously associated with the $\vec{P}_{\mathrm{T}}^{\mathrm{miss}}$ in the event. The response of this jet is then given by

$$R_2 \simeq \frac{\vec{p}_{\mathrm{T}}^{J} \cdot \left(\vec{p}_{\mathrm{T}}^{J} + \vec{P}_{\mathrm{T}}^{\mathrm{miss}}\right)}{\left|\vec{p}_{\mathrm{T}}^{J} + \vec{P}_{\mathrm{T}}^{\mathrm{miss}}\right|^2}, \tag{6.8}$$

where $\vec{p}_{\mathrm{T}}^{J}$ is understood to be the reconstructed p_{T} of the jet associated with the $\vec{P}_{\mathrm{T}}^{\mathrm{miss}}$. Figure 6.7b shows the R_2 distribution measured with data, Monte Carlo simulation using the jet-smearing method.

Figure 6.8 shows comparisons between SM MC predictions, data and the jet-smearing estimate for non-'LAr hole' events, for distributions of the $\Delta\varphi$ variable used to distin-

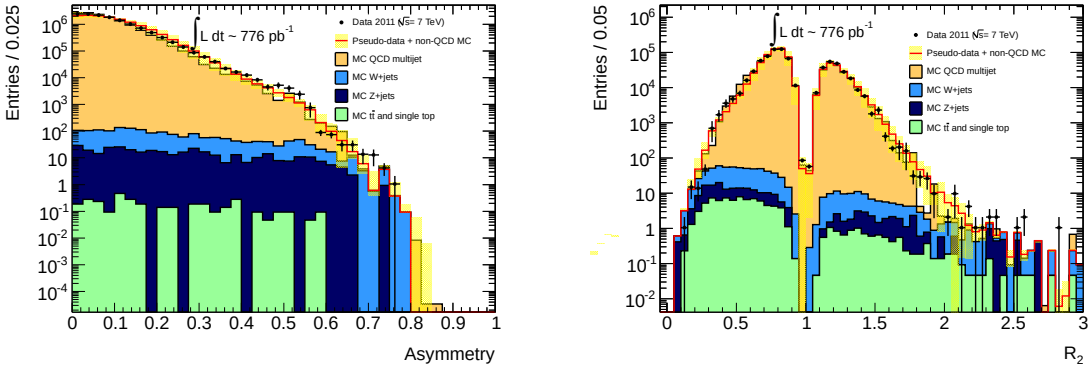

(a) (b)

Figure 6.7: Distributions for response function measurement using the dijet and Mercedes analyses, showing data, Monte Carlo simulations and distributions estimated with the jet-smearing method [10].

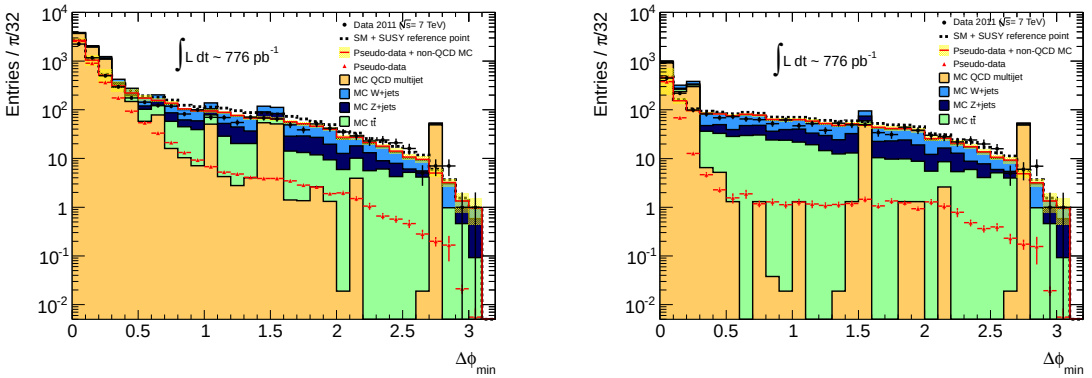

(a) SR C (b) SR C

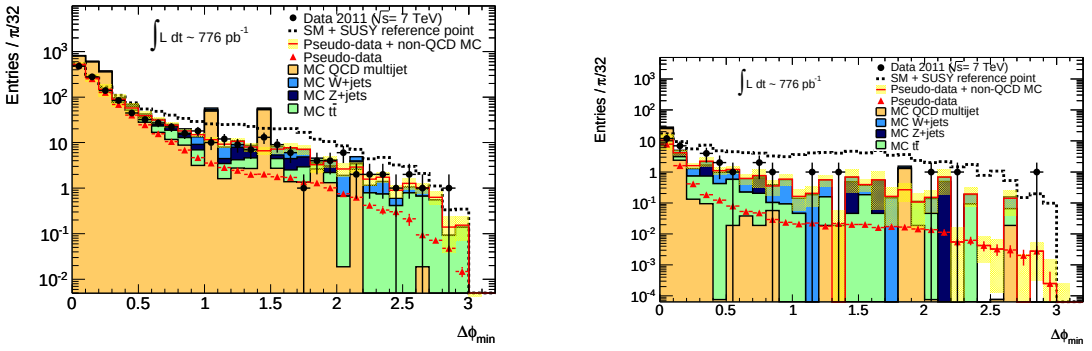

(c) SR E (d) SR E

Figure 6.8: Comparison of observed distribution and predicted distributions of $\Delta\varphi$, after all cuts except the $\Delta\varphi$, M_{eff} and $E_{\text{T}}^{\text{miss}}$ $/M_{\text{eff}}$ cuts (*left*) and after all cuts except the $\Delta\varphi$ cut (*right*) for signal region C, or E respectively. Only statistical uncertainties are shown [10].

Signal Region	$N_{\mathrm{SR}}/N_{\mathrm{CR2}}$ ($\times 10^{-3}$)				
	value	(stat.)	(mean)	($\sigma_{correction}$)	(tail)
A	7.2	$\pm$ 0.6	$^{+0.1}_{-0.0}$	$\pm$ 1.9	$^{+3.2}_{-0.7}$
B	11.6	$\pm$ 0.5	$^{+0.5}_{-0.5}$	$\pm$ 1.2	$^{+4.4}_{-2.2}$
C	52	$\pm$ 2	$^{+0}_{-1}$	$\pm$ 5	$^{+42}_{-24}$
D	22	$\pm$ 1	$^{+1}_{-2}$	$\pm$ 1	$^{+14}_{-8}$
E	63	$\pm$ 3	$^{+2}_{-2}$	$\pm$ 7	$^{+17}_{-16}$

Table 6.4: Predicted ratios of events in control and signal region for the five analysis channels using the jet-smearing method. Mean uncertainty refers to shifting the mean of the jet response up and down by the JES uncertainty [10].

guish CR2 from its associated SR. The plots correspond to the event selections for SR-C and SR-E and their associated QCD control regions. Good agreement is seen both between the data and Monte Carlo and the data and the smearing estimate. The QCD TF is effectively the ratio of predicted numbers of QCD jet events in the regions above $\Delta\varphi = 0.4$ and below $\Delta\varphi = 0.2$ in the right hand panel. Table 6.4 shows the obtained TFs including its statistical and systematic uncertainties arising from the mean (i.e. JES variation), the widening of the Gaussian smearing $\sigma_{correction}$ and the tail uncertainty DC_{LS}.

6.5.2 QCD jet background estimate using a reversed $\Delta\varphi$ cut

In this method, the CR2 $\rightarrow$ SR transfer factors TF for each of the five channels are calculated using the ratio of the observed numbers of Monte Carlo events in the SR and in a control region with reversed and tightened $\Delta\varphi$ cut (CR2, $\Delta\varphi < 0.2$ instead of $\Delta\varphi > 0.4$) for each channel. Although the intermediate region ($0.2 < \Delta\varphi < 0.4$) is already dominated by QCD, their contamination with W, Z and *top* is too high to be used within this method. Instead, it serves as additional cross-check region for the Likelihood fit later.

This region preferentially selects events in which one of the leading three jets contains a neutrino from a heavy-flavour decay, or in which that jet has been mismeasured in the calorimeters.
The Standard Model background composition of this CR for all different channels is

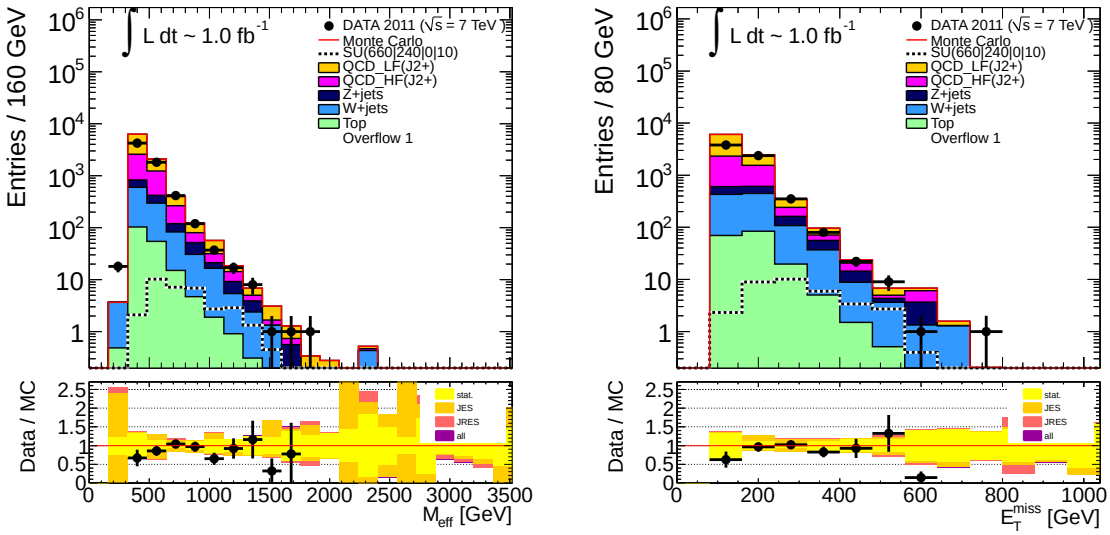

(a) Effective mass M_{eff}

(b) Missing transverse energy

(c) Leading jet p_{T}

(d) Sub-leading jet p_{T}

Figure 6.9: Distributions for the reversed $\Delta\varphi$ control region for the two-jet channel: M_{eff}, $E_{\text{T}}^{\text{miss}}$, leading and sub-leading jet p_{T} are shown before the final cut on M_{eff}. The MC simulation describes the data quite good.

	SR-A	SR-B	SR-C	SR-D	SR-E
Data	57 ± 7.5	97 ± 9.8	763 ± 27.6	41 ± 6.4	34 ± 5.8
SM	64.5 ± 11.5	80.8 ± 10.7	957 ± 270.4	38.2 ± 8.2	26.4 ± 7.6
QCD:	31.9 ± 6.9	49.2 ± 9.4	761.8 ± 270.2	24 ± 7.5	22 ± 7.5
LF	15.4 ± 3.5	28.9 ± 7.2	486.5 ± 241.4	14.7 ± 5.6	11.3 ± 4.8
HF	16.5 ± 5.9	20.3 ± 6	275.3 ± 121.3	9.3 ± 4.9	10.6 ± 5.8
non-QCD:	32.7 ± 9.2	31.6 ± 5.2	195.2 ± 11.5	14.2 ± 3.4	4.4 ± 1.2
W	22.8 ± 8.4	16.2 ± 2.6	79.8 ± 5.9	5.9 ± 1.6	1 ± 0.61
Z	7.5 ± 3.7	10.4 ± 4.2	41.4 ± 8.5	4.6 ± 2.7	0.78 ± 0.51
top	2.4 ± 0.89	5.1 ± 1.4	74 ± 4.8	3.8 ± 1.3	2.7 ± 0.91

Table 6.5: Background composition in the QCD control region: The QCD MC is split into *light- (LF)* and *heavy-flavour* QCD. CR2 is indeed dominated by QCD events as was assumed.

shown in Table 6.5, the CR is indeed dominated by QCD multijet events as was assumed, besides the two-jet channel, where the W,Z and *top* contamination reaches 50% and thus the obtained estimates practically cannot be trusted.
Figures 6.9 show some distributions of the two-jet channel in CR2: the effective mass, the missing transverse energy and the leading and sub-leading jet p_{T}. The overall agreement between data and MC is quite good. The distributions of the other remaining channels can be found in Appendix C.1.

The CR2 TFs including the statistical and systematic uncertainties for signal regions A-E are given in Table 6.6. The extremely large systematic uncertainties ($\geq$ 100%) mainly arise from limited statistics: Not only is the statistics of the QCD simulation, especially in regions with high effective mass, rather limited, but also reduces the applied pile-up reweighting the statistics even more (see Section 5.2.1): With the number of pile-up interactions in the MC simulation being much higher than in the analyzed data set, many simulated events with high pile-up activity are neglected due to extremely small weights, while events with low pile-up activity getting very large weights.

Besides the Jet Energy Scale (JES), the Jet Energy Resolution (JRES), the *Cellout*-term of $E_{\mathrm{T}}^{\mathrm{miss}}$ and the pile-up reweighting, additional uncertainties due to the heavy-flavour component and cross-section uncertainties on the non-QCD MC are considered

$TF = N_{\mathrm{SR}}/N_{\mathrm{CR2}}$	SR A	SR B	SR C	SR D	SR E
central	6.3e-05	8.0e-05	0.020	0.0057	0.0079
(stat.)	± 5.5e-05	± 5.4e-05	± 0.011	± 0.0052	± 0.0062
JESup	8.7e-05	0.0019	0.016	0.0042	0.0065
(stat.)	± 6.0e-05	± 0.0019	± 0.009	± 0.0038	± 0.0050
JESdown	0.0025	0.00055	0.040	0.010	0.010
(stat.)	± 0.0019	± 0.00047	± 0.022	± 0.009	± 0.008
JRES	0.0021	0.00063	0.074	0.0071	0.0077
(stat.)	± 0.0013	± 0.00041	± 0.062	± 0.0059	± 0.0052
PileUp	0.00027	0.0048	0.024	0.029	0.022
(stat.)	± 0.00020	± 0.0047	± 0.012	± 0.022	± 0.020
METCellOut	6.3e-05	8e-05	0.02	0.0057	0.0079
(stat.)	± 5.5e-05	± 5.4e-05	± 0.011	± 0.0052	± 0.0062
HFup	4.2e-05	5.6e-05	0.028	0.0041	0.0065
(stat.)	± 3.6e-05	± 3.8e-05	± 0.012	± 0.0037	± 0.0044
HFdown	0.00013	0.00014	0.0032	0.0092	0.012
(stat.)	± 0.00011	± 9.4e-05	± 0.0030	± 0.0086	± 0.011

Table 6.6: Predicted ratios of events in signal region and control region 2 for the five analysis channels using the control region with reversed $\Delta\phi(\mathrm{jet}, \vec{P}_{\mathrm{T}}^{\mathrm{miss}})$ cut including systematic errors (see Section 6.4 for details about systematics).

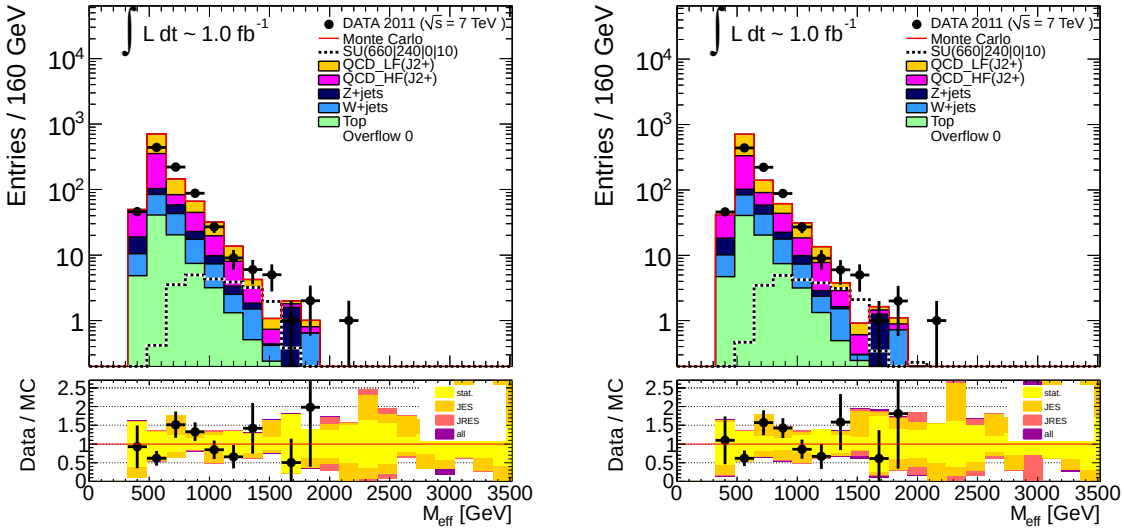

(a) default PU rew. **(b)** alternative PU rew.

Figure 6.10: Comparing the default pile-up reweighting (left) with the alternative non-averaged BCID reweighting (right): M_{eff}-distribution before the last M_{eff}-cut for the 4-jet channel. Both models describe the data quite good.

(see Section 6.4). Roughly half of the QCD events entering the SRs being heavy flavour events (see Table 6.5), resulting in the need to assign a separate systematic uncertainty due to the limited knowledge of heavy flavour QCD: the number of those events has been conservatively scaled by a factor two up and down, as was done before in the 2010 analysis.

Comparing the obtained TF results (see Table 6.6) with the data-driven TFs (see Table 6.4) one can find differences up to two orders of magnitude. These are the result of the discussed shortcomings, especially the limited statistics, as a few events, migrating in or out of a signal region, results in a very unstable prediction of the TFs – which practically cannot be trusted.
However, the situation is improved by applying an alternative non-averaged BCID pile-up reweighting (see Table 6.6, fifth row) and the QCD predictions stabilize as no longer 50% of the events are killed by pile-up reweighting but only of the order of 20% (see Figure 5.4a). Nevertheless, as the remaining SR and CR1,3,4 still use the default pile-up reweighting method as baseline, it could not be switched within this method for coherence reasons. Apart of the two-jet channel, which anyhow suffers from a large contamination with non-QCD events, quite good agreement with the data-driven estimates is observed, and also the alternative pile-up reweighting procedure describes the data quite well (see Figure 6.10).

SR^{exp}_{QCD}	SR-A	SR-B	SR-C	SR-D	SR-E
central	0.0015 ± 0.0015	0.0052 ± 0.0036	11.2 ± 6.3	0.15 ± 0.14	0.23 ± 0.19
JES up	0.0019 ± 0.0016	0.1 ± 0.1	8.5 ± 4.5	0.1 ± 0.096	0.16 ± 0.13
JES down	0.074 ± 0.063	0.04 ± 0.034	24.1 ± 13.8	0.32 ± 0.28	0.32 ± 0.25
JRES	0.054 ± 0.042	0.038 ± 0.026	42.3 ± 35.1	0.22 ± 0.19	0.22 ± 0.16
METCellOut	0.0015 ± 0.0015	0.0052 ± 0.0036	11.2 ± 6.3	0.15 ± 0.14	0.23 ± 0.19
PileUp	0.0067 ± 0.0058	0.31 ± 0.31	13.4 ± 6.7	0.76 ± 0.61	0.65 ± 0.6
HF up	0.001 ± 0.001	0.0037 ± 0.0025	15.6 ± 6.7	0.11 ± 0.1	0.19 ± 0.14
HF down	0.0032 ± 0.0032	0.0089 ± 0.0064	1.8 ± 1.7	0.25 ± 0.24	0.35 ± 0.34
WZTop up	0.00071 ± 0.0011	0.0042 ± 0.003	9.7 ± 5.4	0.12 ± 0.12	0.22 ± 0.18
WZTop down	0.0024 ± 0.0021	0.0062 ± 0.0043	12.8 ± 7.2	0.18 ± 0.17	0.25 ± 0.2

Table 6.7: Expected number of QCD events in the SR together with the systematic uncertainties (see Equation (6.9)), based on the CR2 → SR TFs estimates from the QCD control region with reversed $\Delta\varphi$ -cut.

Finally, the according expectations for the estimated number of QCD events in the SR are shown in Table 6.7:

$$SR^{exp}_{QCD} \approx \left(CR^{obs}_{DATA} - CR^{exp}_{W,Z,top}\right) \cdot TF, \tag{6.9}$$

which represents only a rough estimate of the expected numbers, as for the final numbers a Likelihood fit is performed in all CRs to determine the normalization factors for all individual Standard Model backgrounds separately. This approach will be explained in more detail in the following Section 6.5.3.

A few conclusions can be drawn anyway: Besides SR-C with $\sim$10 events, in all channels less than one single QCD event is expected in the SRs. Compared to the

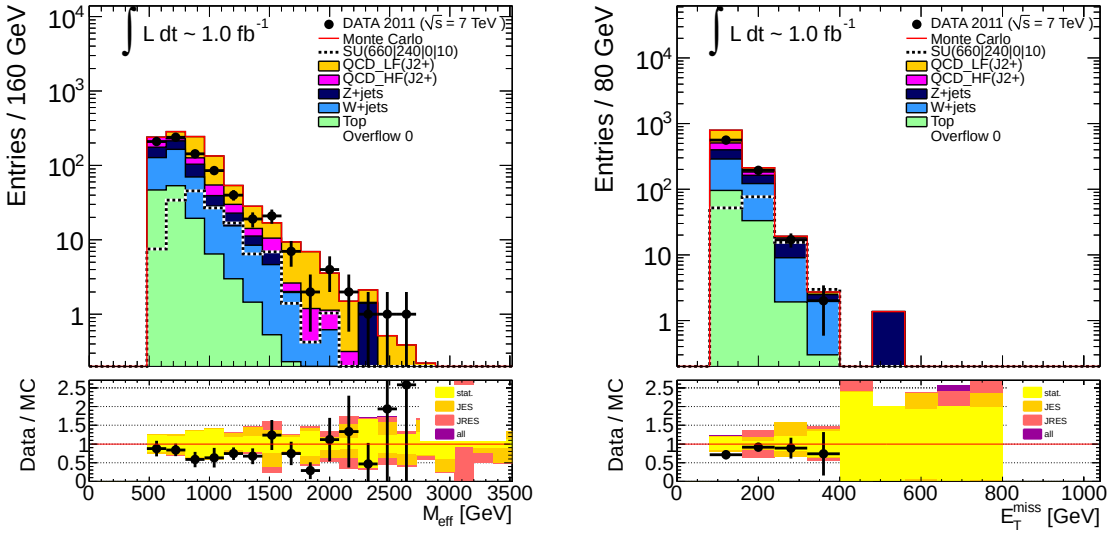

(a) Effective mass M_{eff} **(b)** Missing transverse energy

Figure 6.11: Effective mass and missing transverse energy distributions for the 3-jet channel with reversed $E_{\text{T}}^{\text{miss}}/M_{\text{eff}}$ cut (before final M_{eff} cut). The simulation describes the data well.

remaining W, Z and *top* backgrounds, the contribution from QCD multijet events in all SRs is indeed negligible.

6.5.3 QCD jet background estimate using a reversed $E_{\text{T}}^{\text{miss}}/M_{\text{eff}}$ cut

Another measure to distinguish QCD from non-QCD background is the ratio of effective mass and missing transverse energy (see Section 6.1.3), which is used in this method to define another QCD control region by reversing the $E_{\text{T}}^{\text{miss}}/M_{\text{eff}}$ cut.
The ansatz is similar to the QCD background estimate using a reversed $\Delta\varphi$ -cut (see Section 6.5.2) although the selection is nearly orthogonal (i.e. multijet events at higher effective mass are favoured). However, the estimated numbers of expected QCD events in the SR are calculated directly and not via TFs for the likelihood fit. Thus, for comparing the outcome of this approach with the previous methods, one needs to estimate the number of expected QCD events in the SRs from the previously obtained TFs.

Figure 6.11, showing both the effective mass and the missing transverse energy in the 3-jet channel, reflects a good agreement between the data and the MC simulation,

	SR-A	SR-B	SR-C	SR-D	SR-E
Data	116 ± 10.8	158 ± 12.6	632 ± 25.1	130 ± 11.4	0
SM	152.6 ± 15.6	214.3 ± 47.7	640.7 ± 51.7	139.2 ± 14.4	–
QCD:	67.4 ± 11	144.2 ± 47.1	176.9 ± 48.3	81.3 ± 12.7	–
LF	53.4 ± 9.4	114.8 ± 46.3	61.5 ± 10.5	46.6 ± 8.3	–
HF	14 ± 5.7	29.4 ± 9	115.4 ± 47.1	34.7 ± 9.7	–
non-QCD:	85.2 ± 11	70.1 ± 7.4	463.8 ± 18.5	57.9 ± 6.7	–
W	44.9 ± 4.3	42.8 ± 4.3	191.9 ± 9.6	31.8 ± 3.7	–
Z	35.9 ± 10.1	19.2 ± 5.8	99.8 ± 13.6	13.3 ± 5	–
top	4.4 ± 1.2	8.1 ± 1.8	172.1 ± 8	12.8 ± 2.4	–

Table 6.8: Background composition in the reversed $E_{\mathrm{T}}^{\mathrm{miss}}$ $/M_{\mathrm{eff}}$ QCD control region: this CR suffers from a large contamination with non-QCD events. The uncertainties quoted for the signal region QCD expectations are statistical uncertainties only.

that is also found in this alternate control region. The plots of the remaining channels can be found in Appendix C.2.

The composition of this CR can be found in Table 6.8. As already indicated by Figure 6.11, the contamination with non-QCD events inside this CR is relatively high ($\leq 60\%$), thus the non-QCD component can no longer be neglected. Furthermore, SR-E suffers from bad statistics, hence no predictions can be done here.

Using a partially data-driven approach, a MC normalization factor, a so called (MC to data) k-factor, is determined in a first step, which is later used to determine the expected number of QCD events in the SR from the raw (un-normalised) number of events in the signal region predicted by QCD Monte Carlo, $N_{\mathrm{MC\ QCD}}^{\mathrm{SR}}$, with:

$$N_{\mathrm{expected}}^{\mathrm{SR}} = k \cdot N_{\mathrm{MC\ QCD}}^{\mathrm{SR}}. \tag{6.10}$$

The k-factor itself is obtained within the following procedure: From the measured number of data events in the reversed $E_{\mathrm{T}}^{\mathrm{miss}}$ $/M_{\mathrm{eff}}$ control region, $N_{\mathrm{Data}}^{\mathrm{CR}}$, the simulated contamination by non-QCD MC is subtracted in order to minimize the sensitivity of the k-factor on these processes, where $N_{\mathrm{MC\ W,Z,top}}^{\mathrm{CR}}$ is the number of events predicted in the control region by Standard Model Monte Carlo for the according processes.
The ratio of this quantity with the raw (un-normalised) number of events predicted in

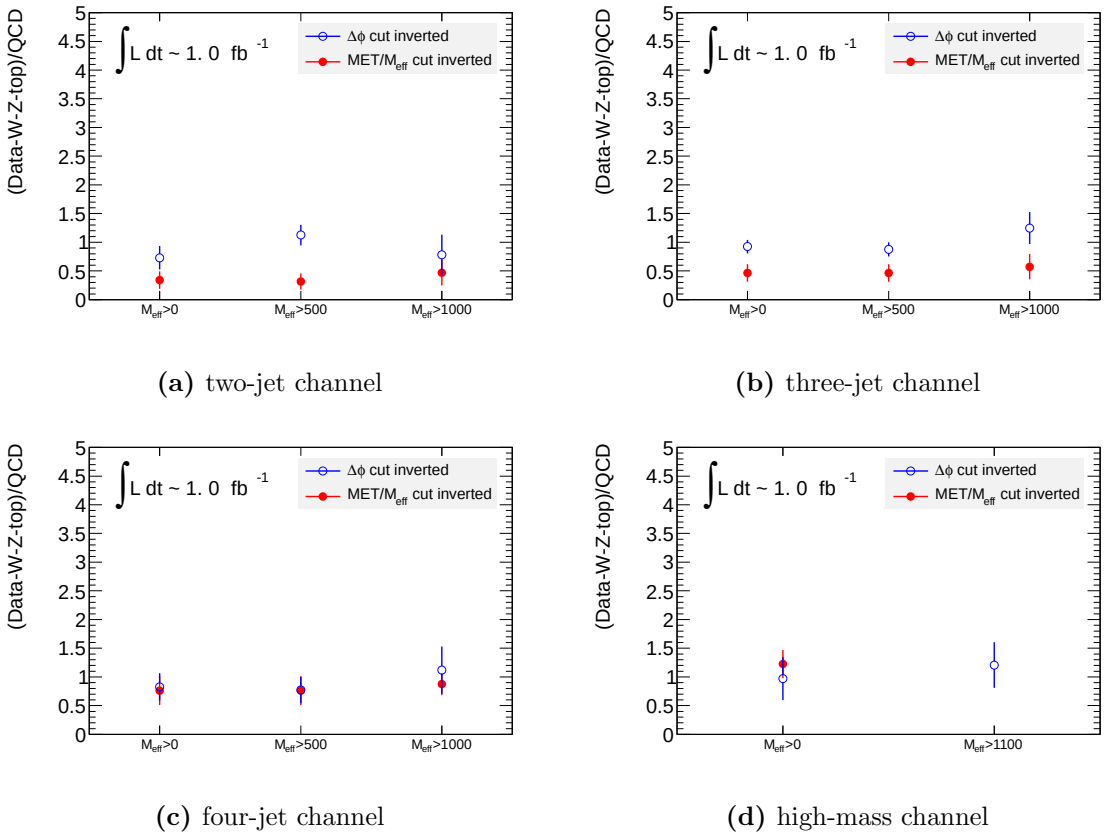

(a) two-jet channel

(b) three-jet channel

(c) four-jet channel

(d) high-mass channel

Figure 6.12: k-factors (see Equation (6.11)) for different cut values of M_{eff}, both for the control region with reversed $\Delta\varphi$ cut (blue) and reversed $E_{\text{T}}^{\text{miss}}/M_{\text{eff}}$ cut (red). Showing mostly no dependence on M_{eff}, the reliability of the method is confirmed.

the control region by QCD Monte Carlo, $N_{\text{MC QCD}}^{\text{CR}}$, defines the final k-factor:

$$k = \frac{N_{\text{Data}}^{\text{CR}} - N_{\text{MC W,Z,top}}^{\text{CR}}}{N_{\text{MC QCD}}^{\text{CR}}}. \tag{6.11}$$

The experimental results for the k-factors are given in Table 6.9. Figure 6.12 shows the k-factors for the individual channels for different values of the M_{eff} cut. While the method using the reversed $E_{\text{T}}^{\text{miss}}/M_{\text{eff}}$ cut provides stable results, the dependence of the reversed $\Delta\varphi$ k-factors on the value of M_{eff} especially for the low jet multiplicities lets one question the reliability of the method even further.

With the improved understanding of detector performance in 2011 a significant decrease in the number of QCD jet events with mismeasured $E_{\text{T}}^{\text{miss}}$ in this control region is

	SR-A	SR-B	SR-C	SR-D	SR-E
k-factor	0.46 ± 0.24	0.61 ± 0.22	0.95 ± 0.31	0.89 ± 0.21	–

Table 6.9: k-factors in the reversed $E_{\mathrm{T}}^{\mathrm{miss}}$ $/M_{\mathrm{eff}}$ QCD control region. Note: For SR-E, no value can be obtained. The uncertainties quoted for the k-factors are statistical uncertainties only.

$\mathrm{SR}_{\mathrm{QCD}}^{\mathrm{exp}}$	SR A	SR B	SR C	SR D	SR E
central	0.00092 ± 0.00092	0.0024 ± 0.0018	14.3 ± 7.8	0.12 ± 0.11	–
JES up	0.00074 ± 0.00086	0.052 ± 0.053	4.0 ± 3.1	0.079 ± 0.071	–
JES down	0.039 ± 0.033	0.025 ± 0.022	35.7 ± 19.1	0.2 ± 0.16	–
JRES	0.029 ± 0.023	0.021 ± 0.015	54.6 ± 44.4	0.1 ± 0.083	–
METCellOut	0.00092 ± 0.00092	0.0024 ± 0.0018	14.3 ± 7.8	0.12 ± 0.11	–
PileUp	0.0041 ± 0.0036	0.15 ± 0.15	17.0 ± 8.6	0.6 ± 0.45	–
HF up	0.00076 ± 0.00076	0.002 ± 0.0014	16.4 ± 7.2	0.085 ± 0.075	–
HF down	0.0012 ± 0.0012	0.003 ± 0.0023	4.2 ± 3.5	0.21 ± 0.19	–
WZTop up	-0 ± 0.00057	0.0016 ± 0.0013	-1.5 ± 3.2	0.082 ± 0.075	–
WZTop down	0.0019 ± 0.0017	0.0031 ± 0.0023	30.1 ± 15.6	0.16 ± 0.14	–

Table 6.10: Systematic error estimates for the estimates of QCD jet background populations in signal regions A-E using an alternative control region with inverted $E_{\mathrm{T}}^{\mathrm{miss}}$ $/M_{\mathrm{eff}}$ cut.

observed with respect to the 2010 analysis [57, 58]. In contrast to the CR2 region where half of the QCD events were heavy flavoured events, here light flavoured QCD events dominate. Monte Carlo as well as data statistics in this control region are even smaller than in the case of CR2. Hence no estimates could be obtained for signal region E, and the statistical errors in regions A-D are $\sim$100%.

The impact of variation of systematic uncertainties on the number of expected QCD events in the signal regions A-E is shown in Table 6.10. The following uncertainties were considered: JES and JER uncertainty, QCD heavy flavour uncertainty (procedure described in Section 6.5.2) and the uncertainty on the non-QCD contamination of the Control Region, which was conservatively assumed to be 40%.

Unfortunately due to limited QCD Monte Carlo statistics in the high M_{eff} regions, but also due to the pile-up reweighting method which is applied on the MC, the results are quite unstable which yields sometimes in $\sim$1000% systematic uncertainties (see discussion in Section 6.5.2). Nevertheless, it was seen that using an alternative pile-up reweighting method results in much more stable results. The number of expected QCD events obtained by this method are listed in the Table 6.10 in the fifth row. These are consistent with the N_{QCD}^{exp} obtained with the reversed $\Delta\varphi$ approach (see Table 6.7, fifth row). With the different QCD estimation methods nicely confirming the smallness of the QCD background, the large uncertainties of the estimate are well contained within tolerable limits.

6.6 Motivation for a new approach

Following the previous Sections about the QCD background estimation, one stumbles upon several open questions or smaller issues. The baseline method (see Section 6.5.1) itself is quite complicated and due to this complexity, its (systematic) uncertainties are difficult to estimate. The main MC-based cross-checks have quite some problems concerning too low MC-statistics in combination with huge pile-up weights (see Section 6.5.2 and Section 6.5.3). While the MC-based approaches still worked out under the conditions of the first 2011 analysis, where the data luminosity was small and thus the MC statistics sufficient (see Section 6.2, the *reversed* $\Delta\varphi$ *method* was even used as baseline back then), this leads to instable results with high (sometimes up to 1000%) uncertainties and thus conclusions of low significance in the later analyses.

A robust approach finally can be reached only by the combination of different and independent measurements. It is the mind of the author finally, that the existing purely-MC-based cross-checks are no longer sufficient for the ongoing high precision SUSY studies. Therefore a new method, incorporating the advantageous aspects of the previous ones, will be proposed as replacement in the following.

Chapter 7

Alternative QCD background estimation technique

In Section 6.1.2, the different behaviour of QCD and non-QCD processes concerning the angular separation between jets and $\vec{P}_{\mathrm{T}}^{\mathrm{miss}}$ was already discussed. Based on this variable, a new method to estimate the QCD background inside the signal regions is introduced in Section 7.1 and the application of this ansatz on ATLAS data shown subsequently (see Section 7.3).
Based on the official ATLAS SUSY analysis as introduced in the previous chapters, only small modifications on e.g. the event selection and the trigger choice will become necessary due to a partially lower $E_{\mathrm{T}}^{\mathrm{miss}}$ cut (see Section 7.2).
This study understands itself as an combination and advancement of different existing approaches under a new perspective, to not only determine both the CR2 $\rightarrow$ SR transfer factors TFs for each of the five channels but also the expected number of QCD events in the signal regions.
While the development and tuning of the method was done completely on the smaller dataset with $1\,\mathrm{fb}^{-1}$ (see Section 6.3.1), the application on the complete 2011 dataset ($4.7\,\mathrm{fb}^{-1}$) will be shown in Chapter 8. The following Sections describe the personal work of the author and were published in a similar way in the supporting documentation for Morion 2012 [12].

7.1 Theoretical overview

The QCD control region is defined by reversing and tightening the SR cut 12 (see Table 6.1) to select events in which the $\vec{P}_{\mathrm{T}}^{\mathrm{miss}}$ -vector is aligned in the transverse plane with one of the three leading jets with $p_{\mathrm{T}} > 40$ GeV.

The QCD transfer factor, TF_{QCD}, is then given as the ratio of events in the signal region and the QCD control region (see Section 2.7.4, Equation (2.8)),

$$TF_{QCD} = \frac{N_{QCD}^{SR}}{N_{QCD}^{CR}} \equiv \frac{N_{events} \,|\, \Delta\varphi^{min} > 0.4}{N_{events} \,|\, \Delta\varphi^{min} < 0.2} \tag{7.1}$$

.

A non-trivial relation between the angular jet separation $\Delta\varphi$ and $E_{\mathrm{T}}^{\mathrm{miss}}$ itself is expected and thus the ratio (see Equation (7.1)) is studied as a function of $E_{\mathrm{T}}^{\mathrm{miss}}$. The goal is to extrapolate from the low-$E_{\mathrm{T}}^{\mathrm{miss}}$ regions - where the MC simulations are better understood and predictive - to the signal region, where both the MC statistics is poor and the predictions not reliable as well as the possibility of a SUSY signal contamination exists (see Figure 7.1). Another advantage is that effects, which affect both the signal and control regions in the same way, will to some extend cancel inside the ratio: trigger efficiencies, some systematic uncertainties like JES or JRES. In first order approximation, this TF depends only on the missing transverse energy. In second order approximation, it also depends on the number of jets and their transverse momentum. Therefore, a separate TF must be determined for each of the five channels.

The method is designed in the following steps:

(1) Define several intervals in the region 40 GeV $< E_{\mathrm{T}}^{\mathrm{miss}} <$ 130 GeV with a width between 5 GeV at the lower edge up to 20 GeV at the upper one to ensure enough statistics in the individual bins.

(2) Apply the SUSY-selection (see Table 6.1) up to cut 12 ($\Delta\varphi^{min}$), but with a modified $E_{\mathrm{T}}^{\mathrm{miss}}$ -cut according to the particular interval from (1). Postpone the $E_{\mathrm{T}}^{\mathrm{miss}}$ /M_{eff}- and the M_{eff}-cut as these were designed against QCD and would eliminate all the statistics in the lower $E_{\mathrm{T}}^{\mathrm{miss}}$ -regions.

(3) Define a second, independent control region with a reversed $E_{\mathrm{T}}^{\mathrm{miss}}$ /M_{eff}-cut to explore the region with $E_{\mathrm{T}}^{\mathrm{miss}} \geq 130$ GeV.

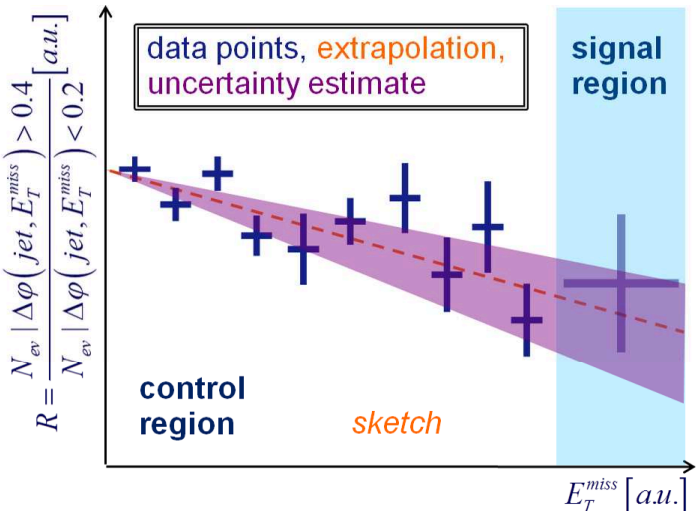

Figure 7.1: Ratio of events with $\Delta\varphi < 0.2$ and $\Delta\varphi > 0.4$ as function of $E_{\mathrm{T}}^{\mathrm{miss}}$ (*sketch*): a non-trivial relation is expected, which allows extrapolation from the low into high-$E_{\mathrm{T}}^{\mathrm{miss}}$ regions.

(4) Assuming a higher reliability of non-QCD MC than simulations of QCD multijet production, extract the numbers in a semi-data-driven way by subtracting non-QCD MC from real data, where N_{Data} is the number of data events in the specific region and $N_{\mathrm{MC\ W,Z,top}}$ is the number of events in this region for the specified processes, predicted by the Standard Model MC.

$$R_{QCD} = \frac{N_{SR}^{QCD}}{N_{CR}^{QCD}} \approx \frac{N_{\mathrm{Data}}^{\mathrm{SR}} - N_{\mathrm{MC\ W,Z,top}}^{\mathrm{SR}}}{N_{\mathrm{Data}}^{\mathrm{CR}} - N_{\mathrm{MC\ W,Z,top}}^{\mathrm{CR}}} \tag{7.2}$$

(5) Fit both control regions (from (2) and (3)) with different functions like Landau or Exponential, separately for each channel, to extrapolate the behaviour of R_{QCD} to the high $E_{\mathrm{T}}^{\mathrm{miss}}$ regions. *Note:* R_{QCD} is not yet the final TF (see Equations 7.1 and 7.2) because of the missing cuts in (2).

(6) Emulate the missing cuts from (2):
Derive a "$E_{\mathrm{T}}^{\mathrm{miss}}$-probability" from data, obtained from another separate control region, with the typical signal selection (including the $E_{\mathrm{T}}^{\mathrm{miss}}$ /M_{eff}- and the M_{eff}-cut) but a reversed $\Delta\varphi$ -cut. Convolve it with the previously determined ratios R_{QCD} to extract the transfer factors.

$$TF = \int_0^{\infty} \underbrace{p_{QCD}\left(E_{\mathrm{T}}^{\mathrm{miss}}\right)}_{E_{\mathrm{T}}^{\mathrm{miss}}\ probability} \cdot \underbrace{R_{QCD}\left(E_{\mathrm{T}}^{\mathrm{miss}}\right)}_{fit} dE_{\mathrm{T}}^{\mathrm{miss}} \tag{7.3}$$

7.2 Trigger selection

The jet + $E_{\mathrm{T}}^{\mathrm{miss}}$ -trigger *EF_j75_a4_EFFS_xe45_loose_noMu* which is commonly used inside other 0-lepton analyses reaches its plateau both for the leading jet-p_{T} and $E_{\mathrm{T}}^{\mathrm{miss}}$ around 130 GeV. When studying the ratio of QCD signal to background events (see Equation (7.1)), the low-$E_{\mathrm{T}}^{\mathrm{miss}}$ -control region (steps 1-2) requires an $E_{\mathrm{T}}^{\mathrm{miss}}$ -cut far below the turn-on of the combined $jet+$ $E_{\mathrm{T}}^{\mathrm{miss}}$ -trigger, with the lowest $E_{\mathrm{T}}^{\mathrm{miss}}$ interval starting already at 40 GeV.

Thus, a prescaled single jet trigger is chosen with a jet-p_{T} trigger threshold of 75 GeV at the highest trigger level ("event filter"), seeded by *L1_J50* and *L2_j70*, single jet-triggers with a threshold of 50 GeV at L1 and 70 GeV at L2 respectively, representing the jet-related part of the combined $jet+E_{\mathrm{T}}^{\mathrm{miss}}$ trigger (see Section 5.1.1 for details about triggers). The offline leading jet-p_{T} cut of 130 GeV ensures that events in the trigger turn-on are rejected. The extremely high rates of a single-jet-trigger with no additional restrictions require a heavy prescale, and the integrated luminosity of the *summer 2011* analysis with this single-jet trigger is only $2.64\,\mathrm{pb}^{-1}$. This seems to be only a small trade-off compared to the problems of being inside the badly-modelled turn-on region of a $E_{\mathrm{T}}^{\mathrm{miss}}$ -trigger in the MC simulations.

For the control region with the reversed $E_{\mathrm{T}}^{\mathrm{miss}}$ $/M_{\mathrm{eff}}$-cut (step 3), events are selected using the default $jet+E_{\mathrm{T}}^{\mathrm{miss}}$ -trigger. This second dataset reaches the full available integrated luminosity of $1.0\,\mathrm{fb}^{-1}$.

7.3 Details

The complete procedure as described in Section 7.1 is then applied to ATLAS data. Instead of the `JIMMY` $t\bar{t}$ samples used in the official analysis, `ALPGEN` top samples are used for the $t\bar{t} \to l\nu qq$ and $t\bar{t} \to l\nu l\nu$ processes, as these have been found to better describe the data especially at high-jet multiplicities.

Figure 7.2 shows the distribution of $\Delta\varphi^{min}$ after the $E_{\mathrm{T}}^{\mathrm{miss}}$ -cut (before applying cut 12) for different $E_{\mathrm{T}}^{\mathrm{miss}}$ -intervals, from 50 GeV to 60 GeV, from 80 GeV to 90 GeV and from 100 GeV to 110 GeV. All MC samples are normalized according to their cross-sections, and the QCD MC has an additional k-factor of 1.06 applied, based on the $E_{\mathrm{T}}^{\mathrm{miss}}$ -distribution from a two-jet selection applying a reversed $\Delta\varphi$ cut. With `PYTHIA`

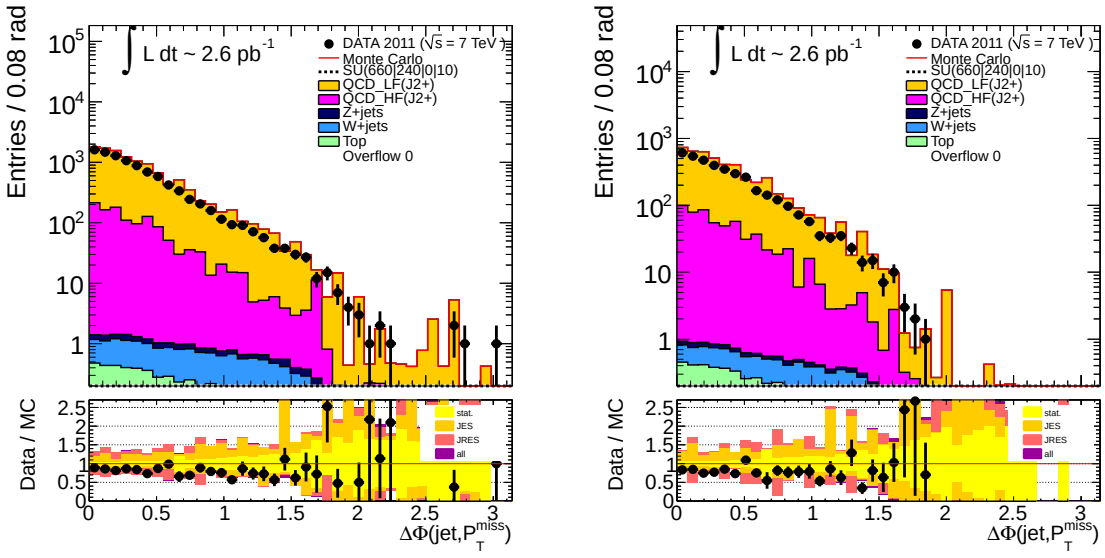

(a) two-jet channel: $50 < E_{\mathrm{T}}^{\mathrm{miss}} < 60$

(b) three-jet channel: $50 < E_{\mathrm{T}}^{\mathrm{miss}} < 60$

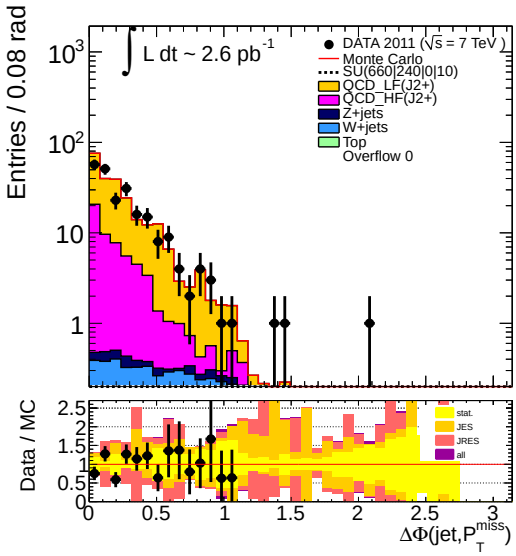

(c) three-jet channel: $80 < E_{\mathrm{T}}^{\mathrm{miss}} < 90$

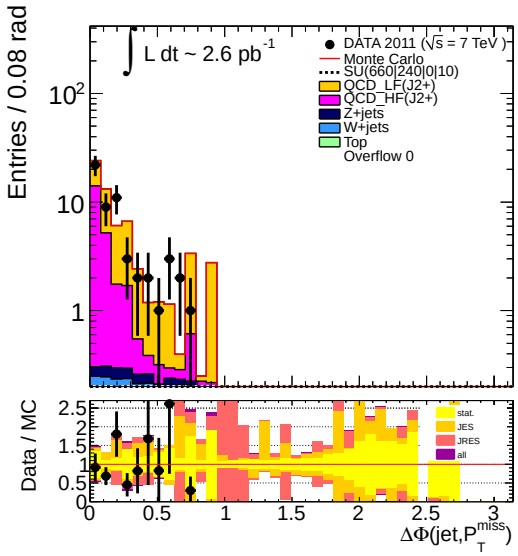

(d) three-jet channel: $100 < E_{\mathrm{T}}^{\mathrm{miss}} < 110$

Figure 7.2: $\Delta\varphi$ -distributions for different $E_{\mathrm{T}}^{\mathrm{miss}}$ -intervals: $E_{\mathrm{T}}^{\mathrm{miss}}$ ϵ [50;60[GeV, $E_{\mathrm{T}}^{\mathrm{miss}}$ ϵ [80;90[GeV and $E_{\mathrm{T}}^{\mathrm{miss}}$ ϵ [100;110[GeV: As expected, not only shows $\Delta\varphi$ a dependence on the jet-multiplicity, but also a clear dependence on $E_{\mathrm{T}}^{\mathrm{miss}}$.

MC being only LO, the normalization of the QCD samples is a priori not expected to match the data. The plots are taken mainly from the three-jet channel, but without the signal region cuts 12 - 14. The shape of the $\Delta\varphi$ -distributions, both for the QCD enriched and the suppressed region, differs as function of jet multiplicity and $E_{\mathrm{T}}^{\mathrm{miss}}$ as expected. The higher the $E_{\mathrm{T}}^{\mathrm{miss}}$ interval, the steeper fall the $\Delta\varphi$ distributions.

It has to be mentioned, that the two lowest samples, J0 and J1 (see Table A.4), are removed from the QCD MC due to low statistics. Furthermore, also the pile-up overlays cause trouble since the pile-up events do not have a cut on $\hat{p}_T$ and thus jet-p_{T} values up to 100 GeV are possible. Those samples are not expected to contribute to any SR-like regions at all and to medium-$E_{\mathrm{T}}^{\mathrm{miss}}$ -regions only insignificantly (in total three single events, surviving the selection, would otherwise end up with extremely high weights, resulting both from the huge cross-sections in combination with the pile-up reweighting, and produce spikes in the otherwise flat distributions). The normalization of the remaining samples J2 - J8 is then adapted accordingly. As during this analysis, QCD MC is used for illustration only, the final results are not affected. Overall, the agreement between simulation and data is acceptable, main discrepancies come from the QCD MC.

In the following paragraphs, the plots are taken from the four-jet channel for illustration. The full set can be found in the Appendix C.3. All conclusions drawn and results obtained hold for the other channels as well.

After selecting the events according to step (1-3), the obtained ratios in all four channels (four-jet channel see Figure 7.3, two-jet, three-jet and high-mass channel see Appendix C.3) show a good agreement between data and the Standard Model MC. Moreover, the $data - MC_{W,Z,top}$, called *subtraction* in the following (see Equation (7.2)), is shown together with the QCD MC and agrees also reasonably well within the uncertainties. In general, one can say that R_{QCD} is steeply falling with increasing $E_{\mathrm{T}}^{\mathrm{miss}}$. With a truth-level filter, the QCD MC is split in its two components: light- and heavy-flavour. By definition, heavy flavour events are those with at least one jet with $p_T >$ 30 GeV and $|\eta| < 2.5$ associated with a parton-level b-quark. The ratio was studied separately for both flavours and besides the lowish statistics, no significant difference is seen at this stage of the analysis. Hence, the light- and heavy-flavour components are combined within the subsequent steps.

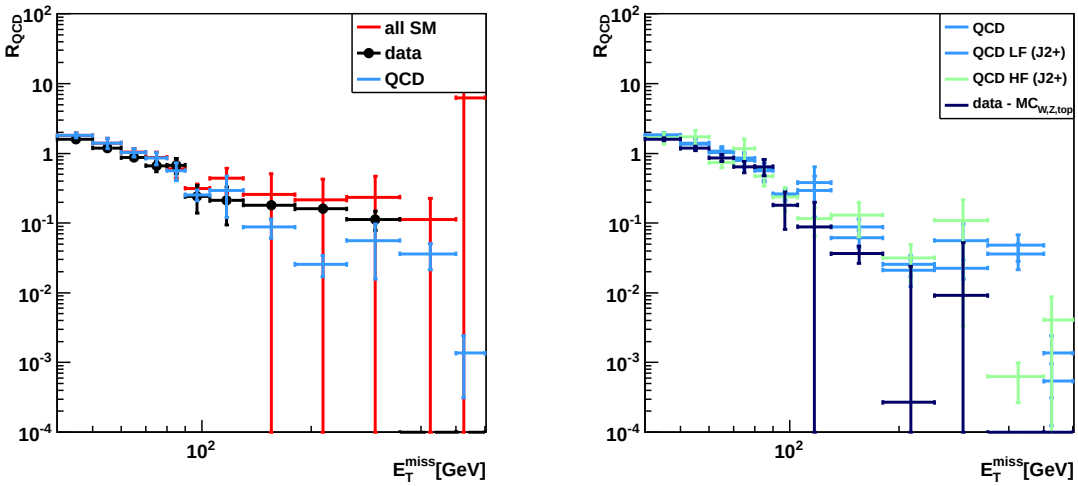

(a) uncorrected **(b)** without contamination

Figure 7.3: R_{QCD} in the four-jet channel, before (see Figure 7.3a) and after (see Figure 7.3b) correction for contamination by non-QCD processes: the overall agreement between all Standard Model MC and data is fine, while $data - MC_{W,Z,top}$ compares well to the QCD MC prediction. Errors are of statistical nature only.

The ratios are fitted with a Landau function f_1,

$$f_1(x) = c \cdot Landau(x, \mu, \sigma), \tag{7.4}$$

in order to extrapolate into the signal regions at higher $E_{\mathrm{T}}^{\mathrm{miss}}$ -values (see Figure 7.4).

Last (step 6), the "$E_{\mathrm{T}}^{\mathrm{miss}}$ "-probabilities are extracted by applying the full event selection with only one minor modification: the $\Delta\varphi$ -cut is reversed to ensure no contamination from a possible signal. The obtained distributions are normalized to unity and are fitted with an exponential function $e^{-\lambda x}$ to extract the most-dominant features at $E_{\mathrm{T}}^{\mathrm{miss}}$ values close to the signal region thresholds.

The $E_{\mathrm{T}}^{\mathrm{miss}}$ -probabilities for the medium and tight selection of the four-jet channel are shown in Figure 7.5 as well as those for the high-mass channel (for two- and three-jet channel, see Figure C.9 in Appendix C.3). In general, the distributions are taken from data where possible, subtracting the non-QCD components. In case of too low data statistics, the distributions are determined from the QCD MC simulation, but no discrepancy between data and MC has been found. Otherwise, the QCD-MC in this plots is shown for illustration only.

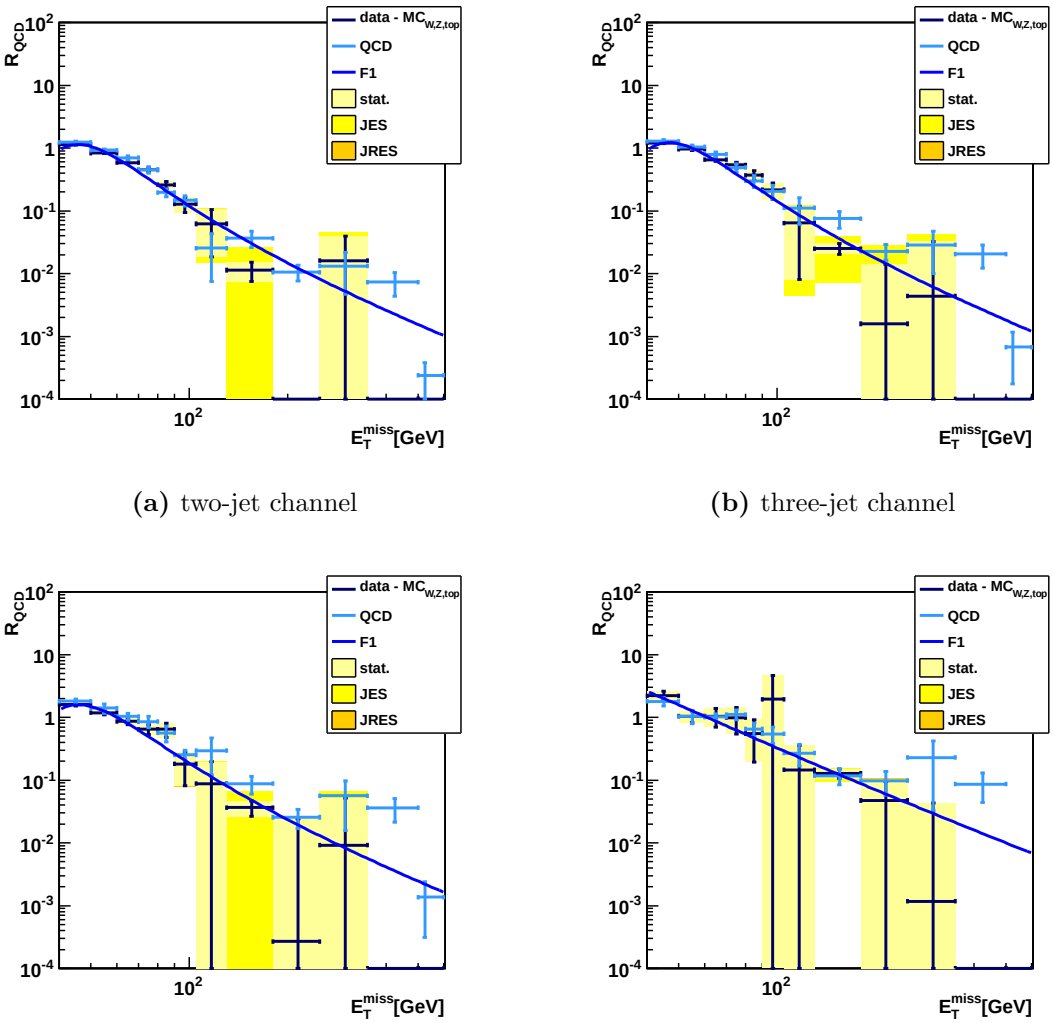

(a) two-jet channel

(b) three-jet channel

(c) four-jet channel

(d) high-mass channel

Figure 7.4: The Landau fits of R_{QCD} are shown for the different channels.

In the end, the R_{QCD} fit is convolved with the $E_{\mathrm{T}}^{\mathrm{miss}}$ - probabilities in order to extract the final numbers for TF.
It has to be mentioned that in order to extract the absolute number of expected QCD events in the signal regions, one has to multiply the final TF with the number of measured events in the control region, i.e. the integral of the unnormalised "$E_{\mathrm{T}}^{\mathrm{miss}}$ "-probability distributions.

Results will be presented at the end of Chapter 7.4 together with an estimate for the systematic uncertainties of this method.

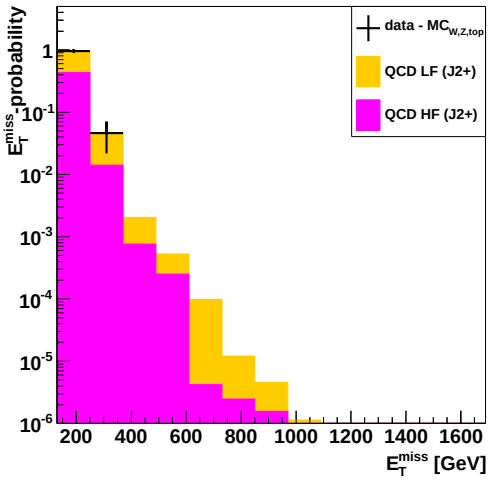

(a) $E_{\mathrm{T}}^{\mathrm{miss}}$ - probability for four-jet loose selection

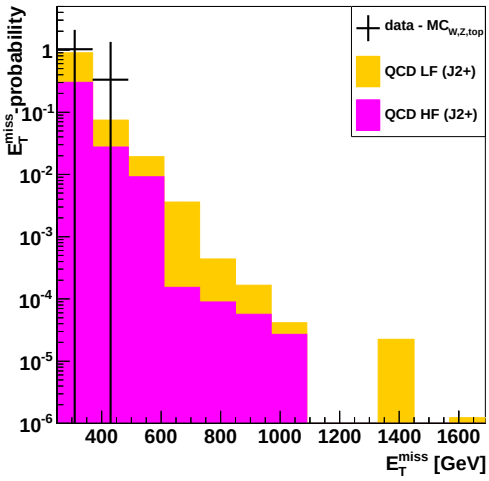

(b) $E_{\mathrm{T}}^{\mathrm{miss}}$ - probability for four-jet tight selection

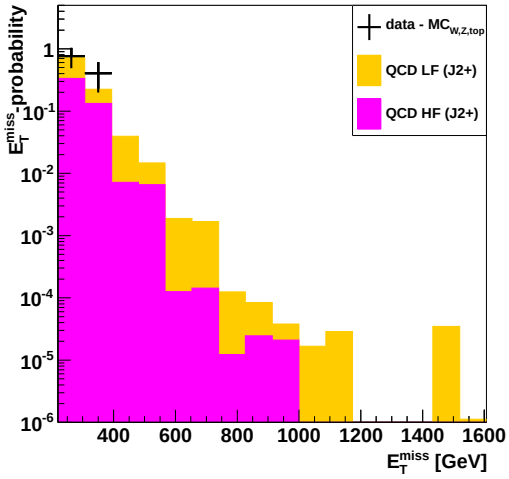

(c) $E_{\mathrm{T}}^{\mathrm{miss}}$ - probability for high-mass selection

Figure 7.5: The obtained $E_{\mathrm{T}}^{\mathrm{miss}}$ - probabilities for the four-jet and high-mass channels are shown. With these distributions being determined from data if possible, the QCD MC is shown for illustration only.

7.4 Systematics

This chapter is dedicated to systematic studies for the new method: firstly, the effects of the common systematics like the jet uncertainty scale, the jet energy resolution and pile up are discussed, secondly systematics special to the method such as fit uncertainties or the fit shapes are introduced.

common systematics JES, JRES, pile-up, theoretical uncertainties such as the HF- as well as the W, T, top cross-section uncertainties are treated in a complete analogous

way to the official analysis (see Section 6.4). $R_{\mathrm{QCD}}^{\mathrm{mod.}}$ is determined on the modified MC simulation instead of the nominal one, and the difference between the TF obtained with the nominal R_{QCD} and $R_{\mathrm{QCD}}^{\mathrm{mod.}}$ is quoted as systematic uncertainty. The impact of the common systematic uncertainties on the $E_{\mathrm{T}}^{\mathrm{miss}}$ -probability are only a sub-dominant effect and thus obtained in a different way (see below).

fit shape With the steeply falling ratios $R_{\mathrm{QCD}}\left(E_{\mathrm{T}}^{\mathrm{miss}}\right)$ not following any obvious functional form, the choice of the fit function may influence the outcome in a critical way. Thus, different fit-functions are tested and the differences between them are quoted as *shape uncertainty*. The main fit is performed with a Landau function (see Equation (7.4)), while Power-Law, convoluted with a polynomial of degree 1, serves as backup,

$$f_2(x) = (c_0 + c_1 \cdot x) \cdot x^{\alpha}. \tag{7.5}$$

Both fit functions lead to similar χ^2/NdF values of the order of one and describe the data equally well, whereas the fits with the Power-Law show some convergence problems in case of too low statistics in the high $E_{\mathrm{T}}^{\mathrm{miss}}$ regions, which however can be fixed by limiting the allowed parameter ranges.

fit uncertainty The fit uncertainties are estimated from the parameter uncertainties given by the fits numerically[1].

Let c_i be the parameter outcome of the fit f, w.l.o.g. be c_j the parameter of interest and σ_j its according error, then the derivative $\frac{\partial f}{\partial \sigma_i}(x)$ is estimated in a first step with $D(x, c_i, h)$, given by the *central difference formula* as

$$D(x, c_i, h) \approx \frac{f(x, c_i, \ldots, c_j + h, \ldots, c_n) - f(x, c_i, \ldots, c_j - h, \ldots, c_n)}{2 \cdot h}. \tag{7.6}$$

This estimate $D(x, c_i, h)$ is used as input for the final estimate

$$\frac{\partial f}{\partial \sigma_j}(x, c_i) \approx \frac{4 \cdot D(x, c_i, \sigma_j/2) - D(x, c_i, \sigma_j)}{3}, \tag{7.7}$$

which is combined to yield the total fit uncertainty σ_f

$$\sigma_f^2(x) \approx \sum_{i=0}^{n} \left(\sigma_i \cdot \frac{\partial f}{\partial \sigma_i}(x) \right)^2, \tag{7.8}$$

[1] The method is called Richardson extrapolation method [160], using two derivative estimates to calculate a more precise third approximation.

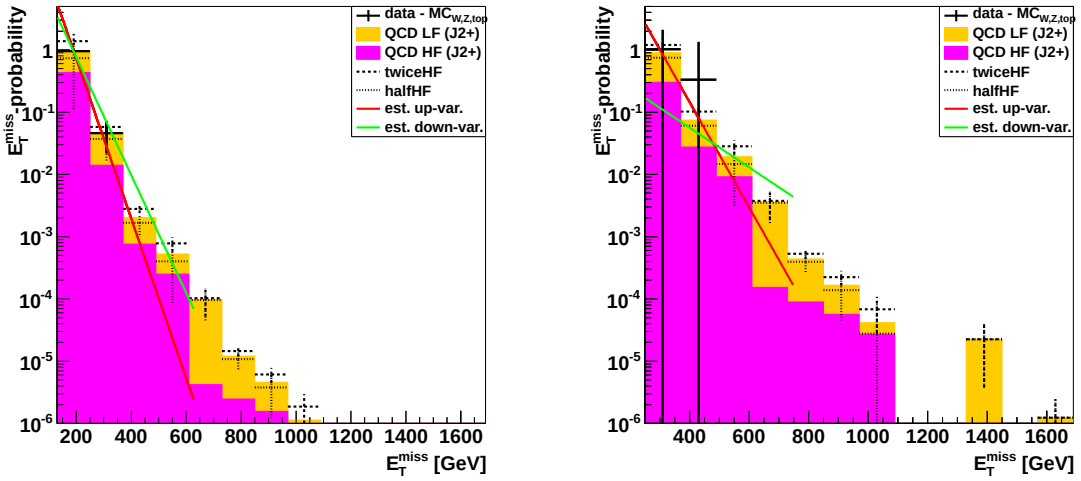

(a) $E_{\mathrm{T}}^{\mathrm{miss}}$ - probability for 4-jet loose selection **(b)** $E_{\mathrm{T}}^{\mathrm{miss}}$ - probability for 4-jet tight selection

Figure 7.6: The obtained $E_{\mathrm{T}}^{\mathrm{miss}}$ - probabilities for the 4-jet channel are shown for the loose (left), and tight (right) selection including its assumed shape uncertainties (red and green).

being then propagated to the TF calculation (see Equation (7.3)).

$E_{\mathrm{T}}^{\mathrm{miss}}$ -probability Fitted with an exponential function $e^{-\lambda x}$ to more easily model the dominant low-$E_{\mathrm{T}}^{\mathrm{miss}}$ end of the "$E_{\mathrm{T}}^{\mathrm{miss}}$"-probability distributions, an additional shape uncertainty is assigned conservatively via variation of the fit parameter $e^{-(\lambda \pm \sigma_\lambda)x}$. This accounts for the lowish statistics and the large uncertainties of the QCD MC, e.g. from the heavy-flavour component, which is well included in this estimate (see Figure 7.6 and Figure C.10).

7.5 Results

The results for the TFs including all systematic uncertainties are given in Table 7.1. The resulting estimated numbers of QCD events in the SRs are displayed in Table 7.2. Clearly the most dominant systematic uncertainties are those that arise from the shape of the fit-function and the variation of the W, Z, top component, yielding in total to errors of about 100%.

channel	SR	N_{SR}/N_{CR2}*	fit uncert.*	fit-shape*	METprob.*	JES*	JRES*	WZtop-cont.*	PileUp*
2-jet	A	3.41	± 0.13	± 2.69	$^{+0.36}_{-0.54}$	$^{+0.38}_{-0.64}$	± 0.00	$^{+2.68}_{-0.21}$	± 0.07
	rel. error in %	$(^{+112.65}_{-82.99})$	± 3.94	± 78.91	$^{+10.50}_{-15.93}$	$^{+11.11}_{-18.67}$	± 0.08	$^{+78.81}_{-6.21}$	± 1.97
3-jet	B	6.42	± 0.38	± 3.94	$^{+0.43}_{-0.54}$	$^{+1.30}_{-1.78}$	± 0.01	$^{+4.82}_{-1.55}$	± 0.16
	rel. error in %	$(^{+99.58}_{-72.38})$	± 5.97	± 61.40	$^{+6.65}_{-8.45}$	$^{+20.26}_{-27.72}$	± 0.12	$^{+75.16}_{-24.23}$	± 2.48
4-jet	C	56.82	± 7.18	± 4.59	$^{+3.00}_{-3.59}$	$^{+17.19}_{-23.57}$	± 0.63	$^{+54.69}_{-15.09}$	± 1.19
	rel. error in %	$(^{+102.16}_{-51.93})$	± 12.63	± 8.07	$^{+5.27}_{-6.32}$	$^{+30.26}_{-41.48}$	± 1.10	$^{+96.24}_{-26.56}$	± 2.09
4-jet	D	8.81	± 0.83	± 5.06	$^{+1.11}_{-1.92}$	$^{+2.85}_{-4.40}$	± 0.11	$^{+11.58}_{-2.51}$	± 0.21
	rel. error in %	$(^{+147.86}_{-84.68})$	± 9.45	± 57.38	$^{+12.58}_{-21.83}$	$^{+32.34}_{-49.94}$	± 1.24	$^{+131.42}_{-28.50}$	± 2.35
high-mass	E	40.67	± 15.61	± 1.54	$^{+4.10}_{-6.80}$	$^{+9.06}_{-7.34}$	± 1.77	$^{+13.46}_{-12.30}$	± 0.53
	rel. error in %	$(^{+56.59}_{-55.03})$	± 38.38	± 3.78	$^{+10.08}_{-16.72}$	$^{+22.28}_{-18.04}$	± 4.34	$^{+33.10}_{-30.25}$	± 1.30

Table 7.1: *TF* for the *summer 2011* analysis obtained with the new QCD method including statistical and systematic uncertainties. $(*) \cdot 10^{-3}$

channel	SR	$N_{SR,exp.}^{QCD}$ *	fit uncert.*	fit-shape*	METprob.*	JES*	JRES*	WZtop-cont.*	PileUp *
2-jet	A	9.29	± 0.37	± 7.33	$^{+0.98}_{-1.48}$	$^{+1.03}_{-1.73}$	± 0.01	$^{+7.32}_{-0.58}$	± 0.18
	rel. error in %	$(^{+112.65}_{-82.99})$	± 3.94	± 78.91	$^{+10.50}_{-15.93}$	$^{+11.11}_{-18.67}$	± 0.08	$^{+78.81}_{-6.21}$	± 1.97
3-jet	B	152.70	± 9.12	± 93.77	$^{+10.15}_{-12.91}$	$^{+30.93}_{-42.33}$	± 0.18	$^{+114.77}_{-36.99}$	± 3.79
	rel. error in %	$(^{+99.58}_{-72.38})$	± 5.97	± 61.40	$^{+6.65}_{-8.45}$	$^{+20.26}_{-27.72}$	± 0.12	$^{+75.16}_{-24.23}$	± 2.48
4-jet	C	15783.98	± 1993.60	± 1274.11	$^{+832.38}_{-997.51}$	$^{+4775.66}_{-6547.89}$	± 173.72	$^{+15190.93}_{-4191.66}$	± 329.70
	rel. error in %	$(^{+102.16}_{-51.93})$	± 12.63	± 8.07	$^{+5.27}_{-6.32}$	$^{+30.26}_{-41.48}$	± 1.10	$^{+96.24}_{-26.56}$	± 2.09
4-jet	D	28.21	± 2.67	± 16.19	$^{+3.55}_{-6.16}$	$^{+9.12}_{-14.09}$	± 0.35	$^{+37.08}_{-8.04}$	± 0.66
	rel. error in %	$(^{+147.86}_{-84.68})$	± 9.45	± 57.38	$^{+12.58}_{-21.83}$	$^{+32.34}_{-49.94}$	± 1.24	$^{+131.42}_{-28.50}$	± 2.35
high-mass	E	565.67	± 217.11	± 21.36	$^{+57.05}_{-94.59}$	$^{+126.03}_{-102.07}$	± 24.56	$^{+187.26}_{-171.09}$	± 7.36
	rel. error in %	$(^{+56.59}_{-55.03})$	± 38.38	± 3.78	$^{+10.08}_{-16.72}$	$^{+22.28}_{-18.04}$	± 4.34	$^{+33.10}_{-30.25}$	± 1.30

Table 7.2: Expected N_{SR}^{QCD} for the *summer 2011* analysis obtained with the new QCD method including statistical and systematic uncertainties. $(*) \cdot 10^{-3}$

This new approach shows some clear advantages over the previous, mainly MC-based methods: the reversed $\Delta\varphi$ cut (see Table 6.6 and Table 6.7) and the reversed $E_{\mathrm{T}}^{\mathrm{miss}}/M_{\mathrm{eff}}$ cut (see Table 6.10). While the later does not even provide an estimate for SR-E, the former's results mostly cannot be trusted because of the troubles concerning the lowish statistics and pile-up reweighting. Apart from that, the previous methods and the new approach produce similar results, while not showing any severe intrinsic problems of the above type.

Compared to the baseline method (see Table 6.4), however, both the central values and the estimated uncertainties agree reasonably well within the quoted uncertainties, which is a nice confirmation of the baseline approach.

Chapter 8

The complete 2011 analysis with 4.7 fb^{-1}

This Chapter presents the results of applying the new QCD background estimation method on the complete 2011 dataset of 4.7 fb^{-1}. Section 8.1 provides a short summary of the relevant introductory paragraphs of the according publications (see below), as the differences compared to the previous analysis are small.

The outcome of the new QCD background estimation technique, as introduced in the previous Chapter, is compared to the results of the baseline jet-smearing method. The new background estimation technique represents the work of the author and was published in the Moriond 2012 Conference-Note and supporting documentation [11, 12] and (with minor modifications) in a second paper and supporting documentation [13, 14].

8.1 Differences to the previous analysis

The main differences between the updated full hadronic SUSY search, targeted at Moriond 2012, and the previous *summer 2011* analysis [9, 10] are presented in the following:

- This analysis is run over the complete 2011 dataset, corresponding to an integrated luminosity of 4.7 fb^{-1} after application of basic data quality criteria.
- The sensitivity is mainly extended by including additional signal regions from channels with higher jet multiplicities (up to 6 jets), targeted at models with long cas-

cade decay chains dominantly from $\tilde{g}$ production. Hence the QCD suppression strategy, mainly the $\Delta\varphi$ cut, has also been revised.

- The LAr hole, affecting data taking periods E onwards, is now included in the MC simulation. The η-ϕ based 'LAr hole veto' used for the *summer 2011* analysis is replaced with a 'smart veto' providing a better performance. Control distributions from events potentially affected by the hole were studied closely both on the MC simulation and the data. As good agreement was found and the overall fraction of the data sample affected decreased after a partial fix, there is no further need to distinguish between events with jets in the vicinity of the hole and elsewhere, as was done e.g. by the jet-smearing QCD estimate.

- The trigger thresholds of the lowest unprescaled trigger are increased: the plateau is reached for events containing $E_{\mathrm{T}}^{\mathrm{miss}} > 160$ GeV and leading jet-$p_{\mathrm{T}} > 130$ GeV, yielding to a trigger efficiency of $\geq 98\,\%$.

- The p_{T} threshold of the muon veto has been reduced to 10 GeV (instead of 20 GeV as for the *summer 2011* analysis).

- With the transfer factors and related uncertainties mainly estimated from the MC simulation, a lack of statistics in the simulation and the thus resulting presence of large statistical fluctuations were the dominant source of uncertainty in the *summer 2011* analysis. Therefore, the Monte Carlo samples of the new mc11b/c production (see below) possess a significantly increased equivalent luminosity.

- The new analysis distinguishes between main backgrounds, those expected to contribute at least 20% of the total background in each signal region, and minor backgrounds ($\lesssim 20\%$). While the M_{eff} cut on the control regions of minor backgrounds can still be lowered to maximize the statistics, the M_{eff} selection of main backgrounds must be identical for the signal and control regions to reduce uncertainties.

- The `ALPGEN` W+jets, Z+jets and $t\bar{t}$+jets distributions in all cases are scaled by factors of respectively 0.75, 0.78 and 0.73 with respect to the raw normalisation by cross-section times luminosity. This is believed to be due to `ALPGEN` generating a harder p_{T} spectrum than data for at least Z and W bosons. Hence the hard cuts on $E_{\mathrm{T}}^{\mathrm{miss}}$ and $E_{\mathrm{T}}^{\mathrm{miss}}/M_{\mathrm{eff}}$ in this analysis were causing the MC distributions to overshoot the data. The scaling factors are within the expected range of the systematic uncertainties and are determined by normalisation to all data (i.e. without any M_{eff} cut) in CR3, CR1b and CR4 respectively in channel A (i.e. di-jet events).

- With the increase of the available dataset, the signal regions for a 3σ observation and 95% CL exclusion were optimized, especially concerning the tight selection, where both sufficient statistics for the main backgrounds is needed in the control regions (the same M_{eff} cut is chosen to minimise the systematic uncertainties) as well as a good discovery reach in a wide range of SUSY model parameter spaces.
- The QCD jet-smearing estimate uses binned distributions (both in η and p_{T}) for the 'dijet balance' and 'Mercedes' analysis to estimate the response function and related uncertainties. Furthermore, the systematic uncertainties of this method are better understood.
- The method to cross-check the QCD background estimate is improved: The purely MC-based method using a reversed $\Delta\varphi$ cut and the semi-data-driven approach using a reversed $E_{\text{T}}^{\text{miss}}/M_{\text{eff}}$ cut, suffering severely from lowish statistics and the pile-up reweighting in the previous analyses, are replaced with the new technique as introduced in Chapter 7 in order to increase the reliability and to weaken the problems especially with the poor (QCD) MC statistics.

8.1.1 Data and Monte Carlo samples

Data

The complete 2011 ATLAS raw data were recorded over the period 22$^{\text{nd}}$ March 2011 – 30$^{\text{th}}$ October 2011, corresponding to runs 178044 to 191933 (data-taking periods B2 – M10). Period C was excluded due to reduced $\sqrt{s}$. The former analysis used a subset of this sample, periods B2 – H4, corresponding to runs 178044 to 184169, providing an integrated luminosity of roughly 1 fb^{-1}.
While the peak instantaneous luminosity increased from 1.3×10^{30} to 3.6×10^{33} cm^{-2}s^{-1}, the peak mean number of interactions per bunch crossing increased from 2.6 to 17.5. The raw recorded data corresponds to an integrated luminosity of 5.25 fb^{-1}, falling to 4.7 fb^{-1} after application of basic data quality requirements via the SUSY working group Good Run List [1] (see Figure 5.1). The uncertainty on the luminosity decreased to 3.9%.

All AODs from official productions are converted into SUSYD3PDs using the SUSYD3PDMaker package [148]. This is done using the ATLAS production system corre-

[1] The official GRL for 2011 data for Moriond2012 (`data11_7TeV.periodAllYear_DetStatus-v36-pro10_CoolRunQuery00-04-08_Susy.xml`) is used.

sponding to tag p832. The final offline analysis is done with a self-written ROOT-based framework and extensively cross-checked and validated against official numbers.

Monte Carlo samples

The MC samples used are very similar to those from the *summer 2011* analysis (see Section 5.2 and Appendix A), however, these new sets are produced using the ATLAS `GEANT4` [73] based detector simulation [161] in combination with the default ATLAS `MC11b` (`pythia8` pile-up) or `MC11c` (`pythia6` pile-up) parameter sets [162–164]. With pile-up conditions differing as a function of the instantaneous luminosity of the LHC machine, events are reweighted according to the mean number of interactions expected. A complete list of the MC samples used in this analysis can be found in Appendix B.

8.1.2 Event selection

The motivation and strategy of the ongoing search for SUSY particles is identical to the previous analyses, defined mostly by cuts on M_{eff} and $E_{\text{T}}^{\text{miss}}$. Expecting two- to four-jet events from decaying $\tilde{q}\tilde{q}$, $\tilde{q}\tilde{g}$ and $\tilde{g}\tilde{g}$ pairs, the final state jet multiplicity can be further increased by cascade decays of heavy particles. Therefore, new signal regions and additional channels are defined, the higher jet-multiplicities targeting especially at those long decay-chains and $\tilde{g}$ pair production, the lower ones at $\tilde{q}$ pair production with short decay chains.

An overview about the selection is given in Table 8.1. Cuts $3a$ to 5 define the cleaning cuts, i.e. quality selection criteria for suppression of detector noise and non-collision backgrounds. Five analysis channels, labelled A - E, are defined by increasing jet multiplicity (two to six), whereas the two-jet channels are split further into A and A' using the ratio of $E_{\text{T}}^{\text{miss}}/M_{\text{eff}}$. Irrespective of the visibility of the sparticle decay products, channel A' may use the presence of initial state radiation jets to tag signal events and thus improves the sensitivity to models with small sparticle mass splittings. When extending the $\Delta\varphi^{min}\left(jet, \vec{P}_{\text{T}}^{\text{miss}}\right)$ cut (cut 14) to higher jet multiplicities, a good trade-off between QCD background suppression and keeping high signal efficiency was sought: on the leading three jets a tight cut of $\Delta\varphi^{min} > 0.4$ is imposed and a looser cut ($\Delta\varphi^{min} > 0.2$) on all additional jets with $p_{\text{T}} > 40$ GeV. The QCD CR, however, is still defined by reversing the $\Delta\varphi$ cut ($\Delta\varphi^{min} < 0.2$).

Cut	Description	Channel					
		A	A'	B	C	D	E
1	DQ (data)	Run / lumi block appears in SUSY GRL `data11_7TeV.periodAllYear_DetStatus-v36-prod10_CoolRunQuery-00-04-08_Susy.xml`					
2	Trigger	EF_j75_a4_EFFS_xe45_loose_noMu (data period B) / EF_j75_a4tc_EFFS_xe45_loose_noMu (K $\geq$ data period $\geq$ D) / EF_j75_a4tc_EFFS_xe55_noMu (data period $\geq$ L) / None (MC)					
3a	*EvC* jets (data)	No Looser bad jets after jet-lepton overlap removal with $p_{\mathrm{T}} > 20$ GeV and any η					
3b	*EvC* jets (data and MC)	Reject if leading up to 2 selected jets with $p_{\mathrm{T}} > 100$ GeV after overlap removal possess (chf < 0.02 and $\lvert\eta\rvert < 2.0$) or (chf < 0.05 and emf > 0.9 and $\lvert\eta\rvert < 2.0$)					
3c	*EvC* jet timing	Energy-weighted mean time of leading N selected jets after overlap removal in N jet analysis $\lvert\langle t\rangle\rvert < 5$ ns.					
3d	*EvC* LAr hole	'Smart' LAr hole veto					
3e	*EvC* cosmics	No selected muons after overlap removal with (fabs(mu_staco_z0_exPV) ≥ 1) or (fabs(mu_staco_d0_exPV) ≥ 0.2)					
3f	*EvC* bad muon veto	No selected muons before overlap removal with sqrt(mu_staco_cov_qoverp_exPV)/fabs(mu_staco_qoverp_exPV) ≥ 0.2					
3g	*EvC MET_MUON*	Veto event if $(MET\_MUON/E_{\mathrm{T}}^{\mathrm{miss}}) \times \cos(MET\_MUON\_phi - MET\_phi) > 0.5$					
3h	*EvC* bad tile drawers	Veto event if any selected jet with $p_{\mathrm{T}} > 40$ GeV and $BCH\_CORR\_JET > 5\%$ satisfies $\Delta\varphi < 0.2$					
3i	*EvC MET_CellOut*	Veto event if $(MET\_CellOut/E_{\mathrm{T}}^{\mathrm{miss}}) \times \cos(MET\_CellOut\_phi - MET\_phi) > 0.5$					
4	*EvC* LAr (data)	LArError == 0					
5	*EvC* Prim. vtx.	Leading primary vertex with > 4 tracks					
6	Lepton veto	No selected e/μ after overlap removal with $p_{\mathrm{T}} > 20/10$ GeV.					
7	$E_{\mathrm{T}}^{\mathrm{miss}}$ [GeV] $>$	160					
8	$p_{\mathrm{T}}(j_1)$ [GeV] $>$	130					
9	$p_{\mathrm{T}}(j_2)$ [GeV] $>$	60	60	60	60	60	60
10	$p_{\mathrm{T}}(j_3)$ [GeV] $>$	–	–	60	60	60	60
11	$p_{\mathrm{T}}(j_4)$ [GeV] $>$	–	–	–	60	60	60
12	$p_{\mathrm{T}}(j_5)$ [GeV] $>$	–	–	–	–	40	40
13	$p_{\mathrm{T}}(j_6)$ [GeV] $>$	–	–	–	–	–	40
14	$\Delta\varphi >$	0.4 ($i = \{1, 2, (3)\}$)			0.4 ($i = \{1, 2, 3\}$), 0.2 ($p_{\mathrm{T}} > 40$ GeV jets)		
15	$E_{\mathrm{T}}^{\mathrm{miss}}/M_{\mathrm{eff}}(Nj) >$	0.3 (2j)	0.4 (2j)	0.25 (3j)	0.25 (4j)	0.2 (5j)	0.15 (6j)
16	M_{eff}(incl.) [GeV] $>$	1900/1400/–	–/1200/–	1900/–/–	1500/1200/900	1500/–/–	1400/1200/900

Table 8.1: Cleaning and SR-defining cuts for each of the channels in the analysis [11–14]. SRs are defined by the last cut on M_{eff} (incl.), denoting the 'tight', 'medium' and 'loose' selections where available. Note that M_{eff} constructed from the leading N jets is used in the $E_{\mathrm{T}}^{\mathrm{miss}}/M_{\mathrm{eff}}$ cut for the N jet analysis while M_{eff} constructed from all jets with $p_{\mathrm{T}} > 40$ GeV is used for the final M_{eff} selection. *EvC* denotes cuts motivated by event cleaning.

CR	SR Background	CR process	CR selection
CR1a	$Z(\to\nu\nu)$+jets	γ+jets	Isolated photon
CR1b	$Z(\to\nu\nu)$+jets	$Z(\to\ell\ell)$+jets	$\lvert m(\ell,\ell) - m(Z)\rvert < 25$ GeV
CR2	QCD jets	QCD jets	Reversed $\Delta\varphi$ cut
CR3	$W(\to\ell\nu)$+jets	$W(\to\ell\nu)$+jets	30 GeV $< m_T(\ell, E_{\mathrm{T}}^{\mathrm{miss}}) <$ 100 GeV, b-veto
CR4	$t\bar{t}$ and single-t	$t\bar{t}\to bbqq'\ell\nu$	30 GeV $< m_T(\ell, E_{\mathrm{T}}^{\mathrm{miss}}) <$ 100 GeV, b-tag

Table 8.2: Control Regions used in the analysis, indicating the main SR background targeted, the process used to model the background, and main CR cut(s) used to select this process [11–14].

The dominant background processes, yielding to a significant amount of events in the SRs, are still W+jets, Z+jets, top quark pair, single top quark, and multi-jet production with the focus shifting slightly to top events of any kind.
Each of the eleven SRs possesses five orthogonal CRs, creating uncorrelated data samples enriched in the particular background sources (see Table 8.2), adding up to a total number of 55 CRs.

Coherently normalized Standard Model background expectations in the SRs are obtained with a likelihood fit, enabling CR contamination by other Standard Model backgrounds and/or possible SUSY signals, through the use of TFs (see Section 2.7.4), connecting SR background estimates to the measurements obtained in the individual CRs (see Section 9.2).

8.2 Control plots

In order to gain confidence in the new QCD estimation technique providing reasonable values, key distributions of its attached control regions, i.e. the region with the reversed $\Delta\varphi$ cut for low to medium $E_{\mathrm{T}}^{\mathrm{miss}}$ values and the reversed $E_{\mathrm{T}}^{\mathrm{miss}}/M_{\mathrm{eff}}$ region at high $E_{\mathrm{T}}^{\mathrm{miss}}$ values, need to be checked for any obvious discrepancies.

The obtained scaling factors for `ALPGEN` W+jets, Z+jets and $t\bar{t}$+jets distributions of 0.75, 0.78 and 0.73 respectively (with respect to the raw normalisation by cross-section times luminosity) are applied to all subsequent distributions, in order to improve the

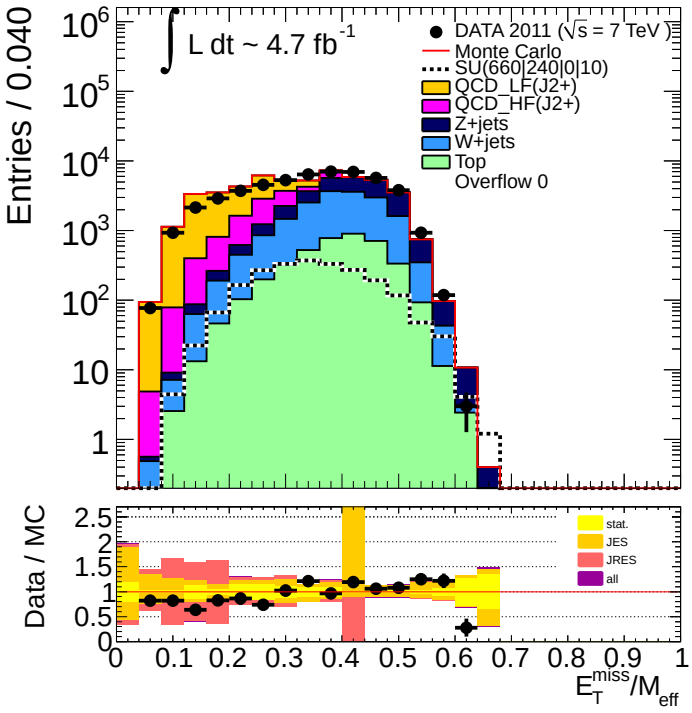

Figure 8.1: Distribution of $E_{\mathrm{T}}^{\mathrm{miss}}$ $/M_{\mathrm{eff}}$ in the two-jet prime channel prior to cut 14: Applying the tightened cut on $E_{\mathrm{T}}^{\mathrm{miss}}$ $/M_{\mathrm{eff}}>$ 0.4, the available phase-space for QCD is drastically reduced to a rare region, which is not anymore populated by events in the QCD MC simulation due to statistics reasons.

agreement with the data. These scaling factors are within the expected range of the systematic uncertainties.

The control plots for the reversed $\Delta\varphi$ control regions in the five-jet channel for $E_{\mathrm{T}}^{\mathrm{miss}}$ values above 160 GeV are shown in Figure 8.2, while the other five channels are presented in Appendix D.1. In general, the distributions show a good agreement between the data and the MC simulation, with all MC samples being normalized according to their cross-sections (only the QCD MC has an additional k-factor of 1.06 applied, based on the $E_{\mathrm{T}}^{\mathrm{miss}}$ -distribution from a two-jet selection applying a reversed $\Delta\varphi$ cut). The two-jet prime channel, however, shows some problems (see Figure D.2). The tightened cut on $E_{\mathrm{T}}^{\mathrm{miss}}$ $/M_{\mathrm{eff}}>$ 0.4 (see Figure 8.1) reduces the available phase-space region for QCD drastically in such a way, that it is not anymore populated by events in the QCD MC simulation due to statistics reasons. This causes a large discrepancy between the data and the MC simulation in the QCD-dominated regions, where the appropriate QCD events are missing from the QCD MC simulation (due to a lack of statistics). The deficit does affect any analysis which relies on the event counts of simulated QCD events

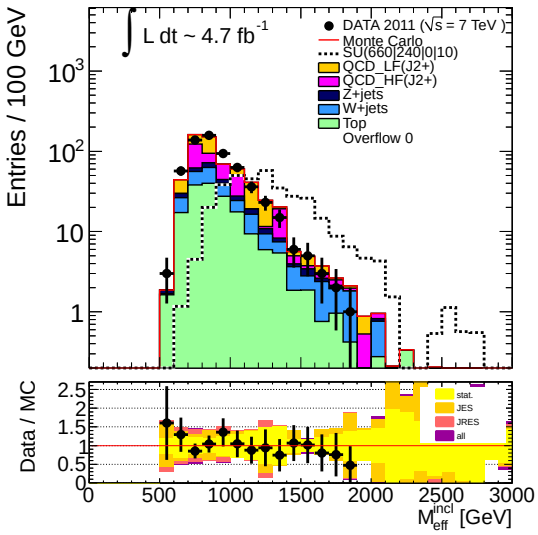

(a) Effective mass M_{eff} (incl.)

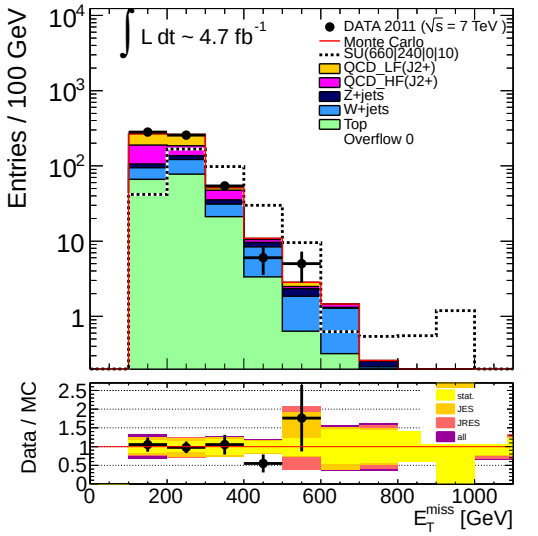

(b) Missing transverse energy

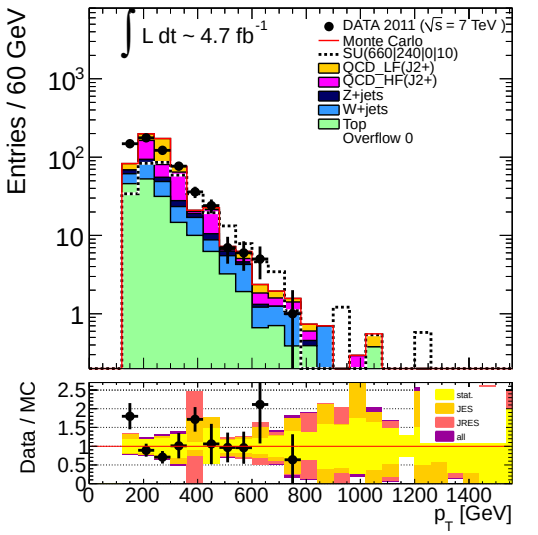

(c) Leading jet p_{T}

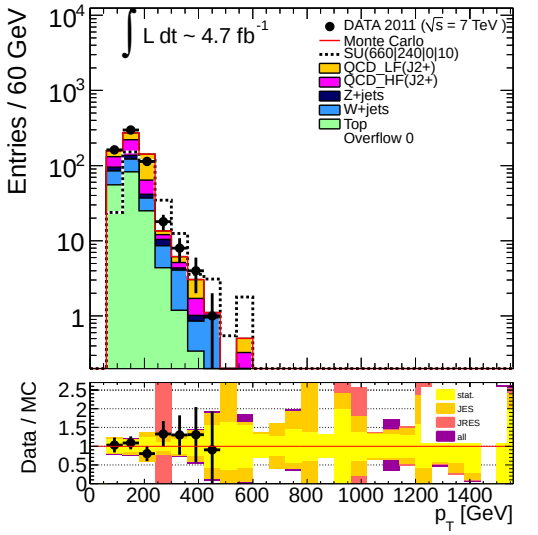

(d) Sub-leading jet p_{T}

Figure 8.2: Distributions for the reversed $\Delta\varphi$ control region for the five-jet channel: $M_{\text{eff}}^{\text{incl}}$, $E_{\text{T}}^{\text{miss}}$, leading and sub-leading jet p_{T} are shown prior to the final cut on M_{eff}. The MC simulation describes the data quite good.

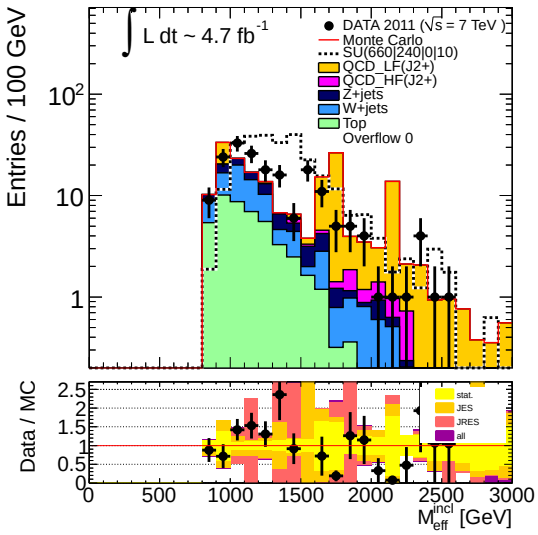

(a) Effective mass M_{eff} (incl.)

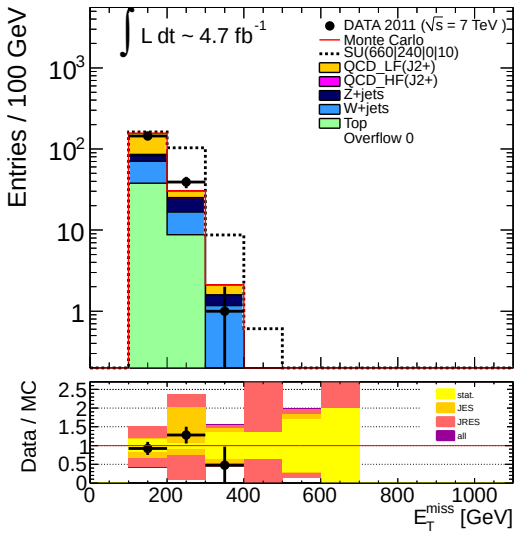

(b) Missing transverse energy

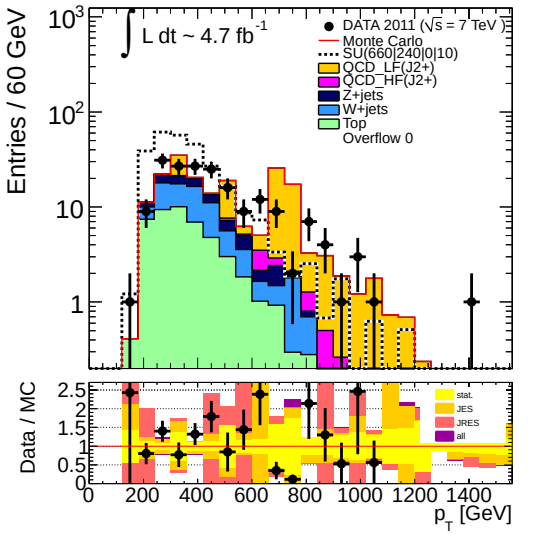

(c) Leading jet p_{T}

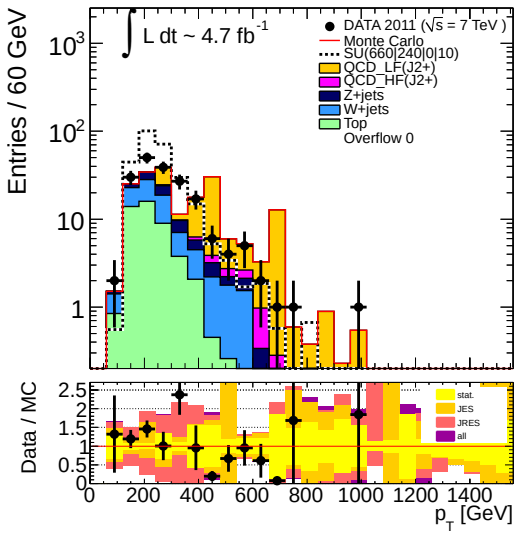

(d) Sub-leading jet p_{T}

Figure 8.3: Effective mass (incl.), missing transverse energy, leading and sub-leading jet-p_{T} distributions for the five-jet channel with reversed $E_{\text{T}}^{\text{miss}}$ /M_{eff} cut (prior to the final M_{eff} cut). Besides the low statistics (especially QCD MC), the simulation describes the data well.

in the SRs, such as the QCD estimation methods which were used as backup in the *summer 2011* analysis. In contrast, it does not affect the new technique which uses the QCD MC simulation predominantly for illustration reasons only (besides the $E_{\mathrm{T}}^{\mathrm{miss}}$ -probability estimate, where the shape of the QCD MC distributions is used as backup solution in case of too low data statistics). Certainly, the issue at hand confirms the need for developing a new QCD estimation technique.

The plots for the reversed $E_{\mathrm{T}}^{\mathrm{miss}}$ $/M_{\mathrm{eff}}$ CR are displayed in Figure 8.3 (five-jet channel, the other channels can be found in Appendix D.2). Good agreement between the data and the MC simulation is found.

8.2.1 The $E_{\mathrm{T}}^{\mathrm{miss}}$ -intervals

The low-$E_{\mathrm{T}}^{\mathrm{miss}}$ control region is still selected using the jet-component of the official combined jet + $E_{\mathrm{T}}^{\mathrm{miss}}$ trigger: this single-jet trigger, possessing a threshold of 75 GeV at the highest trigger level, yields an integrated luminosity of only 5.6 pb^{-1} in total for the complete 2011 dataset due to its high prescaling.

Figure 8.4 shows the distribution of $\Delta\varphi^{min}$ after the $E_{\mathrm{T}}^{\mathrm{miss}}$ -cut (prior to cut 14) for different $E_{\mathrm{T}}^{\mathrm{miss}}$ -intervals in different channels, from 50 GeV to 60 GeV and from 100 GeV to 120 GeV. All MC samples are normalized according to their cross-sections, and the QCD MC has an additional k-factor of 0.84 applied, based on the $E_{\mathrm{T}}^{\mathrm{miss}}$ -distribution from a two-jet selection applying a reversed $\Delta\varphi$ cut. With `PYTHIA` MC being only LO, the normalization of the `PYTHIA` QCD samples is a priori not expected to match the data.The large discrepancy in the QCD k-factor, however, is a result of the lower $E_{\mathrm{T}}^{\mathrm{miss}}$ -cut (40 GeV instead of 160 GeV), selecting a different phase-space region.
The plots are taken from different channels, but without the signal region cuts 14 - 16. Due to the problems discussed in Section 7.3, the two lowest `PYTHIA` QCD samples, $J0$ and $J1$, are excluded. The shape of the $\Delta\varphi$ -distributions, both for the QCD enriched and the suppressed region, differs as function of jet multiplicity and $E_{\mathrm{T}}^{\mathrm{miss}}$ as expected and the simulation is in general describing the data, besides the poor statistics, well.

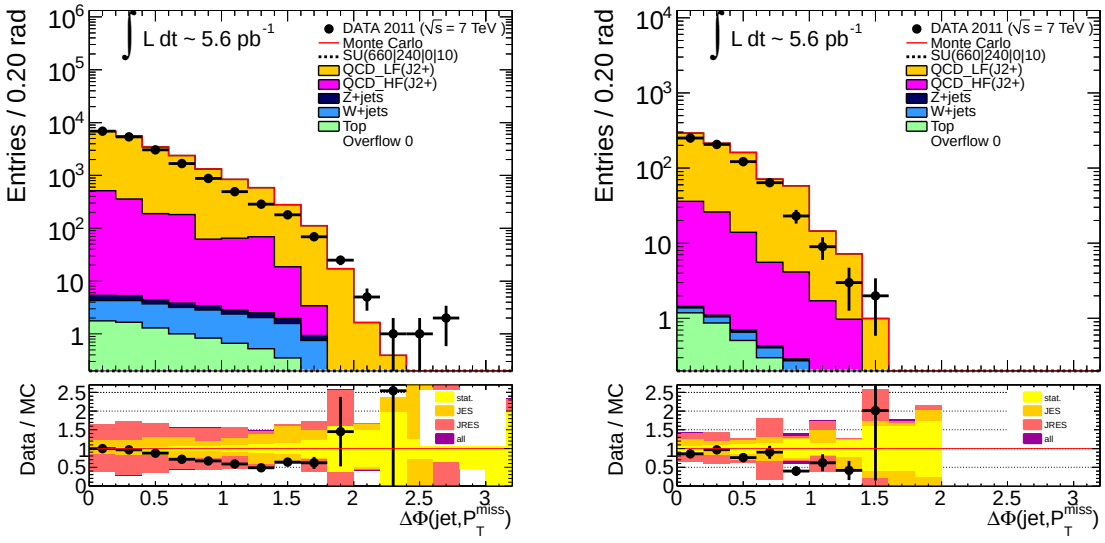

(a) two-jet channel: $50 < E_{\mathrm{T}}^{\mathrm{miss}} < 60$

(b) four-jet channel: $50 < E_{\mathrm{T}}^{\mathrm{miss}} < 60$

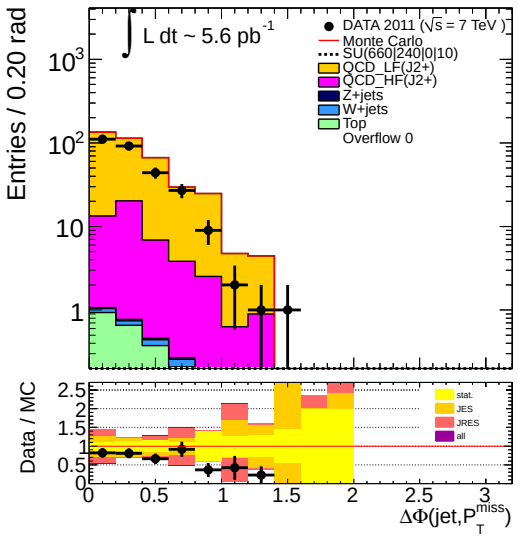

(c) five-jet channel: $50 < E_{\mathrm{T}}^{\mathrm{miss}} < 60$

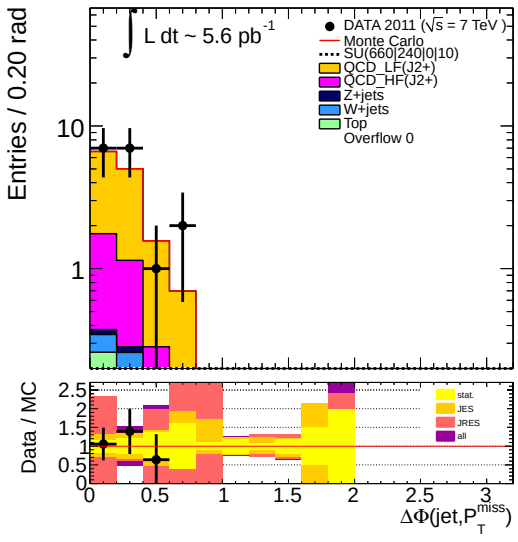

(d) five-jet channel: $100 < E_{\mathrm{T}}^{\mathrm{miss}} < 120$

Figure 8.4: $\Delta\varphi$ -distributions for different $E_{\mathrm{T}}^{\mathrm{miss}}$ -intervals and different channels (two-, four- and five-jet channel): $E_{\mathrm{T}}^{\mathrm{miss}}$ ϵ [50;60[GeV and $E_{\mathrm{T}}^{\mathrm{miss}}$ ϵ [100;120[GeV: As expected, not only shows $\Delta\varphi$ a dependence on the jet-multiplicity, but also a clear dependence on $E_{\mathrm{T}}^{\mathrm{miss}}$.

8.2.2 R_{QCD}

In the following paragraphs, the plots are taken from the four- and five-jet channel for illustration. The full set can be found in the Appendix D.3. All conclusions drawn and results obtained hold for the other channels as well.

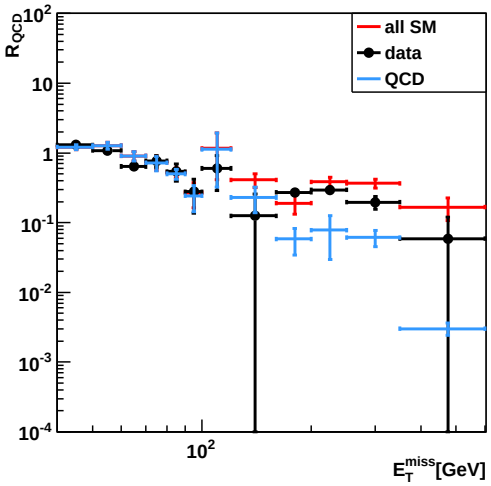

(a) four-jet channel: uncorrected

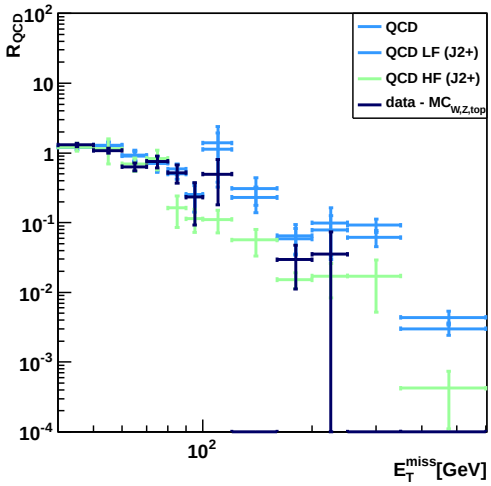

(b) four-jet channel: without contamination

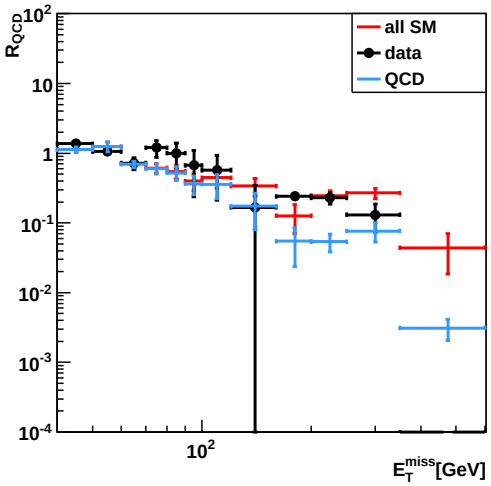

(c) five-jet channel: uncorrected

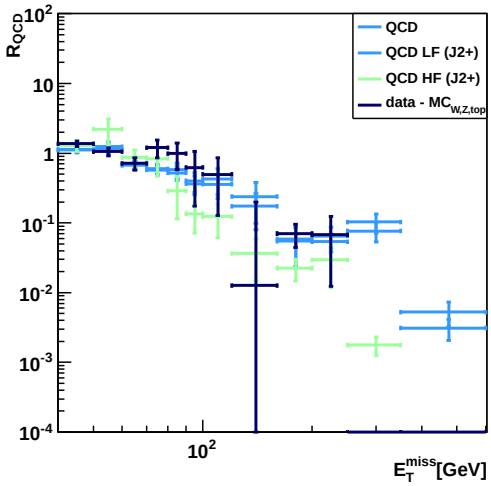

(d) five-jet channel: without contamination

Figure 8.5: R_{QCD} in the four-jet channel *(upper row)* and the five-jet channel *(lower row)*, before *(left column)* and after *(right column)* correction for contamination by non-QCD processes: the overall agreement between all Standard Model MC and data is fine, while $data - MC_{W,Z,top}$ compares well to the QCD MC prediction. Errors are of statistical nature only.

After selecting the events according to step (1-3), the obtained ratios in all six channels (four- and five-jet channel see Figure 8.5, the remaining channels see Figure D.11 and Figure D.12) show a good agreement between data and the Standard Model MC. R_{QCD} is still steeply falling with increasing $E_{\mathrm{T}}^{\mathrm{miss}}$, and both the agreement with the QCD MC is confirmed as well as the agreement between light- and heavy-flavour QCD within the large uncertainties.

8.2.3 Extrapolation into the Signal Regions

The fitting procedure has been improved compared to the previous approach:

- Additional fit functions are considered:

$$f_3(x) = c \cdot \mathrm{BreitWigner}(x, \mu, \gamma), \tag{8.1}$$

$$f_4(x) = \mathrm{CrystalBall}(x, \alpha, n, \mu, \sigma, N) \tag{8.2}$$

$$\equiv N \cdot \begin{cases} \exp\left(-\frac{(x-\mu)^2}{2\sigma^2}\right), & \text{for } \frac{(x-\mu)}{\sigma} > -\alpha \\ A \cdot \left(B - \frac{x-\mu}{\sigma}\right)^{-n}, & \text{for } \frac{(x-\mu)}{\sigma} \leq -\alpha \end{cases} \tag{8.3}$$

$$\text{with } A = \left(\frac{n}{|\alpha|}\right)^n \cdot \exp\left(-\frac{|\alpha|^2}{2}\right) \text{ and } B = \frac{n}{|\alpha|} - |\alpha|\,. \tag{8.4}$$

Although the four different functions in principle being capable of describing the R_{QCD}-shape in an acceptable way (as can be demonstrated on the QCD-MC samples, see Figure 8.6) for an example, yielding to χ^2 values around one, the Power-law (f_2, see Equation (7.5)) and the CrystalBall function (f_4, see Equation (8.2)) encounter problems to describe the $data - MC_{W,Z,top}$ in the higher $E_{\mathrm{T}}^{\mathrm{miss}}$ -region when both fit-functions are under-determined due to the lowish data statistics. Narrowing down the available parameter space of the fits, one can indeed compensate this deficiency and force both fitting functions to describe the data and to converge in an acceptable way. Nevertheless, the preference in this analysis is given to the two remaining functions, which describe the data equally well, but do not need the manual intervention. While the Landau-function is still used as main choice for the fitting, the Power-Law, used as backup-function to estimate the systematic uncertainties of the fit shape before, is switched in favour of the BreitWigner (f_3, see Equation (8.1)).

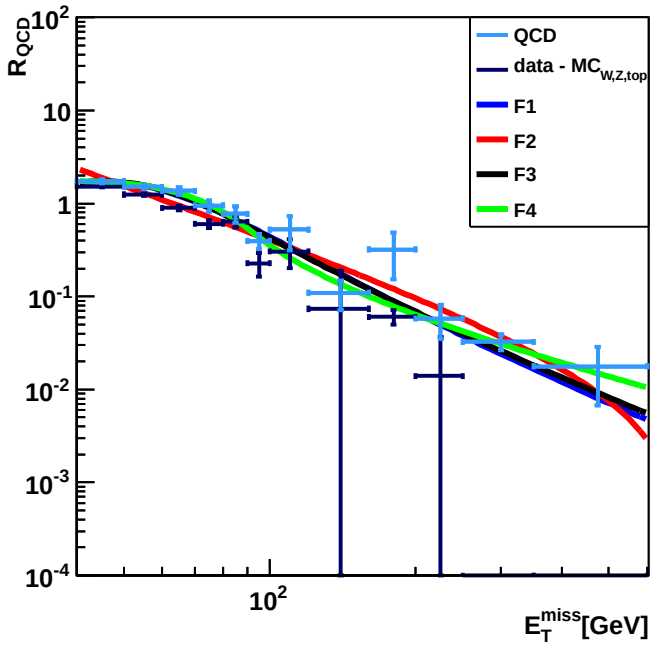

Figure 8.6: R_{QCD}, determined from the three-jet channel of the QCD MC, is fitted with the different fit functions: Landau (blue), Power-Low (red), BreitWigner (black) and CrystallBall (green). All functions are technically capable of describing the QCD MC graph well, yielding to χ^2/N_{df} values of 1.3, 3.8, 1.3 and 0.78 respectively.

- The estimation of the actual fit-uncertainty is no longer based on the uncertainties quoted by the fitting routine.Instead, a large number of toy-MCs are generated from the original distributions, assuming simple one-σ Gaussian errors on the data points, each analyzed separately with a fit and yielding in combination with the $E_{\mathrm{T}}^{\mathrm{miss}}$ -probabilities to an estimate for the TFs. The distribution of quantity of interest is fitted with a Gaussian function, and the extracted width is quoted as uncertainty on the individual fits.

The fits of the ratios, used in order to extrapolate into the signal regions at higher $E_{\mathrm{T}}^{\mathrm{miss}}$ -values, are shown in Figure 8.7. While the four different functions are shown together, only the Landau- and the BreitWigner function are used to calculate the results, the difference between both is taken as systematic error.

8.2.4 $E_{\mathrm{T}}^{\mathrm{miss}}$ -probabilities

The $E_{\mathrm{T}}^{\mathrm{miss}}$ -probabilities (step 6) are extracted by applying the full event selection with only one minor modification: the $\Delta\varphi$ -cut is reversed to ensure no contamination from

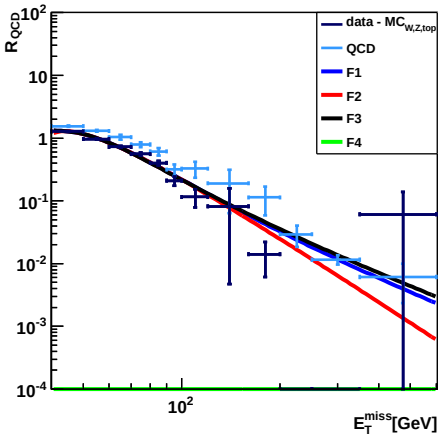

(a) two-jet channel

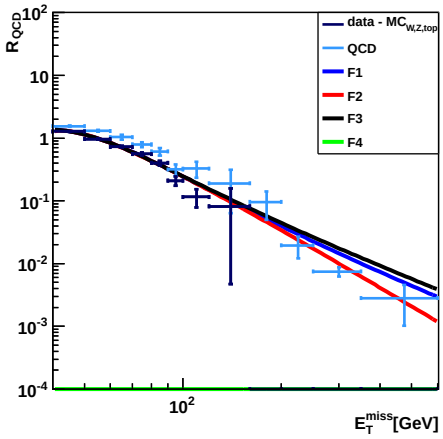

(b) two-jet prime channel

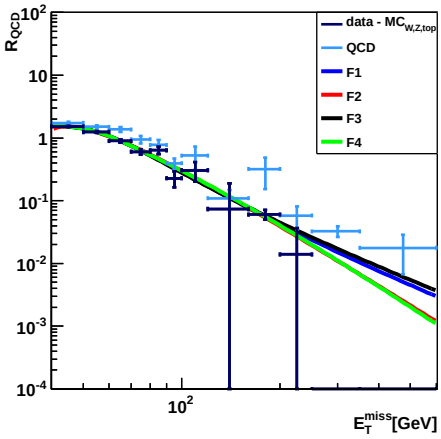

(c) three-jet channel

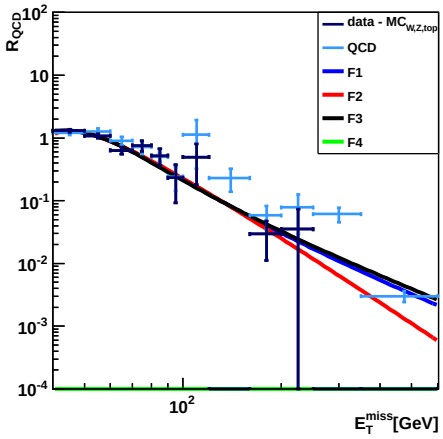

(d) four-jet channel

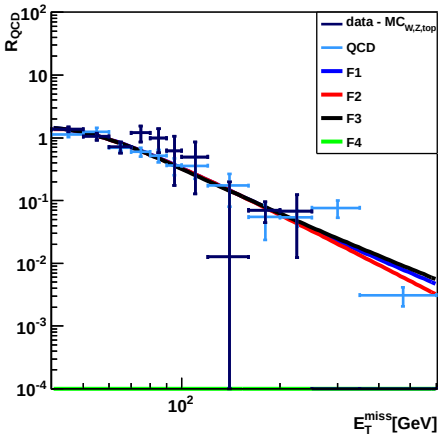

(e) five-jet channel

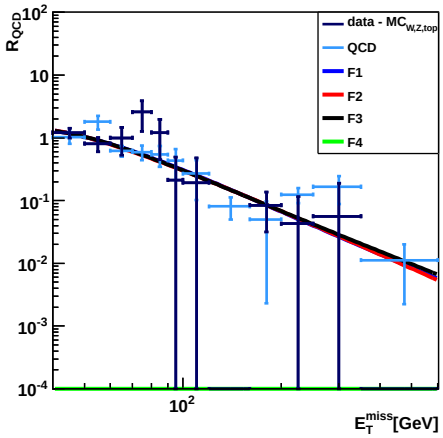

(f) six-jet channel

Figure 8.7: R_{QCD}, determined from $data - MC_{W,Z,top}$, is fitted for the different channels of the *complete 2011* analysis.

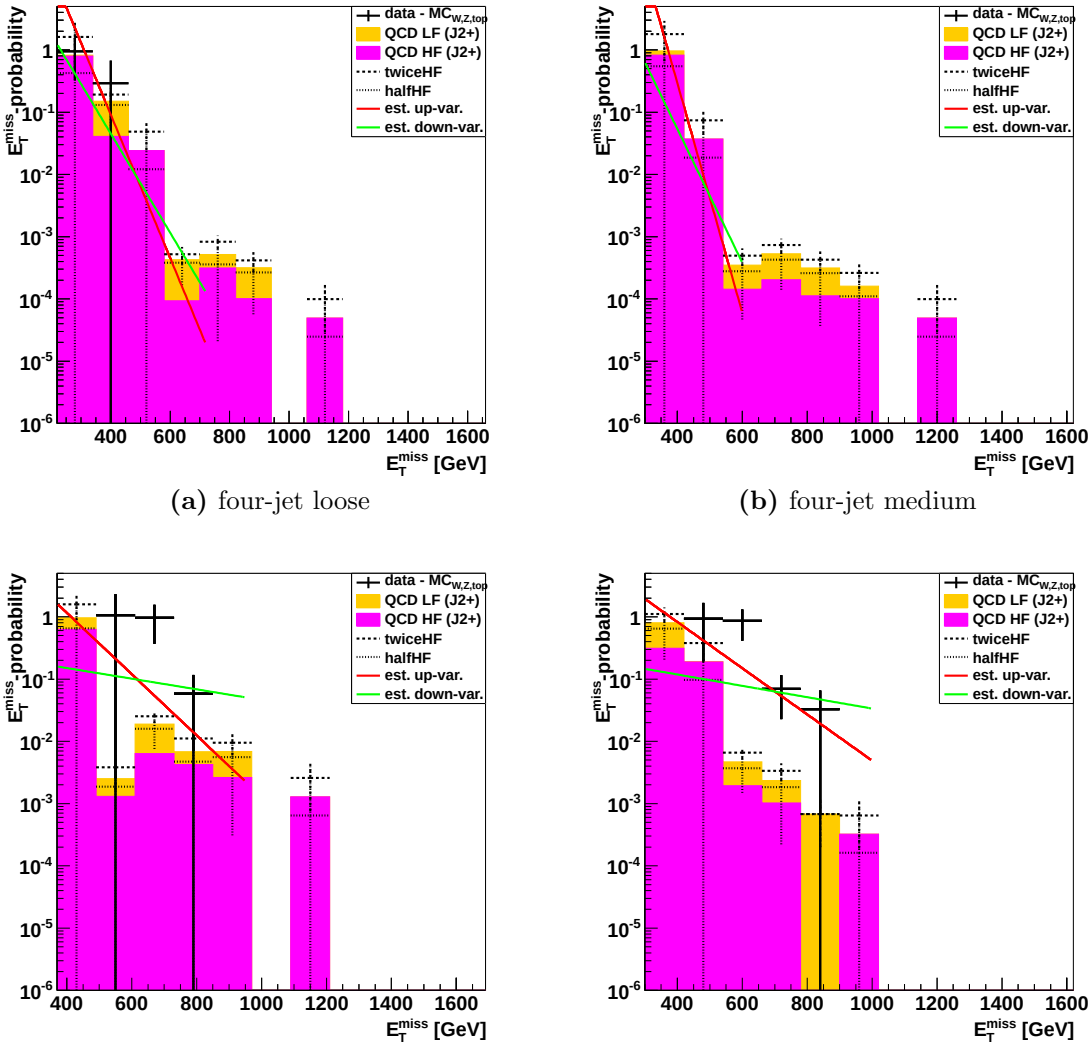

(a) four-jet loose **(b)** four-jet medium

(c) four-jet tight **(d)** five-jet tight

Figure 8.8: The obtained $E_{\mathrm{T}}^{\mathrm{miss}}$ -probabilities for four- and five-jet channel of the *complete 2011* analysis are shown including the assumed shape uncertainties (red and green). With these distributions being determined from data where possible, the QCD MC is shown for illustration only.

a possible signal. The obtained distributions are normalized to unity. Fitted with an exponential function $e^{-\lambda x}$ to more easily model the dominant low-$E_{\mathrm{T}}^{\mathrm{miss}}$ end of the probability distributions, an additional shape uncertainty is assigned conservatively via variation of the fit parameter $e^{-(\lambda \pm \sigma_\lambda)x}$. This accounts for the lowish statistics and the large uncertainties of the QCD MC, e.g. from the heavy-flavour component, which is well included in this estimated uncertainty.

The $E_{\mathrm{T}}^{\mathrm{miss}}$ -probabilities for the loose, medium and tight selection of the four- and respectively the five-jet channel are shown in Figure 8.8 (for the remaining channels and SRs, see Figure D.13 and Figure D.14 in Appendix D.4). In general, the distributions are taken from data where possible, subtracting the non-QCD components - in case of too low data statistics, the distributions are determined on the QCD MC simulation, but no discrepancy between data and MC has been found so far. Otherwise, the QCD-MC in this plots is shown for illustration only.

Overall, no obvious discrepancy in the behaviour between the 4.7 fb^{-1} dataset and the smaller 1 fb^{-1} dataset (see Section 7.3 and Section 7.4) is found for the $E_{\mathrm{T}}^{\mathrm{miss}}$ -probabilities and the uncertainty estimate still holds.

8.3 Results and discussion

Applying the new QCD estimation technique to the *complete 2011* dataset of 4.7 fb^{-1}, one gets for the TFs the results presented in Table 8.3 and the expected numbers of events in the SRs (see Table 8.4)[2].

It has to be emphasized, that the scaling of the `ALPGEN` W, Z and *top* MC samples is not applied when obtaining the final numbers as those scale factors were optimized on a dijet control region with $E_{\mathrm{T}}^{\mathrm{miss}}$ and hence do not reflect the special low-$E_{\mathrm{T}}^{\mathrm{miss}}$ regions used within this analysis. However, the effect is still accounted for as a systematic uncertainty by scaling the W+jets, Z+jets and $t\bar{t}$+jets simulation up and down by 20%.

The new QCD method quotes uncertainties on the TF estimates, and the expected number of QCD events inside the SRs, of 50% - 200%, whereas the dominant sources of uncertainty are the Jet Energy Scale and the contamination from W, Z and *top* background.

However, the expected number of QCD events inside the signal regions is, besides in region *E medium* with six expected QCD events, well below one event and the new estimation technique has nicely confirmed the sub-dominance of the multijet background within this 0-lepton SUSY search.

[2]These numbers differ slightly from [12, 14] due to minor ongoing improvements (the small amount of previously missing datasets was re-included, the second fit was switched from the Power-Law to the BreitWigner and the statistics of the toy simulation and fitting was increased where necessary).

channel	SR	N_{SR}/N_{CR2}*	fit uncert.*	fit-shape*	METprob.*	JES*	JRES*	WZtop-cont.*	PileUp*
A	medium	4.12	± 0.35	± 0.96	$^{+0.14}_{-0.88}$	$^{+0.38}_{-0.61}$	± 0.10	$^{+1.47}_{-0.68}$	± 0.17
	rel. error in %		± 8.50	± 23.43	$^{+3.52}_{-21.34}$	$^{+9.12}_{-14.93}$	± 2.35	$^{+35.72}_{-16.64}$	± 4.11
A	tight	2.07	± 0.18	± 0.57	$^{+0.16}_{-0.31}$	$^{+0.19}_{-0.31}$	± 0.05	$^{+0.76}_{-0.35}$	± 0.09
	rel. error in %		± 8.70	± 27.34	$^{+7.63}_{-15.07}$	$^{+9.21}_{-15.16}$	± 2.38	$^{+36.45}_{-16.94}$	± 4.16
A'	medium	3.00	± 0.36	± 0.92	$^{+1.17}_{-0.20}$	$^{+0.12}_{-0.20}$	± 0.04	$^{+0.80}_{-0.22}$	± 0.01
	rel. error in %		± 12.15	± 30.80	$^{+38.92}_{-6.62}$	$^{+3.99}_{-6.66}$	± 1.19	$^{+26.78}_{-7.28}$	± 0.47
B	tight	3.80	± 0.48	± 0.81	$^{+0.44}_{-1.05}$	$^{+0.79}_{-2.10}$	± 0.13	$^{+3.42}_{-0.99}$	± 0.17
	rel. error in %		± 12.63	± 21.36	$^{+11.48}_{-27.57}$	$^{+20.71}_{-55.19}$	± 3.33	$^{+89.91}_{-25.98}$	± 4.57
C	loose	18.32	± 5.11	± 1.79	$^{+0.84}_{-1.08}$	$^{+5.92}_{-19.31}$	± 1.41	$^{+25.61}_{-4.19}$	± 1.60
	rel. error in %		± 27.89	± 9.79	$^{+4.58}_{-5.88}$	$^{+32.34}_{-105.42}$	± 7.69	$^{+139.82}_{-22.88}$	± 8.74
C	medium	9.63	± 2.97	± 1.38	$^{+0.34}_{-0.53}$	$^{+3.18}_{-11.20}$	± 0.76	$^{+15.22}_{-2.31}$	± 0.88
	rel. error in %		± 30.84	± 14.31	$^{+3.50}_{-5.51}$	$^{+33.00}_{-116.30}$	± 7.93	$^{+158.03}_{-24.01}$	± 9.09
C	tight	3.51	± 1.12	± 0.69	$^{+1.21}_{-1.38}$	$^{+1.17}_{-4.40}$	± 0.28	$^{+6.12}_{-0.87}$	± 0.33
	rel. error in %		± 31.91	± 19.57	$^{+34.55}_{-39.44}$	$^{+33.35}_{-125.37}$	± 8.08	$^{+174.44}_{-24.78}$	± 9.31
D	tight	11.48	± 3.50	± 1.39	$^{+2.62}_{-4.67}$	$^{+4.52}_{-7.49}$	± 0.39	$^{+7.55}_{-4.53}$	± 1.66
	rel. error in %		± 30.49	± 12.07	$^{+22.79}_{-40.63}$	$^{+39.38}_{-65.25}$	± 3.40	$^{+65.71}_{-39.46}$	± 14.45
E	loose	105.29	± 55.16	± 0.14	$^{+12.95}_{-18.09}$	$^{+16.48}_{-20.73}$	± 18.77	$^{+22.94}_{-22.21}$	± 12.60
	rel. error in %		± 52.39	± 0.13	$^{+12.30}_{-17.18}$	$^{+15.65}_{-19.69}$	± 17.83	$^{+21.79}_{-21.09}$	± 11.97
E	medium	52.05	± 34.86	± 1.56	$^{+9.38}_{-17.80}$	$^{+10.14}_{-14.30}$	± 13.69	$^{+16.36}_{-13.42}$	± 8.55
	rel. error in %		± 66.97	± 3.00	$^{+18.02}_{-34.20}$	$^{+19.48}_{-27.47}$	± 26.29	$^{+31.44}_{-25.79}$	± 16.43
E	tight	36.13	± 22.72	± 1.79	$^{+7.38}_{-15.95}$	$^{+7.55}_{-11.17}$	± 10.91	$^{+12.96}_{-9.93}$	± 6.63
	rel. error in %		± 62.88	± 4.95	$^{+20.43}_{-44.15}$	$^{+20.89}_{-30.92}$	± 30.18	$^{+35.86}_{-27.48}$	± 18.35

Table 8.3: *TFs* for the *complete 2011* analysis obtained with the new QCD method including statistical and systematic uncertainties. $(*) \cdot 10^{-3}$

channel	SR	$N_{SR,exp.}^{QCD}$ *	fit uncert.*	fit-shape*	METprob.*	JES*	JRES*	WZtop-cont.*	PileUp *
A	medium	17.36	± 1.46	± 4.07	$^{+0.61}_{-3.71}$	$^{+1.58}_{-2.59}$	± 0.41	$^{+6.20}_{-2.89}$	± 0.71
	rel. error in %		± 8.50	± 23.43	$^{+3.52}_{-21.34}$	$^{+9.12}_{-14.93}$	± 2.35	$^{+35.72}_{-16.64}$	± 4.11
A	tight	0.92	± 0.08	± 0.25	$^{+0.07}_{-0.14}$	$^{+0.08}_{-0.14}$	± 0.02	$^{+0.33}_{-0.16}$	± 0.04
	rel. error in %		± 8.70	± 27.34	$^{+7.63}_{-15.07}$	$^{+9.21}_{-15.16}$	± 2.38	$^{+36.45}_{-16.94}$	± 4.16
A'	medium	0.52	± 0.06	± 0.16	$^{+0.20}_{-0.03}$	$^{+0.02}_{-0.03}$	± 0.01	$^{+0.14}_{-0.04}$	± 0.00
	rel. error in %		± 12.15	± 30.80	$^{+38.92}_{-6.62}$	$^{+3.99}_{-6.66}$	± 1.19	$^{+26.78}_{-7.28}$	± 0.47
B	tight	6.46	± 0.82	± 1.38	$^{+0.74}_{-1.78}$	$^{+1.34}_{-3.57}$	± 0.22	$^{+5.81}_{-1.68}$	± 0.30
	rel. error in %		± 12.63	± 21.36	$^{+11.48}_{-27.57}$	$^{+20.71}_{-55.19}$	± 3.33	$^{+89.91}_{-25.98}$	± 4.57
C	loose	247.46	± 68.98	± 24.22	$^{+11.32}_{-14.55}$	$^{+80.03}_{-260.88}$	± 19.02	$^{+345.99}_{-56.62}$	± 21.62
	rel. error in %		± 27.89	± 9.79	$^{+4.58}_{-5.88}$	$^{+32.34}_{-105.42}$	± 7.69	$^{+139.82}_{-22.88}$	± 8.74
C	medium	8.08	± 2.49	± 1.16	$^{+0.28}_{-0.45}$	$^{+2.66}_{-9.39}$	± 0.64	$^{+12.76}_{-1.94}$	± 0.73
	rel. error in %		± 30.84	± 14.31	$^{+3.50}_{-5.51}$	$^{+33.00}_{-116.30}$	± 7.93	$^{+158.03}_{-24.01}$	± 9.09
C	tight	1.77	± 0.57	± 0.35	$^{+0.61}_{-0.70}$	$^{+0.59}_{-2.22}$	± 0.14	$^{+3.09}_{-0.44}$	± 0.16
	rel. error in %		± 31.91	± 19.57	$^{+34.55}_{-39.44}$	$^{+33.35}_{-125.37}$	± 8.08	$^{+174.44}_{-24.78}$	± 9.31
D	tight	22.98	± 7.01	± 2.77	$^{+5.24}_{-9.34}$	$^{+9.05}_{-15.00}$	± 0.78	$^{+15.10}_{-9.07}$	± 3.32
	rel. error in %		± 30.49	± 12.07	$^{+22.79}_{-40.63}$	$^{+39.38}_{-65.25}$	± 3.40	$^{+65.71}_{-39.46}$	± 14.45
E	loose	6514.32	± 3412.77	± 8.48	$^{+801.19}_{-1119.06}$	$^{+1019.67}_{-1282.54}$	± 1161.55	$^{+1419.33}_{-1374.04}$	± 779.65
	rel. error in %		± 52.39	± 0.13	$^{+12.30}_{-17.18}$	$^{+15.65}_{-19.69}$	± 17.83	$^{+21.79}_{-21.09}$	± 11.97
E	medium	677.40	± 453.64	± 20.34	$^{+122.10}_{-231.66}$	$^{+131.93}_{-186.06}$	± 178.12	$^{+212.96}_{-174.69}$	± 111.31
	rel. error in %		± 66.97	± 3.00	$^{+18.02}_{-34.20}$	$^{+19.48}_{-27.47}$	± 26.29	$^{+31.44}_{-25.79}$	± 16.43
E	tight	259.86	± 163.40	± 12.86	$^{+53.09}_{-114.74}$	$^{+54.28}_{-80.35}$	± 78.43	$^{+93.20}_{-71.40}$	± 47.68
	rel. error in %		± 62.88	± 4.95	$^{+20.43}_{-44.15}$	$^{+20.89}_{-30.92}$	± 30.18	$^{+35.86}_{-27.48}$	± 18.35

Table 8.4: Expected N_{SR}^{QCD} for the *complete 2011* analysis obtained with the new QCD method including statistical and systematic uncertainties. $(*) \cdot 10^{-3}$

The jet-smearing method, used as baseline within the *complete 2011* analysis, provides updated numbers on the TFs (see Appendix D.5), reducing their quoted systematics to 50% and below. Comparing the results of the new technique to the outcome of the jet-smearing method, the overall agreement between the numbers is fine and more or less covered within the reduced uncertainties, while in some cases, especially in the low jet-multiplicity channels, considerable deviations are found. This might be an indication of additional, yet unconsidered systematic uncertainties affecting either one of the methods or both, as no obvious reason or problem was found so far. In conclusion, one might consider the deviations between the different methods to reflect the general precision, within which a QCD determination is possible, and consider these to be added to the overall systematics calculation.

Chapter 9

The overall picture: SUSY exclusion limits

This Chapter explains how the QCD estimate is combined with the other background estimation techniques (as shortly introduced in Section 6.3.1) to form a complete SUSY search. The M_{eff} distributions in the SRs of the *complete 2011* analysis are shown (see Section 9.1) and the likelihood test approach to either set exclusion limits on supersymmetric particle masses or discover SUSY particles is elaborated in Section 9.2.
As no signs of any new SUSY-like particles have been found so far, Section 9.3 is presenting the latest exclusion limits.

9.1 The signal region plots for 4.7 fb^{-1}

The effective mass distributions in the different channels of the *complete 2011* analysis (see Table 8.1, but without applying the final M_{eff} cut) are shown in Figure 9.1. As before, the `ALPGEN` W+jets, Z+jets and $t\bar{t}$+jets samples are scaled by factors of 0.75, 0.78 and 0.73 to better describe the data. No excess of the data over the background estimation, which could indicate the presence of a SUSY signal, is found in any of the distributions which will finally lead to new limits on the possible SUSY masses.

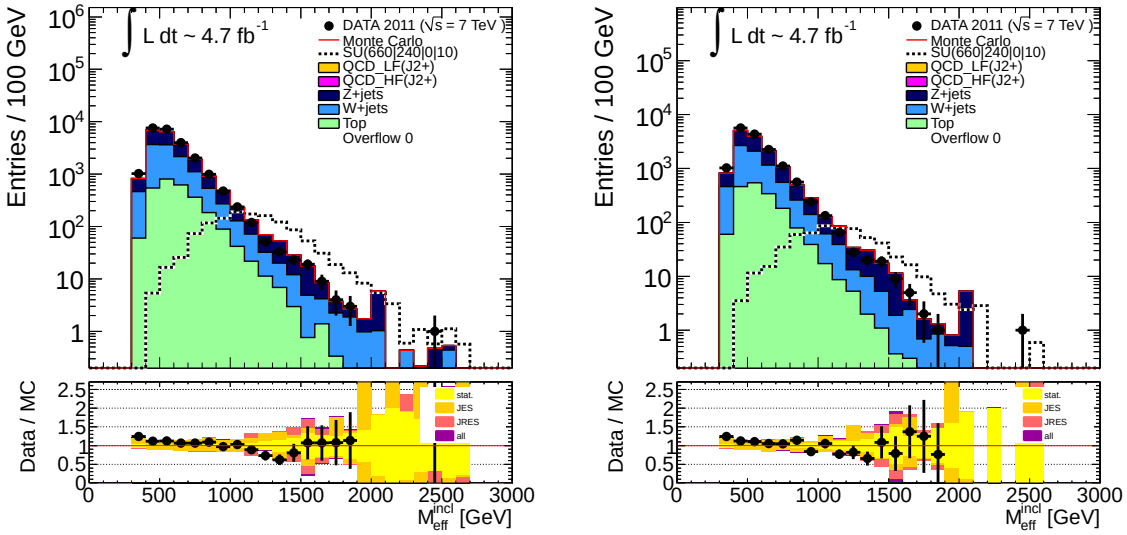

(a) two-jet channel

(b) two-jet prime channel

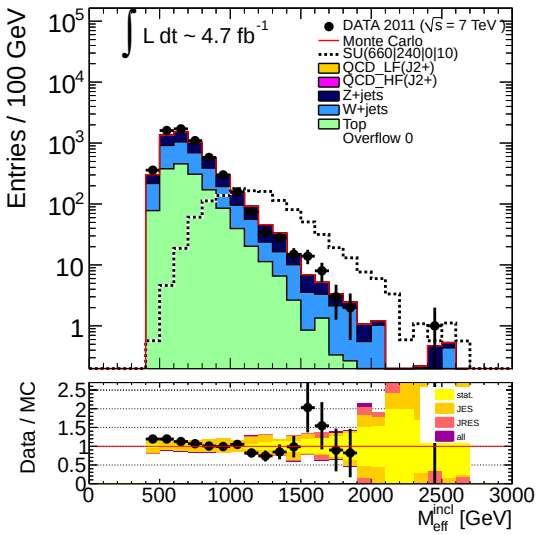

(c) three-jet channel

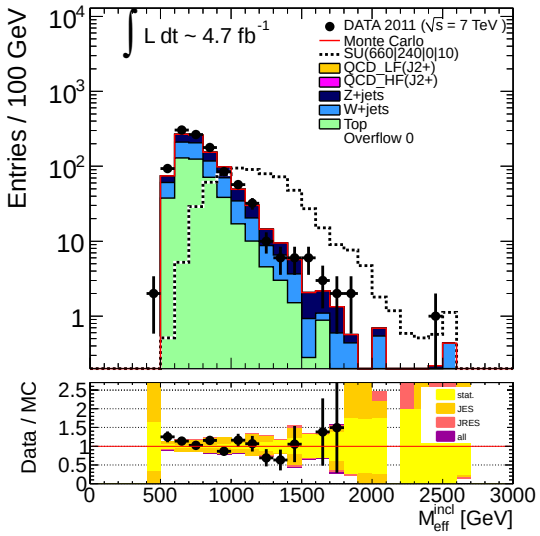

(d) four-jet channel

Figure 9.1: Effective mass distributions in the signal regions of the *complete 2011* analysis (without the latest cut on M_{eff}). The `ALPGEN` samples for W, Z and *top* are scaled with the according factors found by the likelihood fit.

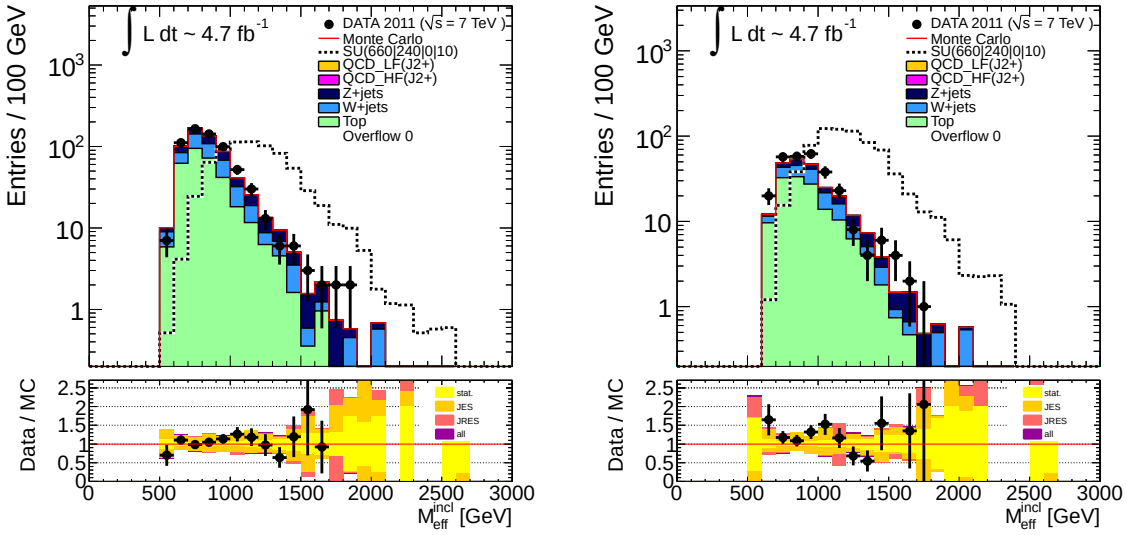

(e) five-jet channel **(f)** six-jet channel

Figure 9.1: Effective mass distributions in the signal regions of the *complete 2011* analysis (prior to the M_{eff} cut). The `ALPGEN` samples for W, Z and *top* are scaled with the according factors found by the likelihood fit.

9.2 The likelihood fit

This Section introduces the basic principles of the likelihood test, summarizing the relevant paragraphs from [11–14]. A more formal description can be found in Appendix E.

Each of the six analysis channels possesses one – three signal regions, defined by different M_{eff} cuts, yielding in total to eleven SRs. For a robust and consistent background estimate, each SR has five associated control regions, adding up to 55 CRs in total. A combination of a SR together with its five CRs is denoted a *stream* in the following.

Using the determined transfer factors TF, i.e. the ratio of the unscaled event yields in signal- and control region (see Section 2.7.4), the estimated number of background events for a given process, $N(\text{SR, scaled})$, is given by

$$N(\text{SR, scaled}) = N(\text{CR, observed}) \cdot TF. \tag{9.1}$$

These TFs together with the observed event counts in the associated CRs form the basis of a likelihood fit, used in order to generate internally consistent Standard Model background estimates for the SRs. Defining similarly inter-CR transfer factors in addition, also the contamination of the CRs by other Standard Model processes and/or

possible SUSY signals can be taken into account and the background estimates will be normalized coherently across all CRs.

Constrained by the TFs and the unscaled CR event counts, and taking into account their associated correlated and uncorrelated uncertainties as well as nuisance parameters, the likelihood fit adjusts the predicted background components in the SRs and CRs, whereas the scaled values are provided as output. Furthermore, the fit allows to determine the statistical significance of the observations in the SRs compared to the Standard Model expectations by providing a p-value, giving the probability for the hypothesis that the observed SR event count is compatible with background alone (see Table 9.1).

The migration of SUSY signal events between regions is treated conservatively. When searching for an excess due to a SUSY signal in a particular SR, the SUSY signal is assumed not to contribute in the CRs (i.e. by construction all SUSY TFs are set to zero), but only in the SR.

When no excess is observed, limits can be set within specific SUSY parameter spaces, considering the theoretical and experimental uncertainties of the particular SUSY model on the production cross-section as well as kinematic distributions. The assumption of a particular model allows moreover to take into account a signal contamination in the CRs, as the required SUSY TFs are precisely predicted by the signal hypothesis.

Exclusion limits then can be set using a likelihood test, comparing the fitted background expectations and expected signal contributions to the observed event rates in the SRs.

Table 9.1 opposes the number of events observed in the data to the number of Standard Model events expected to enter each of the SRs, determined using the likelihood fit. Good agreement is observed between the Standard Model prediction and the data, with no significant excess. Moreover, taking into account theoretical uncertainties as well, the expectations from the simulation for the various background components before the fits agrees well with the fitted predictions.

The last two rows of Table 9.1 provide an interpretation of the obtained results: exclusion limits are given for N_{BSM}, the event count in a specific channel, caused by a new physics signal, and the associated cross-section, σ_{BSM}.

Process	Signal Region					
	SRC loose	SRE loose	SRA medium	SRA' medium	SRC medium	SRE medium
$t\bar{t}$+ single top	74 ± 14 (75)	73 ± 25 (68)	6.8 ± 4.7 (5.3)	11 ± 4 (10)	13 ± 5 (11)	19 ± 6 (15)
Z+jets	71 ± 19 (78)	21 ± 7 (17)	32 ± 9 (44)	66 ± 18 (88)	16 ± 5 (20)	8.4 ± 3.2 (5.6)
W+jets	61 ± 11 (61)	23 ± 13 (23)	19 ± 5 (21)	25 ± 5 (30)	7.7 ± 3.0 (11)	6.2 ± 2.6 (4.7)
Multi-jets	0.9 ± 1.2 (0.8)	8.4 ± 7.3 (25)	0.1 ± 0.3 (0.2)	0.0 ± 0.1 (0.5)	0.03 ± 0.05 (0.03)	1.4 ± 1.2 (2.7)
Di-bosons	7.9 ± 4.0 (7.9)	4.2 ± 2.1 (4.2)	7.3 ± 3.7 (7.5)	14 ± 7 (16)	1.7 ± 0.9 (1.7)	2.7 ± 1.3 (2.7)
Total	$214 \pm 8 \pm 22$	$129 \pm 8 \pm 30$	$65 \pm 4 \pm 11$	$116 \pm 5 \pm 19$	$39 \pm 3 \pm 7$	$38 \pm 4 \pm 5$
Data	210	148	59	85	36	25
Local p-value (Gauss. σ)	0.56(−0.15)	0.21(0.81)	0.66(−0.40)	0.90(−1.3)	0.61(−0.27)	0.87(−1.1)
Upper limit on N_{BSM}	$51(55^{\uparrow 42}_{\downarrow 76})$	$77(67^{\uparrow 49}_{\downarrow 91})$	$24(28^{\uparrow 20}_{\downarrow 39})$	$28(42^{\uparrow 31}_{\downarrow 58})$	$17(19^{\uparrow 14}_{\downarrow 26})$	$11(16^{\uparrow 12}_{\downarrow 23})$
Upper limit on σ (fb)	$11(12^{\uparrow 8.8}_{\downarrow 16})$	$16(14^{\uparrow 10}_{\downarrow 19})$	$5.1(5.9^{\uparrow 4.3}_{\downarrow 8.3})$	$6.0(8.9^{\uparrow 6.6}_{\downarrow 12})$	$3.6(4^{\uparrow 2.9}_{\downarrow 5.6})$	$2.2(3.4^{\uparrow 2.5}_{\downarrow 4.8})$

Table 9.1: Observed numbers of events in data and fitted background components in the loose and medium SRs. For the total background estimates, the quoted uncertainties give the statistical (MC simulation and CR combined) and systematic uncertainties respectively. For the individual background components, the total uncertainties are given, while the values in parenthesis indicate the pre-fit predictions. The predictions for W+jets, Z+jets and $t\bar{t}$ plus single top quark are from `ALPGEN` and are normalized to luminosity. In the case of the multi-jet background, the pre-fit values are from the data-driven jet-smearing method, normalized at low M_{eff}. The di-boson background is estimated with MC simulation normalized to luminosity. The p-values give the probability of the observation being consistent with the estimated background, and the 'Gauss. σ' values give the number of standard deviations in a Gaussian approximation, evaluated for a single observation at a time. The last two rows show the upper limits on the excess number of events, and the excess cross-section, above that expected from the SM. The observed upper limit is followed in brackets by the expected limit, with the super- and sub-scripts showing the expectation from $\pm 1\sigma$ changes in the background (denoted by $\uparrow$ and $\downarrow$ respectively). Taken from [11–14].

Process	Signal Region				
	SRA tight	SRB tight	SRC tight	SRD tight	SRE tight
$t\bar{t}$+ single top	0.2 ± 0.2 (0.1)	0.3 ± 0.3 (0.2)	2.0 ± 1.5 (1.2)	2.4 ± 1.7 (1.4)	4.2 ± 4.7 (3.0)
Z+jets	3.3 ± 1.5 (4.0)	2.0 ± 1.3 (2.1)	2.0 ± 1.0 (5.6)	0.9 ± 0.6 (3.4)	3.4 ± 1.6 (2.3)
W+jets	2.2 ± 1.0 (1.9)	1.0 ± 0.6 (0.8)	1.5 ± 1.3 (2.7)	2.4 ± 1.4 (2.5)	2.8 ± 1.9 (1.5)
Multi-jets	0.00 ± 0.02 (0.01)	0.00 ± 0.07 (0.02)	0.00 ± 0.03 (0.01)	0.0 ± 0.3 (0.1)	0.5 ± 0.4 (0.9)
Di-bosons	1.8 ± 0.9 (2.0)	1.8 ± 0.9 (1.9)	0.5 ± 0.3 (0.5)	2.2 ± 1.1 (2.2)	2.5 ± 1.3 (2.5)
Total	$7.4 \pm 1.3 \pm 1.9$	$5.0 \pm 0.9 \pm 1.7$	$6.0 \pm 1.0 \pm 2.0$	$7.8 \pm 1.0 \pm 2.4$	$13 \pm 2 \pm 6$
Data	1	1	14	9	13
Local p-value (Gauss. σ)	0.98(−2.1)	0.96(−1.7)	0.016(2.1)	0.29(0.55)	0.45(0.14)
Upper limit on N_{BSM}	$3.1(6.4^{\uparrow 4.5}_{\downarrow 9.4})$	$3.0(5.6^{\uparrow 3.9}_{\downarrow 8.3})$	$16(9.5^{\uparrow 6.9}_{\downarrow 14})$	$9.6(8.5^{\uparrow 6.1}_{\downarrow 12})$	$12(12^{\uparrow 8.4}_{\downarrow 17})$
Upper limit on σ (fb)	$0.66(1.4^{\uparrow 0.96}_{\downarrow 2.0})$	$0.64(1.2^{\uparrow 0.83}_{\downarrow 1.8})$	$3.4(2.0^{\uparrow 1.5}_{\downarrow 2.9})$	$2.0(1.8^{\uparrow 1.3}_{\downarrow 2.6})$	$2.5(2.5^{\uparrow 1.8}_{\downarrow 3.5})$

Table 9.1: Observed numbers of events in data and fitted background components in the tight SRs. For the total background estimates, the quoted uncertainties give the statistical (MC simulation and CR combined) and systematic uncertainties respectively. For the individual background components, the total uncertainties are given, while the values in parenthesis indicate the pre-fit predictions. The predictions for W+jets, Z+jets and $t\bar{t}$ plus single top quark are from `ALPGEN` and are normalized to luminosity. In the case of the multi-jet background, the pre-fit values are from the data-driven jet-smearing method, normalized at low M_{eff}. The di-boson background is estimated with MC simulation normalized to luminosity. The p-values give the probability of the observation being consistent with the estimated background, and the 'Gauss. σ' values give the number of standard deviations in a Gaussian approximation, evaluated for a single observation at a time. The last two rows show the upper limits on the excess number of events, and the excess cross-section, above that expected from the SM. The observed upper limit is followed in brackets by the expected limit, with the super- and sub-scripts showing the expectation from $\pm 1\sigma$ changes in the background (denoted by $\uparrow$ and $\downarrow$ respectively). Taken from [11–14].

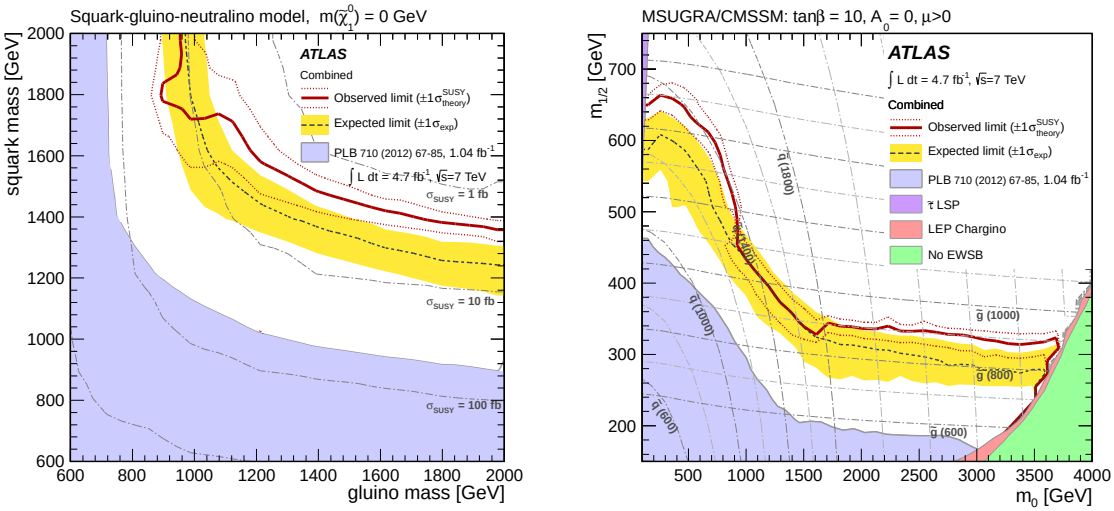

(a) (b)

Figure 9.2: The 95% CL_s exclusion limits on (9.2a) the ($m_{\tilde{g}}$, m_{squark})-plane in a simplified MSSM scenario with only strong production of gluinos and first- and second-generation squarks, with direct decays to jets and neutralinos (with $m_{\tilde{\chi}_1^0} = 0$ GeV); (9.2b) the (m_0, $m_{1/2}$) plane of mSUGRA/CMSSM for $\tan(\beta) = 10$, $A_0 = 0$ and $\mu > 0$. Exclusion limits are obtained by using the signal region with the best expected sensitivity at each point. The black dashed lines show the expected limits, with the light (yellow) bands indicating the 1 sigma excursions due to experimental uncertainties. Observed limits are indicated by medium (maroon) curves, where the solid contour represents the nominal limit, and the dotted lines are obtained by varying the cross-section by the theoretical scale and PDF uncertainties. Previous results from ATLAS are represented by the shaded region (blue) at bottom left in each case. The region excluded by chargino searches at LEP is taken from Reference [166]. Taken from [11–14].

9.3 Exclusion Limits

The final limits are set using data from all channels, choosing the SR with the best expected sensitivity at each point of the parameter space. Combining the CL_s prescription [165] with a profile loglikelihood ratio test, 95% exclusion regions are derived. A conservative consideration of the theoretical uncertainties on the SUSY cross-sections lets one quote the actual numbers from the lower edge of the 1σ observed limit band.

Assuming mSUGRA/CMSSM models with $\tan(\beta) = 10$, $A_0 = 0$ and $\mu > 0$, squarks and gluinos of equal mass are excluded at 95% confidence level for masses below 1360 GeV (see Figure 9.2b). The ATLAS reach at high m_0 values is increased especially from the inclusion of channels with higher jet multiplicities.

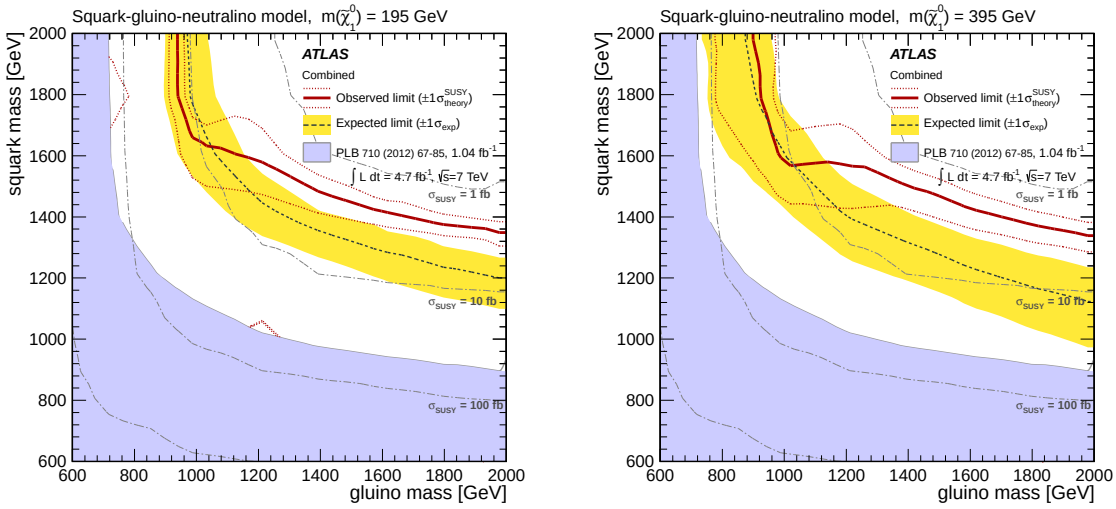

(a) **(b)**

Figure 9.3: The 95% CL_s exclusion limits on the ($m_{\tilde{g}}$, m_{squark})-plane in MSSM models with non-zero neutralino masses. Combined observed exclusion limits are based on the best expected CL_s per grid point as for Figure 9.2a, but with an LSP mass of (Figure 9.3a) 195 GeV and (Figure 9.3b) 395 GeV. Curves are as defined in Figure 9.2a. Previous results from ATLAS are represented by the shaded region (blue) at bottom left in each case. Taken from [11–14].

Assuming a simplified model with squarks of the first two generations only, a light neutralino and a gluino octet, however, gluino masses below 860 GeV and squark masses below 1320 GeV are excluded for squark and gluino masses below 2 TeV respectively (see Figure 9.2a). The limit rises to 1410 GeV for squarks and gluinos of equal mass.

Comparing Figure 9.2a with Figures 9.3, the influence of different neutralino masses ($m_{\tilde{\chi}_1^0} = 0, 195, 395$ GeV) on the exclusion limits is studied. Only minor differences in the limit curves indicate that the search is sensitive to a range of LSP masses.

Chapter 10

Conclusions

In order to detect SUSY particles at hadron colliders such as the LHC, various efforts have been made to develop significant analyses providing the largest possible discovery reach. Hereby, one of the most powerful channels examines the signature of fully hadronic final states combined with large missing transverse momentum ($\vec{P}_{\mathrm{T}}^{\mathrm{miss}}$), originating from the stable lightest supersymmetric particle escaping the detectors unseen.

A key ingredient for any new physics searches, however, is the precise knowledge both of the detector performance and the background determination, as classically the data are scanned for deviations from the Standard Model predictions.
At hadron colliders, the fully hadronic final state naturally suffers from a huge QCD multijet background, which is to be suppressed by several orders of magnitude by a dedicated event selection, leaving the probability for QCD multijet events to pass any of the signal region cuts by design to be small. Nevertheless, the low acceptance could be outmatched by the large QCD cross-section, leading to a significant SR contamination: As typical QCD multijet events possesses only few real missing energy, additional sources of missing transverse energy ($E_{\mathrm{T}}^{\mathrm{miss}}$) are needed, e.g. from leptonic decays of heavy quarks producing neutrinos or only apparent missing transverse energy from the mismeasurements of jets. Thus, the estimation of the QCD background is crucial and one of the most challenging backgrounds to determine, as the conventional use and the reliability of the MC simulation is limited (mainly due to statistics reasons) and a very detailed detector understanding, especially of the modelling of $E_{\mathrm{T}}^{\mathrm{miss}}$, would be required.

At ATLAS, SUSY searches in general use transfer factors (TF) to derive the background estimates from several control regions, whereas the TFs are mainly determined from MC simulations and validated in control regions with data.
This thesis discusses several possibilities to estimate the QCD background for SUSY

searches with jets and $E_{\mathrm{T}}^{\mathrm{miss}}$, also showing the limitations of the early mainly MC-based approaches. As a remedy, a new semi-data-driven method has been developed estimating the QCD background by a direct measurement of the transfer factor. An important variable hereby is found to be the minimum angular separation between the jets and $\vec{P}_{\mathrm{T}}^{\mathrm{miss}}$, $\Delta\varphi^{min}\left(jet, \vec{P}_{\mathrm{T}}^{\mathrm{miss}}\right)$, providing good distinction power between QCD and non-QCD processes, which is also used in the main selection to explicitly suppress the QCD multijet background.
The QCD TF, i.e. the ratio of events in a QCD-enhanced and a QCD-suppressed region, is evaluated as function of $E_{\mathrm{T}}^{\mathrm{miss}}$ in two different control regions, defined using the regime of low $E_{\mathrm{T}}^{\mathrm{miss}}$ and another key variable, commonly used for QCD suppression, namely the ratio $E_{\mathrm{T}}^{\mathrm{miss}}$ $/M_{\mathrm{eff}}$, where the effective mass, M_{eff}, is the sum of the jets' transverse momentum and $E_{\mathrm{T}}^{\mathrm{miss}}$. Correcting the observed event counts in the data for the non-QCD contamination, the QCD TFs are fitted and the final numbers are extracted from a interpolation of the fits into the signal regions. This thesis provides also a comprehensive estimation of the systematic uncertainties on the TFs, arising e.g. from jet energy scale uncertainty and pile-up, the overlay of several hard interactions within one event. Although the uncertainties on the method are of $\mathcal{O}(100\%)$, the QCD background was found to be negligible compared to the other backgrounds (W, Z and *top*). The obtained results of the different methods are indeed compatible with each other, and furthermore also with the results of the jet-smearing method, which has been used as baseline-method in previous ATLAS publications so far.

Finally, the obtained QCD TFs can be combined with other background estimates to set competitive exclusion limits on the allowed SUSY particle masses, as no significant deviations from the Standard Model have been found so far. ATLAS has placed large constraints on the parameter space of possible SUSY models, extending the exclusion limits of previous searches considerably. Assuming e.g. mSUGRA/CMSSM models with $\tan(\beta) = 10$, $A_0 = 0$ and $\mu > 0$, squarks and gluinos of equal mass are excluded at 95% confidence level for masses below 1360 GeV. Nevertheless, there are plenty of SUSY scenarios left and the ongoing searches do not only need to become smarter, but also (systematic) uncertainties are to be reduced and background estimates improved.

Part III

Appendices

Appendix A

Monte Carlo Samples for the summer 2011 analysis

A.1 Signal samples

Sample ID	Name	Generator	Cross-section [pb]	N_{gen}
106484	SUSY SU4 point	HERWIG++	59.6	49949
123440	SUSY $m_0 = 660\,\text{GeV}$, $m_{1/2} = 240\,\text{GeV}$, $\tan\beta = 10$	HERWIG++	1.249	9980

Table A.1: SUSY benchmark point Monte Carlo samples used in the 0-lepton analyses including cross-section times branching ratio and the number of generated events of the sample [9, 10].

A.2 Background Samples

Sample ID	Name	Generator	Cross-section [pb]	k–factor	N_{gen}
107680	WenuNp0_pt20	ALPGEN JIMMY	6921.6	1.20	3455037
107681	WenuNp1_pt20	ALPGEN JIMMY	1304.3	1.20	641361
107682	WenuNp2_pt20	ALPGEN JIMMY	378.3	1.20	3768265
107683	WenuNp3_pt20	ALPGEN JIMMY	101.4	1.20	1009641
107684	WenuNp4_pt20	ALPGEN JIMMY	25.9	1.20	249869
107685	WenuNp5_pt20	ALPGEN JIMMY	7.0	1.20	69953
107690	WmunuNp0_pt20	ALPGEN JIMMY	6919.6	1.20	3466523
107691	WmunuNp1_pt20	ALPGEN JIMMY	1304.2	1.20	641867
107692	WmunuNp2_pt20	ALPGEN JIMMY	377.8	1.20	3768893
107693	WmunuNp3_pt20	ALPGEN JIMMY	101.9	1.20	1009589
107694	WmunuNp4_pt20	ALPGEN JIMMY	25.8	1.20	254879
107695	WmunuNp5_pt20	ALPGEN JIMMY	6.9	1.20	69958
107700	WtaunuNp0_pt20	ALPGEN JIMMY	6918.6	1.20	3416438
107701	WtaunuNp1_pt20	ALPGEN JIMMY	1303.2	1.20	641809
107702	WtaunuNp2_pt20	ALPGEN JIMMY	378.2	1.20	3768750
107703	WtaunuNp3_pt20	ALPGEN JIMMY	101.5	1.20	1009548
107704	WtaunuNp4_pt20	ALPGEN JIMMY	25.6	1.20	249853
107705	WtaunuNp5_pt20	ALPGEN JIMMY	7.0	1.20	63692
106280	WbbNp0_pt20	ALPGEN JIMMY	3.3	1.20	6496
106281	WbbNp1_pt20	ALPGEN JIMMY	2.7	1.20	5500
106282	WbbNp2_pt20	ALPGEN JIMMY	1.4	1.20	2998
106283	WbbNp3_pt20	ALPGEN JIMMY	0.7	1.20	1499

Table A.2: W + jet Monte Carlo samples used in the 0-lepton analyses including cross-section times branching ratio, the k–factors and the number of generated events of the sample. The k–factors are the NNLO/LO scaling factors used to scale the overall cross-section for $W \to l\nu$ to the total NNLO inclusive cross-section [9, 10].

Sample ID	Name	Generator	Cross-section [pb]	k–factor	N_{gen}
107650	ZeeNp0_pt20	ALPGEN JIMMY	668.3	1.25	6612265
107651	ZeeNp1_pt20	ALPGEN JIMMY	134.4	1.25	1333745
107652	ZeeNp2_pt20	ALPGEN JIMMY	40.54	1.25	404873
107653	ZeeNp3_pt20	ALPGEN JIMMY	11.16	1.25	109942
107654	ZeeNp4_pt20	ALPGEN JIMMY	2.88	1.25	29992
107655	ZeeNp5_pt20	ALPGEN JIMMY	0.83	1.25	8992
107660	ZmumuNp0_pt20	ALPGEN JIMMY	668.7	1.25	6619010
107661	ZmumuNp1_pt20	ALPGEN JIMMY	134.1	1.25	1334723
107662	ZmumuNp2_pt20	ALPGEN JIMMY	40.33	1.25	403886
107663	ZmumuNp3_pt20	ALPGEN JIMMY	11.19	1.25	109954
107664	ZmumuNp4_pt20	ALPGEN JIMMY	2.75	1.25	29978
107665	ZmumuNp5_pt20	ALPGEN JIMMY	0.77	1.25	9993
107670	ZtautauNp0_pt20	ALPGEN JIMMY	668.4	1.25	6618801
107671	ZtautauNp1_pt20	ALPGEN JIMMY	134.8	1.25	1334664
107672	ZtautauNp2_pt20	ALPGEN JIMMY	40.36	1.25	404853
107673	ZtautauNp3_pt20	ALPGEN JIMMY	11.25	1.25	109944
107674	ZtautauNp4_pt20	ALPGEN JIMMY	2.79	1.25	29982
107675	ZtautauNp5_pt20	ALPGEN JIMMY	0.77	1.25	9993
107710	ZnunuNp0_pt20	ALPGEN JIMMY	26.71	1.282	63482
107711	ZnunuNp1_pt20	ALPGEN JIMMY	451.4	1.282	909288
107712	ZnunuNp2_pt20	ALPGEN JIMMY	197.6	1.282	204942
107713	ZnunuNp3_pt20	ALPGEN JIMMY	59.89	1.282	140929
107714	ZnunuNp4_pt20	ALPGEN JIMMY	15.61	1.282	32980
107715	ZnunuNp5_pt20	ALPGEN JIMMY	4.165	1.282	9492

Table A.3: $Z+$jet Monte Carlo samples used in the 0-lepton analyses including cross-section times branching ratio, the k–factors and the number of generated events of the sample. The k–factors are the NNLO/LO scaling factors used to scale the overall cross-section for $Z \to \nu\bar{\nu}$ and $Z \to l^+l^-$ to the total NNLO inclusive cross-section [9, 10].

Sample ID	Name	Generator	$\hat{p}_T$ [GeV]	Cross-section [pb]	N_{gen}
105200	T1	MC@NLO JIMMY		89.4	1498987
105204	TTbar_FullHad	MC@NLO JIMMY		75.2	1198875
108340	st_tchan_enu	MC@NLO JIMMY		7.12	299897
108341	st_tchan_munu	MC@NLO JIMMY		7.12	299879
108342	st_tchan_taunu	MC@NLO JIMMY		7.10	299879
108343	st_schan_enu	MC@NLO JIMMY		0.47	299831
108344	st_schan_munu	MC@NLO JIMMY		0.47	299877
108345	st_schan_taunu	MC@NLO JIMMY		0.47	299864
108346	st_Wt	MC@NLO JIMMY		14.59	899336
105009	J0 jetjet	PYTHIA	8 – 17	$9860 \cdot 10^6$	16358258
105010	J1 jetjet	PYTHIA	17 – 35	$678 \cdot 10^6$	7392565
105011	J2 jetjet	PYTHIA	35 – 70	$41.0 \cdot 10^6$	2796084
105012	J3 jetjet	PYTHIA	70 – 140	$2.19 \cdot 10^6$	2796879
105013	J4 jetjet	PYTHIA	140 – 280	$87.7 \cdot 10^3$	2793179
105014	J5 jetjet	PYTHIA	280 – 560	2350	2790576
105015	J6 jetjet	PYTHIA	560 – 1120	33.6	2790601
105016	J7 jetjet	PYTHIA	1120 – 2240	0.137	1395025
105017	J8 jetjet	PYTHIA	> 2240	$6.2 \cdot 10^{-6}$	1353250

Table A.4: Top Monte Carlo samples at NLO with NLL and QCD samples used in the 0-lepton analyses including cross-section times branching ratio and the number of generated events of the sample [9, 10]. The QCD samples are split at generator level according to the specified p_{T} intervals [167].

Appendix B

Monte Carlo Samples for the complete 2011 analysis

B.1 Signal samples

Sample ID	Name	Generator	Cross Section [pb]	N_{gen}
106484	SUSY SU4 point	HERWIG++	59.6	49949
123577	SUSY $m_0 = 1220$ GeV, $m_{1/2} = 360$ GeV, $\tan\beta = 10$	HERWIG++	0.030	9899

Table B.1: Simulated SUSY benchmark points used in the 0-lepton analyses including cross section times branching ratio and the number of generated events of the sample [11–14].

B.2 Background Samples

Sample ID	Name	Generator	Cross Section [pb]	k–factor	N_{gen}
107680	WenuNp0_pt20	ALPGENJIMMY	6921.6	1.20	3458883
107681	WenuNp1_pt20	ALPGENJIMMY	1304.3	1.20	2499645
107682	WenuNp2_pt20	ALPGENJIMMY	378.3	1.20	3768632
107683	WenuNp3_pt20	ALPGENJIMMY	101.4	1.20	1008947
107684	WenuNp4_pt20	ALPGENJIMMY	25.9	1.20	250000
144018	WenuNp5_excl_pt20	ALPGENJIMMY	5.8	1.20	979197
144022	WenuNp6_pt20	ALPGENJIMMY	1.5	1.20	144998
144196	WenuNp1_pt20_susyfilt	ALPGENJIMMY	7.4	1.20	180899
144197	WenuNp2_pt20_susyfilt	ALPGENJIMMY	6.3	1.20	134998
144198	WenuNp3_pt20_susyfilt	ALPGENJIMMY	3.5	1.20	139999
144199	WenuNp4_pt20_susyfilt	ALPGENJIMMY	1.4	1.20	75000
107690	WmunuNp0_pt20	ALPGENJIMMY	6919.6	1.20	3462942
107691	WmunuNp1_pt20	ALPGENJIMMY	1304.2	1.20	2499593
107692	WmunuNp2_pt20	ALPGENJIMMY	377.8	1.20	3768737
107693	WmunuNp3_pt20	ALPGENJIMMY	101.9	1.20	1008446
107694	WmunuNp4_pt20	ALPGENJIMMY	25.8	1.20	254950
144019	WmunuNp5_excl_pt20	ALPGENJIMMY	5.8	1.20	979794
144023	WmunuNp6_pt20	ALPGENJIMMY	1.5	1.20	144999
144200	WmunuNp1_pt20_susyfilt	ALPGENJIMMY	7.1	1.20	171000
144201	WmunuNp2_pt20_susyfilt	ALPGENJIMMY	6.2	1.20	139900
144202	WmunuNp3_pt20_susyfilt	ALPGENJIMMY	3.4	1.20	139899
144203	WmunuNp4_pt20_susyfilt	ALPGENJIMMY	1.4	1.20	70000
107700	WtaunuNp0_pt20	ALPGENJIMMY	6918.6	1.20	3418296
107701	WtaunuNp1_pt20	ALPGENJIMMY	1303.2	1.20	2499194
107702	WtaunuNp2_pt20	ALPGENJIMMY	378.2	1.20	3750986
107703	WtaunuNp3_pt20	ALPGENJIMMY	101.5	1.20	1009946
107704	WtaunuNp4_pt20	ALPGENJIMMY	25.6	1.20	249998
107705	WtaunuNp5_excl_pt20	ALPGENJIMMY	5.8	1.20	989595
144024	WtaunuNp6_pt20	ALPGENJIMMY	1.5	1.20	149999
144204	WtaunuNp1_pt20_susyfilt	ALPGENJIMMY	10.9	1.20	265000
144205	WtaunuNp2_pt20_susyfilt	ALPGENJIMMY	9.3	1.20	204999
144206	WtaunuNp3_pt20_susyfilt	ALPGENJIMMY	5.1	1.20	209900
144207	WtaunuNp4_pt20_susyfilt	ALPGENJIMMY	2.1	1.20	104999

Table B.2: W + jet Monte Carlo samples used in the 0-lepton analyses including cross section times branching ratio, the k–factors and the number of generated events of the sample [11–14]. The k–factors are the NNLO/LO scaling factors used to scale the overall cross-section for $W \to l\nu$ to the total NNLO inclusive cross section.

Sample ID	Name	Generator	Cross Section [pb]	k–factor	N_{gen}
107650	ZeeNp0_pt20	ALPGENJIMMY	668.3	1.25	6617284
107651	ZeeNp1_pt20	ALPGENJIMMY	134.4	1.25	1334897
107652	ZeeNp2_pt20	ALPGENJIMMY	40.54	1.25	809999
107653	ZeeNp3_pt20	ALPGENJIMMY	11.16	1.25	220000
107654	ZeeNp4_pt20	ALPGENJIMMY	2.88	1.25	60000
107655	ZeeNp5_pt20	ALPGENJIMMY	0.83	1.25	20000
116250	ZeeNp0_Mll10to40_pt20	ALPGENJIMMY	3054.7	1.25	994949
116251	ZeeNp1_Mll10to40_pt20	ALPGENJIMMY	84.9	1.25	299998
116252	ZeeNp2_Mll10to40_pt20	ALPGENJIMMY	41.2	1.25	939946
116253	ZeeNp3_Mll10to40_pt20	ALPGENJIMMY	8.4	1.25	149998
116254	ZeeNp4_Mll10to40_pt20	ALPGENJIMMY	1.9	1.25	40000
116255	ZeeNp5_Mll10to40_pt20	ALPGENJIMMY	0.5	1.25	10000
107660	ZmumuNp0_pt20	ALPGENJIMMY	668.7	1.25	6615230
107661	ZmumuNp1_pt20	ALPGENJIMMY	134.1	1.25	1334296
107662	ZmumuNp2_pt20	ALPGENJIMMY	40.33	1.25	404947
107663	ZmumuNp3_pt20	ALPGENJIMMY	11.19	1.25	110000
107664	ZmumuNp4_pt20	ALPGENJIMMY	2.75	1.25	30000
107665	ZmumuNp5_pt20	ALPGENJIMMY	0.77	1.25	10000
116260	ZmumuNp0_Mll10to40_pt20	ALPGENJIMMY	3054.9	1.25	999849
116261	ZmumuNp1_Mll10to40_pt20	ALPGENJIMMY	84.8	1.25	300000
116262	ZmumuNp2_Mll10to40_pt20	ALPGENJIMMY	41.1	1.25	999995
116263	ZmumuNp3_Mll10to40_pt20	ALPGENJIMMY	8.3	1.25	150000
116264	ZmumuNp4_Mll10to40_pt20	ALPGENJIMMY	1.9	1.25	39999
116265	ZmumuNp5_Mll10to40_pt20	ALPGENJIMMY	0.5	1.25	10000
107670	ZtautauNp0_pt20	ALPGENJIMMY	668.4	1.25	10613179
107671	ZtautauNp1_pt20	ALPGENJIMMY	134.8	1.25	3334137
107672	ZtautauNp2_pt20	ALPGENJIMMY	40.36	1.25	1004847
107673	ZtautauNp3_pt20	ALPGENJIMMY	11.25	1.25	509847
107674	ZtautauNp4_pt20	ALPGENJIMMY	2.79	1.25	144999
107675	ZtautauNp5_pt20	ALPGENJIMMY	0.77	1.25	45000
116940	ZtautauNp0_Mll10to40_pt20	ALPGENJIMMY	3054.8	1.25	41500
116941	ZtautauNp1_Mll10to40_pt20	ALPGENJIMMY	84.9	1.25	79950
116942	ZtautauNp2_Mll10to40_pt20	ALPGENJIMMY	41.3	1.25	34500
116943	ZtautauNp3_Mll10to40_pt20	ALPGENJIMMY	8.4	1.25	15000
116944	ZtautauNp4_Mll10to40_pt20	ALPGENJIMMY	1.8	1.25	5000
116945	ZtautauNp5_Mll10to40_pt20	ALPGENJIMMY	0.5	1.25	2000

Table B.3: Z + jet Monte Carlo samples used in the 0-lepton analyses including cross section times branching ratio, the k–factors and the number of generated events of the sample [11–14]. The k–factors are the NNLO/LO scaling factors used to scale the overall cross-section for $Z \to \nu\bar{\nu}$ and $Z \to l^+l^-$ to the total NNLO inclusive cross section.

Sample ID	Name	Generator	Cross Section [pb]	k–factor	N_{gen}
107280	WbbFullNp0_pt20	ALPGENJIMMY	47.3	1.20	474997
107281	WbbFullNp1_pt20	ALPGENJIMMY	35.8	1.20	205000
107282	WbbFullNp2_pt20	ALPGENJIMMY	17.3	1.20	174499
107283	WbbFullNp3_pt20	ALPGENJIMMY	6.6	1.20	69999
117284	WccFullNp0_pt20	ALPGENJIMMY	127.5	1.20	1274846
117285	WccFullNp1_pt20	ALPGENJIMMY	104.7	1.20	1049847
117286	WccFullNp2_pt20	ALPGENJIMMY	52.1	1.20	524947
117287	WccFullNp3_pt20	ALPGENJIMMY	17.0	1.20	170000
117293	WcNp0_pt20	ALPGENJIMMY	644.4	1.20	6498837
117294	WcNp1_pt20	ALPGENJIMMY	205.0	1.20	2069646
117295	WcNp2_pt20	ALPGENJIMMY	51.0	1.20	519998
117296	WcNp3_pt20	ALPGENJIMMY	11.4	1.20	115000
117297	WcNp4_pt20	ALPGENJIMMY	2.8	1.20	30000

Table B.4: (*Continued*) W + jet Monte Carlo samples used in the 0-lepton analyses including cross section times branching ratio, the k–factors and the number of generated events of the sample [11–14]. The k–factors are the NNLO/LO scaling factors used to scale the overall cross-section for $W \to l\nu$ to the total NNLO inclusive cross section.

Sample ID	Name	Generator	Cross Section [pb]	k–factor	N_{gen}
107710	ZnunuNp0_pt20	ALPGENJIMMY	26.71	1.282	54949
107711	ZnunuNp1_pt20	ALPGENJIMMY	451.4	1.282	909848
107712	ZnunuNp2_pt20	ALPGENJIMMY	197.6	1.282	169899
107713	ZnunuNp3_pt20	ALPGENJIMMY	59.89	1.282	144999
107714	ZnunuNp4_pt20	ALPGENJIMMY	15.61	1.282	309899
144017	ZnunuNp5_excl_pt20	ALPGENJIMMY	3.6	1.282	185000
144021	ZnunuNp6_pt20	ALPGENJIMMY	0.92	1.282	114999
144192	ZnunuNp1_pt20_susyfilt	ALPGENJIMMY	12.9	1.282	
144193	ZnunuNp2_pt20_susyfilt	ALPGENJIMMY	10.1	1.282	399999
144194	ZnunuNp3_pt20_susyfilt	ALPGENJIMMY	5.4	1.282	299998
144195	ZnunuNp4_pt20_susyfilt	ALPGENJIMMY	2.2	1.282	184998

Table B.5: (*Continued*) Z + jet Monte Carlo samples used in the 0-lepton analyses including cross section times branching ratio, the k–factors and the number of generated events of the sample [11–14]. The k–factors are the NNLO/LO scaling factors used to scale the overall cross-section for $Z \to \nu\bar{\nu}$ and $Z \to l^+l^-$ to the total NNLO inclusive cross section.

Sample ID	Name	Generator	Cross Section [pb]	k–factor	N_{gen}
105890	AlpgenJimmyttbarlnlnNp0	ALPGENJIMMY	3.47	1.67	59000
105891	AlpgenJimmyttbarlnlnNp1	ALPGENJIMMY	3.40	1.67	59000
105892	AlpgenJimmyttbarlnlnNp2	ALPGENJIMMY	2.12	1.67	36900
117897	AlpgenJimmyttbarlnlnNp3	ALPGENJIMMY	0.95	1.67	88500
117898	AlpgenJimmyttbarlnlnNp4	ALPGENJIMMY	0.33	1.67	22500
117899	AlpgenJimmyttbarlnlnNp5	ALPGENJIMMY	0.13	1.67	7000
105894	AlpgenJimmyttbarlnqqNp0	ALPGENJIMMY	13.76	1.75	238999
105895	AlpgenJimmyttbarlnqqNp1	ALPGENJIMMY	13.61	1.75	240999
105896	AlpgenJimmyttbarlnqqNp2	ALPGENJIMMY	8.42	1.75	146999
117887	AlpgenJimmyttbarlnqqNp3	ALPGENJIMMY	3.78	1.75	66500
117888	AlpgenJimmyttbarlnqqNp4	ALPGENJIMMY	1.34	1.75	22499
117889	AlpgenJimmyttbarlnqqNp5	ALPGENJIMMY	0.50	1.75	7999
105204	TTbar_FullHad	MC@NLOJIMMY	75.2		1198875
108340	st_tchan_enu	MC@NLOJIMMY	7.12		299897
108341	st_tchan_munu	MC@NLOJIMMY	7.12		299879
108342	st_tchan_taunu	MC@NLOJIMMY	7.10		299879
108343	st_schan_enu	MC@NLOJIMMY	0.47		299831
108344	st_schan_munu	MC@NLOJIMMY	0.47		299877
108345	st_schan_taunu	MC@NLOJIMMY	0.47		299864
108346	st_Wt	MC@NLOJIMMY	14.59		899336

Table B.6: Top Monte Carlo samples used in the 0-lepton analyses including cross section times branching ratio, the k–factors and the number of generated events of the sample [11–14]. The k–factors are the NNLO/LO scaling factors used to scale the overall cross-section to the total NNLO inclusive cross section.

Sample ID	Name	Generator	Cross Section [pb]	$\hat{p}_T$ [GeV]	N_{gen}
105009	J0 jetjet	PYTHIA	$9860 \cdot 10^6$	8 – 17	999997
105010	J1 jetjet	PYTHIA	$678 \cdot 10^6$	17 – 35	999993
105011	J2 jetjet	PYTHIA	$41.0 \cdot 10^6$	35 – 70	999999
105012	J3 jetjet	PYTHIA	$2.19 \cdot 10^6$	70 – 140	999992
105013	J4 jetjet	PYTHIA	$87.7 \cdot 10^3$	140 – 280	989992
105014	J5 jetjet	PYTHIA	2350	280 – 560	999987
105015	J6 jetjet	PYTHIA	33.6	560 – 1120	999974
105016	J7 jetjet	PYTHIA	0.137	1120 – 2240	998955
105017	J8 jetjet	PYTHIA	$6.2 \cdot 10^{-6}$	> 2240	998948

Table B.7: QCD processes Monte Carlo samples used in the 0-lepton analyses including $\hat{p}_T$ cut (used for generator level splitting), cross section times branching ratio and the number of generated events of the sample [11–14].

Appendix C

Supplementary plots for the summer 2011 analysis

C.1 Additional plots for the reversed $\Delta\varphi$ QCD control region

This Section shows control distributions for the three-jet, four-jet and high-mass channel of CR2 of the *summer 2011* analysis (see Section 6.5.2).
In general, the agreement between the data and the MC simulation is very good, except for the high-mass channel, where the overall MC normalization seems to be a little bit off (data are above MC) and also the statistics is poor.

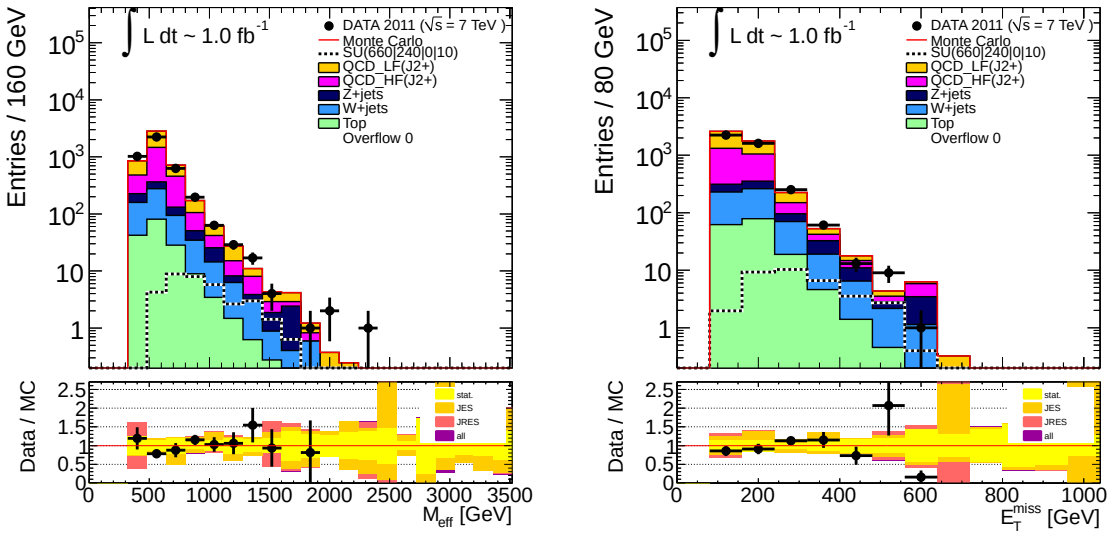

(a) Effective mass M_{eff}

(b) Missing transverse energy

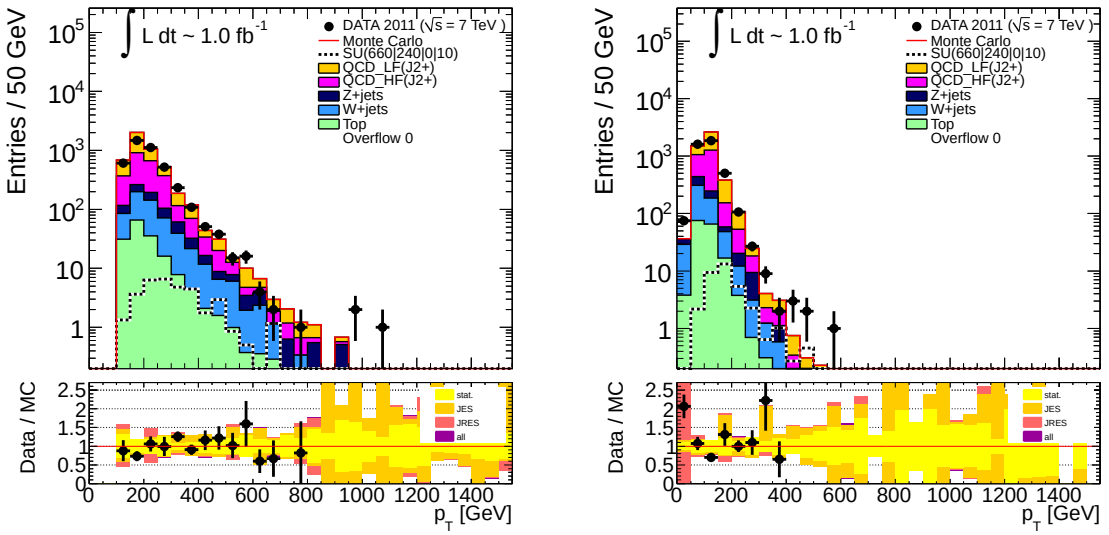

(c) Leading jet p_{T}

(d) Sub-leading jet p_{T}

Figure C.1: Distributions for the reversed $\Delta\varphi$ control region for the three-jet channel: M_{eff}, $E_{\text{T}}^{\text{miss}}$, leading and sub-leading jet p_{T} are shown before the final cut on M_{eff}. The MC simulation describes the data quite good.

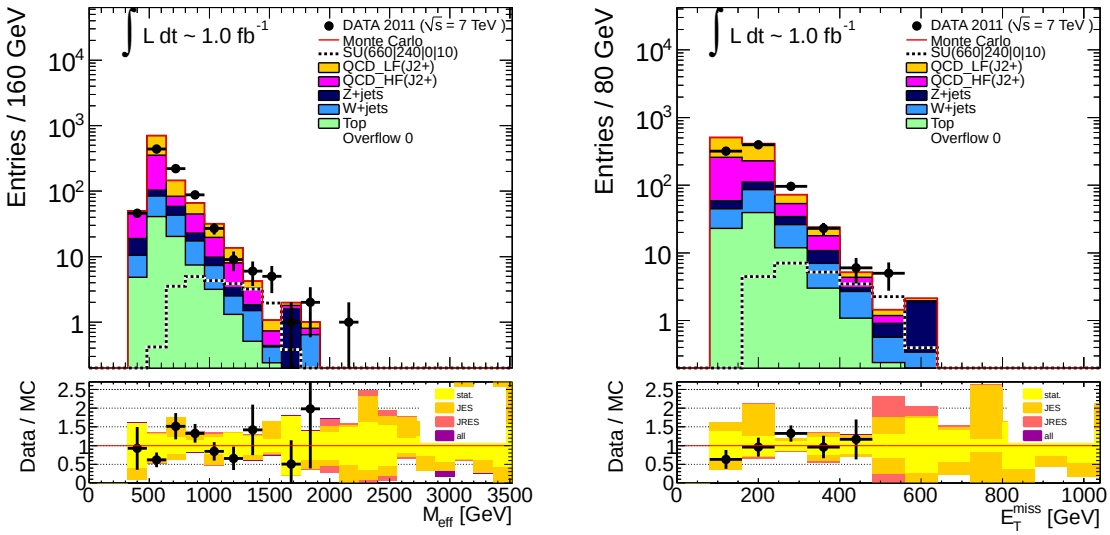

(a) Effective mass M_{eff} **(b)** Missing transverse energy

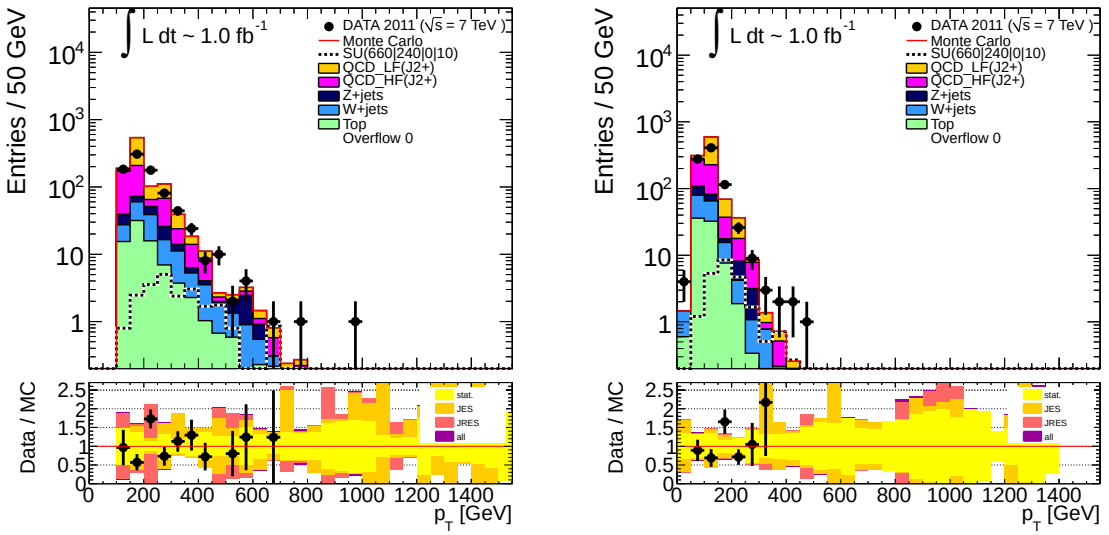

(c) Leading jet p_{T} **(d)** Sub-leading jet p_{T}

Figure C.2: Distributions for the reversed $\Delta\varphi$ control region for the four-jet channel: M_{eff}, $E_{\text{T}}^{\text{miss}}$, leading and sub-leading jet p_{T} are shown before the final cut on M_{eff}. The MC simulation describes the data quite good.

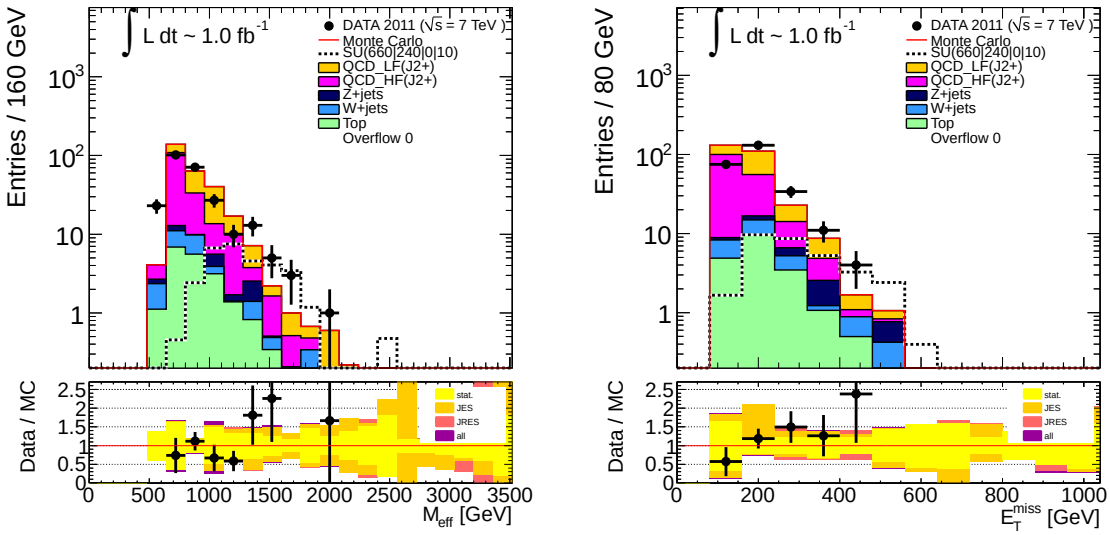

(a) Effective mass M_{eff} **(b)** Missing transverse energy

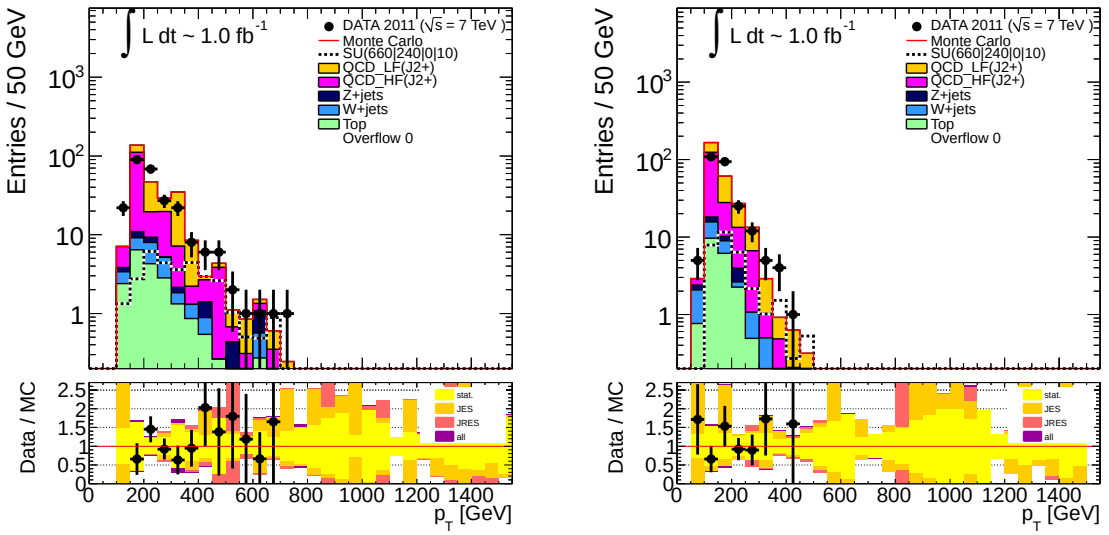

(c) Leading jet p_{T} **(d)** Sub-leading jet p_{T}

Figure C.3: Distributions for the reversed $\Delta\varphi$ control region for the high-mass channel: M_{eff}, $E_{\text{T}}^{\text{miss}}$, leading and sub-leading jet p_{T} are shown before the final cut on M_{eff}. The MC simulation describes the data quite good.

C.2 Additional plots for the rev. $E_{\mathrm{T}}^{\mathrm{miss}}/M_{\mathrm{eff}}$ CR

This Section shows control distributions for the two-jet, four-jet and high-mass channel of the *summer 2011* analysis in the region with reversed $E_{\mathrm{T}}^{\mathrm{miss}}/M_{\mathrm{eff}}$ cut (see Section 6.5.3).

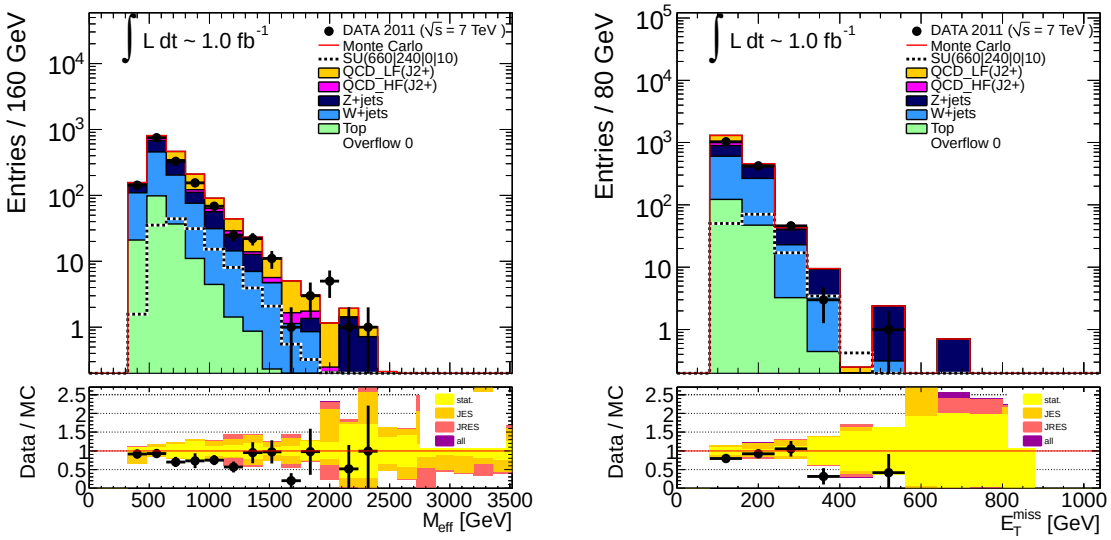

(a) Effective mass M_{eff}

(b) Missing transverse energy

Figure C.4: Effective mass and missing transverse energy in the two-jet channel with reversed $E_{\mathrm{T}}^{\mathrm{miss}}/M_{\mathrm{eff}}$ cut. The simulation describes the data well.

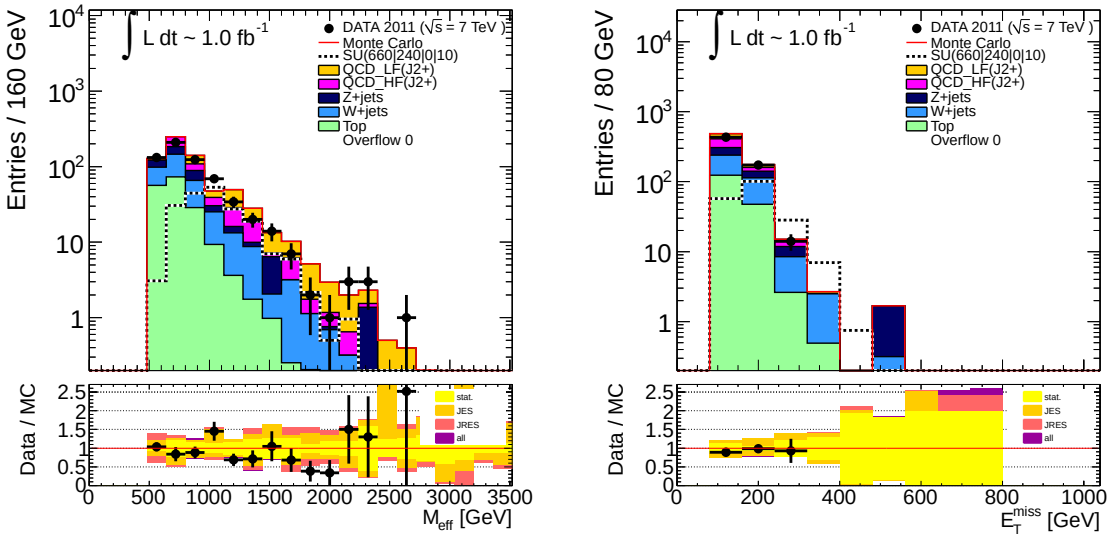

(a) Effective mass M_{eff} **(b)** Missing transverse energy

Figure C.5: Effective mass and missing transverse energy in the four-jet channel with reversed $E_{\text{T}}^{\text{miss}}$ $/M_{\text{eff}}$ cut. The simulation describes the data well.

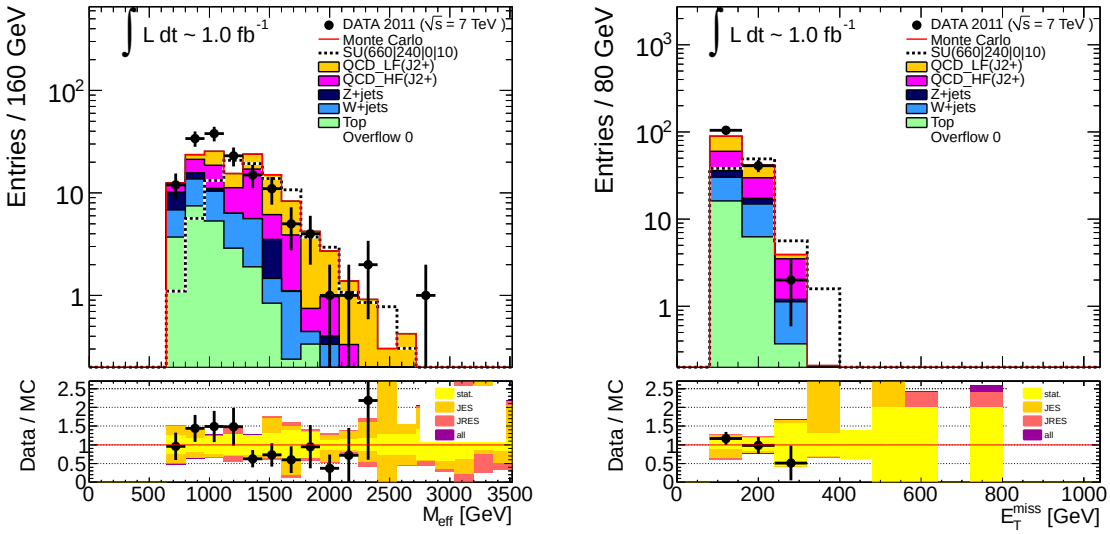

(a) Effective mass M_{eff} **(b)** Missing transverse energy

Figure C.6: Effective mass and missing transverse energy in the high-mass channel with reversed $E_{\text{T}}^{\text{miss}}$ $/M_{\text{eff}}$ cut. The simulation describes the data well.

C.3 Additional plots for the new QCD estimate

This Section shows additional plots from Section 7.3.

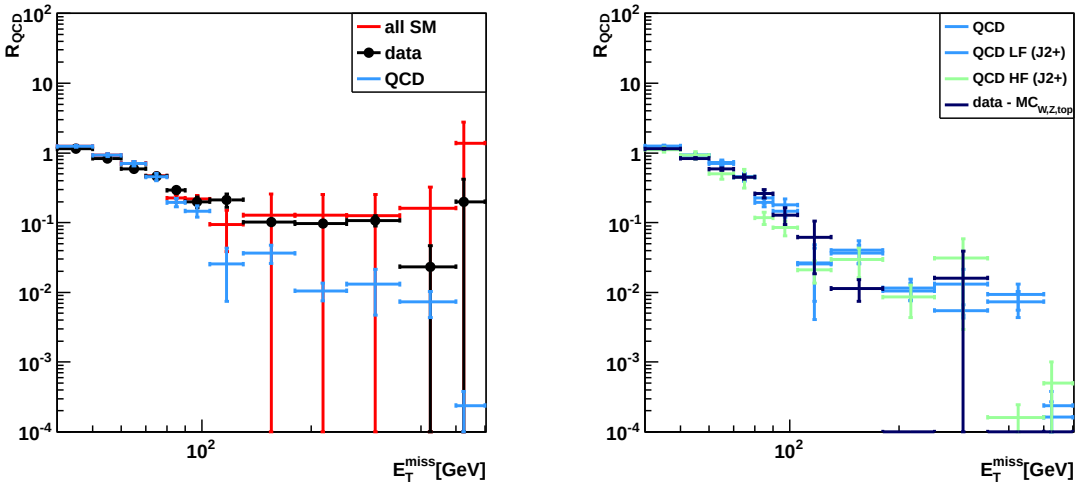

(a) two-jet: uncorrected

(b) two-jet: without contamination

(c) three-jet: uncorrected

(d) three-jet: without contamination

Figure C.7: R_{QCD} in the two-jet channel *(upper row)* and the three-jet channel *(lower row)*, before *(left column)* and after *(right column)* correction for contamination by non-QCD processes: the overall agreement between all Standard Model MC and data is fine, while $data - MC_{W,Z,top}$ compares well to the QCD MC prediction. Errors are of statistical nature only.

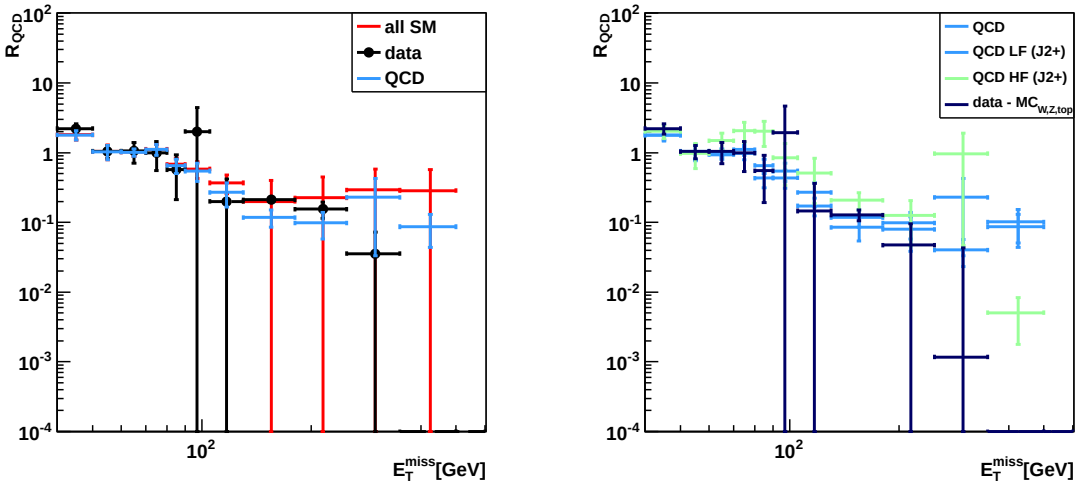

(a) uncorrected **(b)** without contamination

Figure C.8: R_{QCD} in the high-mass channel, before (see Figure C.8a) and (see Figure C.8b) after correction for contamination by non-QCD processes: the overall agreement between all Standard Model MC and data is fine, while $data - MC_{W,Z,top}$ compares well to the QCD MC prediction. Errors are of statistical nature only.

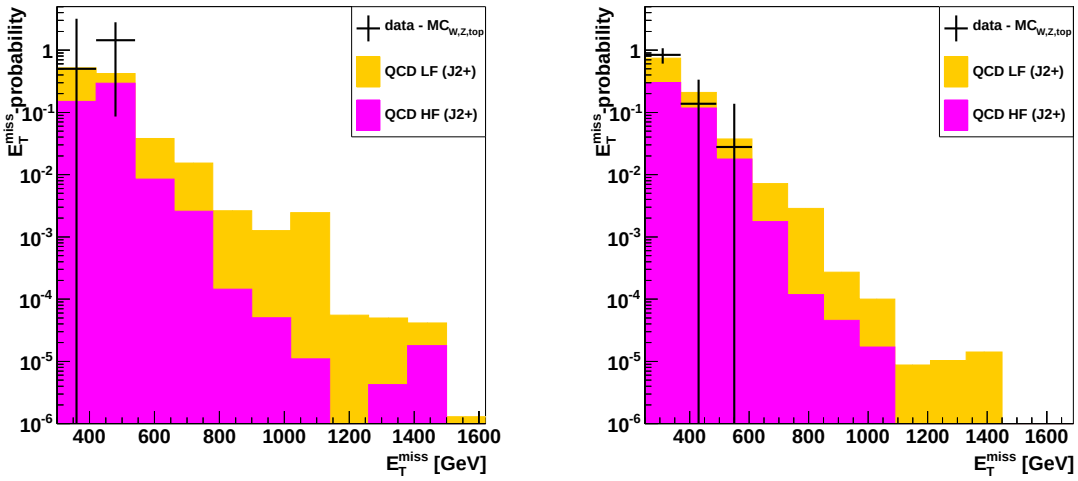

(a) $E_{\mathrm{T}}^{\mathrm{miss}}$ - probability for two-jet selection **(b)** $E_{\mathrm{T}}^{\mathrm{miss}}$ - probability for three-jet selection

Figure C.9: The obtained $E_{\mathrm{T}}^{\mathrm{miss}}$ - probabilities for the two- and three-jet channel are shown. With these distributions being determined from data, the QCD MC is shown for illustration.

C.4 Additional plots for the systematic Studies

This Section shows additional plots from Section 7.4.

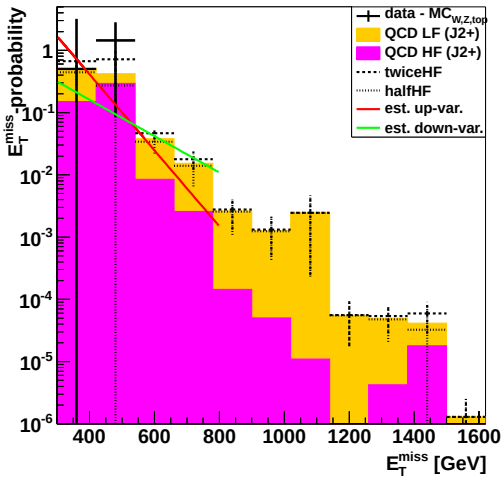

(a) $E_{\mathrm{T}}^{\mathrm{miss}}$ - probability for two-jet selection

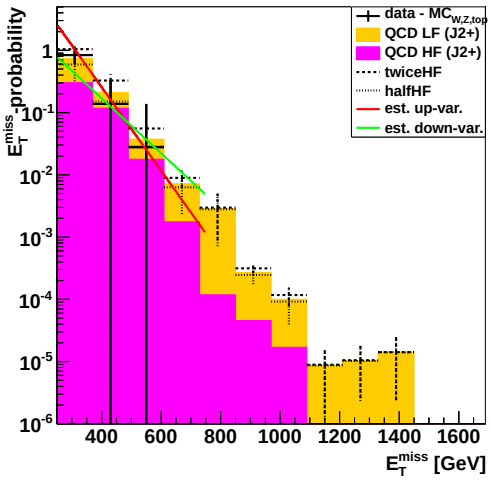

(b) $E_{\mathrm{T}}^{\mathrm{miss}}$ - probability for three-jet selection

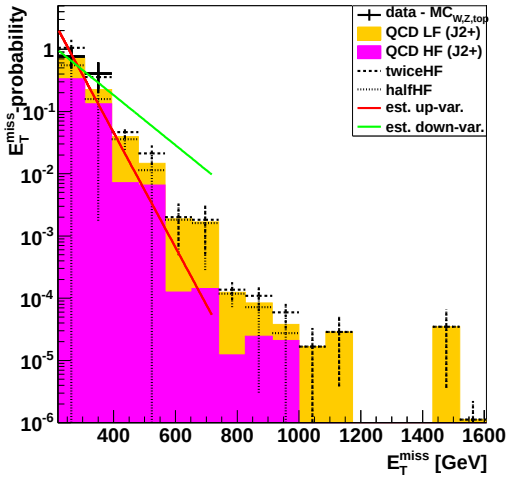

(c) $E_{\mathrm{T}}^{\mathrm{miss}}$ - probability for high-mass selection

Figure C.10: The obtained $E_{\mathrm{T}}^{\mathrm{miss}}$ - probabilities for the two-, three-jet and high-mass channel are shown including its assumed shape uncertainties (red and green).

Appendix D

Supplementary material for the complete 2011 analysis

D.1 Additional plots for the rev. $\Delta\varphi$ QCD CR

This Section shows some key distributions for the reversed $\Delta\varphi$ CR for $E_{\mathrm{T}}^{\mathrm{miss}}$ values above 160 GeV in the remaining channels following the two-jet, two-jet prime, three-jet, four-jet and six-jet selection (see Table 8.1). While the two-jet prime channel shows a discrepancy between the data and the MC simulation in QCD-dominated regions, resulting from a lack of statistics in the QCD MC (see Section 8.2), the remaining channels show a good agreement.

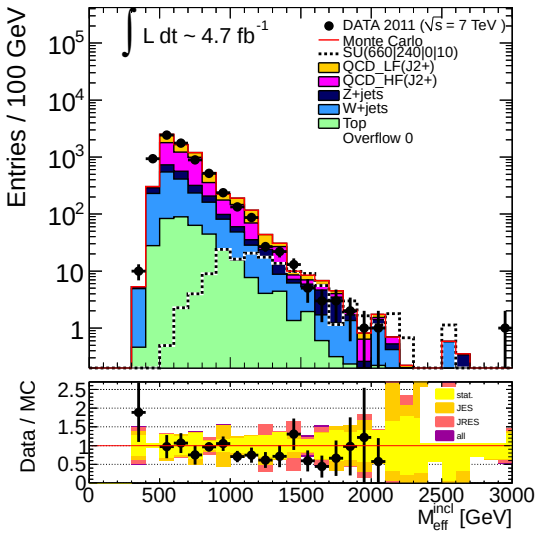

(a) Effective mass M_{eff} (incl.)

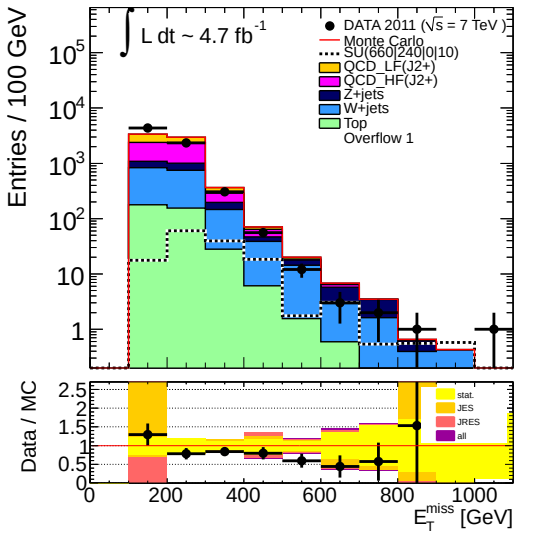

(b) Missing transverse energy

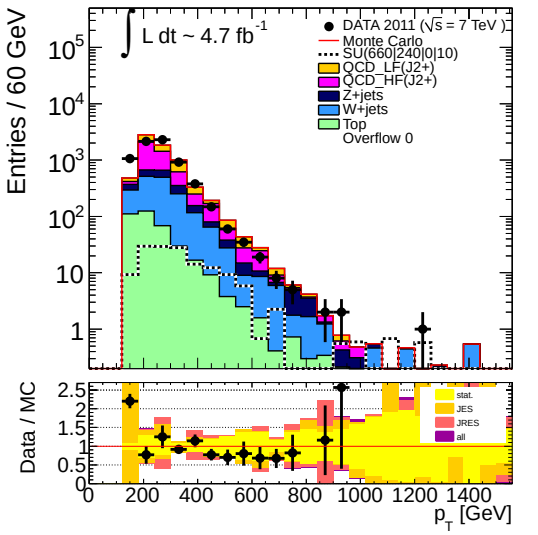

(c) Leading jet p_{T}

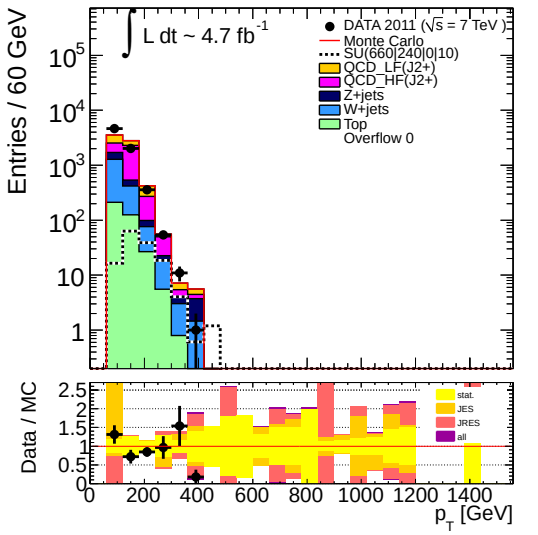

(d) Sub-leading jet p_{T}

Figure D.1: Distributions for the reversed $\Delta\varphi$ control region for the two-jet channel: $M_{\text{eff}}^{\text{incl}}$, $E_{\text{T}}^{\text{miss}}$, leading and sub-leading jet p_{T} are shown before the final cut on M_{eff}. The MC simulation describes the data quite good.

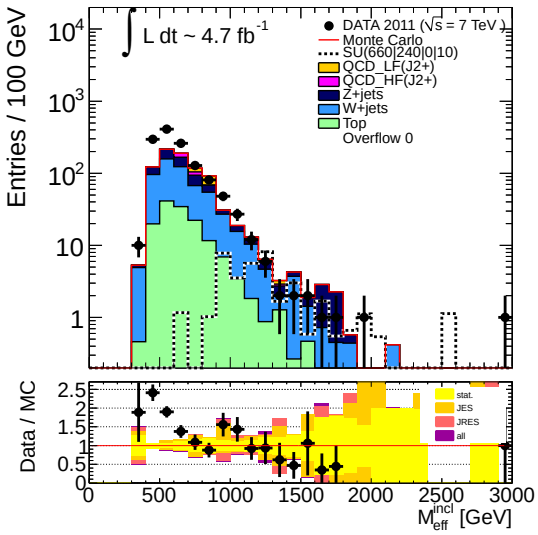

(a) Effective mass M_{eff} (incl.)

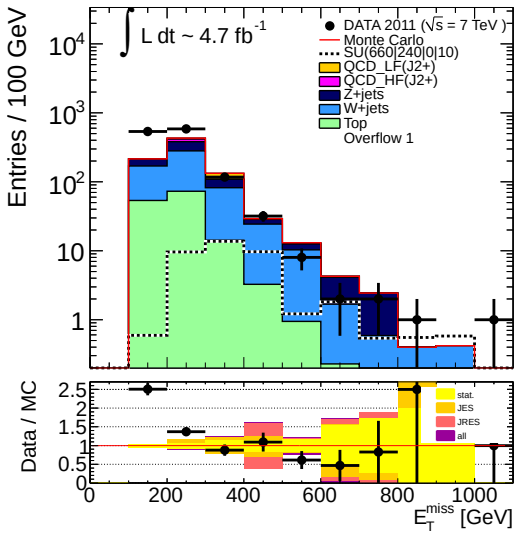

(b) Missing transverse energy

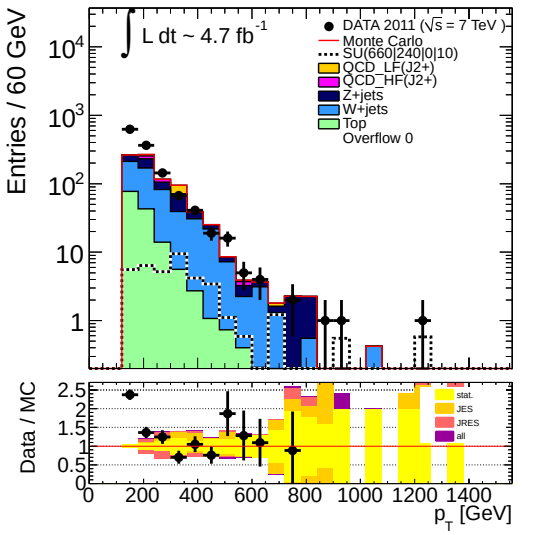

(c) Leading jet p_{T}

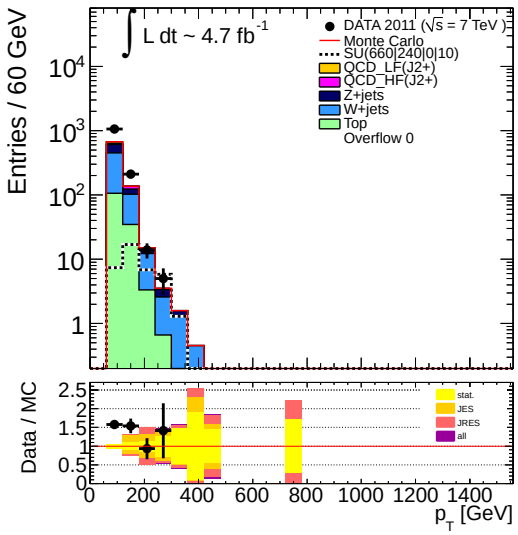

(d) Sub-leading jet p_{T}

Figure D.2: Distributions for the reversed $\Delta\varphi$ control region for the two-jet prime channel: $M_{\text{eff}}^{\text{incl}}$, $E_{\text{T}}^{\text{miss}}$, leading and sub-leading jet p_{T} are shown before the final cut on M_{eff}. Besides the lack of statistics in the QCD MC due to the harsh $E_{\text{T}}^{\text{miss}}$ $/M_{\text{eff}}$ cut (see Section 8.2), the MC simulation describes the data quite good.

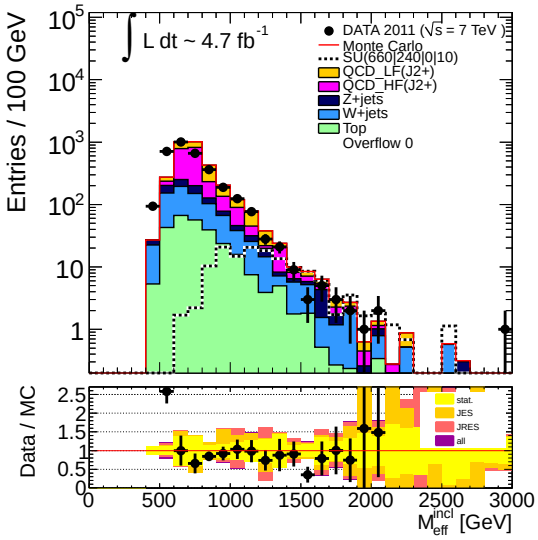

(a) Effective mass M_{eff} (incl.)

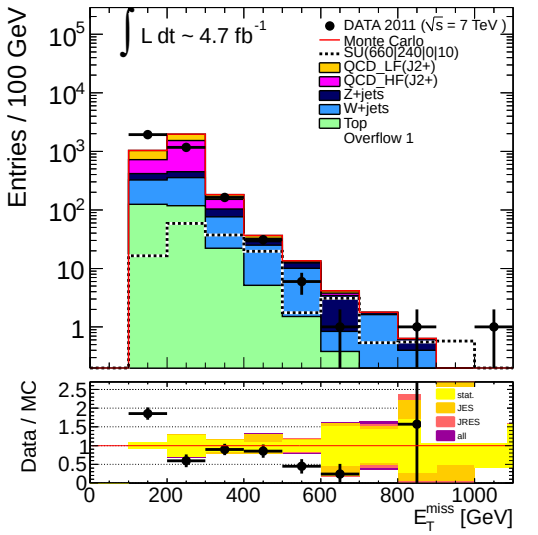

(b) Missing transverse energy

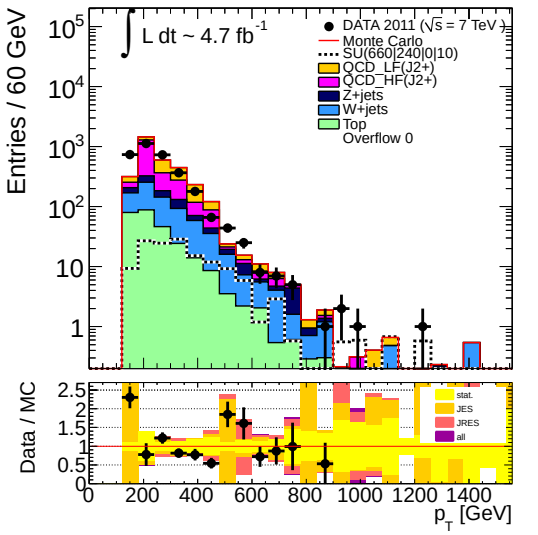

(c) Leading jet p_{T}

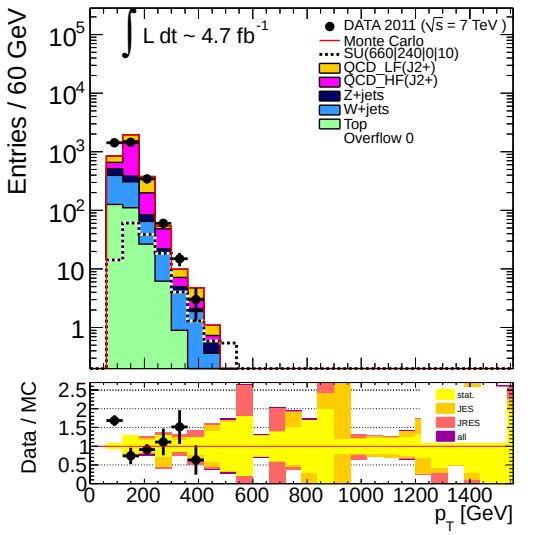

(d) Sub-leading jet p_{T}

Figure D.3: Distributions for the reversed $\Delta\varphi$ control region for the three-jet channel: $M_{\text{eff}}^{\text{incl}}$, $E_{\text{T}}^{\text{miss}}$, leading and sub-leading jet p_{T} are shown before the final cut on M_{eff}. The MC simulation describes the data quite good.

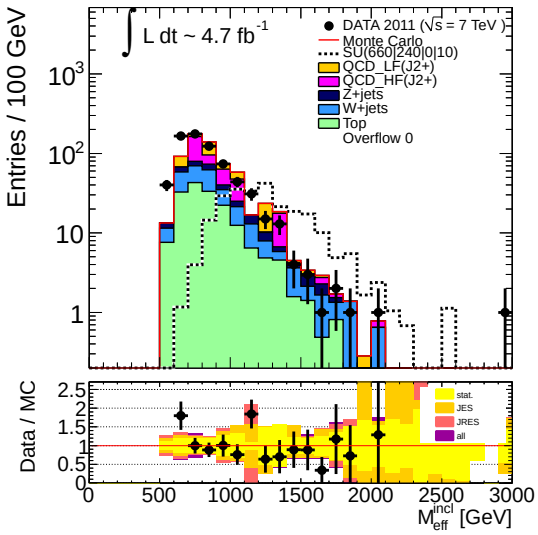

(a) Effective mass M_{eff} (incl.)

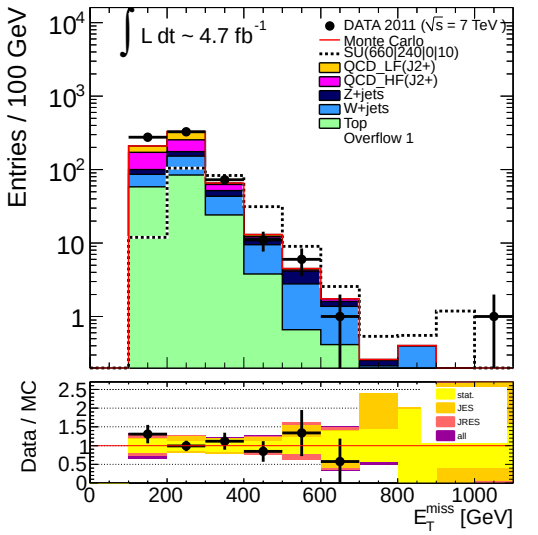

(b) Missing transverse energy

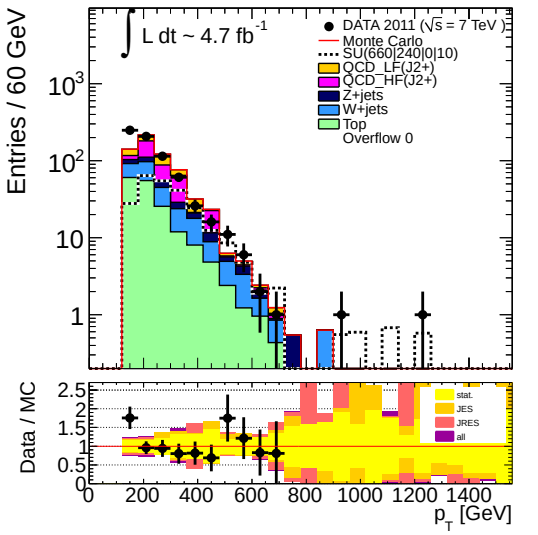

(c) Leading jet p_{T}

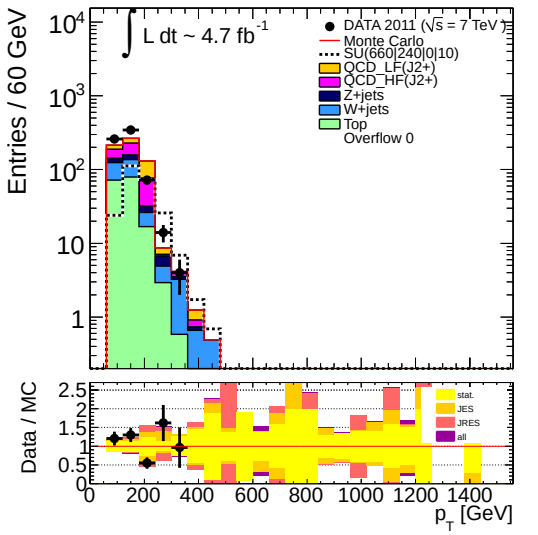

(d) Sub-leading jet p_{T}

Figure D.4: Distributions for the reversed $\Delta\varphi$ control region for the four-jet channel: $M_{\text{eff}}^{\text{incl}}$, $E_{\text{T}}^{\text{miss}}$, leading and sub-leading jet p_{T} are shown before the final cut on M_{eff}. The MC simulation describes the data quite good.

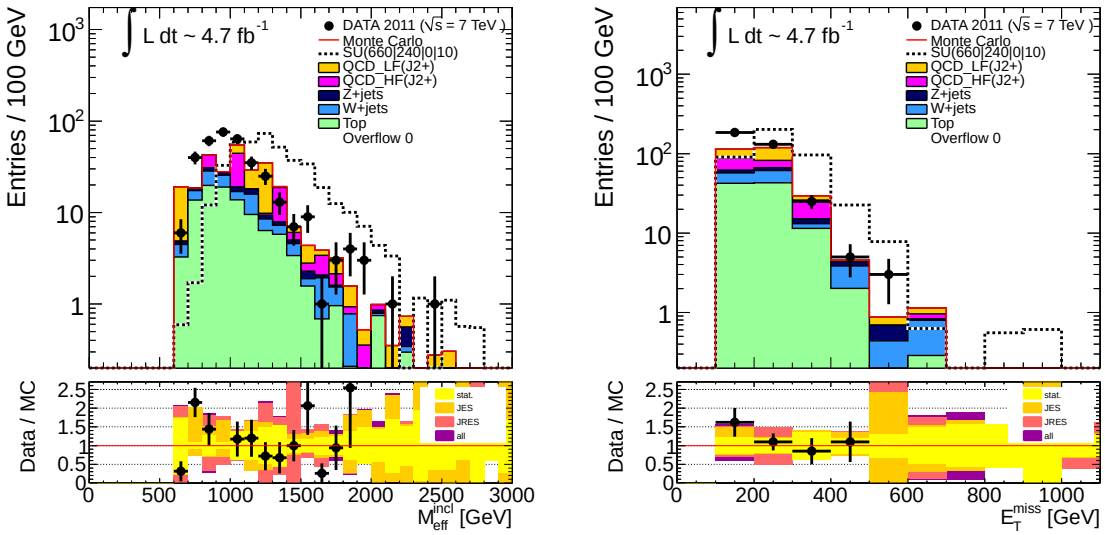

(a) Effective mass M_{eff} (incl.)

(b) Missing transverse energy

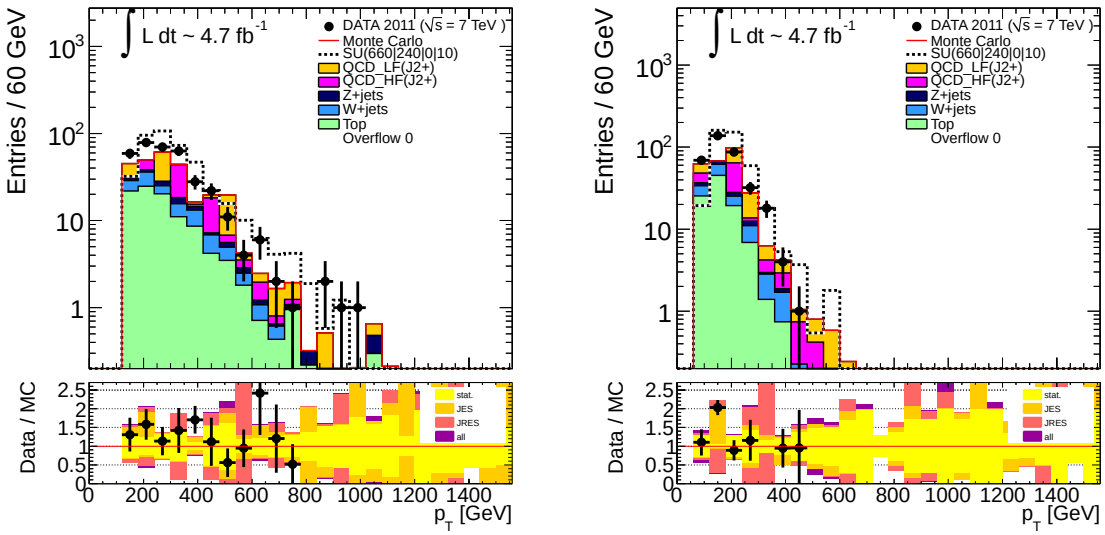

(c) Leading jet p_{T}

(d) Sub-leading jet p_{T}

Figure D.5: Distributions for the reversed $\Delta\varphi$ control region for the six-jet channel: $M_{\text{eff}}^{\text{incl}}$, $E_{\text{T}}^{\text{miss}}$, leading and sub-leading jet p_{T} are shown before the final cut on M_{eff}. The MC simulation describes the data quite good.

D.2 Additional plots for the rev. $E_{\mathrm{T}}^{\mathrm{miss}}/M_{\mathrm{eff}}$ CR

This Section shows some key distributions for the reversed $E_{\mathrm{T}}^{\mathrm{miss}}/M_{\mathrm{eff}}$ CR for $E_{\mathrm{T}}^{\mathrm{miss}}$ values above 160 GeV in the remaining channels following the two-jet, two-jet prime, three-jet, four-jet and six-jet selection (see Table 8.1).

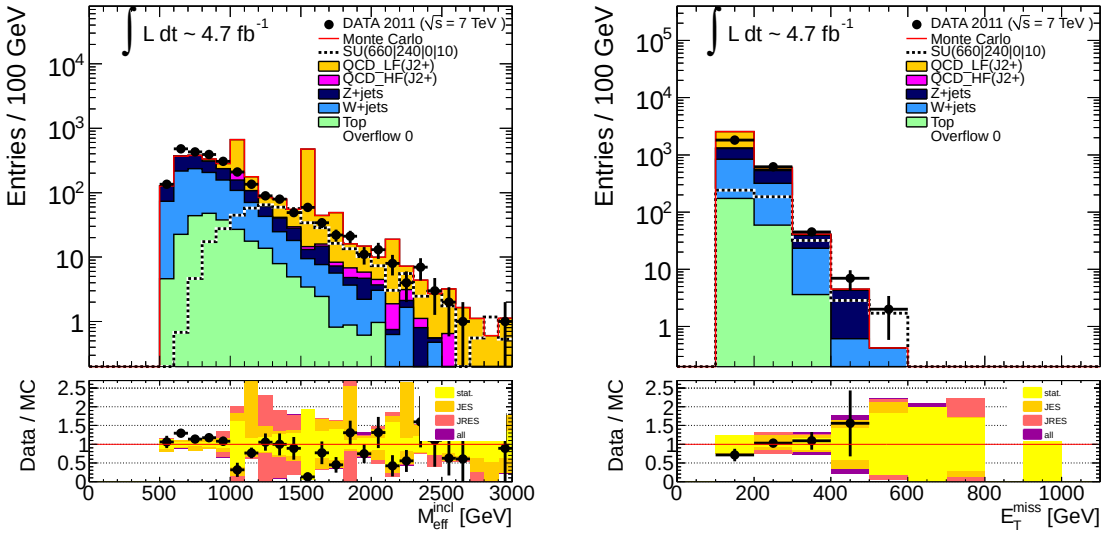

(a) Effective mass M_{eff} (incl.)

(b) Missing transverse energy

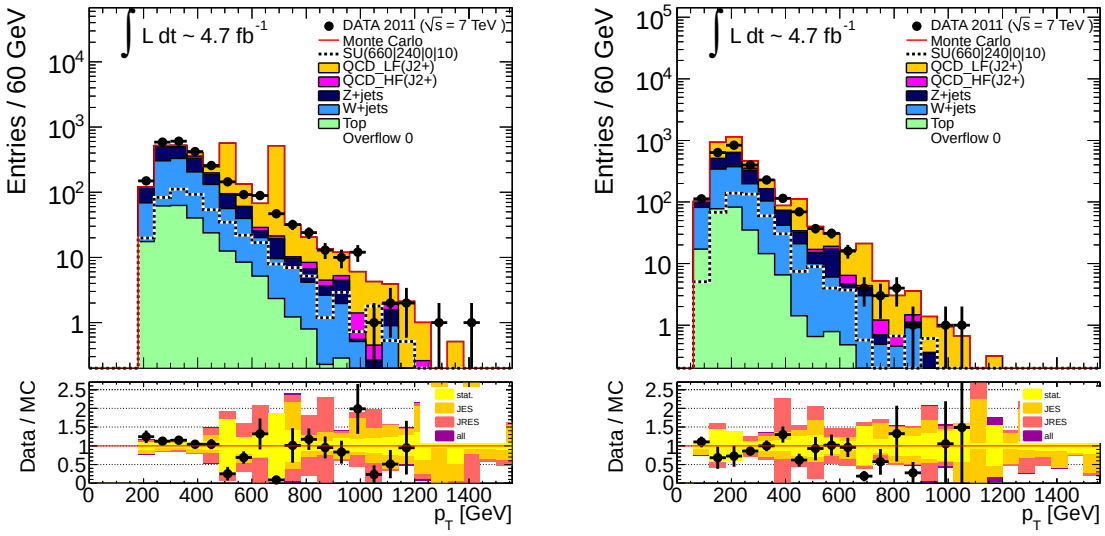

(c) Leading jet p_{T}

(d) Sub-leading jet p_{T}

Figure D.6: Effective mass (incl.), missing transverse energy, leading and sub-leading jet-p_{T} distributions for the two-jet channel with reversed $E_{\mathrm{T}}^{\mathrm{miss}}/M_{\mathrm{eff}}$ cut (before final M_{eff} cut). The simulation describes the data well.

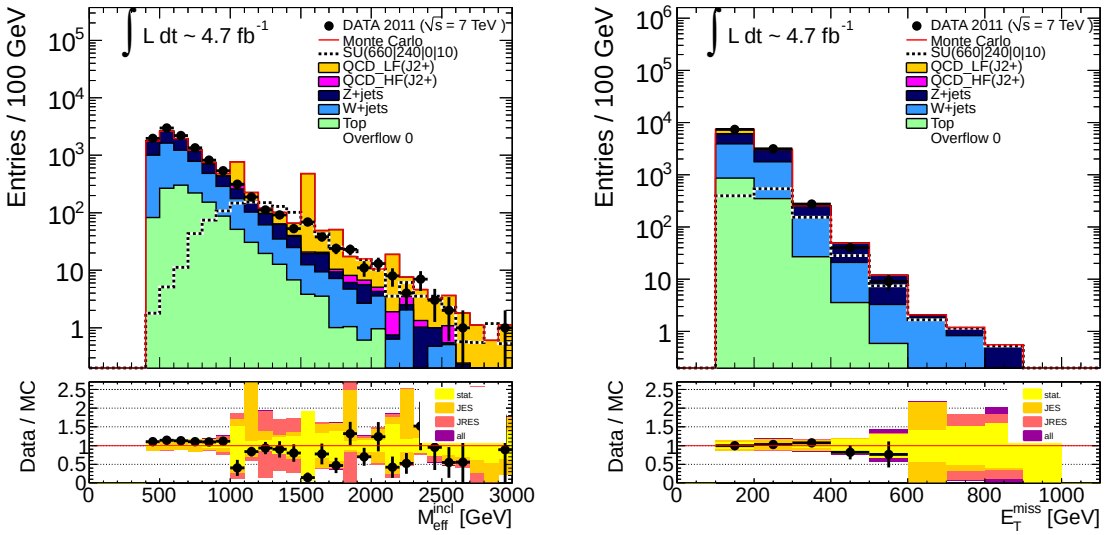

(a) Effective mass M_{eff} (incl.) **(b)** Missing transverse energy

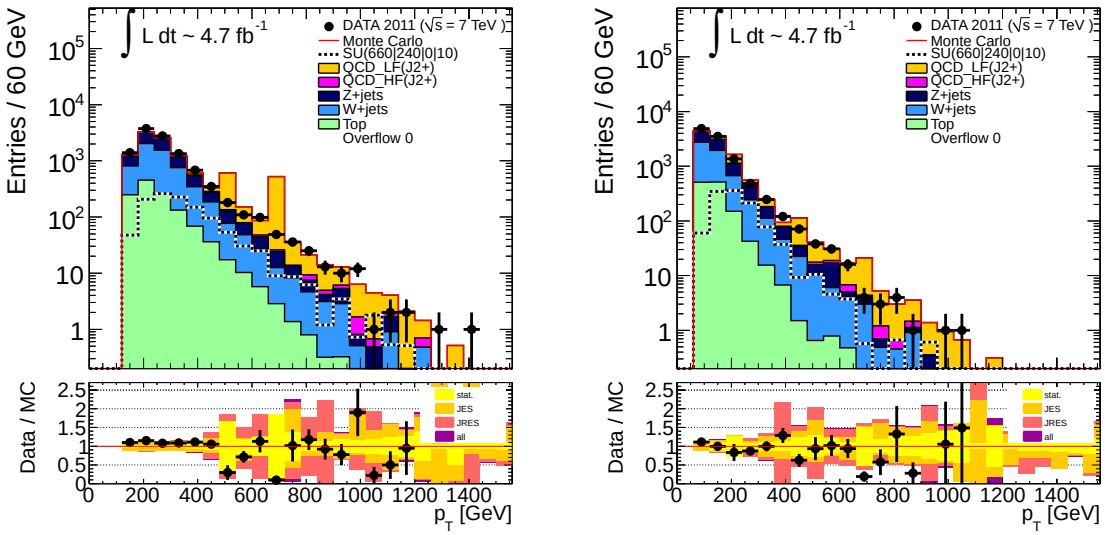

(c) Leading jet p_{T} **(d)** Sub-leading jet p_{T}

Figure D.7: Effective mass (incl.), missing transverse energy, leading and sub-leading jet-p_{T} distributions for the two-jet prime channel with reversed $E_{\text{T}}^{\text{miss}}$ /M_{eff} cut (before final M_{eff} cut). The simulation describes the data well.

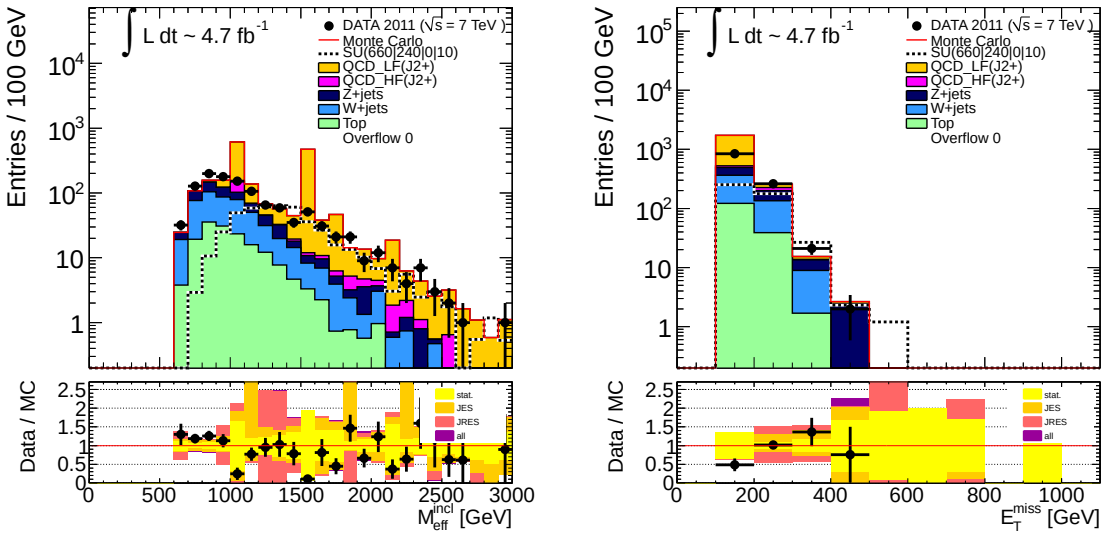

(a) Effective mass M_{eff} (incl.) **(b)** Missing transverse energy

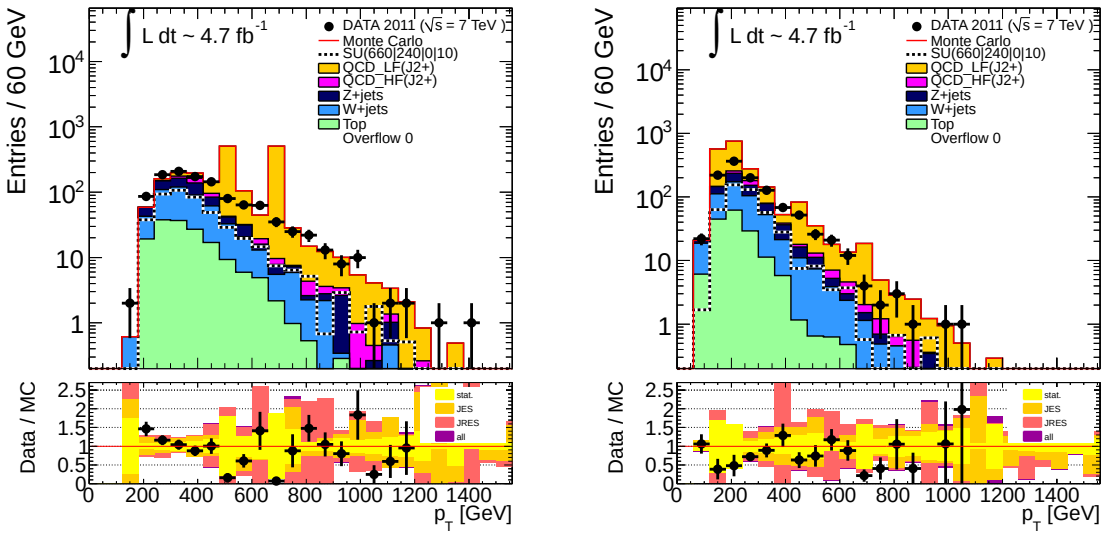

(c) Leading jet p_{T} **(d)** Sub-leading jet p_{T}

Figure D.8: Effective mass (incl.), missing transverse energy, leading and sub-leading jet-p_{T} distributions for the three-jet channel with reversed $E_{\text{T}}^{\text{miss}}$ /M_{eff} cut (before final M_{eff} cut). The simulation describes the data well.

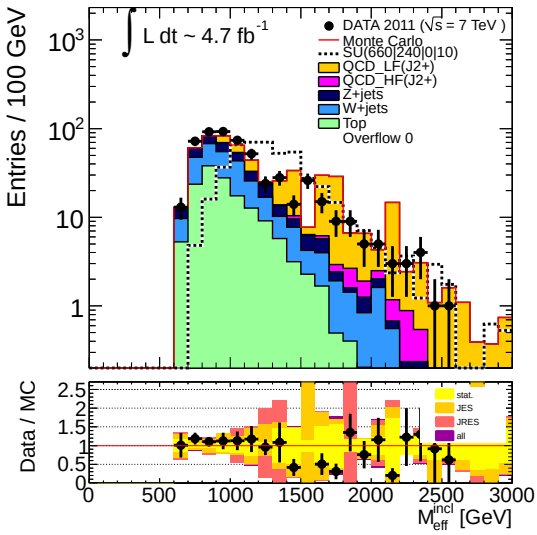

(a) Effective mass M_{eff} (incl.)

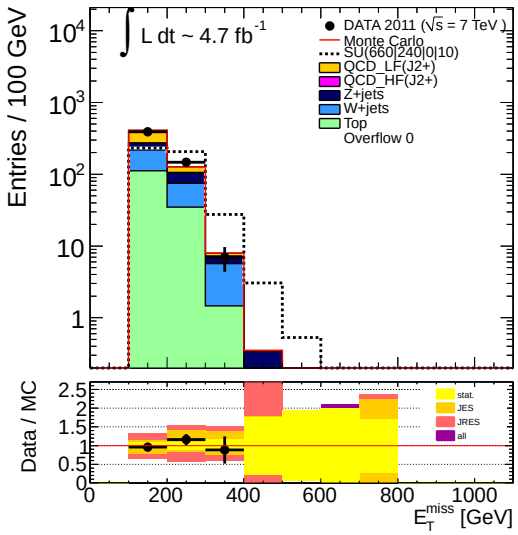

(b) Missing transverse energy

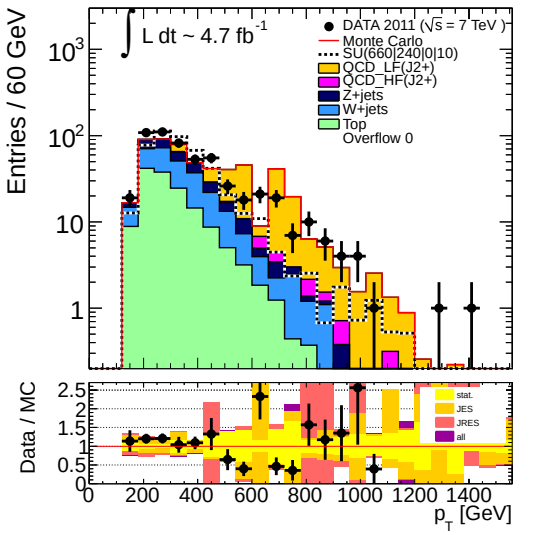

(c) Leading jet p_{T}

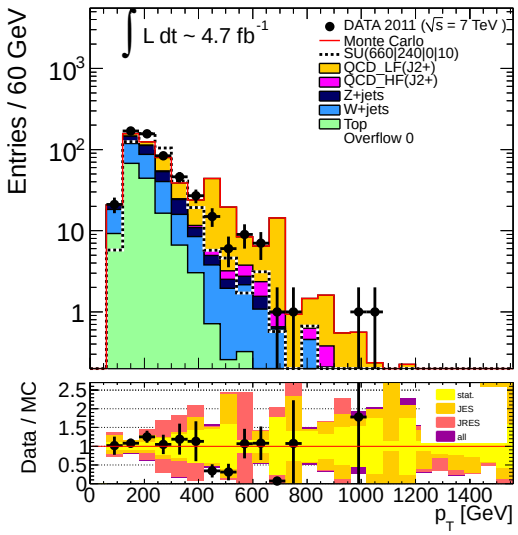

(d) Sub-leading jet p_{T}

Figure D.9: Effective mass (incl.), missing transverse energy, leading and sub-leading jet-p_{T} distributions for the four-jet channel with reversed $E_{\text{T}}^{\text{miss}}$ /M_{eff} cut (before final M_{eff} cut). The simulation describes the data well.

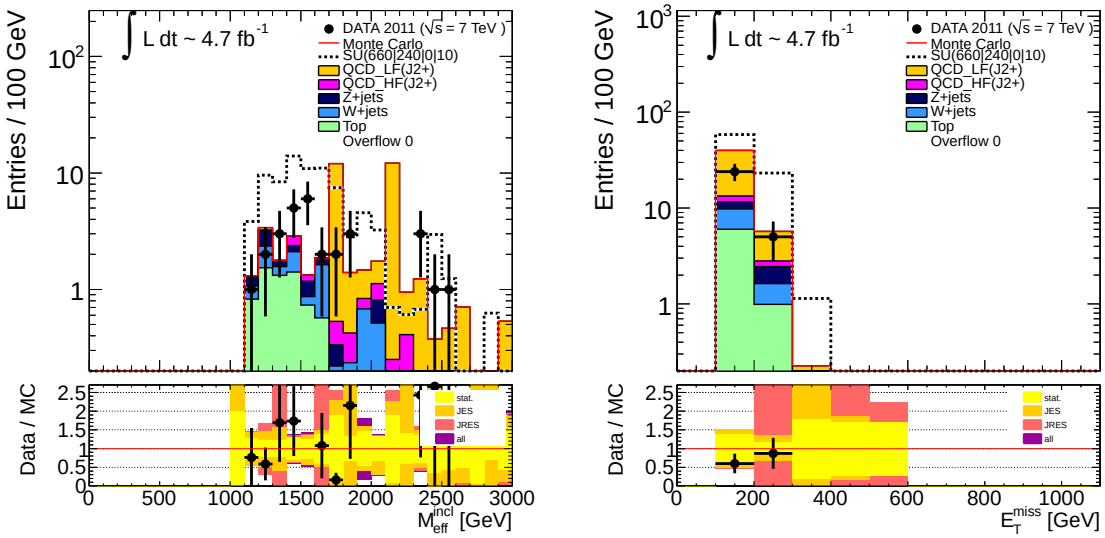

(a) Effective mass M_{eff} (incl.) **(b)** Missing transverse energy

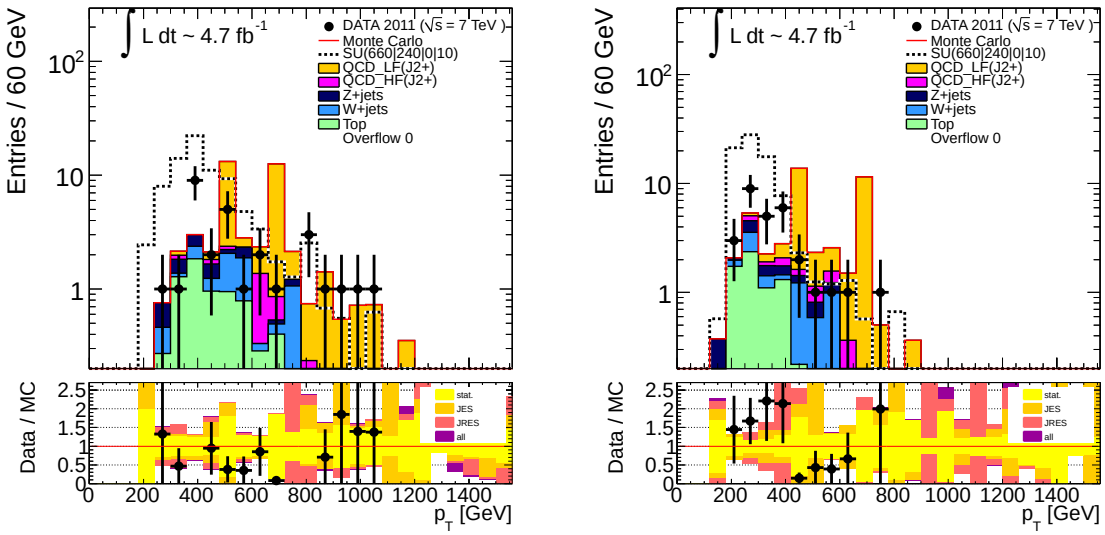

(c) Leading jet p_{T} **(d)** Sub-leading jet p_{T}

Figure D.10: Effective mass (incl.), missing transverse energy, leading and sub-leading jet-p_{T} distributions for the six-jet channel with reversed $E_{\text{T}}^{\text{miss}}$ /M_{eff} cut (before final M_{eff} cut). The simulation describes the data well.

D.3 Additional plots for the new QCD estimate

This Section shows additional plots from Section 8.2.2.

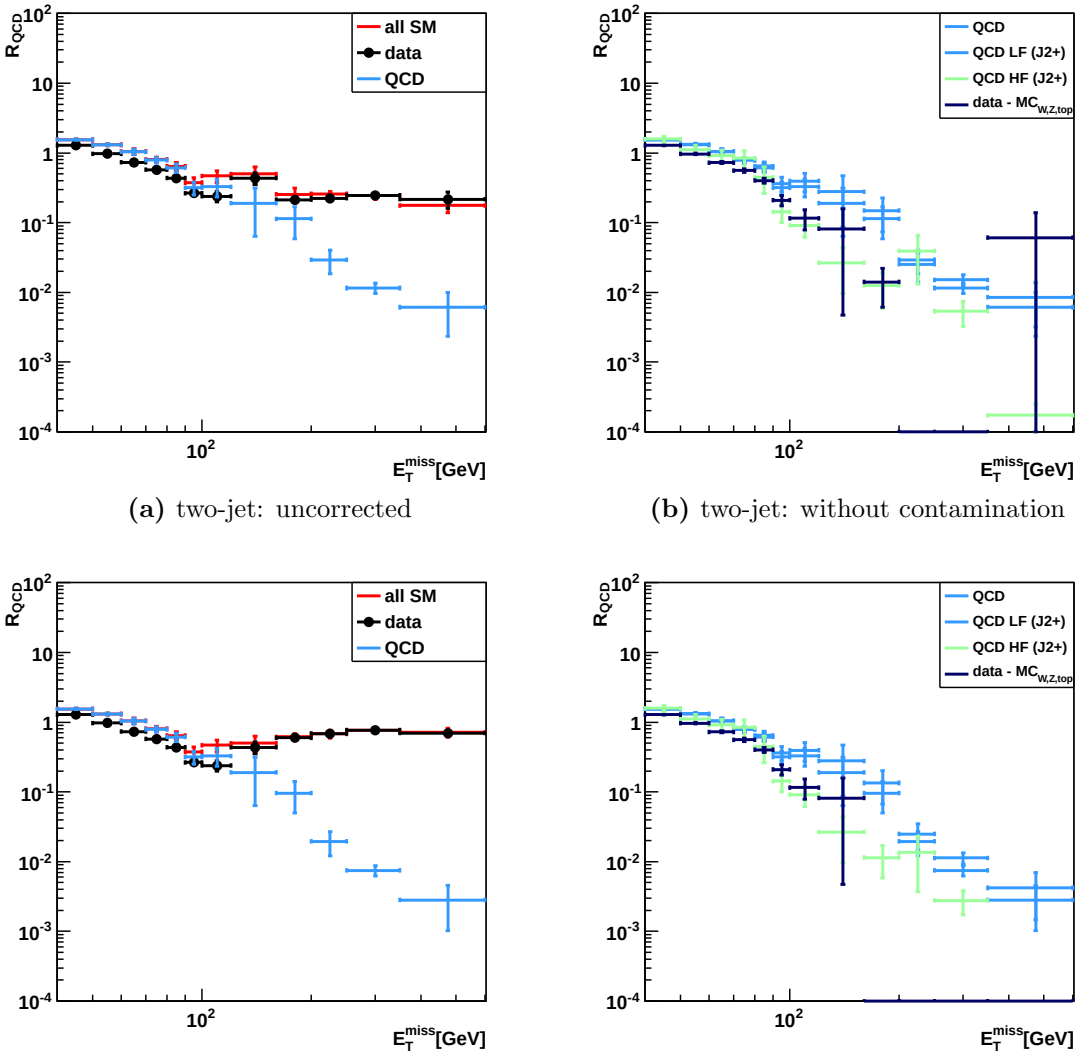

(a) two-jet: uncorrected

(b) two-jet: without contamination

(c) two-jet prime: uncorrected

(d) two-jet prime: without contamination

Figure D.11: R_{QCD} in the two-jet channel *(upper row)* and the two-jet prime channel *(lower row)*, before *(left column)* and after *(right column)* correction for contamination by non-QCD processes: the overall agreement between all Standard Model MC and data is fine, while $data - MC_{W,Z,top}$ compares well to the QCD MC prediction. Errors are of statistical nature only.

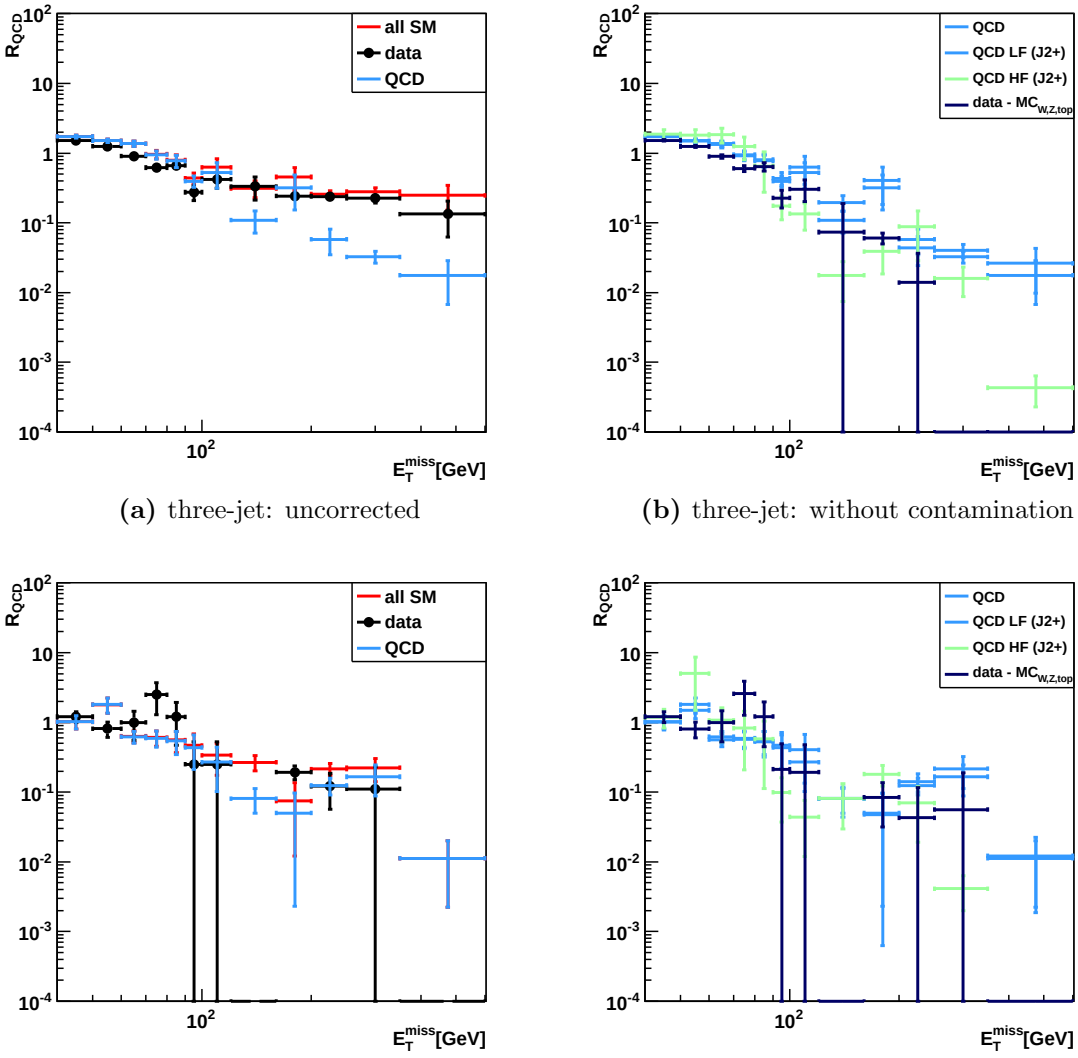

(a) three-jet: uncorrected

(b) three-jet: without contamination

(c) six-jet: uncorrected

(d) six-jet: without contamination

Figure D.12: R_{QCD} in the three-jet channel *(upper row)* and the six-jet channel *(lower row)*, before *(left column)* and after *(right column)* correction for contamination by non-QCD processes: the overall agreement between all Standard Model MC and data is fine, while $data - MC_{W,Z,top}$ compares well to the QCD MC prediction. Errors are of statistical nature only.

D.4 Additional plots for the systematic studies

This Section shows additional plots from Section 8.2.4.

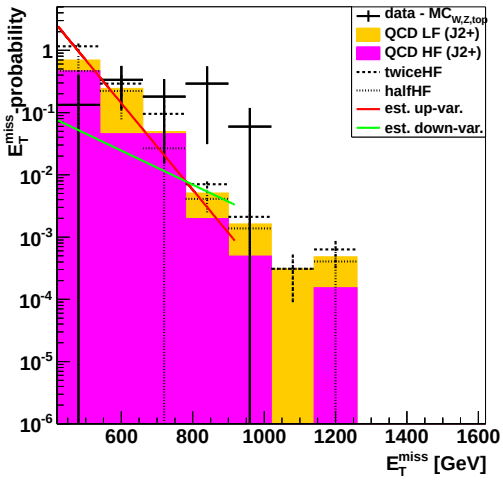

(a) two-jet medium

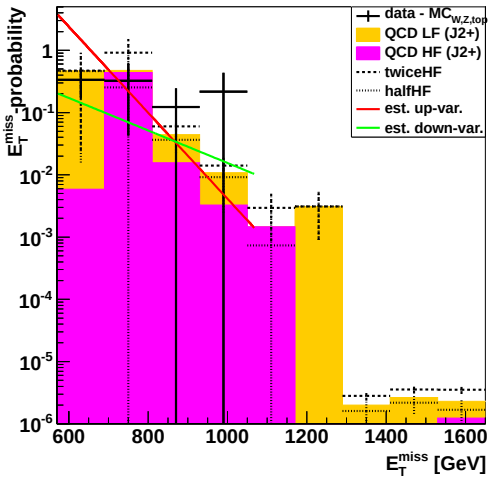

(b) two-jet tight

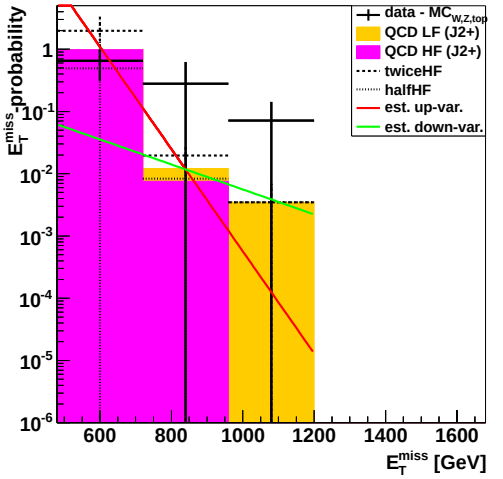

(c) two-jet prime medium

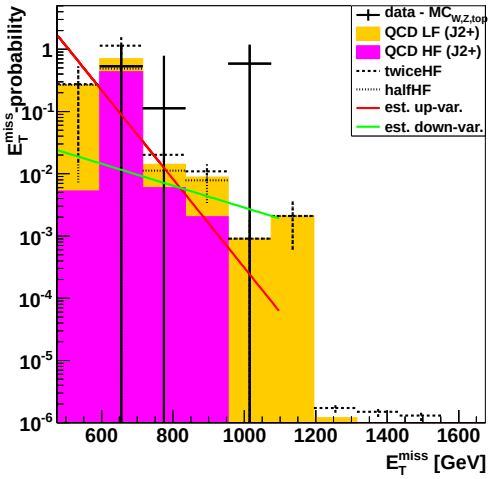

(d) three-jet tight

Figure D.13: The obtained $E_{\mathrm{T}}^{\mathrm{miss}}$ -probabilities for remaining channels of the *complete 2011* analysis are shown including its assumed shape uncertainties (red and green).

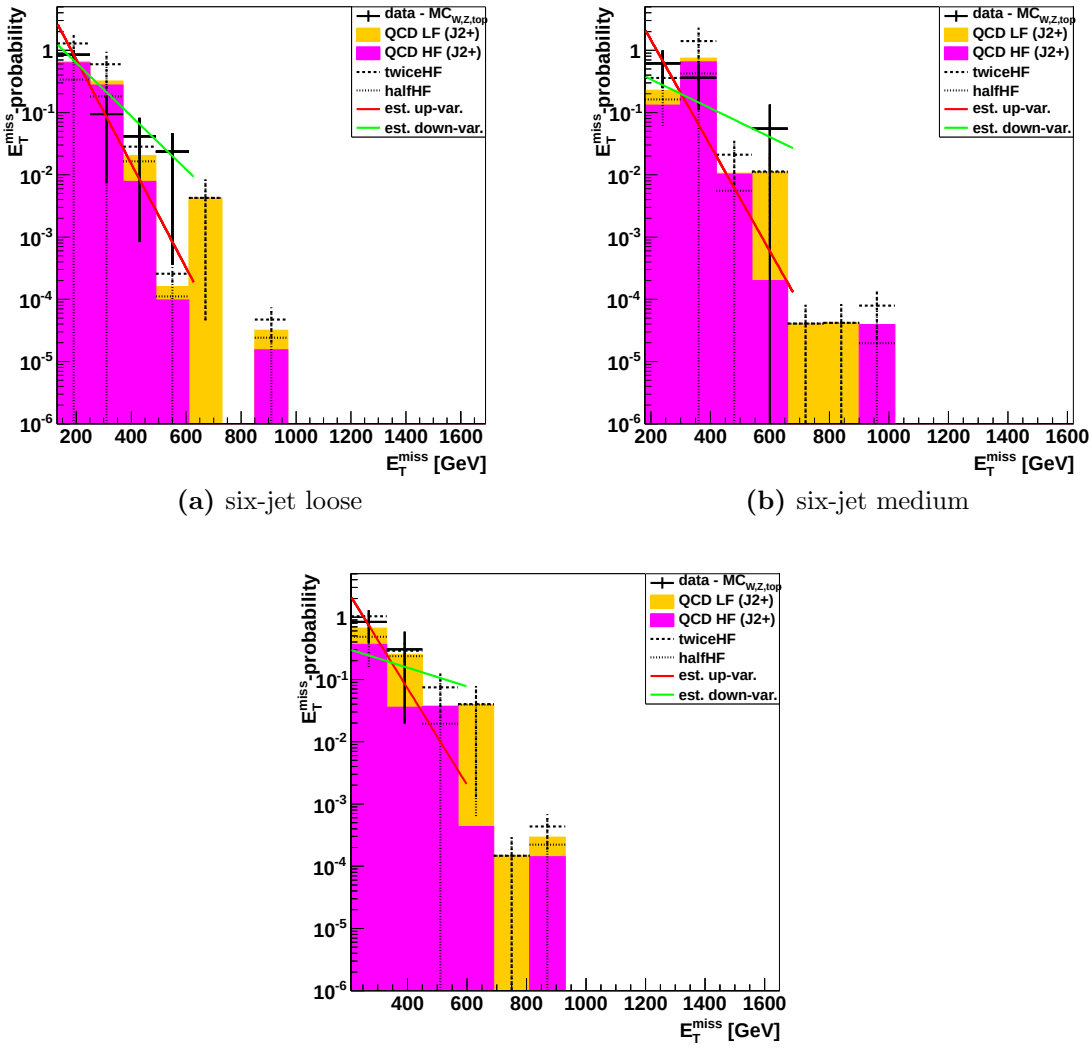

(a) six-jet loose

(b) six-jet medium

(c) six-jet tight

Figure D.14: The obtained $E_{\mathrm{T}}^{\mathrm{miss}}$ -probabilities for remaining channels of the *complete 2011* analysis are shown including its assumed shape uncertainties (red and green).

D.5 Results of the jet-smearing method

The jet-smearing method [168] underwent some improvements such as better understood systematic uncertainties and both the symmetric response function, i.e. the dijet-balance, as well as the asymmetric tail response, i.e. the Mercedes-analysis, are now binned in η and p_{T}. The resulting TFs, as quoted in [11–14] , are shown in Table D.1.

Signal Region	$N_{\mathrm{SR}}/N_{\mathrm{CR2}}$ ($\times 10^{-3}$)				
	(central)	(stat.)	(mean shift)	($\sigma_{correction}$)	(tail)
Moriond numbers (dated: 12.03.2012)					
A Medium	36.3	$\pm$ 12.3	$\pm$ 9.1	$\pm$ 7.3	$^{+35.9}_{-18.1}$
A Tight	2.1	$\pm$ 1.2	$\pm$ 6.5	$\pm$ 0.45	$^{+7.2}_{-0.9}$
A$'$ Medium	98.3	$\pm$ 14.3	$\pm$ 9.7	$\pm$ 8.8	$^{+87.3}_{-17.6}$
B Tight	1.3	$\pm$ 0.7	$\pm$ 2.2	$\pm$ 0.15	$^{+6.0}_{-0.4}$
C Loose	5.1	$\pm$ 0.9	$\pm$ 3.5	$\pm$ 1.45	$^{+11.2}_{-4.0}$
C Medium	2.6	$\pm$ 0.7	$\pm$ 0.9	$\pm$ 0.7	$^{+10.5}_{-1.0}$
C Tight	1.4	$\pm$ 0.9	$\pm$ 0.5	$\pm$ 0.35	$^{+3.8}_{-0.5}$
D Tight	2.8	$\pm$ 1.3	$\pm$ 0.0	$\pm$ 1.1	$^{+8.3}_{-0.5}$
E Loose	24.5	$\pm$ 2.0	$\pm$ 2.0	$\pm$ 9.6	$^{+8.8}_{-3.2}$
E Medium	25.9	$\pm$ 3.7	$\pm$ 6.9	$\pm$ 8.35	$^{+12.4}_{-3.4}$
E Tight	20.7	$\pm$ 5.5	$\pm$ 6.0	$\pm$ 5.05	$^{+18.1}_{-3.5}$
PRD numbers (dated: 24.07.2012)					
A Medium	32.0	$\pm$ 5.7	$\pm$ 6.6	$^{+0.0}_{-2.5}$	$^{+12.0}_{-11.9}$
A Tight	9.0	$\pm$ 3.3	$\pm$ 0.3	$^{+4.4}_{-3.0}$	$^{+6.4}_{-1.6}$
A$'$ Medium	104.9	$\pm$ 13.5	$\pm$ 29.0	$^{+0.0}_{-30.7}$	$^{+29.5}_{-17.1}$
B Tight	11.4	$\pm$ 2.7	$\pm$ 1.5	$^{+5.4}_{-0.2}$	$^{+4.7}_{-0.0}$
C Loose	16.0	$\pm$ 4.6	$\pm$ 1.5	$^{+5.1}_{-9.7}$	$^{+1.5}_{-0.0}$
C Medium	3.0	$\pm$ 0.6	$\pm$ 0.8	$^{+4.1}_{-0.9}$	$^{+1.4}_{-1.1}$
C Tight	3.4	$\pm$ 1.5	$\pm$ 0.1	$^{+3.6}_{-0.4}$	$^{+1.8}_{-0.0}$
D Tight	19.5	$\pm$ 3.1	$\pm$ 4.5	$^{+6.1}_{-6.2}$	$^{+0.0}_{-6.8}$
E Loose	48.3	$\pm$ 2.5	$\pm$ 0.8	$^{+37.4}_{-14.6}$	$^{+2.2}_{-1.3}$
E Medium	38.4	$\pm$ 1.8	$\pm$ 3.7	$^{+29.6}_{-6.4}$	$^{+0.4}_{-2.5}$
E Tight	40.3	$\pm$ 2.3	$\pm$ 6.3	$^{+20.1}_{-4.0}$	$^{+0.0}_{-3.6}$

Table D.1: Predicted ratios of events in control and signal region for the eleven analysis channels using the jet-smearing method [11–14]. Mean uncertainty refers to shifting the mean of the jet response up to take into account a bias in the seed selection. The differences between the numbers result from minor updates, e.g. switching to the newer, better modelled *mc11* simulation.

Appendix E

The likelihood function

The basis of the statistical analysis form Poisson distributions P for the different regions R, depending both on the measured number of events, n_i, and the expected number of events in this specific region, λ_i. The λ_i, however, show a dependence on

the number of background events b. Various sources are considered in the statistical analysis: QCD jets, W+jets, Z+jets, and $t\bar{t}$, denoted as $b_{i\mathrm{R}}$, e.g. $b_{i\mathrm{QCD}}$ for the (QCD) CR2. Minor backgrounds (e.g. single-top) are treated as fixed contributions to the SR and CRs.

a signal normalization factor μ. μ allows the variation of the signal strength, with $\mu = 0$ describing the absence of a signal and $\mu = 1$ describing the expected signal behaviour for the model under consideration, yielding s signal events.

nuisance parameters θ. Systematic uncertainties such as the JES are parametrised as nuisance parameters.

One has to further distinguish between the signal region expectations, λ_S, and the expected number of events for a specific CR, λ_i. In order to connect the various signal and control regions to each other, an extrapolation matrix C is constructed, comprising for $i \neq j$ the different TFs for the transition from region $i \to j$, denoted $C_{i \to j}$, and otherwise 1. While MC-derived transfer factors suffer mostly from theory uncertaintiesdata driven methods are dominated by other uncertainties, e.g. control region statistics.

Finally, the λ_S and $\lambda_{\boldsymbol{b}}$ can be expressed in terms of the fit parameters s and $\boldsymbol{b}$ and the TFs via

$$\lambda_S(\mu, \mathbf{b}, \boldsymbol{\theta}) = \mu \cdot C_{\mathrm{SR}\to\mathrm{SR}}(\boldsymbol{\theta}) \cdot s + \sum_j C_{j\mathrm{R}\to\mathrm{SR}}(\boldsymbol{\theta}) \cdot b_{j\mathrm{R}}\,, \tag{E.1}$$

$$\lambda_i(\mu, \mathbf{b}, \boldsymbol{\theta}) = \mu \cdot C_{\mathrm{SR}\to\mathrm{iR}}(\boldsymbol{\theta}) \cdot s + \sum_j C_{j\mathrm{R}\to\mathrm{iR}}(\boldsymbol{\theta}) \cdot b_{j\mathrm{R}}\,. \tag{E.2}$$

where the index j runs over the different background CRs.

Each stream of the analysis, i.e. the different sets of one SR and the five associated CRs ($Z + jets$CR a/b, QCD CR, $W + jets$ CR and $t\bar{t}$CR), is described by a product of these Poisson distributions and PDFs constraining the systematic uncertainties $C_{syst.}$ (see Section E.1), forming the likelihood function

$$L(\boldsymbol{n}|\mu, \boldsymbol{b}, \boldsymbol{\theta}) = P_{\mathrm{SR}} \times P_{\mathrm{W}} \times P_{\mathrm{t\bar{t}}} \times P_{\mathrm{Z\,regiona}} \times P_{\mathrm{Z\,regionb}} \times P_{\mathrm{QCD}} \times C_{\mathrm{Syst}}\,. \tag{E.3}$$

The resulting likelihood function, however, differs slightly for the discovery and the exclusion modes. While the discovery mode assumes single bin counting experiments and thus single bin likelihoods, the exclusion mode extends the single bin likelihoods to products of single bin likelihoods.

In the extended mode, that is the inclusion of i validation regions VR to the simultaneous normalisation, the likelihood is expanded to

$$L(\boldsymbol{n}|\mu, \boldsymbol{b}, \boldsymbol{\theta}) = P_{\mathrm{SR}} \times P_{\mathrm{W}} \times P_{\mathrm{t\bar{t}}} \times P_{\mathrm{Z\,regiona}} \times P_{\mathrm{Z\,regionb}} \times P_{\mathrm{QCD}} \times \prod_{i/in\mathrm{VR}} P_{\mathrm{VR,i}} \times C_{\mathrm{Syst}}\,. \tag{E.4}$$

Finally, the exclusion mode likelihood expands to this form, given n bins:

$$L(\boldsymbol{n}|\mu, \boldsymbol{b}, \boldsymbol{\theta}) = \sum_j \left(P_{\mathrm{SR,j}} \times P_{\mathrm{W,j}} \times P_{\mathrm{t\bar{t},j}} \times P_{\mathrm{Z\,regiona,j}} \times P_{\mathrm{Z\,regionb,j}} \times P_{\mathrm{QCD,j}} \right) \times C_{\mathrm{Syst}}\,. \tag{E.5}$$

E.1 Treatment of systematic uncertainties

When $\boldsymbol{\theta}$ varies around a nominal value $\boldsymbol{\theta}^0$, the probability density functions $C_{Syst}(\boldsymbol{\theta}^0, \boldsymbol{\theta})$ are used to include the different systematic uncertainties. The dependence on the signal and background expectations can be limited to the TFs, which simplifies C_{Syst} by taking θ_{i}^0 to be zero and normalising the individual constraint PDFs for θ_i appropriately [14].

The functions $\lambda(\mu, \boldsymbol{b}, \boldsymbol{\theta})$ are the only components of the Poisson expectation values affected by a change in the nuisance parameters. Moreover, when the nuisance parameters are independent for a set SU of systematic uncertainties, C_{Syst} is given by a simple product of the according PDFs (typically Gaussians distributions, normalised to unity),

$$C_{Syst}(\boldsymbol{\theta}^0, \boldsymbol{\theta}) = \prod_{j \in \mathrm{SU}} G(\theta_{\mathrm{j}}^0, \theta_{\mathrm{j}}) \,. \tag{E.6}$$

When the nuisance parameters are correlated, a combined distribution of C_{Syst} is used. On the other hand, when the *impact* of a given combination of θ_a, θ_b is correlated, this is described through the transfer factor $C_{\text{process j, region j}\to\text{i}}$ as follows:

$$C_{\text{process j, region j}\to\text{i}} = C^{\text{nominal}}_{\text{process j, region j}\to\text{i}} \times \left(1 \; + \; \sum_k \; \Delta_{j,i;k} \, \theta_k\right) . \tag{E.7}$$

where $\Delta_{j,i;k}$ is the relative change in the transfer factor for the nuisance parameter θ_k [14].

List of Figures

List of Tables

List of Publications

[1] K. Störig, *Alignment Studies of the ATLAS Silicon Trackers with Overlap Residuals*, diploma thesis, II. Institute of Physics, Georg-August-Universität, Göttingen, 2008.

[2] Störig, K and Grosse-Knetter, J and Kröninger, K and Quadt, A and Göttfert, T, *Alignment Studies of the ATLAS Silicon Trackers with Overlap Residuals*, Tech. Rep. ATL-INDET-INT-2009-001. ATL-COM-INDET-2008-012, CERN, Geneva, Aug, 2008.

[3] ATLAS Collaboration, *Prospects for Supersymmetry discovery based on inclusive searches at a 7 TeV centre-of-mass energy with the ATLAS detector*, Tech. Rep. ATL-PHYS-PUB-2010-010, CERN, Geneva, Jul, 2010.

[4] Ahles, F and Bruneliere, R and Caron, S and Consorti, V and Dietrich, J and Meirose, B and Rurikova, Z and Störig, K and Sundermann, J E and Castaneda, A and Chen, X and Poveda, J and Sarangi, T and Wu, S L and Samset, B, *Prospects for Supersymmetry discovery based on inclusive searches at a 7 TeV centre-of-mass energy with the ATLAS detector*, Tech. Rep. ATL-PHYS-INT-2010-051, CERN, Geneva, May, 2010. *Internal Note.*

[5] Störig, K and Rurikova, Z and Caron, S and Herten, G, *Developing data-driven methods to estimate the QCD background for SUSY searches (Poster)*, . 18th European School of High Energy Physics, ESHEP 2010, Raseborg, Finland, 20 Jun. - 3 Jul., 2010.

[6] Störig, K. and Ahles, F. and Herten, G. and Landgraf, U. and Mohr, W. and Song Xie and Zimmermann, S., *Using electron drift velocity measurements for different electric field strengths to precisely monitor the gas composition in gaseous detectors*, Nuclear Science Symposium Conference Record (NSS/MIC), 2010 IEEE (2010) 962–965.

[7] ATLAS Collaboration, *Search for squarks and gluinos using final states with jets and missing transverse momentum with the ATLAS detector in $\sqrt{s}$ = 7 TeV proton-proton collisions*, 2011. ATLAS-CONF-2011-086.

[8] ATLAS Collaboration, *Search for squarks and gluinos using final states with jets and missing transverse momentum with the ATLAS detector in $\sqrt{s}$ = 7 TeV proton-proton collisions: supporting documentation*, Atl-phys-int-2011-055, 2011. *Internal Note*.

[9] ATLAS Collaboration, G. Aad et al., *Search for squarks and gluinos using final states with jets and missing transverse momentum with the ATLAS detector in sqrts = 7 TeV proton-proton collisions*, Phys.Lett. **B710** (2012) 67–85, arXiv:1109.6572 [hep-ex].

[10] Asai, S and Ask, S and Baak, M and Barr, A J and Bruneliere, R and Caron, S and Chavez Baraja, C and Consorti, V and Cote, D and Dietrich, J and Duflot, L and Eifert, T and Flowerdew, M J and Fonseca-Martin, T and Genest, M-H and Henrot-Versille, S and Hodgkinson, M and Kanaya, N and Kataoka, Y and Khoo, T J and LeCompte, T and van der Leeuw, R and Lester, C G and Majewski, S and Makovec, N and Mann, A and McFayden, J and Niedercorn, F and Owen, S and Parker, M A and Pinder, A and Portell Bueso, X and Rammensee, M and Rave, T and Rurikova, Z and Salek, D and Sandoval, T and Scharf, V and Sfyrla, A and Störig, K and Sundermann, J E and Suruliz, K and Triplett, N and Tovey, D R and Tua, A and Vranjes Milosavljevic, M and Young, C J S and Yurkewicz, A and Zhuang, X, *Further search for squarks and gluinos using final states with jets and missing transverse momentum with the ATLAS experiment in $\sqrt{s}$ = 7 TeV proton-proton collisions: supporting documentation*, Tech. Rep. ATL-PHYS-INT-2011-085, CERN, Geneva, Oct, 2011. *Internal Note*.

[11] ATLAS Collaboration, *Search for squarks and gluinos using final states with jets and missing transverse momentum with the ATLAS detector in $\sqrt{s}$ = 7 TeV proton-proton collisions*, Tech. Rep. ATLAS-CONF-2012-033, CERN, Geneva, Mar, 2012.

[12] Asai, S and Ask, S and Baak, M and Barr, A J and Bruneliere, R and Caron, S and Chavez Baraja, C and Consorti, V and Cote, D and Dietrich, J and Duflot, L and Eifert, T and Fletcher, G and Flowerdew, M J and Fonseca-Martin, T and Genest, M-H and Henrot-Versille, S and Hodgkinson, M and Kanaya, N and Kataoka, Y and Khoo, T J and LeCompte, T and van der Leeuw, R and Lester, C

G and Majewski, S and Makovec, N and Mann, A and McFayden, J and Nakahama, Y and Niedercorn, F and Owen, S and Parker, M A and Petersen, B and Pinder, A and Portell Bueso, X and Rammensee, M and Rave, T and Rurikova, Z and Salek, D and Sandoval, T and Scharf, V and Sfyrla, A and Störig, K and Sundermann, J E and Suruliz, K and Triplett, N and Tovey, D R and Tua, A and Vranjes Milosavljevic, M and Young, C J S and Yurkewicz, A and Zhuang, X, *Search for squarks and gluinos using final states with jets and missing transverse momentum with the ATLAS experiment in* $\sqrt{s} = 7$ *TeV proton-proton collisions: supporting documentation*, Tech. Rep. ATL-PHYS-INT-2012-012, CERN, Geneva, Mar, 2012. *Internal Note.*

[13] ATLAS Collaboration, G. Aad et al., *Search for squarks and gluinos with the ATLAS detector in final states with jets and missing transverse momentum using 4.7* $fb^{-}1$ *of* $\sqrt{s} = 7$ *TeV proton-proton collision data*, arXiv:1208.0949 [hep-ex].

[14] Asai, S and Ask, S and Baak, M and Barr, A J and Besjes, G J and Bruneliere, R and Caron, S ; and Chavez Baraja, C and Consorti, V and Cote, D and Dietrich, J and Duflot, L and Eifert, T and Fletcher, G and Flowerdew, M J and Fonseca-Martin, T and Genest, M-H and Gillam, T and Henrot-Versille, S and Hodgkinson, M and Kanaya, N and Kataoka, Y and Khoo, T J and LeCompte, T and van der Leeuw, R and Lester, C G and Majewski, S and Makovec, N and Mann, A and McFayden, J and Nakahama, Y and Nguyen, D and Niedercorn, F and Owen, S and Parker, M A and Petersen, B and Pinder, A and Portell Bueso, X and Rammensee, M and Rave, T and Rurikova, Z and Salek, D and Sandoval, T and Scharf, V and Sfyrla, A and Störig, K and Sundermann, J E and Suruliz, K and Triplett, N and Tovey, D R and Tua, A and Vranjes Milosavljevic, M and Young, C and Yurkewicz, A and Zhuang, X, *Search for squarks and gluinos using final states with jets and missing transverse momentum with the ATLAS experiment in sqrts = 7 TeV proton-proton collisions: supporting documentation*, Tech. Rep. ATL-PHYS-INT-2012-061, CERN, Geneva, Sep, 2012. *Internal Note.*

Bibliography

[15] F. Halzen and A. Martin, *Quarks & Leptons: An introductory course in modern particle physics*. John Wiley & Sons, New York, USA, 1984.

[16] D. Griffiths, *Introduction to Elementary Particles*. John Wiley & Sons, New York, USA, 1987.

[17] C. Grojean and M. Spiropulu, *High-energy Physics. Proceedings, 18th European School, ESHEP 2010, Raseborg, Finland, 20 Jun. - 3 Jul., 2010*, arXiv:1202.1629 [hep-ph].

[18] S. L. Glashow, *Partial Symmetries of Weak Interactions*, Nucl. Phys. **22** (1961) 579–588.

[19] S. Weinberg, *A Model of Leptons*, Phys. Rev. Lett. **19** (Nov, 1967) 1264–1266. http://link.aps.org/doi/10.1103/PhysRevLett.19.1264.

[20] A. Salam, *WEAK AND ELECTROMAGNETIC INTERACTIONS*, . Originally printed in *Svartholm: Elementary Particle Theory, Proceedings Of The Nobel Symposium Held 1968 At Lerum, Sweden*, Stockholm 1968, 367-377.

[21] S. L. Glashow, J. Iliopoulos, and L. Maiani, *WEAK INTERACTIONS WITH LEPTON - HADRON SYMMETRY*, Phys. Rev. **D2** (1970) 1285–1292.

[22] S. Willenbrock, *Symmetries of the standard model*, hep-ph/0410370.

[23] Particle Data Group Collaboration, S. Eidelman et al., *Review of particle physics*, Phys. Lett. **B592** (2004) 1. http://pdg.lbl.gov/.

[24] E. Noether, *Invarianten beliebiger Differentialausdrücke [Invariants of arbitrary differential expressions]*, Nachr. Ges. Wiss. Gött., Math.-Phys. Kl. **1918** (1918) 37–44. Available at http://resolver.sub.uni-goettingen.de/purl?GDZPPN002504979. JFM 46.0675.01.

[25] E. Noether, *Invariante Variationsprobleme [Invariant variational problems]*, Nachr. Ges. Wiss. Gött., Math.-Phys. Kl. (1918) 235–257. Available at http://www.physics.ucla.edu/~cwp/articles/noether.trans/german/emmy235.html. JFM 46.0770.01.

[26] Quantum Diaries, 2011. http://www.quantumdiaries.org/2011/11/21/.

[27] F. Englert and R. Brout, *BROKEN SYMMETRY AND THE MASS OF GAUGE VECTOR MESONS*, Phys. Rev. Lett. **13** (1964) 321–323.

[28] G. S. Guralnik, C. R. Hagen, and T. W. B. Kibble, *Global Conservation Laws and Massless Particles*, Phys. Rev. Lett. **13** (Nov, 1964) 585–587. http://link.aps.org/doi/10.1103/PhysRevLett.13.585.

[29] P. Higgs, *Broken symmetries, massless particles and gauge fields*, Physics Letters **12** (1964) no. 2, 132 – 133. http://www.sciencedirect.com/science/article/pii/0031916364911369.

[30] P. W. Higgs, *Broken Symmetries and the Masses of Gauge Bosons*, Phys. Rev. Lett. **13** (Oct, 1964) 508–509. http://link.aps.org/doi/10.1103/PhysRevLett.13.508.

[31] ATLAS Collaboration, G. Aad et al., *Observation of a new particle in the search for the Standard Model Higgs boson with the ATLAS detector at the LHC*, Phys.Lett. **B716** (2012) 1–29, arXiv:1207.7214 [hep-ex].

[32] M. Baak, M. Goebel, J. Haller, A. Hoecker, D. Ludwig, et al., *Updated Status of the Global Electroweak Fit and Constraints on New Physics*, arXiv:1107.0975 [hep-ph].

[33] Nobelprize.org, *The 2004 Nobel Prize in Physics - Popular Information*, 2012. http://www.nobelprize.org/nobel_prizes/physics/laureates/2004/popular.html.

[34] Y. Golfand and E. Likhtman, *Extension of the Algebra of Poincare Group Generators and Violation of p Invariance*, JETP Lett. **13** (1971) 323–326.

[35] A. Neveu and J. Schwarz, *Factorizable dual model of pions*, Nucl. Phys. **B31** (1971) 86–112.

[36] A. Neveu and J. Schwarz, *Quark Model of Dual Pions*, Phys. Rev. **D4** (1971) 1109–1111.

[37] R. Ramond, *Dual Theory for Free Fermions*, Phys. Rev. **D3** (1971) 2415–2418.

[38] D. Volkov and V. Akulov, *Is the Neutrino a Goldstone Particle?*, Phys. Lett. **B46** (1973) 109–110.

[39] J. Wess and B. Zumino, *A Lagrangian Model Invariant Under Supergauge Transformations*, Phys. Lett. **B49** (1974) 52.

[40] J. Wess and B. Zumino, *Supergauge Transformations in Four-Dimensions*, Nucl. Phys. **B70** (1974) 39–50.

[41] H. Baer and X. Tata, *Weak scale supersymmetry: From superfields to scattering events*. Cambridge University Press, 2006.

[42] S. P. Martin, *A Supersymmetry primer*, arXiv:hep-ph/9709356 [hep-ph].

[43] I. J. Aitchison, *Supersymmetry and the MSSM: An Elementary introduction*, arXiv:hep-ph/0505105 [hep-ph]. Notes of Lectures for Graduate Students in Particle Physics Oxford, 2004 and 2005.

[44] R. N. Mohapatra, *Unification and supersymmetry: the frontiers of quark-lepton physics; 2nd ed.* Graduate texts in contemporary physics. Springer, New York, NY, 1992. Includes exercises.

[45] L. Hall, J. Lykken, and S. Weinberg, *Supergravity as the messenger of supersymmetry breaking*, Phys. Rev. D **27** (May, 1983) 2359–2378.

[46] R. Barbieri, S. Ferrara, and C. Savoy, *Gauge models with spontaneously broken local supersymmetry*, Physics Letters B **119** (1982) no. 4-6, 343 – 347. http://www.sciencedirect.com/science/article/B6TVN-470G3C1-GH/2/e7aa2fcf0a572ba31914582a5f04924d.

[47] ATLAS Collaboration, *Expected Performance of the ATLAS Experiment - Detector, Trigger and Physics*, CERN-OPEN-2008-020. arXiv:0901.0512 [hep-ex].

[48] Particle Data Group Collaboration, K. Nakamura et al., *Review of particle physics*, J.Phys. **G37** (2010) 075021.

[49] Particle Data Group Collaboration, J. Beringer et al., *Review of Particle Physics*, Phys. Rev. D **86** (Jul, 2012) 010001. http://link.aps.org/doi/10.1103/PhysRevD.86.010001.

[50] CDF Collaboration, T. Aaltonen et al., *Inclusive Search for Squark and Gluino Production in $p\bar{p}$ Collisions at $\sqrt{s} = 1.96$-TeV*, Phys. Rev. Lett. **102** (2009) 121801, arXiv:0811.2512 [hep-ex].

[51] D0 Collaboration, V. M. Abazov et al., *Search for squarks and gluinos in events with jets and missing transverse energy using 2.1 fb^{-1} of $p\bar{p}$ collision data at $\sqrt{s} = 1.96$ TeV*, Phys. Lett. **B660** (2008) 449–457, arXiv:0712.3805 [hep-ex].

[52] E. Komatsu, K. M. Smith, J. Dunkley, C. L. Bennett, B. Gold, G. Hinshaw, N. Jarosik, D. Larson, M. R. Nolta, L. Page, D. N. Spergel, M. Halpern, R. S. Hill, A. Kogut, M. Limon, S. S. Meyer, N. Odegard, G. S. Tucker, J. L. Weiland, E. Wollack, and E. L. Wright, *Seven-year Wilkinson Microwave Anisotropy Probe (WMAP) Observations: Cosmological Interpretation*, ApJS**192** (Feb., 2011) 18, arXiv:1001.4538 [astro-ph.CO].

[53] Lep Injector Study Group Collaboration, *LEP DESIGN REPORT. VOL. 1. THE LEP INJECTOR CHAIN*, . CERN-LEP/TH/83-29.

[54] *LEP DESIGN REPORT: VOL. 2. THE LEP MAIN RING*, . CERN-LEP-84-01.

[55] *LEP design report. 1. The LEP injector chain*, . CERN-LEP-84-01.

[56] ATLAS Collaboration, 2012. https://twiki.cern.ch/twiki/bin/view/AtlasPublic/CombinedSummaryPlots.

[57] ATLAS Collaboration, G. Aad et al., *Search for squarks and gluinos using final states with jets and missing transverse momentum with the ATLAS detector in $\sqrt{s} = 7$ TeV proton-proton collisions*, Phys.Lett. **B701** (2011) 186–203, arXiv:1102.5290 [hep-ex].

[58] ATLAS Collaboration, F. Ahles et al., *Search for squarks and gluinos using final states with jets and missing transverse momentum with the ATLAS detector in $\sqrt{s} = 7$ TeV proton-proton collisions: Version 1.0*, Dec, 2010. Support note of the jets+MET SUSY paper.

[59] ATLAS Collaboration, *Search for squarks and gluinos using final states with jets and missing transverse momentum with the ATLAS detector in $\sqrt{s} = 7$ TeV proton-proton collisions: supporting documentation*, Atl-phys-int-2011-055, 2011. *Internal Note.*

[60] ATLAS Collaboration, *Search for squarks and gluinos using final states with jets and missing transverse momentum with the ATLAS detector in $\sqrt{s} = 7$ TeV proton-proton collisions*, 2011. ATLAS-CONF-2011-086.

[61] W.J. Stirling, 2012. private communication.

[62] J. C. Collins, D. E. Soper, and G. F. Sterman, *Factorization of Hard Processes in QCD*, Adv.Ser.Direct.High Energy Phys. **5** (1988) 1–91, arXiv:hep-ph/0409313 [hep-ph]. To be publ. in 'Perturbative QCD' (A.H. Mueller, ed.) (World Scientific Publ., 1989).

[63] B. Andersson, G. Gustafson, G. Ingelman, and T. Sjostrand, *Parton Fragmentation and String Dynamics*, Phys. Rept. **97** (1983) 31–145.

[64] B. Webber, *A QCD Model for Jet Fragmentation Including Soft Gluon Interference*, Nucl.Phys. **B238** (1984) 492.

[65] G. Marchesini and B. Webber, *Monte Carlo Simulation of General Hard Processes with Coherent QCD Radiation*, Nucl.Phys. **B310** (1988) 461.

[66] A. Martin, W. Stirling, R. Thorne, and G. Watt, *Heavy-quark mass dependence in global PDF analyses and 3- and 4-flavour parton distributions*, Eur.Phys.J. **C70** (2010) 51–72, arXiv:1007.2624 [hep-ph].

[67] A. Martin, W. Stirling, R. Thorne, and G. Watt, *Parton distributions for the LHC*, Eur.Phys.J. **C63** (2009) 189–285, arXiv:0901.0002 [hep-ph].

[68] A. Martin, W. Stirling, R. Thorne, and G. Watt, *Uncertainties on alpha(S) in global PDF analyses and implications for predicted hadronic cross sections*, Eur.Phys.J. **C64** (2009) 653–680, arXiv:0905.3531 [hep-ph].

[69] T. Sjostrand, *Monte Carlo Generators*, arXiv:hep-ph/0611247 [hep-ph].

[70] M. Dobbs, S. Frixione, E. Laenen, K. Tollefson, H. Baer, et al., *Les Houches guidebook to Monte Carlo generators for hadron collider physics*, arXiv:hep-ph/0403045 [hep-ph]. Compiled by the Working Group on Quantum Chromodynamics and the Standard Model.

[71] M. Dobbs and J. B. Hansen, *The HepMC C++ Monte Carlo Event Record for High Energy Physics*, Tech. Rep. ATL-SOFT-2000-001, CERN, Geneva, Jun, 2000. revised version number 1 submitted on 2001-02-27 09:54:32.

[72] The ATLAS Collaboration - Workbook, 2012. https://twiki.cern.ch/twiki/bin/viewauth/Atlas/WorkBookFullChain.

[73] GEANT4 Collaboration, S. Agostinelli et al., *GEANT4: A simulation toolkit*, Nucl. Instrum. Meth. **A506** (2003) 250–303.

[74] E. Richter-Was, D. Froidevaux, and L. Poggioli, *ATLFAST 2.0 a fast simulation package for ATLAS*, Tech. Rep. ATL-PHYS-98-131, CERN, Geneva, Nov, 1998.

[75] T. Sjostrand, S. Mrenna, and P. Z. Skands, *PYTHIA 6.4 Physics and Manual*, JHEP **0605** (2006) 026, arXiv:hep-ph/0603175.

[76] T. Sjostrand, S. Mrenna, and P. Z. Skands, *A Brief Introduction to PYTHIA 8.1*, Comput. Phys. Commun. **178** (2008) 852–867, arXiv:0710.3820.

[77] G. Corcella et al., *HERWIG 6.5 release note*, 2002. arXiv:hep-ph/0210213.

[78] F. Krauss, A. Schalicke, S. Schumann, and G. Soff, *Simulating W/Z+jets production at the CERN LHC*, Phys. Rev. **D72** (2005) 054017, arXiv:hep-ph/0503280.

[79] M. L. Mangano, M. Moretti, F. Piccinini, R. Pittau, and A. D. Polosa, *ALPGEN, a generator for hard multiparton processes in hadronic collisions*, JHEP **07** (2003) 001, arXiv:hep-ph/0206293.

[80] W. Kilian, T. Ohl, and J. Reuter, *WHIZARD: Simulating Multi-Particle Processes at LHC and ILC*, Eur.Phys.J. **C71** (2011) 1742, arXiv:0708.4233 [hep-ph].

[81] M. Moretti, T. Ohl, and J. Reuter, *O'Mega: An Optimizing matrix element generator*, arXiv:hep-ph/0102195 [hep-ph].

[82] P. Nason, *A New method for combining NLO QCD with shower Monte Carlo algorithms*, JHEP **0411** (2004) 040, arXiv:hep-ph/0409146 [hep-ph].

[83] S. Frixione, P. Nason, and C. Oleari, *Matching NLO QCD computations with parton shower simulations: the POWHEG method*, JHEP **0711** (2007) 070, arXiv:0709.2092 [hep-ph].

[84] ATLAS Collaboration, *ATLAS Monte Carlo tunes for MC09*, Atl-phys-pub-2010-002, 2010.

[85] G. Altarelli and G. Parisi, *Asymptotic Freedom in Parton Language*, Nucl. Phys. **B126** (1977) 298.

[86] P. Skands, *QCD for Collider Physics. oai:cds.cern.ch:1345043*, . Comments: Lectures from the 2010 European School of High Energy Physics (ESHEP 2010), Raseborg, Finland.

[87] S. Frixione and B. Webber, *The MC@NLO 3.2 event generator, hep-ph/0601192*, 2006. arXiv:hep-ph/0601192.

[88] S. Frixione and B. Webber, *Matching NLO QCD computations and parton shower simulations*, JHEP **06** (2002) 029, arXiv:hep-ph/0204244.

[89] S. Frixione, E. Laenen, P. Motylinski, and B. R. Webber, *Single-top production in MC@NLO*, JHEP **03** (2006) 092, arXiv:hep-ph/0512250.

[90] S. Frixione, E. Laenen, P. Motylinski, B. R. Webber, and C. D. White, *Single-top hadroproduction in association with a W boson*, JHEP **07** (2008) 029, arXiv:0805.3067 [hep-ph].

[91] M. B. *et al.*, *Herwig++ Physics and Manual*, Eur. Phys. J. **C58** (2008) 639–707, arXiv:0803.0883 [hep-ph].

[92] M. B. *et al.*, *Herwig++ 2.3 release note, arXiv:0812.0529*, 2008. arXiv:0812.0529 [hep-ph].

[93] G. Corcella et al., *HERWIG 6.5: an event generator for Hadron Emission Reactions With Interfering Gluons (including supersymmetric processes)*, JHEP **01** (2001) 010, arXiv:hep-ph/0011363.

[94] J. M. Butterworth, J. R. Forshaw, and M. H. Seymour, *Multiparton interactions in photoproduction at HERA*, Z. Phys. **C72** (1996) 637–646, arXiv:hep-ph/9601371.

[95] R. H. W. Beenakker and M. Spira, *PROSPINO: A program for the production of supersymmetric particles In next-to-leading order QCD, hep-ph/9611232*, 1996. arXiv:hep-ph/9611232.

[96] W. Beenakker, R. Hopker, M. Spira, and P. M. Zerwas, *Squark and gluino production at hadron colliders*, Nucl. Phys. **B492** (1997) 51–103, arXiv:hep-ph/9610490.

[97] H. B. F.E. Paige, S.D. Protopopescu and X. Tata, *ISAJET 7.69: A Monte Carlo event generator for p p, anti-p p, and e+ e- reactions, hep-ph/0312045*, 2003. arXiv:hep-ph/0312045.

[98] F. E. Paige, S. D. Protopopescu, H. Baer, and X. Tata, *ISAJET 7.69: A Monte Carlo event generator for pp, anti-p p, and e+e- reactions*, arXiv:hep-ph/0312045 [hep-ph].

[99] G. S. M. Cacciari and G. Soyez, *The anti-k_t jet clustering algorithm*, JHEP **04** (2008) 063, arXiv:0802.1189 [hep-ph].

[100] M. Cacciari and G. P. Salam, *Dispelling the N^3 myth for the k_t jet-finder*, Phys. Lett. **B641** (2006) 57–61, arXiv:hep-ph/0512210.

[101] ATLAS Collaboration, 2009. http://www.ccsem.infn.it/issp2009/newtalents/KPerez_Erice_JetAlgs_20090905.pdf.

[102] ATLAS Collaboration, *Jet energy scale and its systematic uncertainty in proton-proton collisions at $\sqrt{s}$ =7 TeV in ATLAS 2010 data*, Tech. Rep. ATLAS-CONF-2011-032, CERN, Geneva, Mar, 2011.

[103] D0 Collaboration, V. M. *et al.*. Abazov, *Search for squarks and gluinos in events with jets and missing transverse energy using 2.1 fb^{-1} of $p\bar{p}$ collision data at $\sqrt{s}$ = 1.96 TeV*, Phys. Lett. **B660** (2008) 449–457, arXiv:0712.3805 [hep-ex].

[104] ATLAS Collaboration, *The ATLAS Experiment at the CERN Large Hadron Collider*, 2008. JINST **3** (2008) S08003.

[105] The ATLAS experiment - Mapping the Secrets of the Universe, 2008. http://www.atlasexperiment.org.

[106] L. Evans and P. Bryant, *LHC Machine*, JINST **3** (2008) S08001.

[107] Large Hadron Collider - LHC, 2012. http://twitter.com/#!/cern.

[108] O. Bruning et al., *LHC design report. Vol. I: The LHC main ring*, . CERN-2004-003-V-1.

[109] O. Bruning et al., *LHC Design Report. 2. The LHC infrastructure and general services*, . CERN-2004-003-V-2.

[110] CERN - European Organisation for Nuclear Research, 2008. http://public.web.cern.ch/Public.

[111] V. L. Ginzburg, L. D. Landau, *On the Theory of Superconductivity*, Zh. Eksp. Teor. Fiz. **20** (1950) 1064.

[112] ATLAS Collaboration, W. W. Armstrong et al., *ATLAS: Technical proposal for a general-purpose p p experiment at the Large Hadron Collider at CERN*, . CERN-LHCC-94-43.

[113] ATLAS Collaboration, *ATLAS: Detector and physics performance technical design report. Volume 1*, . CERN-LHCC-99-14.

[114] ATLAS Collaboration, *ATLAS detector and physics performance. Technical design report. Vol. 2*, . CERN-LHCC-99-15.

[115] *CMS, the Compact Muon Solenoid: Technical proposal*, . CERN-LHCC-94-38.

[116] CMS Collaboration, G. L. Bayatian et al., *CMS technical design report, volume II: Physics performance*, J. Phys. **G34** (2007) 995–1579.

[117] CMS Collaboration, G. L. Bayatian et al., *CMS physics: Technical design report*, . CERN-LHCC-2006-001.

[118] *ALICE: Technical proposal for a large ion collider experiment at the CERN LHC*, . CERN-LHCC-95-71.

[119] LHCb Collaboration, S. Amato et al., *LHCb technical proposal*, . CERN-LHCC-98-04.

[120] LHCb Collaboration, *LHCb technical design report: Reoptimized detector design and performance*, . CERN-LHCC-2003-030.

[121] LHCf Collaboration, O. Adriani et al., *Technnical proposal for the CERN LHCf experiment: Measurement of photons and neutral pions in the very forward region of LHC*, . CERN-LHCC-2005-032.

[122] LHCf Collaboration, O. Adriani et al., *Technical design report of the LHCf experiment: Measurement of photons and neutral pions in the very forward region of LHC*, . CERN-LHCC-2006-004.

[123] TOTEM Collaboration, V. Berardi et al., *TOTEM: Technical design report. Total cross section, elastic scattering and diffraction dissociation at the Large Hadron Collider at CERN*, . CERN-LHCC-2004-002.

[124] TOTEM Collaboration, V. Berardi et al., *TOTEM: Technical design report - Addendum. Total cross section, elastic scattering and diffraction dissociation at the Large Hadron Collider at CERN*, . CERN-LHCC-2004-020.

[125] L. Rossi, *Superconductivity: its role, its success and its setbacks in the Large Hadron Collider of CERN*, Superconductor Science and Technology **23** (2010) no. 3, 034001. http://stacks.iop.org/0953-2048/23/i=3/a=034001.

[126] I. Bird et al., *LHC computing Grid. Technical design report*, . CERN-LHCC-2005-024.

[127] ATLAS Collaboration, D. Froidevaux and M. Vincter, *ATLAS Detector Paper - Draft 4*, 2008.

[128] Particle Adventure by Particle Data Group, 2012. http://www.particleadventure.org/component_detector.html.

[129] S. Haywood, *Local Coordinate Frames for the Alignment of Silicon Detectors*, Tech. Rep. ATL-COM-INDET-2004 and ATL-INDET-2004-001, RAL, July, 2004.

[130] ATLAS Collaboration, *ATLAS inner detector: Technical design report. Vol. 1*, . CERN-LHCC-97-16.

[131] ATLAS Collaboration, *ATLAS inner detector: Technical design report. Vol. 2*, . CERN-LHCC-97-17.

[132] ATLAS Collaboration, *ATLAS magnet system: Technical design report*, . CERN-LHCC-97-18.

[133] ATLAS Collaboration, *ATLAS central solenoid: Technical design report*, . CERN-LHCC-97-21.

[134] *Atlantis - Event display for ATLAS*, 2008. http://www.cern.ch/atlantis.

[135] ATLAS Collaboration, M. S. Alam et al., *ATLAS pixel detector: Technical design report*, . CERN-LHCC-98-13 and CERN-LHCC-97-16.

[136] ATLAS Collaboration, *ATLAS tile calorimeter: Technical design report*, . CERN-LHCC-96-42.

[137] ATLAS Collaboration, *ATLAS liquid argon calorimeter: Technical design report*, . CERN-LHCC-96-41.

[138] ATLAS Collaboration, *ATLAS barrel toroid: Technical design report*, . CERN-LHCC-97-19.

[139] ATLAS Collaboration, *ATLAS end-cap toroids: Technical design report*, . CERN-LHCC-97-20.

[140] ATLAS Collaboration, *ATLAS muon spectrometer: Technical design report*, . CERN-LHCC-97-22.

[141] ATLAS Level-1 Trigger Group, *Level-1 Trigger Technical Design Report*, 1998.

[142] ATLAS HLT/DAQ/DCS Group, *High-Level Trigger, Data Acquisition and Controls Technical Design Report*, 2003.

[143] W. Lampl et al., *Calorimeter Clustering Algorithms: Description and Performance*, Tech. Rep. ATL-LARG-PUB-2008-002, CERN, 2011 .

[144] ATLAS Collaboration, T. A. collaboration, *Jet energy scale and its systematic uncertainty in ATLAS for jets produced in proton-proton collisions at* $\sqrt{s} = 7\ TeV$, Atlas-conf-2010-056, June, 2010.

[145] ATLAS Collaboration, *Jet energy scale and its systematic uncertainty for jets produced in proton-proton collisions at* $\sqrt{s} = 7\ TeV$ *and measured with the ATLAS detector*, 2010. ATLAS-CONF-2010-056.

[146] ATLAS Luminosity Working Group Collaboration, *Preliminary Calibration of Luminosity for 2011*, https://indico.cern.ch/getFile.py/access?contribId=7&resId=0&materialId=slides&confId=106717.

[147] ATLAS Collaboration, 2012. https://twiki.cern.ch/twiki/bin/view/AtlasPublic/LuminosityPublicResults.

[148] ATLAS SUSY Working Group Collaboration. https://twiki.cern.ch/twiki/bin/view/AtlasProtected/SUSYD3PDMaker, 2011.

[149] ATLAS Jet Trigger Group Collaboration, ATLAS, *The Design and Performance of the ATLAS Jet Trigger for the Event Filter*, 2011.

[150] D. Casadei et al., *The implementation of the ATLAS missing Et triggers for the initial LHC operation*, Feb, 2011.

[151] M. Baak, 2010. http://atlas-service-enews.web.cern.ch/atlas-service-enews/2010/features_10/features_goodrun.php.

[152] ATLAS Collaboration, *First tuning of HERWIG/JIMMY to ATLAS data*, 2010. ATL-PHYS-PUB-2010-014.

[153] ATLAS Collaboration, *Charged particle multiplicities in pp interactions at* $\sqrt{s} = 0.9$ *and 7 TeV in a diffractive limited phase-space measured with the ATLAS detector at the LHC and new PYTHIA6 tune*, 2010. ATLAS-CONF-2010-031.

[154] P. Calafiura, W. Lavrijsen, C. Leggett, M. Marino, and D. Quarrie, *The athena control framework in production, new developments and lessons learned*, .

[155] ATLAS Collaboration, *Search for Supersymmetry with jets and missing transverse momentum and one lepton at* $\sqrt{s} = 7$ TeV *(supporting INT note)*, 2011. ATL-COM-PHYS-2011-507.

[156] A. Sherstnev and R. Thorne, *Parton Distributions for LO Generators*, Eur. Phys. J. **C55** (2008) 553–575, arXiv:0711.2473 [hep-ph].

[157] S. Frixione, P. Nason, and B. R. Webber, *Matching NLO QCD and parton showers in heavy flavour production*, JHEP **08** (2003) 007, arXiv:hep-ph/0305252.

[158] P. M. Nadolsky et al., *Implications of CTEQ global analysis for collider observables*, Phys. Rev. **D78** (2008) 013004.

[159] ATLAS Collaboration, *Jet energy resolution and selection efficiency relative to track jets from in-situ techniques with the ATLAS Detector Using Proton-Proton Collisions at a Center of Mass Energy* $\sqrt{s} = 7$ *TeV*, 2010.

[160] H. M. Antia, *Numerical Methods for Scientists and Engineers*. Birkhäuser Basel, 2nd edition ed., 2002.

[161] ATLAS Collaboration, G. Aad et al., *The ATLAS Simulation Infrastructure*, Eur. Phys. J. **C70** (2010) 823–874, arXiv:1005.4568 [physics.ins-det].

[162] *ATLAS tunes of PYTHIA 6 and Pythia 8 for MC11*, Tech. Rep. ATL-PHYS-PUB-2011-009, CERN, Geneva, Jul, 2011.

[163] *Further ATLAS tunes of PYTHIA6 and Pythia 8*, Tech. Rep. ATL-PHYS-PUB-2011-014, CERN, Geneva, Nov, 2011.

[164] *First tuning of HERWIG/JIMMY to ATLAS data*, Tech. Rep. ATL-PHYS-PUB-2010-014, CERN, Geneva, Oct, 2010.

[165] A. L. Read, *Presentation of search results: the CL s technique*, Journal of Physics G: Nuclear and Particle Physics **28** (2002) no. 10, 2693. http://stacks.iop.org/0954-3899/28/i=10/a=313.

[166] DELPHI Collaboration Collaboration, J. Abdallah et al., *Searches for supersymmetric particles in e+ e- collisions up to 208-GeV and interpretation of the results within the MSSM*, Eur.Phys.J. **C31** (2003) 421–479, arXiv:hep-ex/0311019 [hep-ex].

[167] I. Hinchliffe, 2005. http://alxr.usatlas.bnl.gov/lxr-stb5/source/atlas/Generators/MC10JobOptions/share.

[168] ATLAS Collaboration, S. Owen, *Data-driven estimation of the QCD multijet background to SUSY searches with jets and missing transverse momentum at ATLAS using jet smearing*, 2011. ATL-COM-PHYS-2011-1066.

Acknowledgements

First and foremost, I want to cordially thank Prof. Gregor Herten for giving me the possibility to spent my PhD studies in Freiburg, participating in this unique endeavour of doing particle physics research in these adventuruos early-LHC times.
I also would like to thank Dr. Sascha Caron, who coordinated our local SUSY search efforts, offered corrections for this thesis and always showed an open mind for new ideas. In addition, Dr. Zuzana Rúriková must be mentioned here, who greatly supervised the everyday work, had the hard part in correcting my thesis and offered sheer endless support and new insights whenever needed and/or welcome. Thanks, Zuzana, it was a pleasure to work with you!

Furthermore, I have to thank all my Freiburger colleagues, especially Michael, Valerio, and Kim, not only for the nice work, but also for the distractions whenever needed and pleasant. In addition, I am grateful for the hardware experiences I gained when working with Stephanie, Jörg and Song. Moreover, I have to mention all the interesting people I met during my shifts on the ATLAS muon and run control desk and on various other meetings, conferences and summer schools, Johannes, Peter, Pawel, Bernhard, Kristof, Alex and the others, you know who - it was a wonderful time. Thanks, Ayan, Christian and Debra for proofreading my thesis.
My sincere thanks are also given to Alex, for enlighten me in various exciting discussions with the IT-way of programming and life, and for being caring, uncomplaining and supportive in any circumstance.

Last but not least, my family should be mentioned here, showing support during all phases of my life, encouraging and supporting me, and being especially patient when I forgot the world around while working.